Fracture Mechanics of Silicon: From durability of photovoltaic modules to the production of thin film solar cells

Irene Berardone

Fracture Mechanics of Silicon

From durability of photovoltaic modules to the production of thin film solar cells

Tesi per il conseguimento del titolo di Dottore di Ricerca
XXVIII Ciclo (2014 - 2015 - 2016)

Dottorato di Ricerca in Ingegneria delle Strutture
Politecnico di Torino

Marzo 2016

Dottorato di Ricerca in Ingegneria delle Strutture
Politecnico di Torino, Corso Duca degli Abruzzi 24, 10129 Torino, Italy

Tutore: Prof. Marco Paggi

Coordinatore: Prof. Giuseppe Lacidogna

To my parents

Acknowledgements

The research presented in this thesis was carried out at the Department of Structural, Geotechnical and Building Engineering of Politecnico di Torino and at the IMT Scholar for Advanced studies Lucca, under the supervision of Prof. Marco Paggi and at the ISFH Institute for Solar Energy Research Hamelin (Germany) under the supervision of Dr. Sarah Kajari Schroeder and the support of MEMO group's members, in particular Eng. Jan Hensen.
The results presented in this thesis have received funding from the European Research Council under the European Union's Seventh Framework Programme (FP/2007-2013)/ERC Grant Agreement No. 306622 (ERC Starting Grant Multi-field and Multiscale Computational Approach to Design and Durability of PhotoVoltaic Modules-CA2PVM), from the Italian Ministry of Education, University and Research under the Project FIRB 2010 Future in Research Structural Mechanics Models for Renewable Energy Applications (RBFR107AKG) and from the German Academic Exchange Service (DAAD) with an individual scholarship.
I would like to thank my advisor, Prof. Paggi, who firstly introduced me to Fracture Mechanics, for his advice and suggestions.

Special thanks to my parents for all the support and care they have given me during my whole university studies.

Summary

Nowadays the photovoltaic research is focused on increasing the performances, the durability and reducing the cost of production of solar cells, such as PV modules. These are the paromount fields to make photovoltaics more attractive for the energetic market. In this dissertation two of these aspects are investigated: the durability and the cost reduction issues. The fracture mechanics of the Silicon, the standard material used for the solar cells, is the main subject of the presented study.
In the recent and next years the relevance of the durability studies is expected to increase more and more because of the developing of a new segment of PV, the building integrated Photovoltaic (BIPV). These new products incorporating PV modules in the building materials are curtains, walls, windows, sloped roofs, flat roofs, facades, shading systems and roofing shingles. In the new generation of BIPV systems, PV modules replace parts of the building structure, providing functional considerations and lowering costs.
In this market the thin-film PV is the most promising technology because of its superior flexibility, minimal weight, and the ability to perform in variable lighting conditions. The issues of this particular PV market are not only the energy production but also the structural safety and performance in addition to architectural specifics as the shadowing. In this framework the durability, the degradation and new technology to achieve a cost reduction are of fundamental importance.

In this thesis, experimental diagnostic techniques and interpretative models based on linear and nonlinear fracture mechanics for studying the phenomena of fracture in Silicon are presented. In particular the development and the use of techniques for the quantitative analysis of electroluminescence signals, for the detection of cracks in Silicon caused by thermo-elastic stresses, have been developed. The experimental results have been obtained during an extensive experimental campaign conducted at Politecnico di Torino.
For the interpretation of the experimental evidence it has been proposed an original one-dimensional electrical model for predicting the effect of cracks on the distribution of electric current. Subsequently, the electric field has been coupled to the mechanical, introducing an electric resistance located at the level of the crack and dependent on the crack itself.
In parallel, a numerical analysis has been carried out, using the finite element codes FRANC2D and FEAP, on the phenomenon of peeling in mono-crystalline Silicon induced by thermo-elastic stresses. This study, which can be very important in applications because it may allow the production of ultra-thin solar cells with a significant saving of material, is carried out in collaboration with the Institute for Solar Energy Research (ISFH), Hamelin, Germany. This process exploits the thermo-mechanical stresses due to the contrast between the elastic pro-

perties of Silicon and Aluminium in line with earlier studies of the school of Harvard. It has been proposed a broad campaign experimental and numerical in order to optimize the process.

Sommario

Oggi la ricerca fotovoltaica è incentrata sul miglioramento delle prestazioni, sulla durabilità e sulla riduzione dei costi di produzione delle celle solari e dei moduli fotovoltaici. Il progresso in questi campi è di vitale importanza per rendere il fotovoltaico più attraente per il mercato energetico. In questa dissertazione sono state indagate due delle aree di ricerca sopra mensionate: la durabilità e la riduzione dei costi di produzione. La meccanica della frattura del silicio, il materiale standard utilizzato per le celle solari, è l'argomento principale di questa tesi.
Negli ultimi anni la rilevanza degli studi di durabilità è aumentata sempre di più a causa dello sviluppo di un nuovo segmento del fotovoltaico, il fotovoltaico integrato nell'edificio. Questi nuovi prodotti incorporano moduli fotovoltaici nei materiali da costruzione come (pareti, finestre, tetti inclinati, tetti piani, facciate, sistemi di ombreggiamento e tegole di copertura). Nella nuova generazione di sistemi BIPV, i moduli fotovoltaici sostituiscono parti della struttura dell'edificio, fornendo supporto funzionale e riducendo i costi.
In questo mercato il fotovoltaico a film sottile è la tecnologia più promettente per la sua maggiore flessibilità, peso minimo e la capacità di operare in condizioni di illuminazione variabile. I problemi di questo particolare mercato fotovoltaico sono non solo la produzione di energia, ma anche la sicurezza strutturale, le prestazioni, le specifiche architettoniche e l'ombreggiamento. In questo quadro la durabilità, la degradazione e le nuove tecnologie a film sottile volte ad ottenere una riduzione dei costi, sono di fondamentale importanza.
In questa tesi sono state presentate tecniche diagnostiche sperimentali e modelli interpretativi basati sulla meccanica della frattura lineare e non lineare per lo studio e la modellazione dei materiali usati nelle applicazioni fotovoltaiche.
Il lavoro di ricerca ha riguardato l'analisi sperimentale e modellistica dei fenomeni di microfessurazione nelle celle solari dovuti a carichi di natura meccanica o termica. Si sono sviluppati modelli elettrici in presenza di frattura nelle celle solari di silicio monocristallino considerando diversi tipi di danneggiamento, localizzato o diffuso. I risultati numerici sono stati validati da dati sperimentali ed il modello è stato esteso anche al silicio policristallino. In seguito il campo elettrico è stato accoppiato a quello meccanico introducendo una resistenza elettrica localizzata a livello della fessura e dipendente dall'apertura fessura stessa.
Per quanto riguarda l'ambito della riduzione dei costi di produzione lo studio è stato incentrato sulla possibilità di utilizzare il fenomeno della frattura nel silicio per realizzare celle fotovoltaiche ultra sottili al fine di risparmiare materiale rispetto ai processi industriali basati sui metodi standard di taglio. Il processo analizzato sfrutta le sollecitazioni termo-meccaniche, dovute al contrasto tra le proprietà elastiche del silicio e dell'alluminio, in linea con i pre-

cedenti studi della scuola di Harward. É stata proposta un'ampia campagna sperimentale e numerica al fine di ottimizzare il processo.

Contents

Chapter 1

Introduction

Durability of photovoltaic (PV) modules and the reduction of costs for solar cells production are the main topics of this dissertation. After a review of the state-of-the-art concerning these two topics, a brief description of the research aims and the novel contributions in this doctoral thesis is presented. The Chapter is completed by the dissertation outline.

1.1 Motivation

Increasing the performances, the durability and reducing at the same time the cost of production of solar cells and PV modules are key issues to make photovoltaics even more attractive for the energetic market.
In the recent years and in the future the relevance of durability of PV modules is expected to be revelant due to the development of a new segment of PV, that is the building integrated Photovoltaics (BIPV). The new products incorporating solar cells PV buildings are curtain, wall, windows, sloped roofs, flat roofs, facades, shading systems and roofing shingles. The first generation of BIPV simply proposed solar panels mounted onto the building, without taking into account aesthetic considerations. In the new generation of BIPV systems, PV modules will replace parts of the building structure, providing functional and structural roles. In this market the thin-film PV is one of the most promising technologies because of their superior flexibility, minimal weight, and the ability to produce energy in variable sunlight conditions.

Sometimes this segment of the PV market is erroneously confused with building applied photovoltaics (BAPV). In this latter case photovoltaic solutions are added to the building after its construction. Instead, the BIPV requires a building team composed by architects, building designers, engineers, utility companies working together to build the PV in the building as an unique element. The BIPV is classified in several ways and it is divided into the following group of products: foil, tile, module and solar cell [1]. BIPV foil products are usually made from thin-film solar cells and they are very light, flexible, efficient at high temperatures and for this reason they are used on non-ventilated roofs. The BIPV module products are very similar to standard PV modules but they have in addition weather skin solutions to replace roofing. The BIPV may be customized by the manufactures to fit particular roofs. The BIPV

mounting systems increase the ease of installation. BIPVs as solar cell glazing products, glassed or tiled facades and roofs, available in several colors and transparencies, have a great aesthetically impact. In particular the utility of the solar cell glazing modules is due to the double function of transmitting the daylight and serving as water and sun protection, ensuring both shading, natural lighting and providing electricity.

For this reason the issues of this particular PV market are not only the energy production but also the structural safety and performance in addition to architectural specifics as the shadowing. In this framework the durability, the degradation and new technologies to achieve a cost reduction are of fundamental importance.

1.2 Overview on photovoltaics

In this section, a brief summary of the origin and basic principles of photovoltaics is provided. PV modules are devices able to convert the solar energy into electricity through the photovoltaic effect. The first studies on this effect were carried out by Becquerel in 1839 [2,3]. His device was similar to an electrochemical cell, composed by two electrodes, coated by light sensitive materials, AgCl or AgBr, and carried out in a black box surrounded by an acid solution. The electricity increased with the light intensity. The photovoltaic effect was studied in deep by Heinrich Hertz, Willoughby Smith, William Adam e Richard Day. They reached for the first cell an efficiency of 1-2% at the end of the 19^{th} Century.

The modern photovoltaic was discovered at the Bell Labs in the USA in 1954, when accidentally some researchers noticed that a p-n junction diode illuminated by room light generated a voltage. In the same year they were able to reach the 6% of efficiency with a Si p-n junction solar cell [4]. After them, other US research groups achieved the same efficiency with different solar cells: a thin-film hetero-junction solar cell based on Cu_2S/CdS at the Wright Patterson Air Force Base [5], a GaAs p-n junction solar cell at the RCA Lab, thin films of CdTe by Cusano [6]. In the US there was an increase in the interest for the PV applications due to the US space program. Indeed they started to use Si PV cells for powering satellites.

The 1973 was an important year for photovoltaics: at the IBM laboratory, a group working on GaAs solar cells reached the 13% of efficiency and, at the Cherry Hill Conference, PV researchers together with the US government asserted the importance of photovoltaics for energy production. They obtained the governmental support and the foundation of the *US Energy Research and Development Agency*. This agency, which now is called *US Department of Energy*, was the first one in the World that included in its missions the research on renewable energy. In the same year the Persian Oil producers introduced the first World Oil Embargo, which further drove the need of renewable energy and in particular the research on PV for terrestrial applications. The fundamentals of p-n junction solar cells, their operation and theory were developed from 1960 by Prince [7], Loferski [8] Rappaport and Wysoski [9], Shockley and Queisser [10].

On the market, the most used material for PV is Silicon, not for its light absorbance propriety, but for the high quality and abundance of the product. Solar cells are commonly divided in three main groups, called generations. The first generation is based on Silicon or Germanium doped with Phosphorus and Boron in a p-n junction. This group actually dom-

inates the commercial market with a quite high efficiency in the case of very pure Silicon, although due to the energy-requiring process, the production cost is still high. These modules are further classified in two categories: monocrystalline Silicon, made from thin slices of a single crystal of Silicon (mono-Si or sc-Si) and polycrystalline Silicon, also named as multicrystalline Si (poly-Si or mc-Si). These slides are cut from a block of Silicon, called ingot. The material quality of mc-Si is lower than sc-Si because of presence of the grain boundaries, which reduces the final performances of the solar cells.
The second generation group is the thin film solar cells, which includes thin film Silicon, amorphous Silicon (a-Si), Cadmium Telluride (CdTe) and Copper Indium Gallium Selenide (CIGS) cells. The third generation of solar cells includes a particular type of thin-film technologies defined as *emerging* photovoltaics because they are still in research or development stages. For this reason, unfortunately, their efficiency and stability are not so high. Organic solar cells, Dye Sensitized Solar Cells (DSSC) and tandem solar cells belong to this generation.

This thesis is focused on the first generation, for the durability issues, and on the second generation for the reduction of the production cost of thin mono-crystalline Silicon layers.

The process for the production of PV modules, for the first and second generation, starts with the growing of sc-Si or mc-Si ingots from row material or from chemical process, see Fig.1.1. The ingot is cut with diamond wires to obtain wafers and after a cleaning step the wafers are subjected to the diffusion of dopants (i.e. Phosporous and Boron). Obtained the p-n junction the contacts are usually made with screen printing and the connection are soldered. The last step of the process is lamination, where the connected cells are disposed on the back-sheet (a waterproof material) and covered by the encapsulant (usually EVA) and the transparent glass and sealed in the laminator.

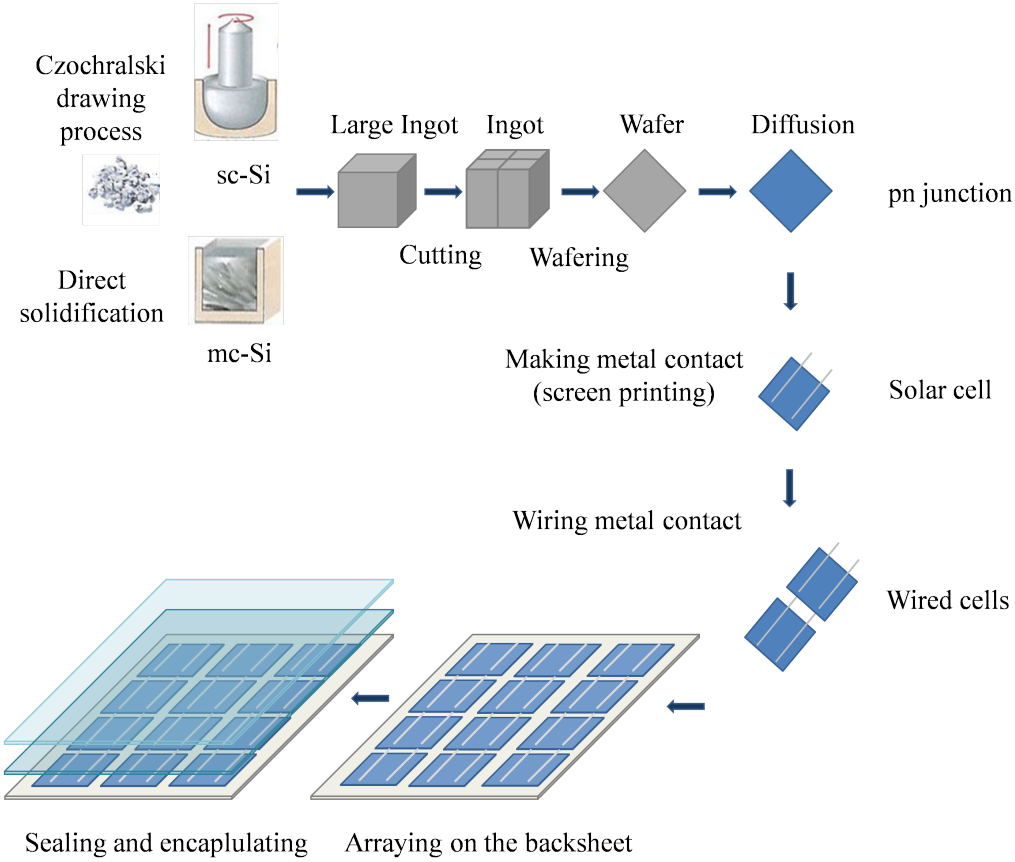

Figure 1.1: General process for the production of PV modules.

In general, the final standard PV modules are laminates composed of a 4 mm thick front glass, a 0.166 mm thick layer of Si solar cells, closed between two 0.5 mm thick encapsulating polymer layers (EVA) and, in the end, a thin multilayered back-sheet made of Tedlar/Aluminum/Tedlar 0.1 mm thick (see Fig.1.2).

1.3 Durability

The scientific community was only partially focusing on durability issues so far, but the raising of the installation of PV modules has increased the interest in warranty and lifetime of PV modules. Initially, according to the warranties given by producers, the lifetime of a PV modules was certified to be 25 years with a maximum power loss of 20 %. Thanks to this first regulation, it was already possible to replace PV modules in case of power losses higher than

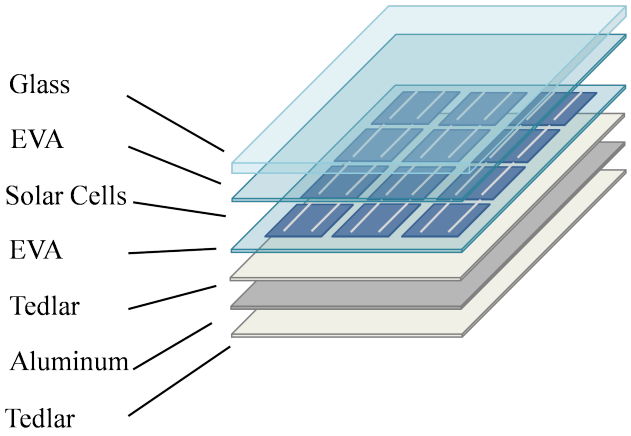

Figure 1.2: Sketch of a standard PV module.

10% in the first 10 years, and then higher than 20% in the following 20 years. Standards also assume a linear decay of the performances of the electric output of PV modules over time. The comparison thermo-hygrometric tests is shown in Fig.1.3 between warranties given by the different producers. To answer to these new requests of the consumers and the producers, durability studies are nowadays of fundamental importance to ascertain with care the power-losses of PV modules when exposed to the environmental loading in the field.

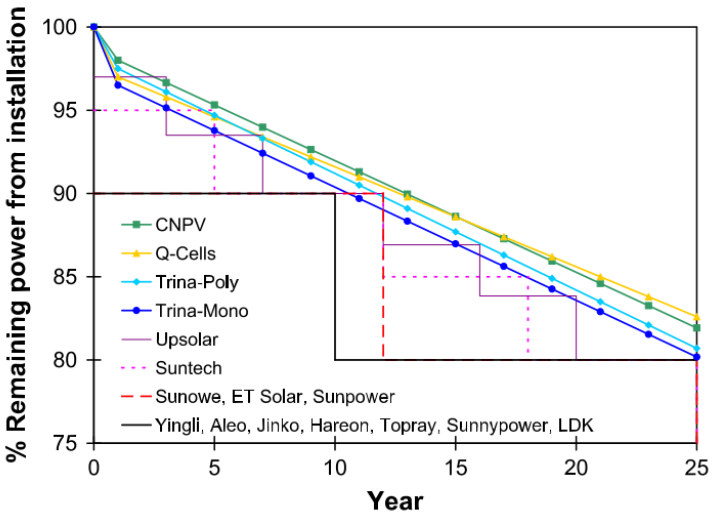

Figure 1.3: Warranties by various producers, adapted by [11].

During production, the aim is the improvement of the process to reduce the number of cells or modules rejected by quality control [12]. The cells passing the quality control are still subjected to other critical events during transport, installation and the working operation (in particular impacts, snow loads and environmental aging caused by temperature and relative humidity variations). The existing qualification standards IEC 61215 require passing of severe laboratory tests in a climate chamber [13]. However, up to now, a quantitative criterion considering cracking has not yet been propoced in standard tests for the quality assessment of PV modules.

1.3.1 State-of-the-art

In this section a state-of-art on failure and damage characterization is presented. Commonly failures are divided in: *infant*, *midlife*, and *wear-out* depending on their time of occurrence and they are briefly summarized in Fig.1.4.

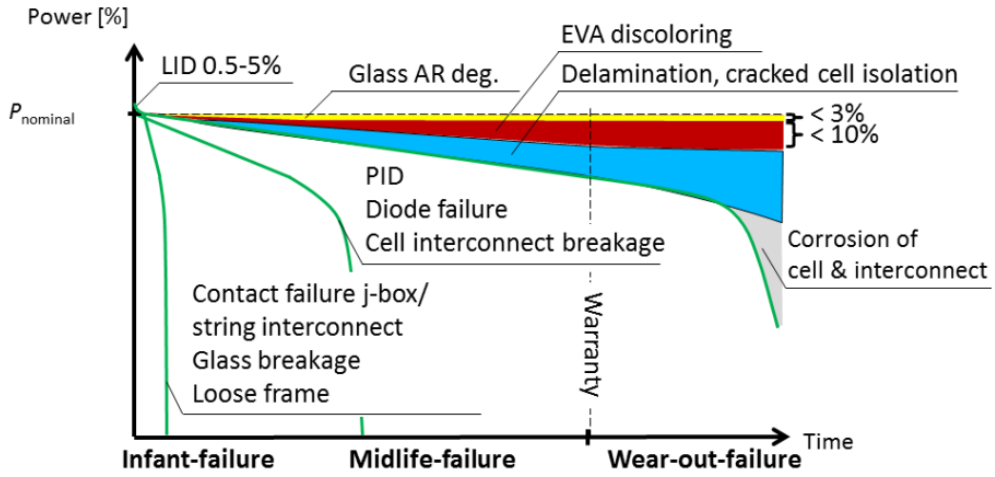

Figure 1.4: Power loss vs. time for three types of failure in wafer-based crystalline photovoltaic modules. LID is light-induced degradation, PID is potential induced degradation, EVA is the ethylene vinyl acetate and j-box is junction box [14].

The first type of failure occurs because of flawed PV modules at the beginning of their working life, when producers and installers are responsible for that. Almost 5% of all failure cases are caused by transportation damages. Among the other failures, the most important ones are related to junction box failure, glass breakage, defective cell interconnection, loose frame and delamination.
DeGraaff [15] studied the midlife failures of PV modules, showing the failure distribution of PV modules after 8 years of operation. The interconnection defects (36%) and glass breakage (33%) were predominant. During this phase, 2% of PV modules is expected not to meet the

manufacturer's warranty after 11-12 years of operation. The last type of failure occurs at the end of the PV working life. It leads to safety problems or to a significant reduction in the produced power, typically between 80% and 70% of the initial power. In this case, the major failures are due to long-term degradation not well understood but almost all PV modules meet the manufacturer's power warranty. The study of long-term aging tests are of increasing importance to better understand these damages phenomena and provide methods to avoid them. Standards actually accepted to qualify PV modules are those of the IEC 61215 for crystalline Silicon [13], and IEC 6146 for thin-film Silicon [16]. However, no international standards certifications for long-term failure do exist. Another important classification, regarding failure, is related to safety issues. It is possible to identify three categories labelled as A, B and C. The first one includes failures that have no effect on safety; the second one includes failures that may cause fire, electrical shock, physical danger; the third covers failures that cause a direct safety problem [14]. In the present thesis, not only failures are characterized, but also the material defects leading to power losses. A defect does not necessarily produce a safety problem or a power loss, but its evolution in the time can be problematic. The typical methods used for detecting failures and defects are: *visual inspections*, *I-V measurements*, *thermography*, *electroluminescence*, *UV-fluorescence* and *signal transmission method*.

Visual inspection

Visual inspection is performed before and after environmental, electrical, or mechanical stress testing of a PV module. Usually stress tests (thermal cycling, humidity-freeze cycling, damp heat exposure, UV irradiation, mechanical loading, hail impact, outdoor exposure and thermal stress) are used to asses the reliability of module design in the pre-phase of production, production quality, and lifetime of the modules. Typical failures detected by this technique are reported in Tab. 1.1.

Table 1.1: Typical failures and damages found during IEC 61215; database of 61646 visual inspections.

Module component	Failure / Damage
Front module	Bubbles, delamination, yellowing, browning
Cell	Broken cell, cracked cell, discolored anti reflection
Cell metallization	Burned, oxidized
Frame	Bend, broken, scratched, misaligne
Back module	Delamination, bubbles, yellowing, scratches, burn
Junction box	Loose, oxidation, corrosion
Wire-connections	Detachment, brittle, exposed electrical parts

Current-Voltage characteristics

The current-voltage (I-V) characteristics provide the short-circuit current (I_{SC}), the open-circuit voltage (V_{OC}) and other important parameters as outcome of the test. A typical module I-V measurement system consists of a light source (natural or artificial), a temperature control and a data acquisition system to measure the I-V curve when the voltage across the module or current through the module is varied with an external electronic load. The standard test conditions (STC) are: irradiance of 1000 W/m^2, temperature of 25° C, AM 1.5G reference spectrum of IEC 60904-3 [17]. The AM is the air mass coefficient corresponding to 1.5 atmosphere thickness. It defines the direct optical path length through the Earth's atmosphere and it is used to help characterize the solar spectrum after solar radiation has traveled through the atmosphere (the specific value of 1.5 has been selected in the 1970s for standardization purposes, based on an analysis of solar irradiance data in the conterminous United States and it is able to represent the overall yearly average for mid-latitudes [18]). From the I-V curve, some key parameters can be extracted to assess the quality of the PV module. A typical I-V curve of an illuminated PV module is shown in Fig.1.5. The V_{OC} is the maximum voltage of a PV module at zero current. The I_{SC} is the current through the module when the voltage across the cell is zero. The maximum power (P_{MPP}) is defined as a point on the I-V curve of a PV module under illumination, where the product of current (I_{MPP}) and voltage (V_{MPP}) is maximum. The fill factor (FF) is essentially a measure of the quality of the solar cell. It is the ratio which compares the maximum power of the PV module to the virtual power (P_T) that would result if V_{MPP} were the open-circuit voltage and I_{MPP} the short-circuit current. The fill factor can be interpreted graphically as the ratio of the rectangular areas depicted in Fig.1.5. From these parameters, optical influences, cell degradation and shunting, and series resistance or inhomogeneity effects can be detected. The detailed description of the connection between the I-V parameters and defects is summarized in Tab.1.2.

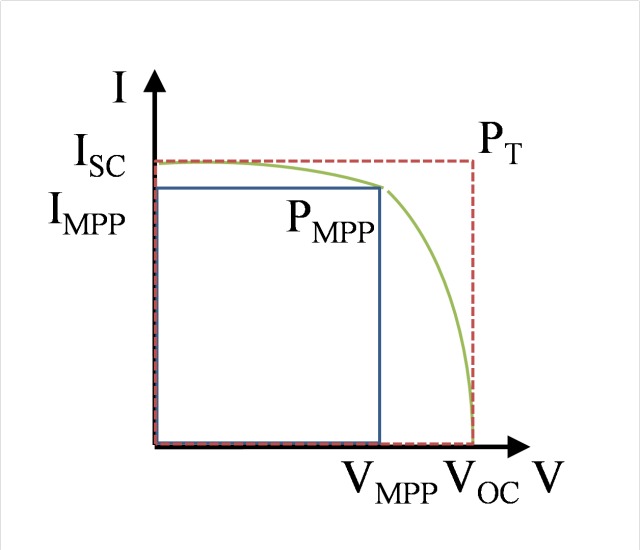

Figure 1.5: I-V curve of an illuminated PV module and the most important parameters: short circuit current I_{SC}, open-circuit voltage V_{OC}, the maximum power point P_{MPP}, the current and voltage belonging to the maximum power point I_{MPP} and V_{MPP}, and the virtual power point P_T.

Table 1.2: Failures and defects detectable from a I-V curve.

Failure	Pmax	Isc	Voc	Roc	Rsc	Slope change	Inflex pt
Disconnected bypass diode	x		x				
Short-circuit bypass diode	x		x				
Inverted bypass diode	x		x				
Homogeneous loss of transparency	x	x					
Heterogeneous loss of transparency	x	x		x			x
Homogeneous glass corrosion	x	x					
Heterogeneous glass corrosion	x	x		x			x
Homogeneous delamination	x	x					
Heterogeneous delamination	x	x			x		x
Homogeneous corrosion AR coating of the cells	x	x					
Heterogeneous corrosion AR coating of the cells	x	x				x	
Passivation degradation	x		x				
PID polarization induced degradation	x		x			x	
LID light-induced degradation for crystalline solar cells	x	x	x				
Short-circuited cells, e.g. by cell interconnection ribbon	x		x				
Solder corrosion	x			x			
Homogeneous soldering disconnections	x			x			
Broken cell interconnect ribbons	x			x			x
Cracked cells	x	x			x		x

Thermography

Thermography or infrared (IR) imaging [19] is a non-destructive measurement technique providing fast, contactless and two-dimensional distributions of some thermal and electrical maps in PV modules. Indeed, it shows temperature differences caused by an external current or by applying light to the PV module. During measurements in the dark, there is no light applied to the module but the external current (typically comparable to the short-circuit current I_{SC}) is supplied in the forward direction [20]. Under normal operating conditions, the incident light generates current, heat and sometimes an inhomogeneous temperature on the PV module. Thermography imaging is performed mostly by means of a portable, uncooled IR-camera. The wavelength of the used IR-detector is typically between 8 and 14 μm [21].

Electroluminescence

Electroluminescence (EL) is based on the detection of near-infrared radiation (nIR) emitted by the Si of solar module. Dark environment is useful but not necessary to decrease the background *noise* during the EL imaging. Additionally a high pass edge filter at 850 nm may be used to reduce interfering light from other sources. Using EL imaging, it is possible to detect cell cracks appearing as dark lines in the solar cell in the EL image. Especially in multicrystalline solar cells, typical crystallographic defects also appear as dark lines. Figs.1.6, 1.7and 1.8 summarize the defects detectable with electroluminescence for wafer-based PV modules [14]. In particular, in Fig.1.6, poly-Si solar cells are displayed. They have crystal dislocation (a), grid failure along the cell (b), grid interruptions caused by soldering (c), cracks completely isolated from the cell interconnected ribbon (d), cracks influencing the current flow to interconnect ribbon of the still connected cell (e), cracks that do not influence the current flow over the crack (f).

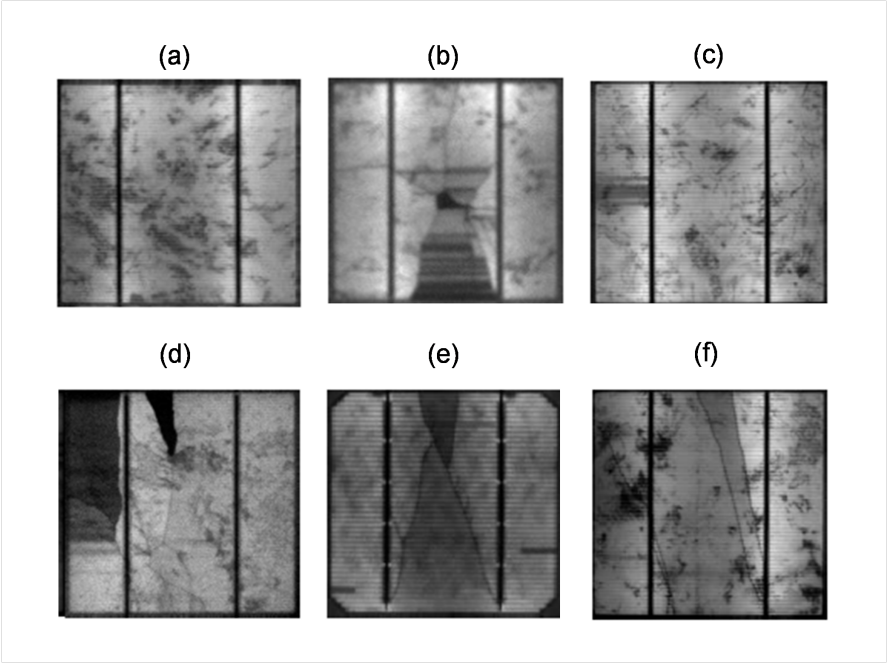

Figure 1.6: EL images of failure in poly-Si solar cells.

Mono-Si Solar cells are shown in Fig.1.7. They present the following failures: cross crack lines (a), contact forming failure A, temperature inhomogeneities of the transport belt during the firing process of the cell process lead to a tire like imprint (b), temperature inhomogeneities during the firing process of the cell process lead to center edge gradient of contact resistance of the cell finger metallization (c), disconnected cell interconnect (d), shunt fault (e).

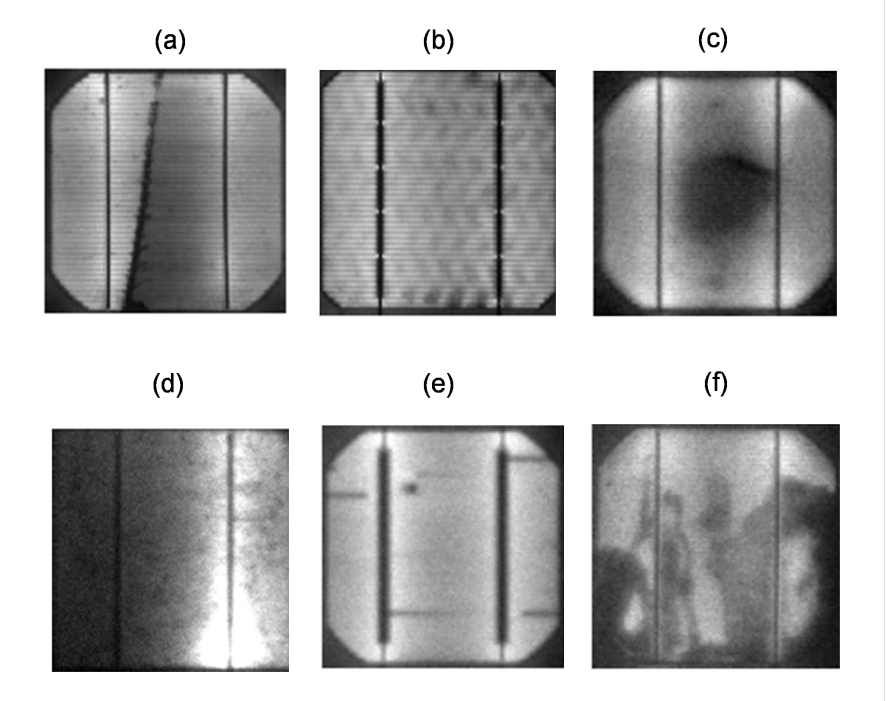

Figure 1.7: EL images of failures in mono-Si solar cells.

Finally, Fig.1.8 shows the cell failure pattern in PV modules: heavy and homogeneous mechanical load (the overall crack pattern in the module looks like a X-crack pattern, see red lines) (a), dendritic like cracks located mainly in the middle of the module (b), shunted by pass diode or break in current flow (c), potential induced degradation (PID) (d), repetitive cracks during the production (e). Thanks to the accuracy in the crack detection, this technique has been chosen as the main tool for detecting and monitoring damages and failures in the present work.

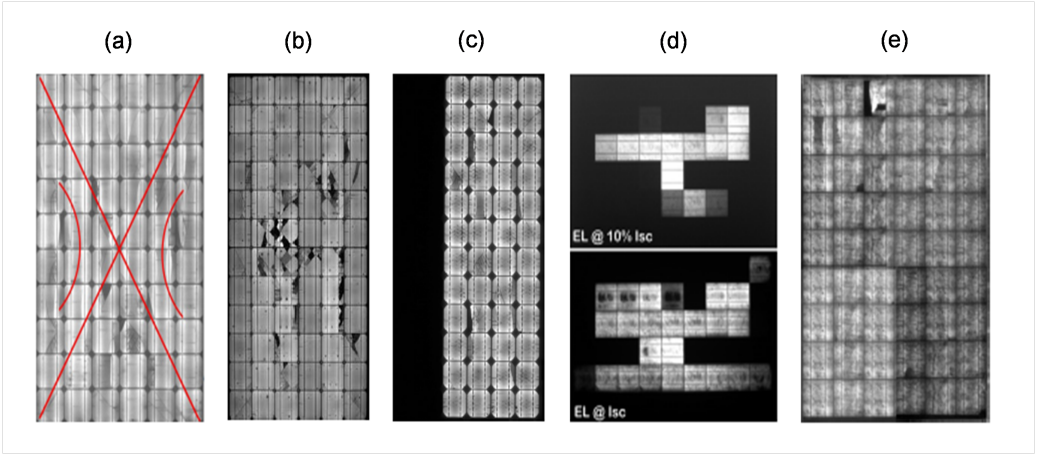

Figure 1.8: Failure in PV modules.

Signal Transmission Device

The Signal Transmission Device (STD) [22] was initially used for field maintenance of electric work (detection of earth-leakage points and wired routes in walls). In the PV systems, STD detects local disconnection of interconnect ribbons in PV modules and open-circuit failure of bypass diodes in junction boxes.

UV fluorescence

The UV fluorescence (FL) of Ethylene Vinyl Acetate (EVA) was used for the first time to analyze the discoloration of photovoltaic (PV) modules by Pern et al. [23]. Due to exposure of EVA to sunlight, especially to the UV spectrum, molecules of the encapsulant decompose to form *lumophores*. A correlation between features in UV fluorescence images and cell cracks was recently presented in [24]. Schlothauer et al. [24] used EL images to identify the cracks in a cell of a PV module and correlate them with the UV fluorescence image. In presence of a crack, Oxygen may penetrate not only from the edge but also from the crack and fluorescent decomposition products are transformed into non-fluorescent one through a photo-oxidation process, through a photo degradation. This process marks the cell edge and cell cracks with a non-fluorescent trace. [25]. This process, named *photobleaching*, may be used to determine number, position and orientation of cell cracks in PV modules, even in a dark outdoor environment. The PV module has to be exposed to sunlight for developing lumophore species able to emit a sufficient UV fluorescence signal. The FL detects cell cracks [26], appearing as a dark thick line on the solar cell but cracks near the interconnections, shown as gray zones, are difficult to be identified. Moreover the major drawback of this technique is its invasiveness. Indeed, it needs of a direct access to the encapsulant because the typically used front glasses or back sheets are not transparent to UV light below 350 nm.

Therefore, the layers of a PV module have to be separated for a full fluorescence spectroscopy analysis.

1.4 Cost reduction

Several elements influence the cost of PV modules and the trend of their production cost is summarized in Fig.1.9. It shows the proportion of the different element costs: Silicon, wafer, cell and module in the years from 2010 to 2014. In addition to the overall cost reductions from 2010 of 1.86 $/W to 2014 of 0.72 $/W, the share of single costs has changed too. According to the International Technology Roadmap for Photovoltaics [27], the possible ways to reduce these costs are:

- Reduction of costs per unit, through the optimization of the actual production capacity and an efficient use of the materials (both Si and non-Si ones);
- Adoption of module products specific for different market applications;
- Increase the module power/cell efficiency limiting the process costs, thus, restricting the investments in new tools.

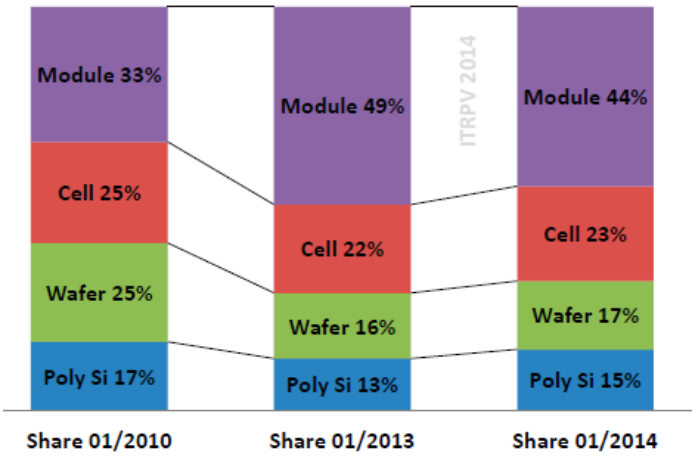

Figure 1.9: Proportion of price related to different module cost element in January 2010, January 2013 and January 2014 [27].

Actually, Si-wafers account for 57% of the cell price. Hence, a way to further reduce the PV module cost is an efficient use of Silicon. One way to achieve that, is to reduce the thickness of the Silicon cell and, at the same time, avoid as much as possible material losses

due to sawing of Silicon ingot. The reduction of wafer thickness requires solutions for the following challenges:

- Improved wafer sawing technologies, reduced kerf-loss and Total Thickness Variation (TTV);
- Innovative handling concepts;
- Introduce new high efficiency cell concepts suitable for thinner wafers;
- Stress-reduced interconnect and encapsulation technologies at module level.

In the last decade, several alternative techniques to obtain Silicon thin foils based on different techniques were developed. The target for the thin layer is to provide a good light absorption and a good passivation of the surfaces, to ensure an optimal efficiency-thickness ratio. This is possible to be achieved for thin films with a thickness less than 50 μm.

The study of an alternative sawing process to save material is discussed in the present dissertation. The standard wafering process is called Multi Wire Saw Slurry-based (MWSS) process. It was invented by the pioneering work of Dr. Charles Hauser, founder of HCT Shaping Systems, Switzerland in the middle of the 1980s [28]. The ingot is placed horizontally and a web of wires, driven by powerful motors at a speed of 10-20 m/s, moves around the ingot. A suspension of abrasive particles in coolant fluid, called slurry, is transported onto the wire. The movement of the abrasive slurry on the Silicon ingot cuts it and produces the thin wafers. Actually, the thickness of a standard wafer is around 180 μm using a wire diameter of 120 μm and a wire length of 1100 km [29]. The drawback of this process is the losses of material in saw dust or kerf-loss. According to Weber [30], the kerf loss is a function of the wire diameter and the particle diameter of the slurry as:

$$\text{Kerf loss} = \text{Wire diameter} + 3.5 \times \text{Particle diameter} \tag{1.1}$$

For this reason, it is possible to reduce the kerf-loss by reducing the wire and the particle diameter, but this increases the wire breakage rate. Several types of layer separation technologies have been developed so far and the most successful ones are: implantation Direct Film Transfer (DFT), implantation free-layer transfer, and spalling-lift. Implantation Direct Film Transfer is a technology developed by the SiGen Company [31] and Twin Creeks Technologies [32]. It uses a beam of mono-energetic protons that crosses a Silicon substrate creating a stressed End-Of-Range (EOR) layer. Depending on the energy of the beam, it is possible to cleave a layer of desired thickness. To control cleavage crack propagation, a second beam is used. The (111) crystal orientation is the best condition for the enhancing crack propagation in Silicon because of its lower surface energy [33]. A part of kerf-less techniques uses an implantation-free layer transfer and is called the Porous Silicon (PSI) process [34]. This process starts from a mono-crystalline Si, into which a porous double layer is etched in the Silicon substrate. In an annealing step at high temperature, the pores reorganize, which leads to a closed mono-crystalline surface on top of the porous Silicon and a mechanically weak buried layer that facilitates the layer transfer. Then an epitaxial Si layer (epi-Si) of thickness is deposited. Subsequently, applying a mechanical stress, the layer is split from the substrate at the position of the porous Silicon layer. Finally, the epitaxial layer is processed to obtain

the solar cell, while the substrate is reused for further lift-off process [34, 35]. The best solar cell results so far achieved 20.1% of efficiency with this were obtained by the Solexel Company. At Institute of Solar Energy Research of Hamelin, Petermann et al. [36] reached an efficiency of 19.1% on a substrate produced with a porous Silicon layer transfer process. In the same institute, Schaefer et al. [37] worked to remove the epitaxial layer by an electrochemical etching process with macroporous Silicon and without epitaxy. This technique allows partitioning a crystalline Si wafer into a multitude of thin Si layers with a stable pore pattern. The periodic structure of the obtained thin layers reduces the surface reflection and enhances light trapping [37].
In the research proposed here, the process that will be analyzed and improved is based on spalling. One of the most important advantages of this kerf-less technique is related to the absence of the porous Silicon layer. It allows the use of Silicon coming from the traditional Silicon ingot. Thus, the high quality of the layer is preserved. The physical mechanism of this technique is due to the presence of a thin layer with residual stresses on the substrate, due to the difference in the thermo-elastic proprieties between the substrate and the layer. Several research groups around the World are working on spalling techniques. The most important company is the AstroWatt [38], and research institutes such as IMEC (Interuniversity Microelectronics Centre, a micro- and nano-electronics research center headquartered in Leuven, Belgium) [39, 40], and the Institute for Solar Energy Research of Hamelin [41].
Each group considers a different process and stressor layer. Thus, the upper layer could be either metals or epoxy. The first category, i.e., metals, includes: Nickel (Ni), Nickel/Chromium alloy, Silver/Aluminum system, Silver (Ag). The technologies used for metal deposition are: screen printing, electroplating and thermal process. The second group of materials is based on epoxy-layers. It has several advantages such as the reduction of metal contamination and the possibility to operate at low temperatures (less than 150° C). There are different ways to use from the mismatch in the thermo-elastic properties between the stressor layer and the substrate to obtain the lift-off. Historically, the first experimental work on spalling-lift-off technique was by Tanielian et al. [42]. They investigated the stability of bilayers composed by a semiconductor substrate (Silicon or Gallium Arsenide) on which they spattered a thin metal layer (Nichrome). They found that was possible to peel off the metal substrate together with a layer of Silicon, thanks to the stress present in the thin film after the deposition. Theoretical studies on the spalling phenomenon were carried out by Suo and Hutchinson [43]. They analyzed various bi-layers composed by a brittle material, as substrate, and a thin film. The residual stress in these bi-layered structures was considered via a particular combination of edge loads. In particular, in [44], the two layers are assumed to be stress free before bonding at a temperature equal to T_0 and subsequently cooled down to a temperature T. The residual thermo-elastic stresses induce a singular stress field at the crack tip that might induce crack propagation under mixed mode condition.

To achieve crack propagation along a certain direction, the stress-intensity factor has to reach a threshold value, called fracture toughness (K_{IC}), which is a material property. In particular, by satisfying the previous condition, two possibilities may occur during propagation: the crack may move out of the plane of the crack or may move collinear with the initial notch. In particular, to achieve a stable crack path and produce a planar thin layer, Mode II should be avoided [45]. Thus, this leads to the condition to obtain a flat spalling, i.e. $K_{\mathrm{II}} = 0$ and $K_{\mathrm{I}} = K_{\mathrm{IC}}$.

1.4.1 State-of-the-art on spalling techniques

The spalling lift-off technique is very attractive for photovoltaic applications because it may allow the production of very thin and high quality crystalline Silicon layers. In fact, Tanielian et al. [42] in 1985 were the first to suggest the application of the spalling process in this field, because of the reduction of costs. Moreover, the free-standing single crystal Silicon layers obtained were very thin and with low defects.
One of the first lift-off process for solar cells was developed at IMEC by Dross et al. [39]. They deposited a layer of Ag paste on Silicon by screen printing with a thickness of 20 μm, followed by two temperature steps at 200° C and at 900° C to dry the solvent and to anneal the metal. Afterwards, a second deposition of Ag with a thickness of 50 μm is performed and consequently the other thermal steps to anneal the last layer. The cooling down caused the contraction of the Silicon and the metal. The mismatch in CTE and Young's moduli induced a high stress in the Silicon substrate. First the substrate bent to release the stress and subsequently a Silicon layer of 40 μm lifted-off. Afterwards, the Si- layer is processed to obtain an a-Si/c-Si hetero-junction emitter and a corresponding cell with 1×1 cm^2 area exposed to AM1.5 reached 9.9% of efficiency.
A second application of the kerf-less spalling is the epoxy induced spalling method has been developed at IMEC by Martini et al. [40]. They obtained a lift-off thin Si layer by depositing and curing an epoxy-layer. Also in this case, the source of stress was the mismatch in the thermo-elastic properties and the cooling from the curing temperature to the ambient one. A notch is inserted by laser in the Si-substrate to create an initial sharp crack. Afterwards, a thermosetting polymer is deposited on the substrate and it is cured at 150° C. The subsequent cooling down induced thermo-elastic stresses. Consequently, the stress intensification at the crack tip increased and, after exceeding the material fracture toughness, the crack will propagate. Afterwards, the polymer is removed by dipping the sample in an organic solution, obtaining a plane foil with a thickness varying from 50 to 100 μm.

In the same period, Bedell et al. [46] used an alternative method to induce stresses into the thin metal layer during deposition at room temperature by using electroplating or sputtering techniques. They deposited Ni by electroplating and they spalled a Si-layer of 20 μm thickness. The same results were obtained starting from a Ge-substrate. In this specific case, they reached an efficiency of 17% for a spalled III-V single-junction PV cells, exposed to AM1.5. In this case it was necessary to assist spalling. This is possible by applying an adhesion layer called *Flexible Handle Layer*, usually a thin tape. It reduces roughness caused by the multiple crack fronts and it allows manipulating the thin Si-spalled without introducing an initial notch. This spalling technique could be profitably adopted to reduce the dislocations generated during brittle-to-ductile transition (BDT) temperature (at 450° C for Silicon).

Finally, Rao et al. [38] induced mechanical stresses in a Silicon substrate by depositing a metal layer by electroplating and then an annealing process. This causes a thermal expansion mismatch between metal and Silicon. The incorporation of Hydrogen, through a plating bath, coupled with the thermo-elastic stresses, leads to the exfoliation of a thin c-Si layer. The thickness of the lifted layer depends on the thickness of the metal layer, by annealing temperature and mechanical wedge parameters. In particular, they further processed the thin layer to obtain a hetero-junction solar cell, and for a small device with 1 cm^2 surface designed area, it has been reported an efficiency of 12.5% [38].

For the project analyzed in this work, a lift-off will be induced by a localized cooling of the bi-layered system composed by a monocrystalline Silicon substrate and an Aluminum layer [41]. The advantages in the localized and controlled cooling are the possibility to promote quasi-continuous crack propagation and to avoid the formation of additional crack fronts. In this way, the exfoliation starts only at the side where the sample is cooled and it continues with the local cooling.
Bellanger et al. [47] performed a SLIM-cut process on a bi-layer where they introduced a laser notch. After that, the sample is heated by a focused radiation and the localized cooling is performed by a flux of liquid Nitrogen [47].

The innovation in the design adopted in the setup of the Institute for Solar Energy Research Hamelin group lies in the simplification of the process, which continues to permit a control of the process. The directed cooling approach allows the spalling at lower temperatures than in the SLIM-cut process [47] using the heating and cooling source at a constant distance, see Fig.1.11. Furthermore, the heating phase is continuative and the cooling is obtained moving the sample in a water-bath at room temperature in order to reach a high control of the process.

1.4.2 Directional controlled spalling

This particular process called directional controlled spalling, designed at the Institute for Solar Energy Research Hamelin and at the basis of the experimental campaign presented in this thesis is briefly described in this section. The features, shown in Fig.1.10 of this spallation technique are the deposition of a stressor layer on the substrate from which a thin layer is exfoliated, the introduction of the crack by laser cutting into the wafer and finally the exfoliation through the directional heating and cooling.

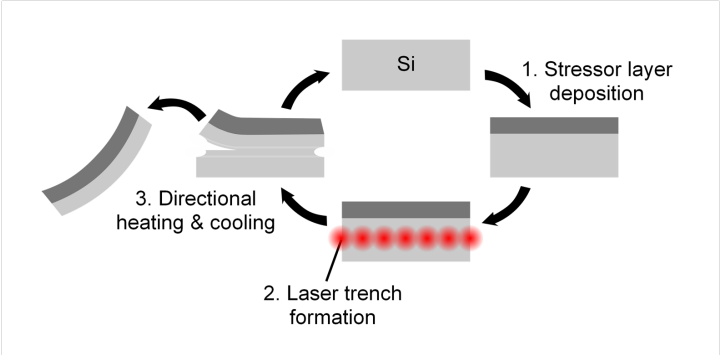

Figure 1.10: Exfoliation cycle: 1. Stressor layer deposition, 2. Laser trench formation, 3. Exfoliation by directional heating and cooling, adapted from [47].

Fig.1.11 shows a schematic representation of the exfoliation setup. The heating source is a halogen-lamp with an elliptical mirror (1) in Fig.1.11. The lamp emits light in the range

of 500-1500 nm. The length of the focus is 28 cm. Due to the elliptical mirror of the UV-lamp the light beam is focused to one horizontal line with a width of 4 mm. The metallized sample (2)in 1.11 is clamped laterally using a sample holder (3) in Fig.1.11. The sample holder is moved vertically (4) in Fig.1.11 along the y-direction. A bath of deionized water, at room temperature, cools the sample (5) in Fig.1.11. The bowl is a cuboid with dimensin of $9 \times 10.5 \times 11$ cm^3. The distance between the water level and the center of line focus of the halogen-lamp is around 6 mm [47].

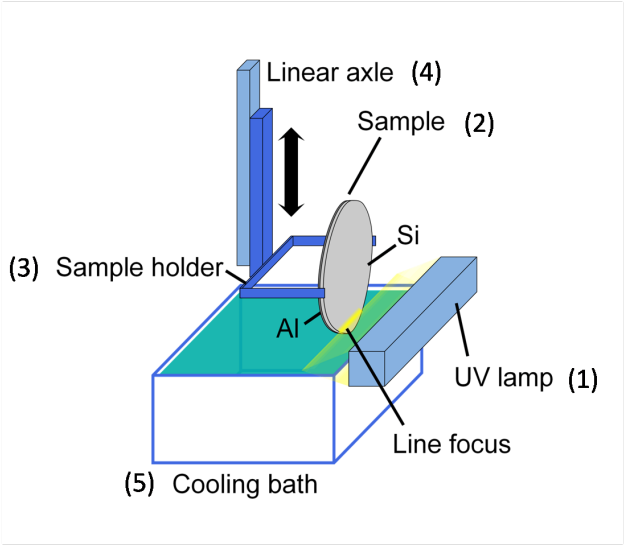

Figure 1.11: Sketch, not in scale, of the experimental setup: halogen-lamp (1), sample (2), sample holder (3), linear axle (4), cooling bath (5), adapted from [47].

1.5 Outline of the dissertation

The presentation of the proposed work is given as follows. In Chapter 2, the most relevant formulation concerning Linear Elastic and non-linear fracture mechanics models of brittle material and quasi-brittle materials such as the Silicon are summarized.
In Chapter 3, the mathematical formulation for a mono-dimensional electric model for a cracked solar cell is introduced. It is extended to the case of localized and distributed resistances for mono-Si solar cells and for a poly-Si.
In Chapter 4 the validation of the electric models presented in Chapter 3 is presented together with the coupling of the electric field and the mechanical one, founding the relation between the crack resistance and the crack opening.
In Chapter 5, humidity corrosion and more in general artificial weathering phenomena are investigated and monitored on PV modules tested in the Lab of the Department of Structural, Geotechnical and Building Engineering of Politecnico di Torino (curtesy of Prof. R. Nelva),

through EL measurements.
In Chapter 6, the study of an innovative methodology to produce thin layers of Silicon, starting from a parental substrate that is split into many thinner wafers is presented.
In Chapter 7, the main conclusions achieved in this thesis are briefly summarized. In addition, further development and open points are discussed.

Chapter 2

Fundamentals of Linear and Nonlinear Fracture Mechanics

In this Chapter, the fundamentals of Linear and Nonlinear Fracture Mechanics theories are presented. In particular, Linear Elastic Fracture Mechanics (LEFM) is discussed in Section 2.1 and Section 2.2.1 introduces the Cohesive Zone Model (CZM) for Nonlinear Fracture Mechanics studies. The LEFM approach assumes pre-existing cracks and treats the materials as linear elastic. Instead, the CZM allows simulation of the nucleation of cracks in addition to their propagation. In this dissertation the LEFM is adopted to study fracture and delamination of elastic thin Silicon films, whereas the CMZ approach is employed to analyze fracture in Silicon solar cells.

2.1 Linear Elastic Fracture Mechanics

Fracture Mechanics and in particular LEFM were developed after the World War II. One of the most important and historical aims of Fracture Mechanics is to avoid catastrophic events due to crack propagation. In general, causes of failure are mostly due to:

- Negligence in the project, construction or operation of the structural component;
- Unexpected behavior due to new design or materials.

The latter is more difficult to prevent and has been the driving force for the study of fracture mechanics. The most famous failures of type 2 in the history are: the Liberty ships, the polyethylene (PE) piping and the Challenger Space Shuttle. During the World War II the U.S. army supplied the U.K. with planes and ships, but the rate of sinking cargo of the Germans was three times the rate of the replacement, thus until the introduction of a new technology. After that the U.S. was able to produce quickly ships using an all-welded hull. Staring from 1943, one of these ships broke completely in two parts while was sailing between Siberia and Alaska. In this period of the roughly 2700 Liberty ships produced, around 400 were subjected to fracture, of which 90 were considered serious [48]. These failures were due to the following reasons:

- The presence of crack-like flaws in welds;
- A high local stress concentration at square hatch corners of the deck, where fractures started;
- the Steel used had poor toughness. It was adequate for the old ship design, because crack could not propagate across panels jointed by rivets.

After the individuation of the problems, Liberty ships were retrofitted, reinforced and rounded hatch corners and the corrections prevented further serious fractures. Starting from this catastrophic event, a group of researchers at the Naval Research Laboratory in Washington DC began to study fracture phenomena in detail. In this laboratory born the field known as fracture mechanics. The research group, lead by Dr. G.R. Irwin, improved the quantitative studies of Griffith [49] and Inglis [50]. Griffith's model correctly predicted the relationship between strength and flaw size in brittle specimens using an energy balance approach. Griffith considered a plate with a crack of length $2a$ subjected to a constant stress σ, see Fig. 2.1. Assuming plane stress condition and a plate width $w >> 2a$, for an incremental increase dA in the cracked area, the energy balance under equilibrium conditions is given by:

$$\frac{\mathrm{d}E}{\mathrm{d}A} = \frac{\mathrm{d}\Pi}{\mathrm{dA}} + \frac{\mathrm{d}W_\mathrm{S}}{\mathrm{dA}} = 0 \tag{2.1}$$

$$-\frac{\mathrm{d}\Pi}{\mathrm{dA}} = \frac{\mathrm{d}W_\mathrm{S}}{\mathrm{dA}} \tag{2.2}$$

where E is the total energy, Π is the potential energy supplied by the internal strain energy and external forces, W_S is the work required to create new surfaces.
The potential energy of an elastic body, U, is given by the strain energy stored in it and the work made by the external load applied, F:

$$\Pi = U - F \tag{2.3}$$

In particular, in this case, the potential energy may be express as:

$$\Pi = \Pi_0 - \frac{\pi\sigma^2 \mathrm{a}^2 B}{E} \tag{2.4}$$

where Π_0 is the potential energy of the un-cracked plate and B is the thickness of the plate. The creation of a crack requires the formation of two surfaces, so that the corresponding required work required is given by:

$$W_\mathrm{S} = 4aB\gamma_\mathrm{S} \tag{2.5}$$

where γ_S is the surface energy. From calculations:

$$-\frac{\mathrm{d}\Pi}{\mathrm{d}A} = \frac{\pi\sigma^2 a}{E} \tag{2.6}$$

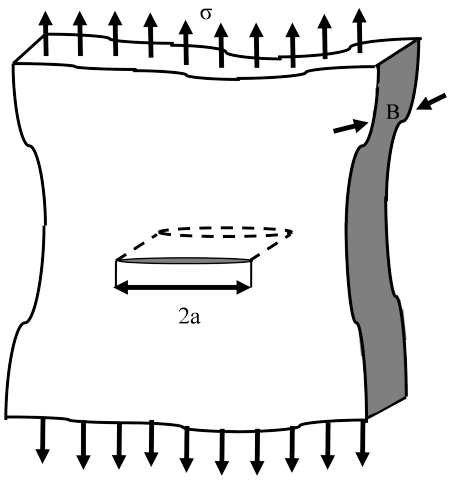

Figure 2.1: A crack of size $2a$ in an infinitely wide plate under a remote tensile stress σ.

and

$$\frac{\mathrm{d}W_\mathrm{S}}{\mathrm{dA}} = 2\gamma_\mathrm{S} \tag{2.7}$$

Using the energy balance equation and the expression (2.7), the resulting fracture stress leading to fracture, σ_f is:

$$\sigma_\mathrm{f} = \sqrt{\frac{2E\gamma_\mathrm{S}}{\pi a}} \tag{2.8}$$

However this model is valid only for brittle solids. A generalization of the model for elasto-plastic materials was achieved by Irwin [51] and Orwon [52] obtaining the following relation:

$$\sigma_\mathrm{f} = \sqrt{\frac{2E(\gamma_\mathrm{S} + \gamma_\mathrm{P})}{\pi a}} \tag{2.9}$$

where γ_P the plastic work per unit area, with $\gamma_\mathrm{P} > \gamma_\mathrm{S}$. In general, crack propagation in brittle solids is due to the breaking of the atomic bonds, instead in the different materials, for example metals, there is additional energy dissipation due to the moving of a dislocation near the crack tip. For this reason, a more general expression should consider also other possible dissipation mechanism. such as plastic, viscoelastic and visco-plastic effects, for instance by introducing a generalized fracture energy w_f which accounts for the different dissipation effects.

$$\sigma_\mathrm{f} = \left(\frac{2Ew_\mathrm{f}}{\pi a}\right)^{\frac{1}{2}} \tag{2.10}$$

Irwin in 1956 [53] proposed the energy release rate model, that is very similar to the Griffith one [49] but more applicable for the solution of engineering problems. The energy release rate is the energy related due to an increment of the crack size, and it is defined as the derivative of the potential energy dΠ:

$$G = -\frac{\mathrm{d}\Pi}{\mathrm{dA}} \tag{2.11}$$

Thus, the energy release rate for a wide plate in plane stress with a crack of length $2a$ (Fig. 2.1) is equal to:

$$G = \frac{\pi\sigma^2 a}{E} \tag{2.12}$$

The crack propagates when the critical conditions are met, i.e. when $G = G_{\mathrm{C}}$, being G_{C} the fracture toughness of the material, defined as:

$$G_{\mathrm{C}} = \frac{\mathrm{d}W_{\mathrm{S}}}{\mathrm{dA}} = 2w_{\mathrm{f}} \tag{2.13}$$

2.1.1 Asymptotic stress field at the crack tip

Another way to study the crack propagation is assuming that the material fails locally under a critical combination of stresses. This approach is called stress-intensity-factor approach. Westergaard [54], Irwin [55], Williams [56] and Sneddon [57] were among the first to publish closed form solutions for the stress at the crack tip in a linear elastic material. The stress field in a polar coordinate system defined by a radius r from the crack tip and an angle θ as in Fig.2.2, is given by:

$$\sigma_{\mathrm{ij}} = \left(\frac{K}{\sqrt{r}}\right) f_{\mathrm{ij}}(\theta) + \sum_{\mathrm{m}=0}^{\infty} A_{\mathrm{m}} r^{\frac{m}{2}} g_{\mathrm{ij}}^{m}(\theta) \tag{2.14}$$

where σ_{ij} is a generic component of the stress tensor. In Eq. (2.14), f_{ij} is a dimensionless function of θ, A_{m} is the amplitude of the non-singular higher order terms, and $g_{\mathrm{ij}}^{\mathrm{m}}$ is a dimensionless function of θ for the m^{th}term.
Hence, the solution for any given configuration is locally governed by the term $1/\sqrt{r}$.
For $r \to 0$, this leading term tends to infinity. Thus, the stresses at the crack tip vary as $1/\sqrt{r}$.
Eq.(2.14) describes a stress singularity. The displacement near the crack tip varies as $\sqrt{r}$ and remains finite.

Stress Intensity Factors

It is possible to use a parameter to characterize the intensity of the stress field at the crack-tip and to describe the singularity-dominated zone: the Stress Intensity Factors (SIF). The SIF defines the amplitude of the singularity at the crack tip and it is the proportionality constant k of Eq. (2.14) divided by $\sqrt{2\pi}$.
In general, it is possible to define three types of loading, shown in Fig.(2.4). In case of Mode I loading, the four field stress σ is applied normal to the crack plane, opening the crack.

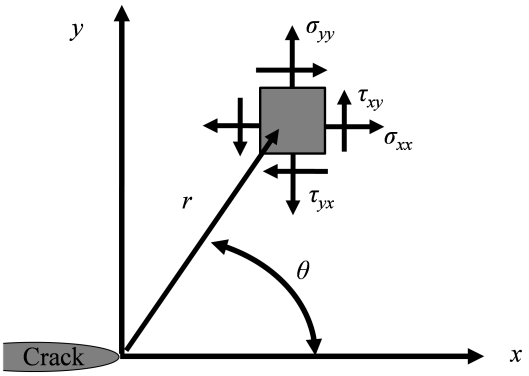

Figure 2.2: Coordinate axis ahead of a crack tip, with z direction is normal to the page.

The in-planar shear loading represents the Mode II loading, where one crack face slides with respect to the other, due to the action of shear stresses acting parallel to the plane of the crack and perpendicular to the crack front. Finally Mode III, called tearing Mode, is due to an out of plane loading and in this case the shear stresses act parallel to the plane of the crack and parallel to the crack front. The components of the Stress Intensity Factors are denoted by a subscript which indicates the type of loading (K_{I}, K_{II}, and K_{III}, respectively). Assuming a linear elastic isotropic material, the stress field at the crack-tip is given by the following equations:

$$\lim_{r\to 0} \sigma_{\mathrm{ij}}^{(\mathrm{I})} = \frac{K_{\mathrm{I}}}{\sqrt{2\pi r}} f_{\mathrm{ij}}^{(\mathrm{I})}(\theta) \tag{2.15}$$

$$\lim_{r\to 0} \sigma_{\mathrm{ij}}^{(\mathrm{II})} = \frac{K_{\mathrm{II}}}{\sqrt{2\pi r}} f_{\mathrm{ij}}^{(\mathrm{II})}(\theta) \tag{2.16}$$

$$\lim_{r\to 0} \sigma_{\mathrm{ij}}^{(\mathrm{III})} = \frac{K_{\mathrm{III}}}{\sqrt{2\pi r}} f_{\mathrm{ij}}^{(\mathrm{III})}(\theta) \tag{2.17}$$

From the definition of SIFs, their physical dimensions are:

$$[K] = \frac{\text{Force}}{\text{Length}^2}\sqrt{\text{Length}} = \text{Force}\ \ \text{Length}^{\frac{3}{2}} = \text{Stress}\ \ \text{Length}^{\frac{1}{2}} \tag{2.18}$$

In this framework, when a material fails locally for a particular combination of stresses, this is the result of crack propagation. This occurs when the Mode I Stress Intensity Factor

achieves a critical value K_{IC}, used to measure the fracture toughness of the material. K_{IC} is material propriety.

In these conditions the asymptotic expression for the stress field components at the crack-tip are summarized in Tab.2.1, while the displacements for Mode I and Mode II are summarized in Tab.2.2. The expressions for the non vanishing stress and displacement components for Mode III are collected in Tab.2.3.

Table 2.1: Stress field components ahead of a crack tip in a linear elastic, isotropic material, for Mode I and Mode II deformations.

	Mode I	Mode II
σ_{xx}	$\frac{K_I}{\sqrt{2\pi r}}\cos\left(\frac{\theta}{2}\right)\left[1-\sin\left(\frac{\theta}{2}\right)\sin\left(\frac{3\theta}{2}\right)\right]$	$-\frac{K_{II}}{\sqrt{2\pi r}}\cos\left(\frac{\theta}{2}\right)\left[2+\cos\left(\frac{\theta}{2}\right)\cos\left(\frac{3\theta}{2}\right)\right]$
σ_{yy}	$\frac{K_I}{\sqrt{2\pi r}}\cos\left(\frac{\theta}{2}\right)\left[1+\sin\left(\frac{\theta}{2}\right)\sin\left(\frac{3\theta}{2}\right)\right]$	$\frac{K_{II}}{\sqrt{2\pi r}}\sin\left(\frac{\theta}{2}\right)\cos\left(\frac{\theta}{2}\right)\cos\left(\frac{3\theta}{2}\right)$
σ_{zz}	0 (Plane stress) $\nu(\sigma_{xx}+\sigma_{yy})$ (Plane strain)	0 (Plane stress) $\nu(\sigma_{xx}+\sigma_{yy})$ (Plane strain)
τ_{xy}	$\frac{K_I}{\sqrt{2\pi r}}\cos\left(\frac{\theta}{2}\right)\sin\left(\frac{\theta}{2}\right)\cos\left(\frac{3\theta}{2}\right)$	$\frac{K_{II}}{\sqrt{2\pi r}}\cos\left(\frac{\theta}{2}\right)\left[1-\sin\left(\frac{\theta}{2}\right)\sin\left(\frac{3\theta}{2}\right)\right]$
τ_{xz}	0	0
τ_{yz}	0	0

Table 2.2: Displacement fields ahead of a crack tip in a linear elastic, isotropic material, for Mode I and Mode II.

	Mode I	Mode II
u_x	$\frac{K_I}{2\mu}\sqrt{\frac{r}{2\pi}}\cos\left(\frac{\theta}{2}\right)\left[\kappa-1+2\sin^2\left(\frac{\theta}{2}\right)\right]$	$\frac{K_{II}}{2\mu}\sqrt{\frac{r}{2\pi}}\sin\left(\frac{\theta}{2}\right)\left[\kappa+1+2\cos^2\left(\frac{\theta}{2}\right)\right]$
u_y	$\frac{K_I}{2\mu}\sqrt{\frac{r}{2\pi}}\sin\left(\frac{\theta}{2}\right)\left[\kappa+1-2\cos^2\left(\frac{\theta}{2}\right)\right]$	$-\frac{K_{II}}{2\mu}\sqrt{\frac{r}{2\pi}}\cos\left(\frac{\theta}{2}\right)\left[\kappa-1-2\sin^2\left(\frac{\theta}{2}\right)\right]$

where μ is the shear modulus, ν is the Poisson's ration and κ is the Kolosoff's constant, related to ν as: $3-4\nu$ for plane strain and $(3-\nu)/(1-\nu)$ for plane stress.
In case of mixed mode loading, the stress field is given by the principle of superposition typical of a linear system:

$$\sigma_{ij}^{total} = \sigma_{ij}^{(I)} + \sigma_{ij}^{(II)} + \sigma_{ij}^{(III)} \tag{2.19}$$

Relation between critical stress-intensity factor and fracture energy

The two material parameters above introduced to describe the Linear Elastic Fracture Mechanics and predict crack propagation events, K_{IC} and G_C, are connected with each other. The same relation holds for any generic nominal values K and G. As mentioned, G quantifies

Table 2.3: Displacement fields ahead of a crack tip in a linear elastic, isotropic material, for Mode III deformation.

	Mode III
τ_{xz}	$-\frac{K_{III}}{\sqrt{2\pi r}}\sin\left(\frac{\theta}{2}\right)$
τ_{yz}	$\frac{K_{III}}{\sqrt{2\pi r}}\cos\left(\frac{\theta}{2}\right)$
u_z	$\frac{2K_{III}}{\mu}\sqrt{\frac{r}{2\pi}}\sin\left(\frac{\theta}{2}\right)$

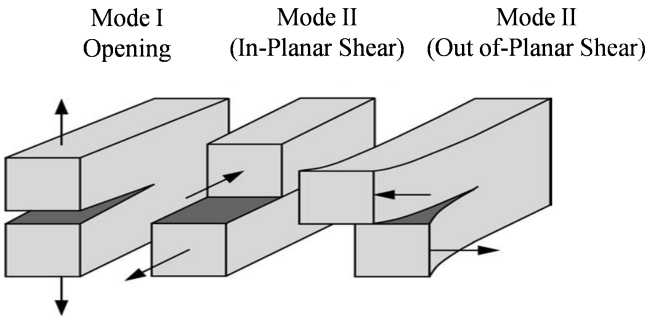

Figure 2.3: The three modes of loading applied to a crack.

the net change in potential energy for an increment of the crack extension, whereas K defines the stress field near the crack tip. Thus, while the energy release rate characterizes a global behavior, the K is a local parameter. In LEFM, K and G are uniquely related, combining the previous equation for a crack subjected to tensile stress (Mode I), in the following way:

$$G = \frac{K_I^2}{2E'} \tag{2.20}$$

where E' is the Young's modulus, which assumes different forms in the case of plane stress or plane strain:

$$E' = E \quad \text{for plane stress} \tag{2.21}$$

$$E' = \frac{E}{1-\nu^2} \quad \text{for plane strain} \tag{2.22}$$

Even if Eqs. (2.21) and (2.22) are valid only for a crack in an infinite plate, Irwin [55] proved that the relation is applicable for all the configurations, obtaining the following expression

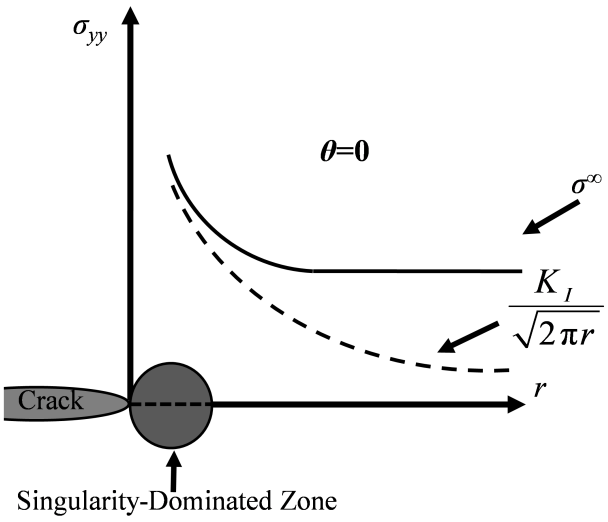

Figure 2.4: Stress normal to the crack plane in Mode I.

for a generic Mixed-Mode configuration:

$$G = \frac{K_{\mathrm{I}}^2}{2E'} + \frac{K_{\mathrm{II}}^2}{2E'} + \frac{K_{\mathrm{III}}^2}{2\mu} \tag{2.23}$$

where μ is the shear modulus.

2.1.2 Numerical methods for the computation of the Stress Intensity Factors

In fracture mechanics problems it is necessary to determine the distribution of stresses and strains, but is not possible achieve a closed-form analytic solution for all the practical problems. For this reason the numerical methods are a fundamental tool for stress analysis. Nowadays, improvements in the computer technology and more efficient algorithms have considerably reduced computation time in fracture mechanics problems. In this field of mechanics, several numerical methods have been used such as: the finite difference method [58], the finite element method [59] and boundary element method [60].
In this section, the finite element method (FE) will be introduced. In the FE, the structural

component to be studied is discretized into discrete *elements*. According to the problem dimension (2D or 3D) different types of elements are available: one-dimensional beams, two-dimensional plane stress or plane strain elements and three-dimensional bricks or tetrahedras are frequently used to discretize complex geometries. Each finite element is connected to the nearest-neighbor elements continuity of the displacements and stresses is imposed [59]. Commonly, in stress analysis problems, the stiffness method is used [58]. An isoparametric continuum element for two-dimensional plane stress or plane strain, with its local and global coordinate axes is shown in Fig.2.5. In the local (natural) system (ξ, η), the coordinates vary from -1 to +1 over the element; the node a, at the lower left-hand corner, has natural coordinates (-1, -1) while node b is at (+1, +1).

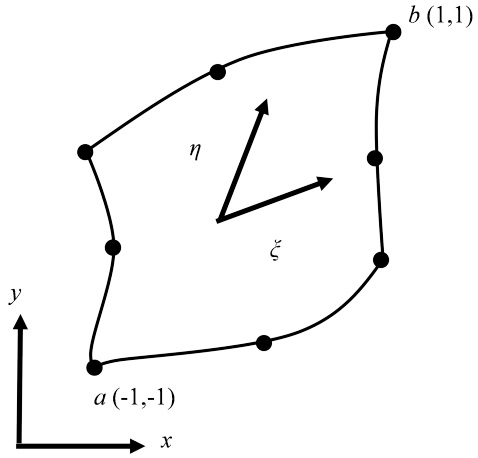

Figure 2.5: Local and global coordinates for a 2D finite quadratic element.

The coordinates x and y of a generic point belonging to the element are given by interpolation formulas:

$$x = \sum_{\mathrm{i}=1}^{n} N_{\mathrm{i}}(\xi, \eta) x_{\mathrm{i}} \tag{2.24}$$

$$y = \sum_{\mathrm{i}=1}^{n} N_{\mathrm{i}}(\xi, \eta) y_{\mathrm{i}} \tag{2.25}$$

where n is the number of nodes of the element, N_{i} is the shape function corresponding to the i-th node, whose coordinates in the local system are (η_{i}, ξ_{i}) and in the global system are (x_{i}, y_{i}). The shape functions are polynomials used to interpolate the field of interest in the element [59]. According to the number of nodes presented in the element, the degree of the shape function changes, for example if an element has only corner nodes, the polynomials are linear while the shape function of the element in Fig.2.5 are quadratic. Within the isoparametric

framework, the same interpolation holds for the displacements field components u and v:

$$u = \sum_{\mathrm{i}=1}^{n} N_{\mathrm{i}}(\xi, \eta) u_{\mathrm{i}} \tag{2.26}$$

$$v = \sum_{\mathrm{i}=1}^{n} N_{\mathrm{i}}(\xi, \eta) v_{\mathrm{i}} \tag{2.27}$$

where (u_{i},v_{i}) are the nodal displacements along the x and y directions of the element nodes. The strain vector is given by:

$$\begin{Bmatrix} \epsilon_{\mathrm{x}} \\ \epsilon_{\mathrm{y}} \\ \gamma_{\mathrm{xy}} \end{Bmatrix} = [\mathbf{B}] \begin{Bmatrix} u_{\mathrm{i}} \\ v_{\mathrm{i}} \end{Bmatrix} \tag{2.28}$$

where the operator [**B**] has the following form:

$$[\mathbf{B}] = \begin{bmatrix} \frac{\partial N_{\mathrm{i}}}{\partial x} & 0 \\ 0 & \frac{\partial N_{\mathrm{i}}}{\partial y} \\ \frac{\partial N_{\mathrm{i}}}{\partial y} & \frac{\partial N_{\mathrm{i}}}{\partial x} \end{bmatrix} \tag{2.29}$$

The derivates of the shape functions with respect to the global system (x, y) are obtained from those in the natural frame using the Jacobian matrix [**J**] :

$$\begin{Bmatrix} \frac{\partial N_{\mathrm{i}}}{\partial x} \\ \frac{\partial N_{\mathrm{i}}}{\partial y} \end{Bmatrix} = \mathbf{J}^{-1} \begin{Bmatrix} \frac{\partial N_{\mathrm{i}}}{\partial \xi} \\ \frac{\partial N_{\mathrm{i}}}{\partial \eta} \end{Bmatrix} \tag{2.30}$$

where:

$$[\mathbf{J}] = \begin{bmatrix} \frac{\partial x}{\partial \xi} & \frac{\partial y}{\partial \xi} \\ \frac{\partial x}{\partial \eta} & \frac{\partial y}{\partial \eta} \end{bmatrix} \tag{2.31}$$

The stress vector is determined by multiplying the strain vector by the constitutive matrix [**D**]:

$$\{\sigma\} = [\mathbf{D}]\{\epsilon\} \tag{2.32}$$

Starting from the expression of the principle of virtual work, which provides the weak form of the problems [59, 61, 62]. The elemental stiffness matrix is given by:

$$[k] = \int_{-1}^{1} \int_{-1}^{1} [\mathbf{B}]^{\mathrm{T}} [\mathbf{D}][\mathbf{B}] \det |\mathbf{J}| \, \mathrm{d}\xi \, \mathrm{d}\eta \tag{2.33}$$

Its solution is obtained first in terms of displacements by solving:

$$[\mathcal{K}]\mathbf{u} = \mathbf{F} \tag{2.34}$$

where $[k]$ is given assembling the element stiffness matrices $[\mathcal{K}]$

Numerical techniques for SIFs computation

In Section 2.1.1 it has been shown as the stress, strain, and displacement fields in the near crack-tip region are determined by the Stress Intensity Factors. There are several techniques, in the literature, used to extract the SIFs from FE results. These are classified in *direct* or *energy* approaches. The former correlates the SIFs directly with the computed displacement of the finite elements, while the latter computes first the energy release rates. The energy approach is usually more accurate and preferable over the direct one.
The techniques presented in this paragraph, selected for their historical importance, simplicity, or accuracy, are: *displacement correlation*, *virtual crack extension*, *modified crack closure integral* and *J-integral*.

Displacement correlation technique

The displacement correlation technique [63] is one of the first and simplest techniques proposed to compute the SIFs. It belongs to the direct approach category. The configuration of displacement correlation technique is shown in Fig. 2.6. In its simplest form, the computed displacements of points *a* and *b* of the finite element at the crack tip are inserted in the analytical expression for the SIFs:

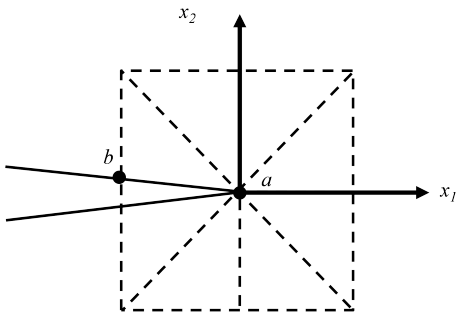

Figure 2.6: Configuration of finite elements and possible sample point location.

The advantages of this technique are the simplicity and inherent separation of the SIFs for the three modes of fracture. Nevertheless, to achieve accurate results for the SIFs it is necessary to use a fine mesh and the correlation point has to be in the singularity dominated zone. A way to improve this approach is to compute SIFs for a series of points approaching the crack tip. Through these points a curve is fitted and K is obtained for $r \rightarrow 0$, where r is the distance from the crack tip to the correlation point, and u_i, v_i, w_i are the x, y, and z displacements at point i.
One of the most important improvements for the displacement correlation technique is the use of the quarter-point crack-tip elements [64,65]. In this case the displacements along the crack face for the quarter-point element interpolation are shown in Fig.2.7 and the SIFs equations

are the following:

$$K_{\mathrm{I}} = \frac{\mu\sqrt{2\pi}(4(v_{\mathrm{b}} - v_{\mathrm{d}}) + v_{\mathrm{e}} - v_{\mathrm{c}}}{\sqrt{r}(2-2\nu)} \tag{2.35}$$

$$K_{\mathrm{II}} = \frac{\mu\sqrt{2\pi}(4(u_{\mathrm{b}} - u_{\mathrm{d}}) + u_{\mathrm{e}} - u_{\mathrm{c}}}{\sqrt{r}(2-2\nu)} \tag{2.36}$$

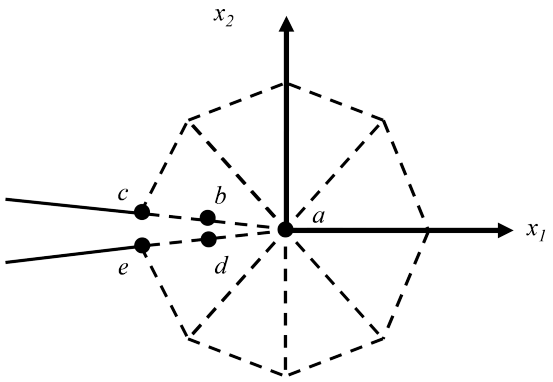

Figure 2.7: Configuration of the displacement correlation technique with quarter-point crack-tip finite elements.

Virtual Crack Extension method

The Virtual Crack Extension method, proposed in [66, 67], belongs to the energy approach category. It computes the rates of change in the potential energy for an infinitesimal (virtual) crack extension. In the LEFM frame, the variation in the potential energy is equal to the energy release rate. In absence of body forces Eq. (2.13) can be expressed as:

$$\Pi = \frac{1}{2}\mathbf{u}^{\mathrm{T}}[\mathbf{K}]\mathbf{u} - \mathbf{up} \tag{2.37}$$

where u is the nodal displacements vector, K is the stiffness matrix and p is the external force vector. Using Eq. (2.11) and assuming that the external forces do not vary during crack propagation, the energy release rate is given by:

$$G = \frac{1}{2}\mathbf{u}^{\mathrm{T}}\frac{\mathrm{d}[\mathbf{K}]}{\mathrm{dA}}\mathbf{u} \tag{2.38}$$

Park [66] simplified the computation proposing a finite difference approximation. Thus, only the elements of the stiffness matrix affected by the virtual crack extension have to be invoked in his version. The advantage of this method is the higher accuracy than the DCT. Nevertheless it is not possible distinguish among the different components of the SIFs.

Modified Crack Closure Integral Method

The Modified Crack Closure Integral method was proposed by Rybicki and Kanninen [68]. They thought to use the Irwin's crack closure [55] as a computational tool. Indeed, for a small crack increment, the Irwin's integral connects the energy release rate to the crack-tip stress and displacement fields. Relating the stresses at the crack-tip to the internal FE forces, through FE equations, the Irwin's integral for G_{I} and G_{II} can be discretized. It may be expressed directly in terms of nodal forces and displacements, which are the primary FE quantities. Using Eq.(2.20), the stress intensity factor is computed. The Modified Crack Closure Integral procedure has been extended for use with higher-order elements, thanks to Ramamurthy et al. [69], Raju [70] and Singh et al. [71]. Generally, the Modified Crack Closure Integral method computes SIFs with a higher accuracy than displacement correlation method for the same mesh size.

J-integral Method

The J-integral belongs to the energy approach techniques, it is a nonlinear fracture mechanic parameter that under LEFM assumptions it becomes equivalent is equivalent to the computation of the energy release rate [72, 73, 74]. In its original definition, is computed via a the energy release rate of a 2D body, contour integral (see Fig.2.8) as follows:

$$J = \lim_{\Gamma \to 0} \int_{\Gamma} \left[W n_1 - \sigma_{ij} \frac{\partial u_{\mathrm{i}}}{\partial x_1} n_j \right] \mathrm{d}\Gamma \tag{2.39}$$

where W is the strain energy density, Γ is the contour and n the unit normal vector to the contour.

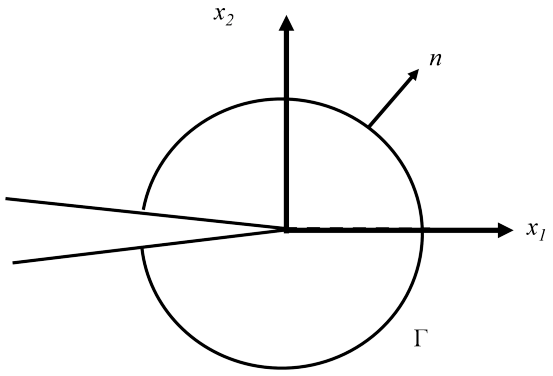

Figure 2.8: A contour Γ for the evaluation of the J-integral.

The simplest form of this integral is not always path-independent and to compensate this

problem Li et al. [75] formulated an *equivalent area integral*:

$$\bar{J} = \int_{\mathcal{A}} \left[\sigma_{\mathrm{ij}} \frac{\partial u_{\mathrm{i}}}{\partial x_1} n_{\mathrm{i}} - W \delta_{1\mathrm{i}} \right] \frac{\partial q_1}{\partial x_{\mathrm{j}}} \, dA \tag{2.40}$$

where δ is the Kronecker's delta function and q is a weight function defined over the domain of integration and it may be seen as the displacement field due to the virtual crack. Based on Li's definition of the J-integral [75], it is possible to have two different domains of integration: the former is an annular around the crack-tip and the latter is the inner contour of the crack-tip see Fig.2.9.

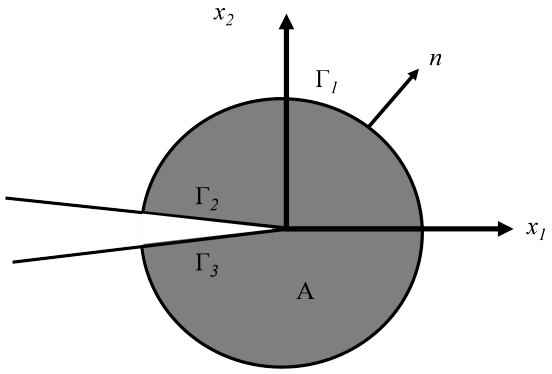

Figure 2.9: Different domains of integration for an equivalent domain evaluation of the J-integral according to the Li's formulation [75].

The second domain is preferable to be implemented in FE codes because only crack-tip elements are involved in the integration. The weight functions q is defined using standard shape function as following:

$$q = \sum_{\mathrm{i}} N_{\mathrm{i}} q_{\mathrm{i}} \quad \text{and} \quad \frac{\partial q}{\partial x_{\mathrm{j}}} = \sum_{\mathrm{i}} \frac{\partial N_{\mathrm{i}}}{\partial x_{\mathrm{j}}} q_{\mathrm{i}} \tag{2.41}$$

The weight function has a unit value in the inner contour or the crack-tip and zero elsewhere. Thanks to further extensions introduced by Ishikawa et al. [76] and independently by Bui [77] it was possible to define the J-integral using the symmetric and anti-symmetric field about the crack plane for the local displacement and the local stress. That allows to have a modal decomposition of J if the mesh is symmetric near the crack. If it is not the case, interpolation can be used to find displacements and stresses for non-symmetric meshes [78]. Finally, another technique for modal decomposition of the J-integral based on Betti's reciprocal work theorem was developed by Yau et al. [79]. Knowing that the J-integral is equal to G and using (2.20) is possible to obtain the modal decomposition of the SIFs.

2.1.3 Crack propagation criteria

The criteria for the determination of the direction of crack propagation are:

- *Maximum Circumferential Criterion* (MCS);
- *Maximum Energy Release Rate Criterion* (MERR);
- *Minimum Strain Energy Density Criterion* (SED).

Maximum circumferential criterion

The maximum circumferential criterion was proposed by Erdogan and Sih [80] assuming that the crack will propagate in the direction corresponding to the maximum circumferential stress, computed on a circle of an enough small radius around the crack-tip. According to this criterion the angle around the crack tip is given as function of K_{I} and K_{II}:

$$\tan\frac{\theta}{2} = \frac{-2K_{\mathrm{II}}}{K_{\mathrm{I}} + \sqrt{(K_{\mathrm{I}})^2 + 8(K_{\mathrm{II}})^2}} \tag{2.42}$$

Maximum energy release rate criterion

The maximum energy release rate criterion criterion was proposed by Griffith [49] and supposes that the crack propagates in the direction where the energy release rate is maximum. Hellen and Blackburn [81] connected the energy release rate to the J_1 and J_2 integrals and they found the following expressions for the angle of crack propagation:

$$\theta = \arctan\left(\frac{J_1}{J_2}\right) \quad \text{or} \quad \theta = \arctan\left(\frac{2K_{\mathrm{I}}K_{\mathrm{II}}}{K_{\mathrm{I}}^2 + K_{\mathrm{II}}^2}\right) \tag{2.43}$$

Minimum strain energy density criterion

The minimum strain energy density criterion was proposed by Sih [82] as a criterion to access the stability of crack propagation. The direction of crack growth is defined by the minimum of the strain energy density around the crack-tip. The strain energy density is defined as:

$$S = \frac{\mathrm{d}W}{\mathrm{d}V}r \tag{2.44}$$

where $\mathrm{d}V = r\mathrm{d}\theta\mathrm{d}r$, $\frac{\mathrm{d}W}{\mathrm{d}V}$ is the elastic energy per unit volume V and r is the radial coordinate of the polar coordinate system centered at the crack-tip. The strain energy density may also be computed from SIFs as:

$$S = \frac{1}{\pi r}\left(a_{11}K_{\mathrm{I}}^2 + a_{12}K_{\mathrm{I}}K_{\mathrm{II}} + a_{22}K_{\mathrm{II}}^2\right) \tag{2.45}$$

where the coefficients a_{11}, a_{12}, a_{22} depend on the Young's modulus E, on the Poisson's ratio ν and on the angle θ as follows:

$$\begin{aligned} a_{11} &= \frac{1}{16\mu\pi}(1+\cos\theta)(\kappa-\cos\theta); \\ a_{12} &= \frac{1}{16\mu\pi}\sin\theta(1\cos\theta-\kappa+1); \\ a_{22} &= \frac{1}{16\mu\pi}[(\kappa+1)(1-\cos\theta)+(1+\cos\theta)(3\cos\theta-1)] \end{aligned} \tag{2.46}$$

The angle θ_0 of crack propagation is obtained by setting:

$$\frac{\partial S}{\partial\theta} = 0, \tag{2.47}$$

Once the crack propagation angle is determined, the propagation criterion requires that the strain-energy-density factor reaches a critical value $S(\theta) = S_C$. The critical value S_C is related to the fracture toughness of the material (K_{IC}) and, in pure Mode I ($K_{II} = 0$), it is given by [82]:

$$S_C = \frac{\kappa-1}{8\mu}K_{IC}^2 \tag{2.48}$$

where κ, ν and μ have been already introduced. Basically, the minimum strain energy density criterion or S-criterion, predicts that the crack propagates when the energy density in a volume element near the crack-tip reaches a critical value.

2.2 Nonlinear Fracture Mechanics

Several material such as concrete and rock are often considered very brittle, even if they are *quasi-brittle* materials and like the so called *advanced ceramics*. Initially research on these materials was carried on towards engineering and developing ceramic composites which behave similarly to concrete. The toughness of quasi-brittle materials is influenced from sub-critical cracking that precedes ultimate failure and resulting into a nonlinear stress-strain response and R-curve behavior (the increase of the toughness with the crack extension typical of the ceramic materials). The fracture strength of these materials is often size dependent [83], due to the fact that nonlinear deformation in these materials is caused by sub-critical cracking rather than plasticity. For this reason, traditional approaches are not sufficient. The first fracture mechanics approaches for quasi-brittle materials were based on LEFM and were not able to consider the process zones formed near the macroscopic cracks. In this section a brief overview of nonlinear fracture mechanics is presented, with particular attention to the *cohesive zone model* used in Chapters 3 and 4. In general, the localized damaged material is modeled with nonlinear fracture mechanics through a pair of surfaces without volume between them, whose action is replaced by an equivalent traction on the surfaces. Dugdale [84] and Barenblatt [85] applied this concept to the quasi-brittle materials such as glassy, polymers, rocks, reinforced ceramics, concrete and composites. Hillerborg et al. [86] were

instead pioneers of the fictitious crack model for concrete. Afterwards, Carpinteri adopted this method, using the terminology *cohesive model*, to analyze the ductile-brittle transition and snap-back instability in concrete [87, 88]. Additional studies on size-scale effects were carried on by Bazant et al. [89]. From the computational point of view some relevant work is collected in [90, 91]. In general the nonlinear methods can be classified according to the loading scenario: normal and tangential behavior. Both are depending on the state of the interface (bonded or debonded) and on the loading type (monotonic and cyclic). A summary of all the constitutive responses of an interfaces crack are reported in Tab. 2.4.

Table 2.4: Normal and tangential behavior of an interfacial crack.

Interface behavior	Interface status	Loading		Mechanical modeling	Ref.
		Type	Condition		
Normal	Bonded	Monotonic	Compression	Constrain formulation	102
			Tension	Decohesion	101 103
		Cyclic	Compression	Constrain formulation	102
			Tension	Decohesion with damage	105
	Debonded	Monotonic	Compression	Micromechanical contact models	105
			Tension	Adhesion (low roughness)	34
				No tensile tractions (high roughness)	34
		Cyclic	Compression	Micromechanical contact models	105
			Tension	No Traction	34
Tangential	Bonded	Monotonic		Decohesion	103
		Cyclic		Decohesion with damage	104
	Debonded	Monotonic		Stick-slip	103
		Cyclic		Stick-slipwith general loading history	104

The crack behavior under normal monotonic and cyclic loading may be modelled with a constraint formulation using the Signorini's unilateral contact condition for modelling contact in compression [92, 93]. In this case, the impenetrability condition is usually imposed by a penalty approach [92].The formulation adopted in the tensile loading regime is usually given by the cohesive zone model.

2.2.1 Cohesive Zone Model

The process zone of a quasi-brittle material is shown in the sketch of Fig.2.10. Herein it is possible to distinguish a *micro-cracked* region. A *bridging* zone and finally a *macroscopic*

stress-free crack region. In particular the bridged zone is a weak interface between the ag-

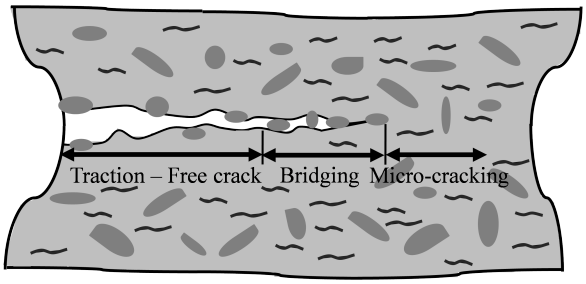

Figure 2.10: Schematic representation of crack growth in quasi-brittle material.

gregates and the matrix. Two models for the process zone are presented in Fig.2.11. The former (Fig.2.11(a)) models the process zone as region of strain softening and distributed damage within the volume. The latter (Fig.2.11(b)) models the process zone as a longer crack subjected to closuring tractions and it derives from the Dugdale-Barenblatt [84] strip-yield model.

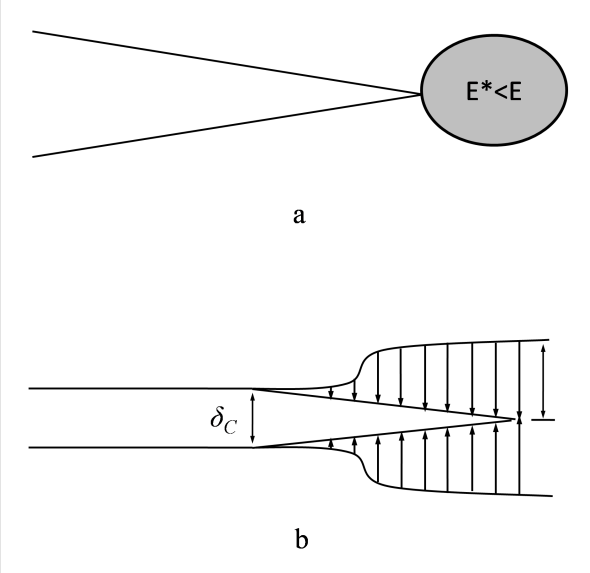

Figure 2.11: Two simplified models of the process zone idealize: (a) as a zone of strain softening, and (b) by closuring tractions.

By applying a tensile load to a brittle material, the stress-strain response is nonlinear because of the micro-cracking. When the material reaches the tensile stress σ_t, softening takes place

and the damaged zone is localized in a narrow zone at the crack tip.Moreover, during the softening it is virtually preferable to use the stress-displacement curve rather than a stress-strain curve, because the nominal strain becomes a function of gage length and the strain localizes in a narrow band. Among all the fracture models for concrete, most of them derive from the fictitious crack model of Hillerborg [86, 94]. It is an application of the Dugdale-Barenblatt approach [84]. By assuming that the stress-displacement behavior, $\sigma - \delta$, of the damaged zone is a material property. The critical displacement δ_c is the value of the displacement at the tip of the traction-free region of the damaged zone, where the tractions vanish. On the other hand, the traction at the tip of the damage zone is equal to the tensile strength σ_t, see Fig.2.11(b). The critical energy release rate for crack growth is given by:

$$G_{IC} = \int_0^{\delta_c} \sigma \mathrm{d}\delta \tag{2.49}$$

The assumption underlying the Hillerborg model [86, 94] that the stress displacement behavior is a material property is not strictly correct. Indeed, if the damaged zone in the fracture process is large enough, the interplay between the process zone and the free boundaries of the body (defining its size) can be important for the behavior of the system. Thus, G_{IC} can depend on the specimen size. As matter of fact, the fracture toughness resulting from small-scale tests tends to be higher than values obtained from larger samples. These size effects has been subject of considerable study [83, 95, 96, 97, 98, 99]. The localized damaged material is often modeled with an *interface* consisting on a pair of surfaces without volume between them. Its behavior is caught by an equivalent traction on the surfaces.
Carpinteri was a pioneer to use a cohesive zone model formulation to the study of ductile-brittle transition and snap-back instability in concrete [88,100]. The description of the gradual interface propagation is presented in [88, 101]. In the CZM for mixed mode simulations, it is necessary to define a relation between normal and tangential cohesive tractions and the relative opening and sliding displacements between the two sides of the crack. In pure Mode I, in particular, this relation is defined by the peak of the cohesive traction, σ_{max}, and the Mode I fracture energy G_{IC}, defined as the area below the CZM curve. Stress-free-cracks appear when the opening displacement, g_n, achieves the critical values, g_{nc}. It is possible to define different shapes of the CMZ curve (see Fig.2.12) inspired also by the shape of atomic potentials [102]. Looking at the CMZ curves, linear or bi-linear softening curves are usually employed in case of brittle materials, whereas trapezoidal or bell-shape are used for ductile fracture. In the linear and bi-linear CZMs it is possible to have an initial elastic branch with very high stiffness, to model interface elements already embedded from the very beginning of the numerical simulation into the FE mesh along predefined directions.

2.2.2 The interface finite element

Traditionally interface finite elements are inserted between the boundaries of the solid elements of the discretization of the continuum for several applications ranging from structural mechanics to materials science [103, 104, 105, 106, 107, 108, 109, 110, 111]. Paggi and Wriggers presented in [112] a 4-node bi-dimensional interface element. Each node i has two translational degrees of freedom, u_i and v_i, which can be expresses as an element displace-

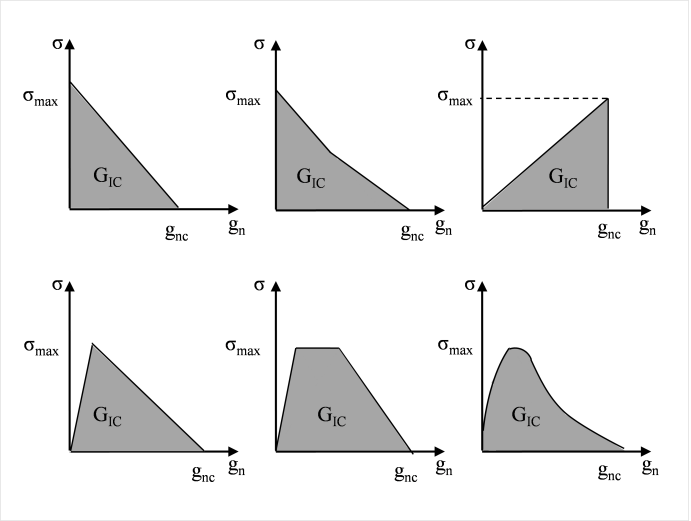

Figure 2.12: Different shapes of the CZMs curve available in the literature [102].

ment vector **u**:

$$\mathbf{u} = (u_1, v_1, u_2, v_2, u_3, v_3, u_4, v_4)^{\mathrm{T}} \tag{2.50}$$

This vector is given in the reference system of the global $x-y$ axis, centered in O and thanks to a rotation matrix **R** it may be expressed in a local system (see Fig.2.13) as : $\mathbf{u}^* = \mathbf{R}\mathbf{u}$. The vector of the tangential and normal gaps at a generic point of the middle line, $g = (g_{\mathrm{T}}, g_{\mathrm{N}})^{\mathrm{T}}$, is derived from the relative displacement vector $\Delta\mathbf{u}^* = (u_1^* - u_4^*, v_1^* - v_4^*, u_3^* - u_2^*, v_3^* - v_2^*)^{\mathrm{T}}$ as follows:

$$\mathbf{g} = \mathbf{N}\Delta\mathbf{u}^* \tag{2.51}$$

where **N** is a collection of linear shape function for the nodes 1* and 2*. The weak form for the interface element is given by:

$$G_{\mathrm{int}} = \int_{\mathrm{S}} \delta\mathbf{g}^{\mathbf{T}}\mathbf{t}\mathrm{d}S \tag{2.52}$$

where $\mathbf{t} = (\tau, \sigma)^{\mathbf{T}}$ is the traction vector. It is a nonlinear function of the normal and tangential relative displacement and it can be linearized by introducing a tangent **C** constitutive matrix **C**:

$$\begin{bmatrix} \frac{\partial\tau}{\partial g_T} & \frac{\partial\tau}{\partial g_N} \\ \frac{\partial\sigma}{\partial g_T} & \frac{\partial\sigma}{\partial g_N} \end{bmatrix} \tag{2.53}$$

The measure of the interface opening, λ, according to Tvergaard [104], is given by:

$$\lambda = \sqrt{\left(\frac{g_n}{g_{\mathrm{nc}}}\right)^2 + \left(\frac{g_t}{g_{\mathrm{tc}}}\right)^2}, \tag{2.54}$$

Relevant models are [113, 114, 115, 116, 117, 118, 119] and the exponential one by Ortiz and Pandolfi [120, 121].

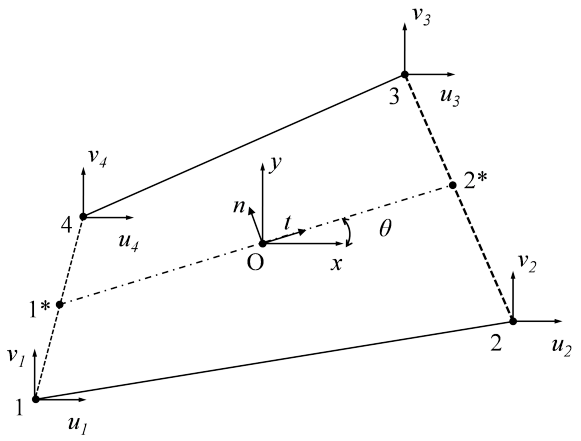

Figure 2.13: Two dimensional interface element.

Chapter 3

Modelling electro-mechanical coupling in cracked solar cells

The most common photovoltaic (PV) solar cells used in PV parks are made of monocrystalline or polycrystaline Silicon. An atom of Silicon in the crystal lattice absorbs a photon of the incident solar radiation and, if the energy of the photon is high enough, then an electron from the outer shell of the atom is freed. This process results in the formation of a hole-electron pair, where the hole is a fictitious positive charge corresponding to a lack of an electron in the crystal structure.
To avoid the natural recombination of electrons and holes, a potential barrier is built into the cells by doping the Silicon on the side exposed to sunlight with Phosphorous, to form $n-$Silicon, which has an excess of electrons in its outer shell. Similarly, on the opposite side, Silicon is doped with Boron, to form $p-$Silicon, which has a deficiency of electrons in its outer shell. By connecting the $p-n$ junction via an external circuit, a current flows through it. Electrical contacts are made by metal bases on the bottom of the cell and by metal grids *fingers* on the top layer. These fingers are soldered to two or three wider lines, referred to as busbars. The fingers collect the electric current from the front side of the solar cell and transfer it to the busbars, which are the main conductors connecting in series the solar cells building the PV module.

The typical width of each finger is around 110-120 μm and the height is around 10-20 μm. Generally the standard width-height ratio for a finger is 0.1-0.15. The improvement of a finger width-height ratio leads to an increase of the finger conductivity and a reduction of the shading, that is possible by printing narrower and thicker fingers [122]. Metallic paste of the fingers is deposited by screen-printing technique. In particular Silver is used as a conductive metal because of its good contact properties, its good conductivity and its excellent solderability. Silver powder represents the 70-85% in weight of the commercial pastes with different shaped particles (flakes or spherical powder grains) and dimension. The rest of the paste components are extremely sensitive to the device surface which has to be contacted and to the specific process parameters for the creations of the contact, such as temperature profiles and processing times. The additives used in the metallic paste are: *powder of glass frits* (metal oxides that are fundamental in the formation of the contact because their adhesion

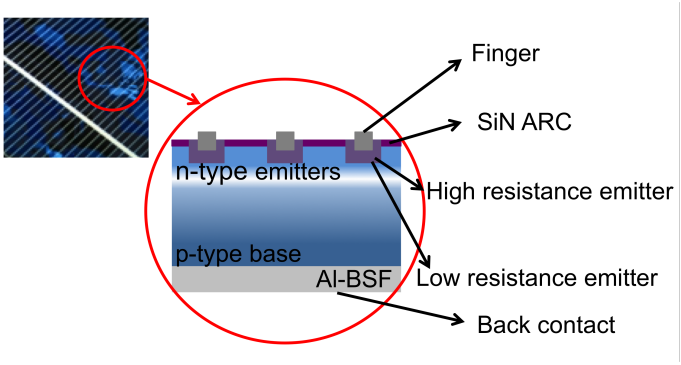

Figure 3.1: A sketch of a p-n junction.

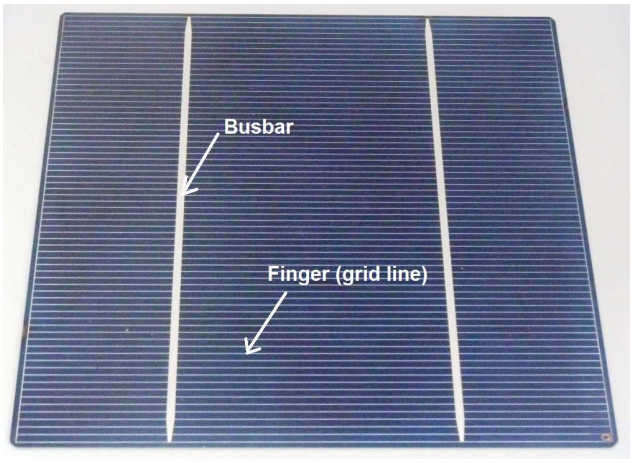

Figure 3.2: Solar cell with fingers and busbars.

function), *organic compounds* (used to transport the suspended Silver) and glass particles and *other additives* (which modify the rheological properties of the mixture and its interaction with the substrate surface wetting agents). Fig.3.2 shows a solar cell with its metallic contacts.
Under the assumption of an ideal semiconductor, which has homogeneous properties everywhere in the plane of the solar cell, a simple one-dimensional electric model is introduced in this Chapter to quantify the amount of current $I_f(\xi)$ along the finger, for each position described by the coordinate ξ ranging from one busbar to the other, see Fig.3.4.

3.1 Electric model of a grid line deposited on solar cells

The staring point for the electric model developed in this work and presented in this Chapter is an equivalent circuit for 1-dimensional current distribution adopted by Breitenstein et al. [123] for simulating the dependence of current on voltage in dark conditions and under illumination. They adopted a two diodes model, where the first diode (with ideality factor of unity) describes the diffusion current and the second diode (with ideality factor 2) takes into account the recombination current in the depletion region. However, only under illumination the second diode has a significant influence on the electric circuit and in this condition the parallel resistance R_P has to be taken into account. The equivalent circuit of the two diode model is shown in Fig.3.3. The series resistance, R_S is a crucial parameter in a solar cell. In the conventional two-diode model, R_S is related to all three current contributions (diffusion, recombination, and ohmic). In general it refers to *area-related series resistance* (Ω cm^2) and to current density for beeing independent from the cell area.

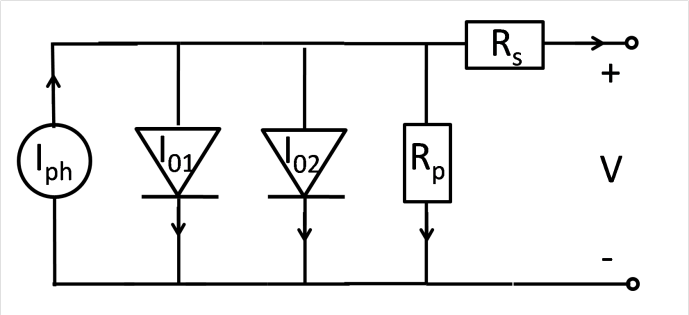

Figure 3.3: Equivalent circuit of a two-diode model for a solar cell under illumination.

Local vales of R_S are quantitatively measured through photoluminescence (PL) imaging. The *area-related* resistance, R_S, is defined over an area corresponding to a single camera pixel. Each area-pixel is connected to the cell terminal through its own R_S. Under this assumption, the metallization and the emitter has a negligible resistance and the R_s is related to the vertical current flow through the cell. The horizontal currents may lead to a distributed series resistance. For each position the voltage drop, is due both to the vertical diode current

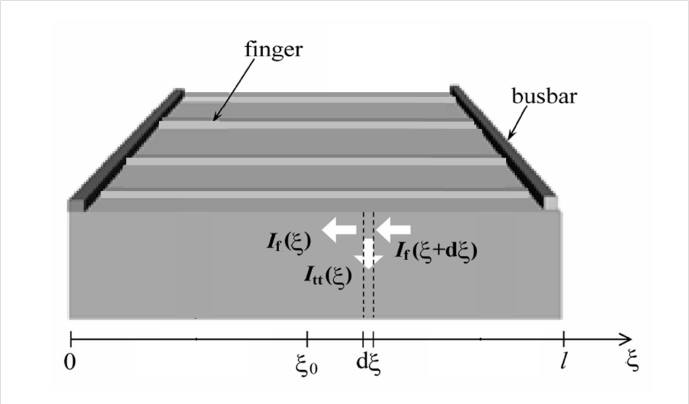

Figure 3.4: A sketch of a finger deposited over a solar cell, linking two busbar.

flowing in this position and to the diode current contributions from the whole lateral current path to the terminal.

During the electroluminescence test without illumination (I_{ph}=0) the one diode equivalent model is a good approximation (with I_{02}=0 and R_P=0 [123]). By introducing for each finger a local reference frame ξ, see Fig.3.4, with the axis ξ directed along the finger direction and ranging from the first busbar at $\xi = 0$ to the second at $\xi = l$, the surface density of electric current through the thickness of the solar cell originated in the semiconductor by the recombination under forward bias is I_{tt} (A/cm^2), the voltage is V (V), and the linear density of current (per unit depth) along the finger is I_f (A/cm) and it depends on the position ξ due to a distributed series resistance ρ_S (Ω/cm^2) evaluated as the grid resistance R_{grid} (Ω/cm) divided by the spacing between two fingers.

According to [123], the voltage is not constant, but it is a function of ξ due to a distributed resistance of the grid line, caused by metallization and emitter resistances. For each voltage $V(\xi)$, the current I_{tt} through the thickness of the cell, i.e., through the $p-n$ junction, can be finally modeled by a single diode equation. Without illumination, as during the conditions of the electroluminescence test performed inside a dark room, where the voltage at the busbars is externally imposed by a power supplier, the ordinary differential equation, assumes this form and relates the linear density of current along the finger $I_f(\xi)$ to the derivative of the voltage:

$$\frac{dV(\xi)}{d\xi} = -\rho_S I_f(\xi) \tag{3.1}$$

Moreover, for continuity conditions on an infinitesimal portion of the grid line and the solar cell below, the derivative of the linear density of current along the finger has to be equal to the surface density of current passing through the solar cell thickness:

$$\frac{dI_f(\xi)}{d\xi} = -I_{tt}(\xi) \tag{3.2}$$

By inserting the expression for I_f in Eq.(3.1) into Eq.(3.2), the following second order ordi-

nary differential equation is derived:

$$\frac{\mathrm{d}^2 V(\xi)}{\mathrm{d}\xi^2} = \rho_{\mathrm{S}} I_{\mathrm{tt}}(\xi) \tag{3.3}$$

The density of current through the thickness of the solar cell, I_{tt}, is due to the semiconductor properties whose response can be approximated by a single diode model [11]:

$$I_{\mathrm{tt}}(\xi) = I_{01} \exp\left(\frac{V(\xi) - R_{\mathrm{hom}} I_{\mathrm{tt}}(x)}{n_1 V_{\mathrm{T}}}\right) \tag{3.4}$$

where R_{hom} is the local sheet resistance in series with the diode, I_{01} is the saturation current density, $n_1 \sim 1$ is the ideality factor, $V_{\mathrm{T}} = k_{\mathrm{B}} T/e$ is the thermal voltage dependent on the absolute temperature T and on the Boltzmann's constant k_{B} and e the magnitude of the electrical charge. The behavior of the current $I_{\mathrm{tt}}(\xi)$ and of the voltage $V(\xi)$ has a parabolic characteristic with its minimum at ξ_0, consequently the profile of the series resistance is parabolic and it shows the maximum at ξ_0. This depends on the current paths, indeed at high voltage in the dark conditions the injection of the current occurs preferably close to the busbars respect to the grid line.

3.2 Generalization of the electric model in case of cracks

In the present Section, the electrical model described in Section 3.1 is generalized to simulate the cell under electroluminescence test conditions and by accounting for one or two cracks intersecting a finger.

Due to the implicit nature of Eq.(3.4), the current I_{tt} cannot be obtained in a closed form and Eq.(3.4) is recasted in a way so that the Newton-Raphson method can be applied:

$$f(I_{\mathrm{tt}}(\xi)) = I_{\mathrm{tt}}(\xi) - I_{01} \exp\left(\frac{V(\xi) - R_{\mathrm{hom}} I_{\mathrm{tt}}(\xi)}{n_1 V_{\mathrm{T}}}\right) = 0 \tag{3.5}$$

The approximation $I_{\mathrm{tt}}^{i+1}(\xi)$ at a generic iteration $i+1$ is obtained from that of the previous iteration $I_{\mathrm{tt}}^{i}(\xi)$ as follows:

$$I_{\mathrm{tt}}^{i+1}(\xi) = I_{\mathrm{tt}}^{i}(\xi) - \left[\frac{\mathrm{d}f}{\mathrm{d}I_{\mathrm{tt}}}\right]_i^{-1} f(I_{\mathrm{tt}}^{i}(\xi)) \tag{3.6}$$

where:

$$\left[\frac{\mathrm{d}f}{\mathrm{d}I_{\mathrm{tt}}}\right]_i = 1 + I_{01} \exp\left(\frac{V(\xi) - R_{\mathrm{hom}} I_{\mathrm{tt}}^{i}(\xi)}{n_1 V_{\mathrm{T}}}\right) - \frac{R_{\mathrm{hom}}}{n_1 V_{\mathrm{T}}} \tag{3.7}$$

Considering $I_{\mathrm{tt}}^{0} = 0.2$ mA/cm^2 as the starting value, the convergence is achieved when the error in the computed I_{v} is less than a prescribed tolerance. Due to the consistent update of the tangent, the rate of convergence is quadratic and few iterations are needed to achieve an error within the machine precision.

Numerical integration of the ODE in Eq.(3.3) is performed by discretizing the grid line in nodes (*nnd*) with a regular spacing $\mathrm{d}\xi$. The starting point for the integration is the point

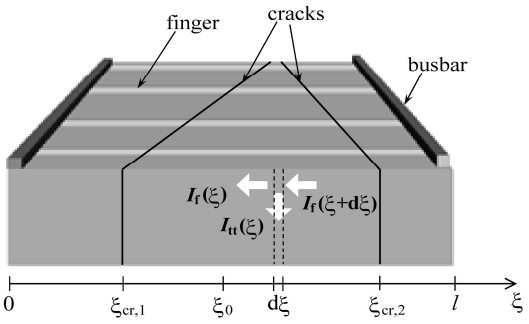

Figure 3.5: Schematic representation of a finger intersected by two cracks.

at $\xi = \xi_0$ where the voltage is minimum, V_0. For a finger not intersected by cracks, this point is simply located in the middle between two busbars ($\xi_0 = l/2$). For a finger intersected by a crack, ξ_0 is a free parameter to be identified by matching the value of the voltage at the busbars, which is a known imposed value in the EL test (see the sketch in Fig.3.5). For a tentative value of ξ_0, whose initial guess can be $\xi_0 = l/2$ and the corresponding voltage, $V(\xi_0) = V_0$, which is in general lower than the applied voltage at the level of busbars (0.7 V for a typical EL test), the integration path is separated in two parts. In reference to Fig.3.5, the first part is comprised between ξ_0 and the busbar on the left, and the second part ranges from ξ_0 and the busbar on the right. The current density $I_{tt}(\xi)$ is assumed to be constant within each integration interval. Under such an hypothesis, the voltage profile within each interval $d\xi$ is parabolic and the following equations hold:

$$V(\xi + d\xi) = V(\xi) + V'(\xi)d\xi + \frac{1}{2}V''(\xi)d\xi^2 \tag{3.8a}$$

$$V'(\xi + d\xi) = V'(\xi) + V''(\xi)d\xi \tag{3.8b}$$

$$I_f(\xi + d\xi) = I_f(\xi) + I_{tt}(\xi)d\xi \tag{3.8c}$$

where ($'$) and ($''$) denote, respectively, first and second order derivatives with respect to ξ.

Examining the integration in the first region (from $\xi = \xi_0$ to $\xi = 0$), the boundary conditions are $V(\xi_0) = V_0$ and $V'(\xi_0) = 0$. The vertical current $I_{tt}(\xi)$ is then computed with the Newton-Raphson method applied to Eq.(3.4). Next step, the voltage $V(\xi - d\xi)$, its derivative $V'(\xi - d\xi)$ and the linear density of current along the finger, $I_f(\xi - d\xi)$ are evaluated at the new integration point $\xi - d\xi$ according to Eq.(3.8). The negative sign of $d\xi$ is due to the integration from $\xi = \xi_0 > 0$ to $\xi = 0$.

At the point $\xi_{cr,1}$, where a crack crosses the finger, an additional localized resistance $R_{cr,1}$ is introduced, dependent on its crack opening, in agreement with experimental findings in [11] recently confirmed by optical microscope images and electric measurements in [124]. Indeed, as firstly pointed out in [11], the effect of a crack on I_{tt} is quite evident from the analysis of EL images. The brightness of the EL image, in fact, is proportional to I_{tt} [125] by a scaling factor. When the crack opening displacement is sufficiently large, a discontinuity in the grey-scale of the EL image takes place. Due to the presence of the concentrated resistance,

a discontinuity in the voltage distribution takes place in correspondence of this crack position, $\xi_{cr,1}$:

$$V(\xi_{cr,1}^{-}) = V(\xi_{cr,1}^{+}) + R_{cr,1} I_f(\xi_{cr,1}) \tag{3.9}$$

Afterwards, the integration proceeds as previously done before meeting the crack. Regarding the integration in the second region, from $\xi = \xi_0$ up to $\xi = l$, the same procedure as before is applied to compute $V(\xi + d\xi)$, $V'(\xi + d\xi)$ and $I_f(\xi + d\xi)$ in the point with coordinate $\xi + d\xi$, starting from the boundary condition imposed at $\xi = \xi_0$.

Again, in case of another crack intersecting the finger at $\xi = \xi_{cr,2}$, the voltage is increased in that point by the action of a concentrated resistance $R_{cr,2}$. The algorithm for two cracks intersecting a finger, which is the most general case found from EL inspections after production, is summarized in Algorithm 1. In the case of a single crack, it is sufficient to set equal to zero one of the two localized crack resistances.

3.2.1 Extension with a non-constant local sheet resistance

A further improvement of the model can be achieved by taking into account the damage of the material (Si) due to dislocation motion and stress relaxation close to the crack. Staring from the electrical model a non-constant resistance which depends on x is added to the constant local sheet resistance in series to the diode R_{ohm}, related to the crack. The non-constant resistance takes into account the degradation of the material proprieties. Generally, Vickers micro-indentation is a suitable methodology to propagate cracks in Silicon solar cells that are similar to those induced by impacts [126, 127]. In the following Section Vickers test and the corresponding the corresponding hardness, extracted from the test, are introduced.

Hardness

The hardness identifies the resistance to deformation and has a particular meaning in each sector of material science. In mechanics of materials, hardness means the resistance to indentation, and for mechanical engineers it often means an easily measured quantity which correlates with the strength and heat treatment of the metal. In general it is a parameter used to characterize the plastic properties of a solid.
Indentation hardness tests together with nano-indentation techniques have been used to measure hardness over a wide range of size scales in various forms of materials (small bulk crystals and thin films on substrate also in the semiconductor industry).

It is usually possible to measure the hardness with three tests [128]:

- scratch hardness;
- indentation hardness;
- rebound, or dynamic, hardness.

Scratch tests are used by mineralogists. It measures the ability of a material, in particular minerals, to scratch each other. The hardness is measured according to the *Mohs'*scale which consists of 10 standard minerals: form 1 (corresponding to Talc) to 10 (corresponding to Diamond).

Data: $\mathrm{d}\xi$, $\xi_{\mathrm{cr},1}$, $\xi_{\mathrm{cr},2}$; number of integration points nnd_1 and nnd_2; distance l between two busbars; tolerance $\mathrm{tol}_0 = 5 \times 10^{-2}$ on the error w.r.t. experimental data; tolerance $\mathrm{tol}_1 = 0.7/10$ w.r.t. the value of the voltage at the busbars, V_b spatial tolerance $\mathrm{tol}_2 = l/\max\{nnd_1, nnd_2\}$; tolerance $\mathrm{tol}_3 = 1 \times 10^{-13}$ of the Newton-Raphson method
Initialize: norm $\leftarrow 1$, $\mathrm{norm}_V \leftarrow 1$, error $\leftarrow 1$, $\mathrm{error}_V \leftarrow 1$, $V_0 \leftarrow 0.7$, $\xi_0 \leftarrow l/2$
while error $>$ tol_0 **do**
  while $\mathrm{error}_V > \mathrm{tol}_1$ **do**
    Integrate from $\xi = \xi_0$ to $\xi = 0$:
    for $j = 1$ **to** nnd_1 **do**
      if $|\xi - \xi_{\mathrm{cr},1}| < \mathrm{tol}_2$ **then**
        Modify the voltage V according to Eq.(3.9)
      end
      Compute $I_{\mathrm{tt},j}$ with the Newton-Raphson method;
      Initialize $i = 1$, $I^i_{\mathrm{tt}} = 0.2$ A;
      while norm $>$ tol_3 **do**
        $i \leftarrow i + 1$;
        Compute I^i_{tt}, Eq.(3.6);
        Compute norm $= \|I^i_{\mathrm{tt}} - I^{i-1}_{\mathrm{tt}}\|$;
      end
      $I_{\mathrm{tt},j} \leftarrow I^{i+1}_{\mathrm{tt}}$;
      Compute $I_{\mathrm{f},j}$, $V^{''}_j$, and $V^{'}_j$ using Eq.(3.8), $\xi \leftarrow \xi - \mathrm{d}\xi$;
    end
    Integrate from $\xi = \xi_0$ to $\xi = l$:
    for $j = 1$ **to** nnd_2 **do**
      if $|\xi - \xi_{\mathrm{cr},2}| < \mathrm{tol}_2$ **then**
        Modify the voltage V according to Eq.(3.9)
      end
      Compute $I_{\mathrm{tt},j}$ with the Newton-Raphson method;
      Initialize $i = 1$, $I^i_{\mathrm{tt}} = 0.2$ A;
      while *error*$>\mathrm{tol}_3$ **do**
        $i \leftarrow i + 1$; Compute I^i_{tt}, Eq.(3.6);
        Compute norm $= \|I^i_{\mathrm{tt}} - I^{i-1}_{\mathrm{tt}}\|$;
      end
      $I_{\mathrm{tt},j} \leftarrow I^{i+1}_{\mathrm{tt}}$;
      Compute $I_{\mathrm{f},j}$, $V^{''}_j$, and $V^{'}_j$ using Eq.(3.8), $\xi \leftarrow \xi + \mathrm{d}\xi$;
    end
    Compute $\mathrm{error}_V = \max\{\|V(\xi = 0) - V_b\|, \|V(\xi = l) - V_b\|\}$ and modify ξ_0;
  end
  Compute error$= \sum_{\mathrm{k}=1}^{nnd_1+nnd_2}(I^k_{\mathrm{tt}} - I^k_{\mathrm{exp}})/I^k_{\mathrm{exp}}$ and reduce V_0;
end

Algorithm 1: Algorithm for the computation of the electric voltage and currents along a finger intersected by one or two cracks.

Standardized indentation tests used in engineering are: Brinell, Meyer, Vickers and Rockwell test [128].
The Brinell hardness test, proposed by J. A. Brinell in the 20^{th} century, consists in the indentation of a relative smooth and free dirt surface with a steel ball with a diameter of 10 mm at a load of 3000 kg. The load and the impression ball might be changed in particular conditions. Indeed in case of soft metals the load is reduced to 500 kg to prevent exceeded impression. A Tungsten Carbide ball is used to minimize distortion of the indenter in case of hard material. The load is applied for a fixed time, around 30 s, afterwards the ball is removed and the diameter of the indentation is measured with a low-power microscope. Two readings of the diameter of the impression are taken and the average is computed. The Brinell hardness number (BHN) is proportional to the applied load as following [128]:

$$BHN = \frac{\mathrm{P}}{\pi D \mathrm{t}} \tag{3.10}$$

where P is the load, D is the diameter of the ball and t is the depth of the impression.
A measure less sensitive to the applied load is the *Meyer* test. It is a more fundamental measure of indentation hardness. The relationship between the size of the indentation and the load is called *Meyer's law* as follows [128]:

$$P = kd^n \tag{3.11}$$

where d is the diameter of indention, n is a material constant related to the strain hardening of the material and k is a material constant related to the resistance to the penetration.

A different shape of the indenter is used in the *Vickers* test, where is a square-base diamond pyramid. The included angle between opposite faces of the pyramid is 136 ° because it approximates better the ratio of indentation diameter to ball diameter in the Brinell hardness test. This test is also called *diamond-pyramid hardness* (DPH) test because of the shape of the indenter. Vickers hardness number (VHN, or VPH), is defined as following [128]:

$$VHN = \frac{2P \sin\left(\frac{\theta}{2}\right)}{L^2} \tag{3.12}$$

where θ is the angle between the opposite face of the pyramid and L the average length of diagonal. The Vickers hardness provides a continuous scale of hardness, for a given load, from very soft metals with a DPH of 5 to extremely hard materials with a DPH of 1500.
Rockwell hardness test uses the depth of indentation, under a constant load, as measure of hardness. During this test a minor load is applied to seat the specimen and minimizes the surface preparation needed. After that the major load is applied, and the depth of indentation measured in terms of arbitrary hardness numbers. Commonly it is necessary to change the load and the indenter at some point of the hardness scale in the Rockwell and the Brinell scale. Because the impressions made by the pyramid indenter are geometrically similar no matter what their size, the DPH should be independent of load [128]. The hardness of various semiconductors against the reciprocal temperature is shown in Fig.3.6 with an applied load of 0.5 N and dwell time of 30 s. In addition the hardness of various semiconductor materials

at room temperature together with the fracture toughness, band-gap energy at 300 K, bonding distance and shear modulus are summarized data from [129] in Tab. 3.1.

Table 3.1: Material proprieties for various semiconductor materials at room temperature with an applied load 0.5 N and dwell time 30 s .

Material	Hardness	Fracture Toughness	Band-gap Energy	Bonding distance	Shear modulus
	GPa	MPa $m^{-1/2}$	eV	Å	GPa
α-SiC(0001)	22.9	3.3	2.9	1.88	192
AlN(0001)	17.7		6.2	1.92	133
GaN(0001)	10.2	1.1	3.4	1.96	116
ZnO(0001)	4.7	0.6	3.6	1.80	50
ZnSe(111)	1.1	0.9	2.5	2.45	25.3
Si(111)	12.0	0.7	1.1	2.35	60.5
Ge(111)	7.12	0.6	0.66	2.44	48.9
GaP(111)	7.73	0.65	2.3	2.36	49.7
GaAs(111)	6.8	0.4	1.5	2.45	41.5
InP(111)	4.49	0.44	1.4	2.54	30.2
InAs(111)	2.63	0.30	0.35	2.63	25.9
CdTe(111)	0.42		1.49	2.80	12.2
α-Al_3O_3(0001)	28**	2.5		1.92	170

In some cases the indentations cause crack patterns. Usually the size of the indents was measured by neglecting such cracks and generating ambiguity. Indeed it is known that the indention of Si (and probably Ge) is associated with a form of phase transformation that leaves an amorphous-like structure after unloading [131, 132]. For $T \leq 500°C$ for Si, the hardness value (HV) is influenced by the pressure for the phase transformation and only weakly by temperature, see Fig.3.6. At low temperatures, HV decreases in the following order: the group IV elemental crystals, the III-V compounds, and the II-VI compounds, without considering the crystal structure (diamond, sphalerite or wurtzite). Thus, SiC, GaN, and AlN have a lower susceptibility to deformation during device processing at elevated temperatures than with the elemental and III-V and possibly II-VI compounds having the sphalerite structure.

Prashant et al. [127] applied a Vickers indentation to mime the wire-saw of Si substrates, to create brittle fracture induced cleavage (radial/median) and residual stress field related sub-surface (lateral) micro-cracks [133, 134]. During this test, radial or lateral micro-cracks appear into Silicon, if the plastic stress overcomes the fracture strength. Indeed Griffith's criterion asserts that when released elastic energy, U, at crack tip overcomes the minimum energy, γ_S, associated to the creation of a free surface, a flaw or micro-crack becomes unstable and fracture occurs. According to Griffith's criterion [49] the critical nominal fracture stress σ_n is given in Chapter 2 by Eq.(2.8), for a given crack length, a, in a material with elastic modulus E. Dislocation motion and stress relaxation might influence the fracture stress near the crack tip [48]. In this region, in Silicon, phase-transformations, crack-branching, and defect generations have been reported [135, 136, 134, 137, 138].

Prashant et al. [127] outlined the distribution of residual stress and the corresponding phase transitions, applying the nano-indentation technique to small samples of 10 mm × 5 mm starting from Czochralski (CZ) grown Si. The resulting samples were chemical and mechanical polished. They created micro-indents with alignment of indenter cleaved face along <110> direction through Vickers micro-indenter. The micro-indents resulted in radial micro-

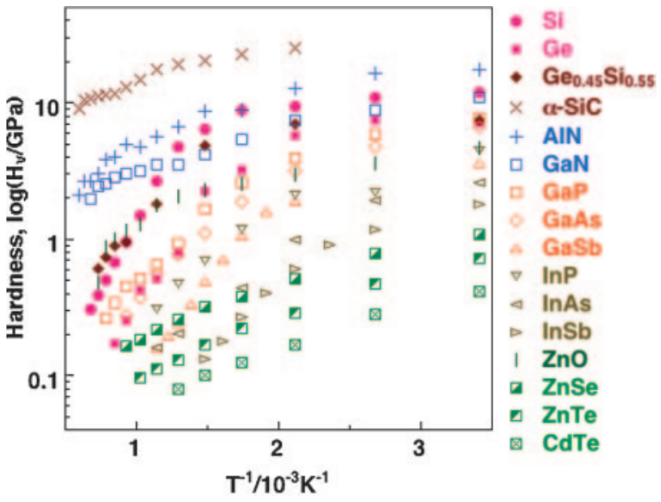

Figure 3.6: Vickers indentation hardness of single crystals of various semiconductors vs. temperatures adapted from [130].

cracks which propagate from indenter corners and few circularly extending lateral cracks from indenter edges. Prashant et al. [127] determinated mechanical properties (hardness, Young's moduli, etc.), phase changes and loading-induced deformation behavior of Silicon via an accurate examination of load (P) vs. displacement (h) curves. Through a micro-Raman tool they examined the phases at the intact, micro-indented and around micro-crack regions of Si sample and the Electron Beam Scattered Diffraction (EBSD) was used to measure the diffraction pattern. The Micro-Raman analysis of the stress distributions showed that the radial cracks exhibit tensile stresses, whereas the extending sub-surface lateral cracks induce compressive stresses in Silicon. Furthermore they found, from EBSD analysis, that the diffraction lines closer to the radial crack became indistinct. This phenomena is the effect of the amorphization of the region around the cleavage cracks in PV Silicon. The hardness data was obtained in [127] from load vs. displacement plot (P-h curves) of each nano-indent on both sides of the micro-crack. The hardness gradually dropped from 10.1 GPa to 6.7 GPa and from 10.2 GPa to 5.4 GPa on left and right sides of the crack, respectively. Thus, they proved that nano-indentation causes a drop in the hardness, which correspond to a gradual weakening of Si-lattice closer to the radial micro-cracks.

Resistance

The one-dimensional model proposed in Section 3.2 can thus be improved by modifying the expression for the electric resistance along the grid line accounting for the effect of damage as indicated by hardness measurements. The experimental trend reported by Prashant et al. [127] can be interpreted by the following equation relating hardness measurement with

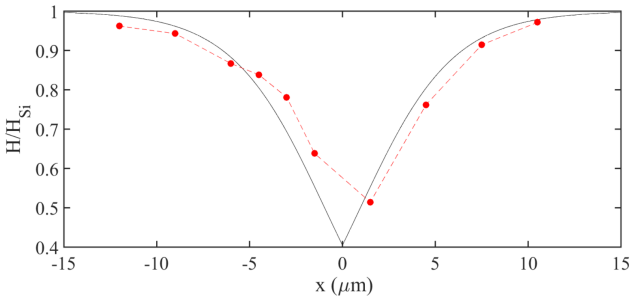

Figure 3.7: Profile of the hardness near the channel crack located at x=0 (experimental data from [127], interpreted by an exponential decay in this thesis, shown with solid line).

the distance from the main channel (see Fig.3.7):

$$\frac{H}{H_{\mathrm{Si}}} = \left[H_{\mathrm{Si}} \exp(x)^{\frac{a}{H_{\mathrm{min}}}} + 1\right]^{-1} \tag{3.13}$$

where the hardness of the undamaged Silicon is H_{Si}=10.5 GPa, H_{min}=7.1 GPa, and a=0.4. The experimental data in red dots [127] and the exponential trend described with the solid black line are shown in Fig.3.7.

In the most general case, a finger can be crossed by two cracks originated by a Vickers indentation and the coordinates of the two crossing points are denoted by x_{cr1} and x_{cr2}. The density of electric current through the thickness, I_{tt}, can be computed according to a classic single diode as per Eq. (3.4) where the local sheet resistance in series with the diode, R_{hom}, is usually treated as a simple constant in the available formulations, and the voltage V is varying along the finger due to the distributed grid line resistance. Here, the use of a non-constant value for R_{hom} is proposed, with a dependency on ξ based on the degradation trend of material properties analogous to that observed as in Fig.3.7, i.e.:

$$R_{\mathrm{hom}}(\xi) = \begin{cases} \exp\left(\frac{\xi-\xi_{\mathrm{cr1}}}{l}\right)^k R_{\mathrm{d1}} + \exp\left(\frac{\xi-\xi_{\mathrm{cr2}}}{l}\right)^k R_{\mathrm{d2}} + R'_{\mathrm{hom}} & \text{if } \xi < \xi_{\mathrm{cr1}} \\ \exp\left(-\frac{\xi-\xi_{\mathrm{cr1}}}{l}\right)^k R_{\mathrm{d1}} + \exp\left(\frac{\xi-\xi_{\mathrm{cr2}}}{l}\right)^k R_{\mathrm{d2}} + R'_{\mathrm{hom}} & \text{if } \xi_{\mathrm{cr1}} \le \xi \le \xi_{\mathrm{cr2}} \\ \exp\left(-\frac{\xi-\xi_{\mathrm{cr1}}}{l}\right)^k R_{\mathrm{d1}} + \exp\left(-\frac{\xi-\xi_{\mathrm{cr2}}}{l}\right)^k R_{\mathrm{d2}} + R'_{\mathrm{hom}} & \text{if} \xi > \xi_{\mathrm{cr2}} \end{cases} \tag{3.14}$$

where R_{d1}, R_{d2}, R'_{hom}, and k are free parameters of the model. Furthermore, a localized resistance R_{cr} is considered at the point where a crack crosses the finger, as done in the previous Section.

3.2.2 Extension in case of poly-crystalline Silicon

In polycrystalline Si cells, the series resistance R_{S}, is in-homogeneous and depends on grain boundaries and defects. This is clearly evidenced by a close analysis of a EL image [139]. The distribution of the brightness within the image does not depend only on the distance from the

busbars as for monocrystalline Si, but several darker spots, representing grain boundaries and defects, are randomly distributed within the cell. To take into account these effects a spatially in-homogeneous series resistance is introduced instead of the constant and homogeneous R_{hom}. Such a resistance can be defined as $R_{\text{ave}} + \mathrm{d}R$, where R_{ave} is a constant average value and $\mathrm{d}R$ takes into account the fluctuations/perturbations, using pseudo-random values taken from a Gaussian distribution with a prescribed variance. In this way is possible to apply the model along a grid line of an intact and a cracked polycrystalline cell and with crack. Results and comparison with experimental data will be presented in the following Chapter focusing on the experimental validation of the electric proposed model.

3.2.3 Algorithm for a complete solar cell

In this Section the electric model to the analysis of the whole Silicon solar cell is detailed. The coordinates of the crack is introduced as additional input and it is checked if each finger crosses a crack. If the crack is found the model follows the Algorithm 1, instead for an intact finger the code is modify removing the modification of the voltage due to the presence of the crack resistance as in Eq.(3.9). The complete model is described in Algorithm 2.

Data: $\mathrm{d}\xi$, $\xi_{\mathrm{cr},1}$, $\xi_{\mathrm{cr},2}$; number of integration points nnd_1 and nnd_2; distance l between two busbars; tolerance $\mathrm{tol}_0 = 5 \times 10^{-2}$ on the error w.r.t. experimental data; tolerance $\mathrm{tol}_1 = 0.7/10$ w.r.t. the value of the voltage at the busbars, V_b spatial tolerance $\mathrm{tol}_2 = l/\max\{nnd_1, nnd_2\}$; tolerance $\mathrm{tol}_3 = 1 \times 10^{-13}$ of the Newton-Raphson method, crack coordinates

for $i = 1$ **to** N_F Number of fingers **do**
  if i , current finger, contains a crack **then**
    Compute V and I_tt with Algorithm 1;
  else
    Initialize: norm $\leftarrow 1$, $\mathrm{norm}_V \leftarrow 1$, error $\leftarrow 1$, $\mathrm{error}_V \leftarrow 1$, $V_0 \leftarrow 0.7$, $\xi_0 \leftarrow l/2$
    while error $>$ tol_0 **do**
      while $\mathrm{error}_V > \mathrm{tol}_1$ **do**
        Integrate from $\xi = \xi_0$ to $\xi = 0$:
        for $j = 1$ **to** nnd_1 **do**
          Compute $I_{\mathrm{tt},j}$ with the Newton-Raphson method;
          Initialize $i = 1$, $I^i_\mathrm{tt} = 0.2$ A;
          while norm $>$ tol_3 **do**
            $i \leftarrow i + 1$;
            Compute I^i_tt, Eq.(3.6);
            Compute norm $= \|I^i_\mathrm{tt} - I^{i-1}_\mathrm{tt}\|$;
          end
          $I_{\mathrm{tt},j} \leftarrow I^{i+1}_\mathrm{tt}$;
          Compute $I_{\mathrm{f},j}$, $V^{''}_j$, and $V^{'}_j$ using Eq.(3.8), $\xi \leftarrow \xi - \mathrm{d}\xi$;
        end
        Integrate from $\xi = \xi_0$ to $\xi = l$:
        for $j = 1$ **to** nnd_2 **do**
          Compute $I_{\mathrm{tt},j}$ with the Newton-Raphson method;
          Initialize $i = 1$, $I^i_\mathrm{tt} = 0.2$ A;
          while *error*$>$$\mathrm{tol}_3$ **do**
            $i \leftarrow i + 1$; Compute I^i_tt, Eq.(3.6);
            Compute norm $= \|I^i_\mathrm{tt} - I^{i-1}_\mathrm{tt}\|$;
          end
          $I_{\mathrm{tt},j} \leftarrow I^{i+1}_\mathrm{tt}$;
          Compute $I_{\mathrm{f},j}$, $V^{''}_j$, and $V^{'}_j$ using Eq.(3.8), $\xi \leftarrow \xi + \mathrm{d}\xi$;
        end
        Compute $\mathrm{error}_V = \max\{\|V(\xi = 0) - V_b\|, \|V(\xi = l) - V_b\|\}$ and modify ξ_0;
      end
      Compute error= $\sum_{\mathrm{k}=1}^{nnd_1+nnd_2}(I^k_\mathrm{tt} - I^k_\mathrm{exp})/I^k_\mathrm{exp}$ and reduce V_0;
    end
  end
end

Algorithm 2: Algorithm for the scanning of a complete Silicon solar cell

3.3 Stress analysis of a photovoltaic module: a global/local approach

In this Section a kinematically consistent global/local finite element approach to the simulation of cracking in solar cells embedded in PV modules is proposed, this approach was also object of a publication [140]. Via a projection of displacements from the global coarse model of the laminate to the fine-scale local model of the solar cells, it is possible to quantify opening of cracks and run fine-scale local analyses in parallel. The computed crack opening displacements obtained by solving the local models can be sequentially transferred as input to the electric model described in Section 3.2, for an accurate simulation of the electric response of cracked solar cells.

A parameters identification procedure has been performed in reference to results obtained in our experimental campaign. The electric resistance vs. crack opening determined by matching the simulated I_{tt} values and the experimental ones is considered to be the first step to determine a robust electro-mechanical constitutive relation for cracks of the type $R_{\mathrm{cr}}(g_{\mathrm{n}})$, to be applied to all the cracks intersecting the grid line. This relation should be independent of boundary conditions and can be used as a constitutive relation for the cracks, as the cohesive traction-relative displacement relation, or the heat flux-temperature jump relation.

The multi-physics capabilities of the proposed computational approach are important to understand the physics behind the electric degradation of cracks, which is a phenomenon strongly affected by thermo-mechanical deformation. Nonetheless, the use of a simplified electric model for each finger makes the application of the model feasible and appealing for the photovoltaics community.

Based on the EL images, coarse-scale and fine-scale finite element meshes of the PV module can be generated by considering the actual stacking sequence and materials composing the module layers based on manufacturer's specifics. The fine-scale finite element mesh can be generated by an automated meshing software able to deal with an arbitrary number of detected cracks. Global/local simulations finally allow the prediction of the EL signal of each cell in the presence of cracks, based on the proposed electric model in Section 3.2 and the identified $R_{\mathrm{cr}}(g_{\mathrm{n}})$ relation. The reliability of the numerical predictions can therefore be ascertain with care in comparison with experimental EL images taken in the laboratory. All the model parameters can therefore be tuned in a condition that can be controlled and reproduced. Then, the predictive capabilities of the proposed numerical tool can be explored to simulate the degradation of the electric response of PV modules with cracked solar cells under different weathering scenarios that cannot be simulated in the laboratory. This can be done by considering the complex stress state inside the PV module, realistic loading conditions, and the actual orientation of cracks impacting the power-loss in different ways depending on their crack opening and therefore on their orientation with respect to the stress field inside the module.

3.3.1 Global/local approach

The global/local approach is a computational strategy often adopted in fiber-reinforced or laminated composites to deal with problems having two very different length scales [141,

142], such as the scale of the component and the scale of its micro-structure. In general, a homogeneous global or *coarse-scale* model is used to compute the displacement field. The displacements from the global model are taken as boundary conditions for the local model, which is a *fine-scale* representation of a portion of the composite where the material micro-structure and its mechanical degradation is simulated with a greater accuracy. In some cases, a feedback from the local model to the global one is required, viz. by updating the global stiffness matrix.

In photovoltaics, to investigate the effect of realistic loading conditions, it is necessary to simulate the whole composite laminate and the phenomenon of cracking at the cell level, which requires much more details than the global stress analysis. A single fine resolution finite element model able to accurately simulate cohesive cracks in solar cells embedded in the PV module would be computationally too expensive to solve. Moreover, the experimental evidence in [143] shows that cracks have a low impact on the stiffness of the module. Therefore, uncoupling of the global finite element model of the PV module from a local finite element model of each solar cell appears to be a viable choice to reduce the computation cost, allowing also the use of parallel computing schemes for each cell.

Paggi et al. [11] were pioneers on this line of research. They proposed a global model of the PV module, discretized by plate finite elements based on the Kirchhoff theory, to perform linear elastic structural analyses. The composite structure of the laminate was accounted for by introducing effective elastic properties depending on the stack composition. A 2D local model of each solar cell was then proposed by using plane stress continuum triangular and quadrilateral linear finite elements separated by interface elements along the grain boundaries of polycrystalline Silicon. The global structural analysis provided the out-of-plane displacement w_z and the rotations ϕ_x and ϕ_y in the finite element nodes of the composite plate. These generalized displacements were used to determine the in-plane displacements at the level of each solar cell, to be imposed as boundary conditions to the local model solved under the assumption of plane stress.

In this Section a refined three-dimensional global/local approach is proposed [140], providing a more accurate description of the physical phenomenon of electric degradation due to cracking, and a more consistent coupling between the coarse-scale and fine-scale finite element models in terms of kinematics as compared to [11].

3.3.2 The coarse-scale finite element model of the laminate

To efficiently deal with different loading conditions and PV module geometries, the global coarse-scale finite element model used to simulate the structural response of the PV module should be as general as possible. To deal with the most complex loading scenario, a linear brick elements is used for thermo-mechanical loading simulations, or solid shell elements like those used in [142, 144]. Alternatively, if geometry and loading allow a simplification, like in case of bending of the whole PV module with respect to one of its two symmetry axes, it might be convenient to consider a cross-section of the module and perform a 2D simulation using two-dimensional linear continuum elements.

In any case, solid-like discretizations (2D plane stress or plane strain solid elements for plane problems; bricks and tetrahedra, or solid shell finite elements for three dimensional

problems) should be preferred over Kirchhoff-Love plate elements used in [11] for the following reasons:

- In the framework of solid-like finite elements it is easier to accurately model the interspace between solar cells than in Kirchhoff plate elements. This task is important when the evolution of the gap between solar cells is a quantity of interest, viz. for the prediction of failure of the busbars due to cyclic thermo-mechanical loads.

- Thermo-visco-elastic constitutive models for the encapsulant are easier to be implemented in solid-like finite elements than in Kirchhoff plate elements. Generalized thermo-visco-elastic models are in fact already available in most of the commercial packages and this might foster the use of the proposed global/local approach at the industrial level for the simulation of degradation processes in PV modules [145,146,147].

- Solid-like finite elements have a kinematics that can be consistently coupled with 2D or 3D interface elements for cohesive fracture [144], since only translational degrees of freedom are present without rotational degrees of freedom like in the Kirchhoff plate elements. This is important for the simulation of the decohesion of the backsheet layer from the other laminate, a phenomenon requiring the discretization of all the laminate composing the PV stack. In the case of problems displaying large displacements, the interface element formulation proposed in [145,142,148] can also be consistently used.

From the global coarse-scale finite element model of the laminate, displacements in the x, y and z directions of the nodes of the finite elements belonging to the edges of the solar cells can be determined by a simple post-processing of the linear finite element results. These displacements have to be passed as input to the local model as boundary conditions. To this aim, it is necessary a projection operation, since the finite element discretization used in the fine-scale model is not required to match the one used in the global mode. From the algorithmic point of view, it is convenient to introduce geometrical entities like facets to distinguish between the nodes of the finite elements belonging to the different sides of the solar cell, namely the lower side, the upper side, the two vertical sides along the $x-$direction, and the two vertical sides along the $y-$direction.

For each node of the finite elements belonging to a given facet of the local model, their displacement boundary conditions are evaluated by performing a linear interpolation between the displacement values of the closest neighboring nodes in the global model. This projection procedure is described in the Algorithm 3.

3.3.3 The fine-scale finite element model of the solar cells

In the fine-scale model of each solar cell, a three dimensional finite element discretization of the continuum is considered by using linear brick elements. A MATLAB pre-processor for the finite element analysis program FEAP [62] has been written to generate the finite element mesh of monocrystalline Silicon solar cells including one or two internal cracks, whose locations are defined by the coordinates of their tips. Block commands in FEAP are used to generate a structured finite element mesh and duplicate the nodes of the elements along the crack. Three dimensional interface elements with a cohesive zone model formulation are

for $t = 1$ **to** T displacement or loading increments **do**
  Impose force or displacement boundary conditions in the global model;
  Solve the global model in terms of displacements using a full Newton-Raphson method in case of nonlinear constitutive laws for cohesive interfaces between the layers, or for geometric nonlinearities, if included;
  for $s = 1$ **to** S solar cells **do**
    for $i = 1$ **to** N facets defining the sides of the cell **do**
      for $j = 1$ **to** M nodes in the local model belonging to the facet i **do**
        Find the two closest nodes P_1 and P_2 belonging to the same facet in the global model;
        Impose a displacement vector $\mathbf{u}_j = N_1\mathbf{u}^{(1)} + N_2\mathbf{u}^{(2)}$, where $\mathbf{u}^{(1)}$ and $\mathbf{u}^{(2)}$ are the displacement vectors of the nodes P_1 and P_2, and N_k are linear shape functions ($k = 1, 2$).
      end
    end
  end
end

Algorithm 3: Numerical algorithm for the displacements projection from the global to the local model.

then inserted through the cell thickness with a certain traction-separation relation that can be defined arbitrarily. An example of a 3D finite element discretization of a solar cell is shown in Fig.3.8.

Since the interface elements are the only elements inducing a nonlinearity in the local model, their modeling is presented with care in [140]. The contribution to the Principle of Virtual Work of the interface cohesive tractions $\mathbf{T}$ acting along the cohesive crack surfaces S_0 is:

$$\Pi_{\text{crack}} = \int_{S_0} \mathbf{g}_{\text{loc}}^{\text{T}} \mathbf{T}\, \mathrm{d}S \tag{3.15}$$

where $\mathbf{g}_{\text{loc}}$ is the gap vector that accounts for opening and sliding displacements between the two faces of the crack. The virtual variation of Π_{crack} reads:

$$\delta\Pi_{\text{crack}} = \delta\mathbf{u}^{\text{T}} \int_{S_0} \left(\frac{\partial \mathbf{g}_{\text{loc}}}{\partial \mathbf{u}}\right)^{\text{T}} \mathbf{T}\mathrm{d}S \tag{3.16}$$

Introducing the discretization of the interface by using isoparametric finite elements, the interpolated position vector of the points belonging to the average plane between the crack faces in the undeformed configuration is obtained by multiplying the interface element nodal values by the operator $\mathbf{N}$ that collects the shape functions:

$$\overline{\mathbf{X}} \cong \overline{\mathbf{X}}^e = \mathbf{NMX}^n, \tag{3.17}$$

where the superscript n denotes quantities evaluated at the nodes of the discretized geometry, viz. $\mathbf{X}^n = (X_1, Y_1, Z_1 \ldots, X_8, Y_8, Z_8)^{\text{T}}$. In case of a 3D quadrilateral linear interface element

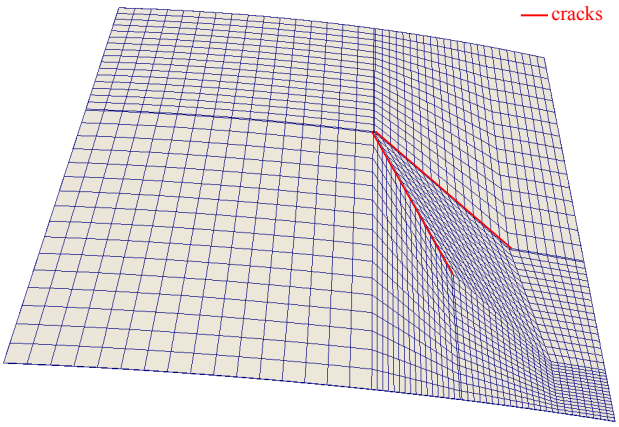

Figure 3.8: An example of a local model with two cohesive cracks.

(see Fig.3.9), the matrix operators have the following expression:

$$\mathbf{N} = \begin{bmatrix} N_1\mathbf{I} & N_2\mathbf{I} & N_3\mathbf{I} & N_4\mathbf{I} \end{bmatrix} \tag{3.18a}$$

$$\mathbf{M} = \frac{1}{2}\begin{bmatrix} \mathbf{I} & \mathbf{0} & \mathbf{0} & \mathbf{0} & \mathbf{I} & \mathbf{0} & \mathbf{0} & \mathbf{0} \\ \mathbf{0} & \mathbf{I} & \mathbf{0} & \mathbf{0} & \mathbf{0} & \mathbf{I} & \mathbf{0} & \mathbf{0} \\ \mathbf{0} & \mathbf{0} & \mathbf{I} & \mathbf{0} & \mathbf{0} & \mathbf{0} & \mathbf{I} & \mathbf{0} \\ \mathbf{0} & \mathbf{0} & \mathbf{0} & \mathbf{I} & \mathbf{0} & \mathbf{0} & \mathbf{0} & \mathbf{I} \end{bmatrix} \tag{3.18b}$$

where $\mathbf{0}$ is a 3×3 null matrix and $\mathbf{I}$ is a 3×3 identity matrix. The shape functions in the standard natural reference system $(s_1, s_2) \in [-1, +1] \times [-1, +1]$ read:

$$N_1 = \frac{1}{4}(1 - s_1)(1 - s_2) \tag{3.19a}$$

$$N_2 = \frac{1}{4}(1 + s_1)(1 - s_2) \tag{3.19b}$$

$$N_3 = \frac{1}{4}(1 + s_1)(1 + s_2) \tag{3.19c}$$

$$N_4 = \frac{1}{4}(1 - s_1)(1 + s_2) \tag{3.19d}$$

The gap vector in the reference cartesian frame, $\mathbf{g}$, can be obtained by pre-multiplying the nodal displacement vector $\mathbf{d} = (u_1, v_1, w_1 \ldots, u_8, v_8, w_8)^{\mathrm{T}}$ by a suitable operator $\mathbf{L}$ which provides the difference between the displacements of the two crack faces. Within the finite element discretization, the interpolation scheme of the gap vector reads:

$$\mathbf{g} \cong \mathbf{g}^e = \mathbf{NLd} \tag{3.20}$$

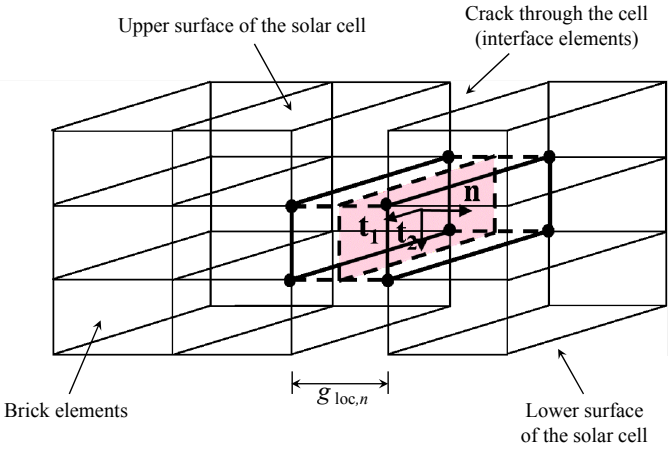

Figure 3.9: A sketch of an interface element embedded between brick elements, through the thickness of Silicon cells.

where the matrix operator **L** is:

$$\mathbf{L} = \begin{bmatrix} -\mathbf{I} & \mathbf{0} & \mathbf{0} & \mathbf{0} & \mathbf{I} & \mathbf{0} & \mathbf{0} & \mathbf{0} \\ \mathbf{0} & -\mathbf{I} & \mathbf{0} & \mathbf{0} & \mathbf{0} & \mathbf{I} & \mathbf{0} & \mathbf{0} \\ \mathbf{0} & \mathbf{0} & -\mathbf{I} & \mathbf{0} & \mathbf{0} & \mathbf{0} & \mathbf{I} & \mathbf{0} \\ \mathbf{0} & \mathbf{0} & \mathbf{0} & -\mathbf{I} & \mathbf{0} & \mathbf{0} & \mathbf{0} & \mathbf{I} \end{bmatrix} \tag{3.21}$$

The constitutive relation for the crack, the so-called cohesive zone model (CZM), is provided in a local frame and defined by the tangential and the normal vectors to the middle surface of the interface element ($\mathbf{t}_1$, $\mathbf{t}_2$ and $\mathbf{n}$), see Fig.3.9. These unit vectors can be determined via differentiation of the average coordinates with respect to the natural coordinates s_1 and s_2.

The gap vector in this local frame, $\mathbf{g}_{\text{loc}} = (g_{\text{loc,t}_1}, g_{\text{loc,t}_2}, g_{\text{loc,n}})^{\text{T}}$, is computed by multiplying the gap vector in the reference frame by a rotation operator **R**:

$$\mathbf{g}^e_{\text{loc}} = \mathbf{R}\mathbf{g}^e \tag{3.22}$$

where the rotation matrix collects the components of the unit vectors $\mathbf{t}_1$, $\mathbf{t}_2$, and $\mathbf{n}$:

$$\mathbf{R} = \begin{bmatrix} t_{1,x} & t_{1,y} & t_{1,z} \\ t_{2,x} & t_{2,y} & t_{2,z} \\ n_x & n_y & n_z \end{bmatrix} \tag{3.23}$$

Introducing the finite element discretization, Eq.(3.22) can be rephrased as:

$$\mathbf{g}^e_{\text{loc}} = \mathbf{RNLd} = \mathbf{RBd} \tag{3.24}$$

where $\mathbf{B} := \mathbf{NL}$ has been introduced to simplify the notation. Examining the terms entering the virtual variation of Eq.(3.16), the partial derivative $(\partial \mathbf{g}_{\text{loc}}/\partial \mathbf{u})$ is given by:

$$\frac{\partial \mathbf{g}_{\text{loc}}}{\partial \mathbf{u}} \cong \frac{\partial \mathbf{g}^e_{\text{loc}}}{\partial \mathbf{d}} = \mathbf{RB} \tag{3.25}$$

Inserting this intermediate result into the discretized version of Eq.(3.16), where $\mathbf{u}$ is simply replaced by $\mathbf{d}$, the following general formulation valid for any CZM relation is derived:

$$\delta \Pi^e_{\text{crack}} = \delta \mathbf{d}^{\text{T}} \int_{S_0} (\mathbf{RB})^{\text{T}} \mathbf{T} \, \text{d}S \tag{3.26}$$

For the cohesive traction vector $\mathbf{T} = (\tau_1, \tau_2, \sigma)^{\text{T}}$, an irreversible CZM whose shape is characterized by a linear ascending branch followed by an exponential softening is used. Coupling between Mode I and Mode II fracture is accounted for. The resulting expressions for the normal and tangential cohesive tractions are:

$$\sigma = \begin{cases} \sigma_{\max} \exp\left(\dfrac{-l_0 - |g_{\text{t}}|}{r}\right) \dfrac{g_{\text{n}}}{l_0}, & \text{if} \quad 0 \le \dfrac{g_{\text{n}}}{r} < \dfrac{l_0}{r} \\ \sigma_{\max} \exp\left(\dfrac{-g_{\text{n}} - |g_{\text{t}}|}{r}\right), & \text{if} \quad \dfrac{l_0}{r} \le \dfrac{g_{\text{n}}}{r} < \dfrac{g_{\text{nc}}}{r} \\ 0, & \text{if} \quad \dfrac{g_{\text{n}}}{r} \ge \dfrac{g_{\text{nc}}}{r} \end{cases} \tag{3.27}$$

$$\tau = \begin{cases} \tau_{\max} \exp\left(\dfrac{-l_0 - g_{\text{n}}}{r}\right) \dfrac{g_{\text{t}}}{l_0}, & \text{if} \quad 0 \le \dfrac{|g_{\text{t}}|}{r} < \dfrac{l_0}{r} \\ \tau_{\max} \operatorname{sgn}(g_{\text{t}}) \exp\left(\dfrac{-g_{\text{n}} - |g_{\text{t}}|}{r}\right), & \text{if} \quad \dfrac{l_0}{r} \le \dfrac{|g_{\text{t}}|}{r} < \dfrac{g_{\text{tc}}}{r} \\ 0, & \text{if} \quad \dfrac{|g_{\text{t}}|}{r} \ge \dfrac{g_{\text{tc}}}{r} \end{cases} \tag{3.28}$$

where the model parameters are: l_0, which defines the opening and sliding displacements corresponding to the peak CZM tractions before the onset of exponential softening; the critical opening and sliding displacements, g_{nc} and g_{tc}, corresponding to complete debonding in pure opening and shearing loading; the root mean square of the microscopic surface roughness of the crack profile, r, computed as in [102]. As compared to other CZM formulations like in [104], defining the cohesive tractions by a single nonlinear equation over the whole separation range which is easier to be numerically implemented, here the ascending branch is treated separately from the softening one. This choice allows us to keep the slope of the linear branch high and not related to the value of $\sigma_{\max}$, and keep constant the interface fracture energy acting on g_{nc} and g_{tc}. A graphical representation of the pure Mode I and Mode II CZM relations is provided in Fig.3.10.

Due to the nonlinearity in the CZM relation, a consistent linearization of Eq.(3.26) is required for the application of the Newton-Raphson solution scheme. The contribution of the weak form at the $k+1$ iteration can be related to that of the previous iteration k by a truncated Taylor series expansion:

$$\delta \Pi^e_{\text{crack}}(\mathbf{d}^{k+1}) \cong \delta \Pi^e_{\text{crack}}(\mathbf{d}^k) + \frac{\partial \delta \Pi^e_{\text{crack}}(\mathbf{d}^k)}{\partial \mathbf{d}} \Delta \mathbf{d} \tag{3.29}$$

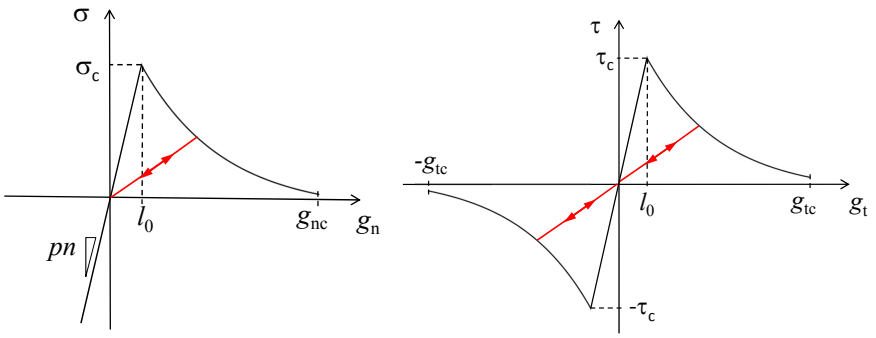

(a) Mode I (b) Mode II

Figure 3.10: CZM formulation for irreversible opening and shearing deformation.

where $\Delta\mathbf{d} = \mathbf{d}^{k+1} - \mathbf{d}^{k}$. Henceforth, the iteration index will be omitted to simplify notation. Performing the linearization of the cohesive traction vector $\mathbf{T} = (\tau_1, \tau_2, \sigma)^{\mathrm{T}}$ as customary, obtaining:

$$\frac{\partial \mathbf{T}}{\partial \mathbf{g}_{\mathrm{loc}}} = \mathbf{C} \tag{3.30}$$

where $\mathbf{C}$ represents the tangent interface constitutive matrix of the element:

$$\mathbf{C} = \begin{bmatrix} \dfrac{\partial \tau_1}{\partial g_{\mathrm{loc,t1}}} & \dfrac{\partial \tau_1}{\partial g_{\mathrm{loc,t2}}} & \dfrac{\partial \tau_1}{\partial g_{\mathrm{loc,n}}} \\ \dfrac{\partial \tau_2}{\partial g_{\mathrm{loc,t1}}} & \dfrac{\partial \tau_2}{\partial g_{\mathrm{loc,t2}}} & \dfrac{\partial \tau_2}{\partial g_{\mathrm{loc,n}}} \\ \dfrac{\partial \sigma}{\partial g_{\mathrm{loc,t1}}} & \dfrac{\partial \sigma}{\partial g_{\mathrm{loc,t2}}} & \dfrac{\partial \sigma}{\partial g_{\mathrm{loc,n}}} \end{bmatrix} \tag{3.31}$$

The final formulation presented in [140] is the following:

$$\frac{\partial \delta \Pi^{e}_{\mathrm{int}}(\mathbf{d})}{\partial \mathbf{d}} = \int_{S_0} \mathbf{B}^{\mathrm{T}} \mathbf{R}^{\mathrm{T}} \mathbf{C} \mathbf{R} \mathbf{B} \, \mathrm{d}S \tag{3.32}$$

providing the residual vector $\mathbf{f}_{\mathrm{crack}}$ and the tangent stiffness matrix $\mathbf{K}$ of the interface element:

$$\mathbf{f}_{\mathrm{crack}} = \int_{S_0} (\mathbf{R}\mathbf{B})^{\mathrm{T}} \, \mathbf{T} \, \mathrm{d}S \tag{3.33a}$$

$$\mathbf{K} = \int_{S_0} \mathbf{B}^{\mathrm{T}} \mathbf{R}^{\mathrm{T}} \mathbf{C} \mathbf{R} \mathbf{B} \, \mathrm{d}S \tag{3.33b}$$

This formulation can also be augmented by considering thermal conduction as proposed for 2D in [102]. The crack opening displacement computed at each node of the interface element is finally passed as input to the electric model, which allows for the simulation of the electric response of the solar cell.

Chapter 4

Experimental validation of the electric model

The aim of this Chapter is the validation, with the use of experimental data, of the one-dimensional electric model introduced and described in Chapter 3. Nevertheless before presenting the numerical and experimental results, the tools and the techniques used during the tests, the electroluminescence and the approach adopted for the detection of the cracks in PV modules are described in Section 4.1.2. After that, the model proposed in Section 3.1 is herein applied to pre-cracked monocrystalline Si cells embedded in semi-flexible modules. Crack patterns in the PV modules have been introduced in three different way: impact tests, indentation tests and bending loading. All these methods are described in the Section 4.2. The electric model proposed in Section 3.2, with the localized resistance, is herein validated in Section 4.3. The degradation in the solar cells due to indention test, connecting the reduction in the hardness with the change in the resistance $R(x)$ as described in Section 3.2.1 is investigated in Section 4.3.2. Furthermore the electric model for polycrystalline solar cells is validate with experimental data in Section 4.5.

4.1 The electroluminescence technique

The electroluminescence (EL) technique is a fast and non destructive method to investigate module defects i.e. micro-cracks, shunts between emitter and base of the solar cell, disruptions within metal grid of the solar cell or of the electrical interconnectors [149, 150]. This tool is also used to evaluate characteristic parameters of a solar cell such as: the diffusion length L_{eff} [151], the carrier collection length L_{C} [152], the local junction voltage [153] and the series resistance [154, 155]. Takahashi et al. [149] were pioneers of EL technique by proposing a photographic investigation, named *luminoscophy*, to detect mechanical damage and process failure during cell fabrication. The set-up consisted of a Si-charge coupled devised camera (CCD) able to capture the infrared light emitted by a solar cell under forward bias [149]. Under this bias condition, solar cells emit infrared light (IR) with a peak at 1150 nm, and the intensity of the resulting signal is proportional to the total excess minority car-

rier density. The electroluminescence intensity is converted in an image. All the defects and the failures coincide with dark parts i.e. spots, lines, areas in the resulting images and they correspond to parts with a decrease in the EL-signal. In particular in monocrystalline solar cell dark spots corresponding to crystal defects are not presents. Instead in poly-Si solar cells the presence of gray and black regions are linked to grain boundaries, non-uniformity of the surface passivation and crystalline defects. Thanks to the fact that EL is not reabsorbed by the Si-substrate, it is possible to get a deficiency map integrated along the depth, like in the *fluoroscopy*. Takahashi et al. [149] performed the tests in a dark room at room temperature, applying an appropriate forward bias (between 0-80 mA/cm^2 corresponding to 1-2 Suns). The cooled CCD camera (around -50°C) equipped with selective IR-lens, detected a range of wavelength of 300-1200 nm and the optical lens defined the resolution. The benefits of the method proposed by Takahashi et al. [149] were the non-destructive approach and the very short measurement time (less than 1 s at room temperature). The same authors improved the set-up and changed the name of the technique in *electroluminescence*. In their following works they were able to obtain a quantitive agreement with the minority carrier diffusion length measured with standard techniques, to estimate the diode ideality factor and the open circuit voltage of a solar cell [125]. The typical spectrum of emission of a infrared sensitive Ge-photodetector, the EL signal at room temperature is shown in Fig.4.1.

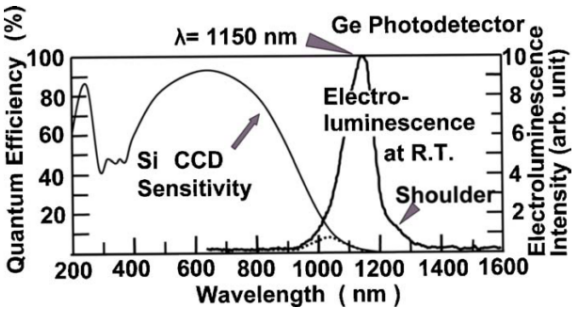

Figure 4.1: Spectrum of emission and the sensitivity of the Si CCD camera [125].

The peak of emission of Silicon is at 1150 nm and it corresponds to the band to band radiative recombination assisted by photons. The sensitivity of the CCD is up to 1200 nm as shows Fig.4.1 therefore the overlapping region, represented by the dotted line is a limited portion of the EL spectrum but it is still enough to obtain a clear EL image of Si-cell.

4.1.1 Physics of electroluminescence

The EL intensity (I_L) is proportional to the effective diffusion length L_e at fixed inject condition and to the total excess of minority carrier along the depth x in the p-active layer (N) integrated along the depth. Due to the very thin n-layer it is possible to neglect the EL resulting from the n-layer of the p-n junction respect to the p-layer, which is the only one considered.

The dependence of I_L on the excess of the minority carriers at the p-n junction edge ($n_{p(0)}$) is governed by the applied forward voltage V_f and can be expressed by the following equation:

$$I_L = A \exp\left(\frac{eV_f}{k_B T}\right) \tag{4.1}$$

thus:

$$\ln I_L = A^{'} + \frac{e}{k_B T} V_f \tag{4.2}$$

where e is the electron charge, k_B is the Boltzmann's constant, T is the measurement temperature, $A^{'}$ and A are two constants respectively.

The injected forward current J_f is defined as:

$$J_f = J_0 \exp\left(\frac{eV_f}{nk_B T}\right) \tag{4.3}$$

where n is the diode ideality factor and J_0 is the dark saturation current. Thus, it is possible to rewrite the term $\ln I_L$, introducing V_f obtained from (4.3) in the (4.2):

$$\ln I_L = A^{''} + n \ln J_f \tag{4.4}$$

where $A^{''}$ is a constant.

4.1.2 Setup of the electrolumiescence test

The experimental tests and the EL analysis were performed in the laboratory *Center for Risk Analysis and Durability of Structures* (Resp. Prof. B. Chiaia, G. Ferro and M. Paggi) of the Department of Structural, Geotechnical and Building Engineering of Politecnico di Torino. The list of equipment used for this aim is the following:

- Infrared sensitive camera, pco.1300solar;
- Programmable DC power supply, Genesys GENH60-12.5 (750W-1U,TDK-Lambda);
- Notebook;
- Control software Camware for the camera system.

Infrared sensitive camera

The pco.1300 solar (see Fig.4.2) is a charge coupled device (CCD) designed for EL applications in the range of 850 nm to 1200 nm. The CCD is an integrated circuit etched onto a Silicon substrate transforming electromagnetic radiation, *light*, in sensitive elements, *pixels*. Photons incident on the devices generate charges that can be collected by electronics and converted into a digital pattern. The CCD is constituted by two parts: an epitaxial photoactive Si-layer, for capturing photons, and a shift register (the real CCD) for the transmission of the charge. In the photoactive region there is a capacitor array to accumulate the electric charge, proportional to the radiation for each location.

Figure 4.2: CCD camera used for the electroluminescence measurements.

It is possible to have a line or a two-dimensional CCD array. In the line-scan cameras, the array is one-dimensional and acquires a single slice of the image whereas in some cameras the array is two-dimensional and acquires the picture projecting it on the focal plane of the sensor. A control circuit manages the charges as in a shift register. At the end of the array an amplifier collects the charges for each point and converts it into a proportional voltage before the digitalization. The quantum efficiency (QE) of the pco.1300 solar is reported in Fig.4.3. The QE is up to 13 % at 880 nm. Thanks to a special offset control algorithm of this camera has very high offset stability (drift $\leq$ 1 count/h), respect to the ambient temperature or signal changes, ensuring accurate and repeatable quantitative measurements over long periods of time. The camera has a FPGA (field-programmable gate array) processor allowing

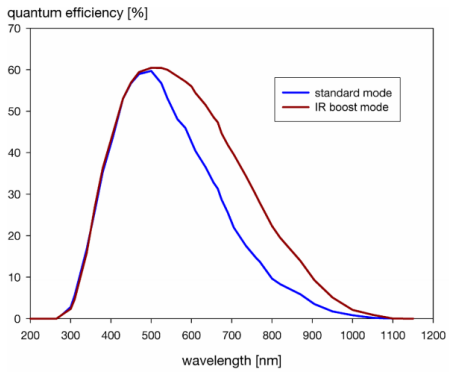

Figure 4.3: Quantum efficiency of the pco.1300solar

a sophisticated control and an accurate timing of the CCD and associated electronics. The camera specifics are listed in Tab. 4.1. The lens used for this camera is a 50 mm f/1.4 by Schneider Kreuznach. Its characteristics are illustrated in Tab. 4.2. The depth-of-field table was used to regulate better the focusing of the lens, in order to find the optimum compromise between the diaphragm aperture and the distance to the panel. To obtain a clear image, an aperture of f/1.8 has been selected and a focus at 9.14 m. In this way the panel is in focus if it

Table 4.1: Technical data of the pco.1300 solar camera.

	pco.130 solar	Units
Resolution	1392 x 1040	pixel
Pixel size	6.45 x 6.45	μm
Dynamic range	12	bit
Exposure time	5 μs to 1 hour	s
Internal frame buffer	64 (min)	MB
Readout noise	6/10	e$^-$rms
Frame rate	5.97 to 11.7	fps
Pixel scan rate	10 to 20	MHz
Ambient temperature	+10 to +40	$^\circ$ C
Operating humidity	10 to 80	%
Storage temperature	-20 to +70	$^\circ$ C
Cooled method	1 stage Peltier cooler with forced air cooling	

is placed at a distance from 7.83 m to 10.76 m. Otherwise, with a lower aperture as f/22, the object is in focus from 2.71 m to infinity. In general, reducing the aperture of the lens, less light comes into the CCD and therefore the exposure time has to be significantly increased (above 6 s, which is normally considered to be an exposure time that guarantees a good EL image quality).

Table 4.2: Depth of field table.

Permissible aberrated circle diameter 3/100 mm (Unit: Meters)														
Aperture	Distance													
	0.46		0.61		0.91		1.52		3.05		9.14		∞	
f/1.4	0.45	0.46	0.60	0.62	0.90	0.93	1.49	1.56	2.90	3.21	7.83	10.76	56.39	∞
f/1.7	0.45	0.46	0.60	0.62	0.90	0.93	1.48	1.57	2.87	3.25	7.65	11.31	46.38	∞
f/2	0.45	0.46	0.60	0.62	0.90	0.93	1.48	1.58	2.84	3.28	7.48	11.71	40.60	∞
f/2.8	0.45	0.46	0.60	0.62	0.89	0.94	1.45	1.60	2.77	3.38	6.97	13.22	29.03	∞
f/4	0.45	0.46	0.59	0.62	0.88	0.95	1.43	1.63	2.67	3.55	6.34	16.38	20.03	∞
f/5.6	0.45	0.47	0.59	0.63	0.87	0.96	1.39	1.68	2.55	3.80	5.65	24.11	14.56	∞
f/8	0.45	0.47	0.59	0.64	0.85	0.99	1.35	1.76	2.38	4.26	4.86	83.51	10.22	∞
f/11	0.44	0.48	0.58	0.65	0.83	1.02	1.29	1.87	2.20	5.02	4.15	∞	7.46	∞
f/16	0.43	0.48	0.56	0.67	0.80	1.07	1.21	2.08	1.96	7.21	3.34	∞	5.16	∞
f/22	0.42	0.50	0.55	0.69	0.76	1.00	1.12	2.44	1.73	15.09	2.71	∞	3.77	∞

The adjustment of the setting parameter is very important to obtain accurate and high quality EL-image. By using nearly the maximum aperture of the camera (F1.8), the focus of the camera was adjusted during the tests to obtain a perfect focus for all the various deflections

of the module. The selected setting parameters for the experiments presented in this Chapter are: exposure time 6 s and cut-off filters 600-8200 nm.

Power supply: Genesys GENH60-12.5

The Genesys GENH60-12.5 750W-1U power supply, see Fig.4.4, is a TDK-Lambda programmable direct current (DC) device used to apply the forward voltage to modules during the EL measurement. It presents the following features:

- High output power density of 750 W in 1U half-rack size;
- Output voltage up to 60 V;
- Current up to 12.5 A.

An input voltage of 7 V have been used for generating a current flow of 10 A in a module containing 10 cells.

Figure 4.4: GENH60-12.5 power supply

HP EVO laptop

The HP EVO laptop is equipped with Windows XP as operating system and a standard IEEE 1394a (Firewire) interface, used to acquire the signal coming from the pco.1300 solar. The notebook supports the Camware software to control the camera. An additional homemade screening box has been added to the notebook to screen the CCD camera during the EL tests and consequently to reduce the noise caused by luminosity of the laptop screen.

Control Software for the camera system: CamWare by PCO

The CamWare software acquires all the information about the EL radiation provided by the camera. Moreover, it allows to elaborate and post-process the images to reduce the impact of external light on the measurements. This operation is performed through a cut-off of wavelength for the EL intensity distribution and selecting only the range that is interesting for these studies. The CamWare command window allows the modification of the acquisition parameters in order to find the optimal setup and to obtain the best EL images of the solar panel. The software gives a preview of the images that the camera is going to take, to adjust the exposure time as well as the focus of the camera, and the external conditions on the solar

panel. From the Camera Control command, it is possible to vary the exposure time of the CCD camera. As mentioned the software allows to select only a part of the EL Spectrum cutting-off the EL intensity distribution from the Camera Convert Control Color window (see Fig.4.5).

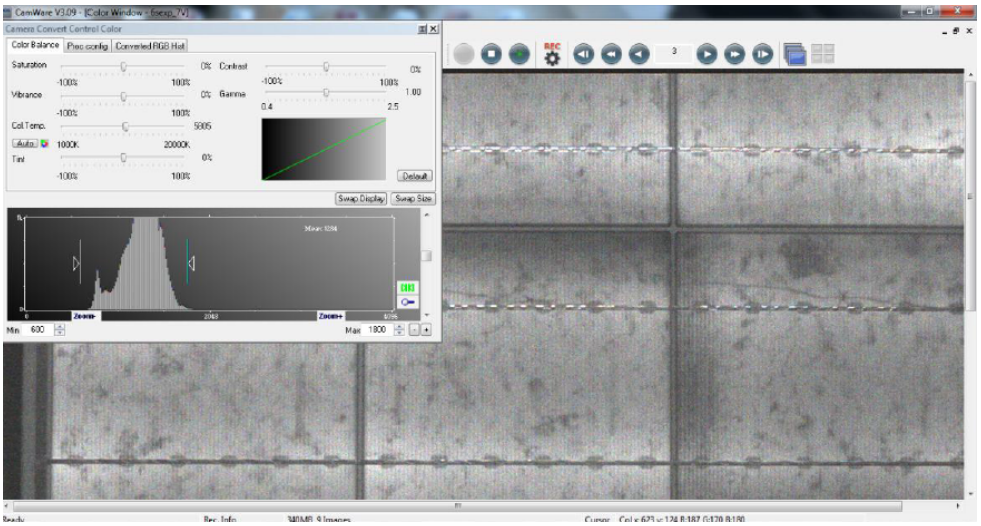

Figure 4.5: Camera Convert Control Color window.

4.2 Design of the experiments

Three type of tests to validate the models presented in Chapter 3 have been designed: impact and bending tests, indentation tests and line bending tests. The impact tests were realized on semi-flexible PV modules made of 2 rows of 5 monocrystalline Silicon solar cells, where the size of each cell is 156×156 mm. The partially symmetric arrangement of the layers through the thickness (0.265 mm of polyethylene terephthalate, 0.600 mm of epoxy-vinyl-acetate, 0.166 mm of Silicon, 0.400 mm of epoxy-vinyl-acetate and 0.345 mm of backsheet, see Fig.4.6) and the different Young's moduli of the materials lead to Si cells just above the neutral axis of the cross-section.

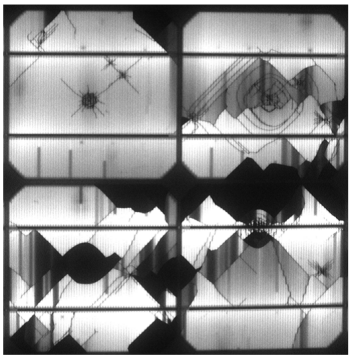

Figure 4.7: Electroluminescence of cells 1-4 reported in Fig.4.8.

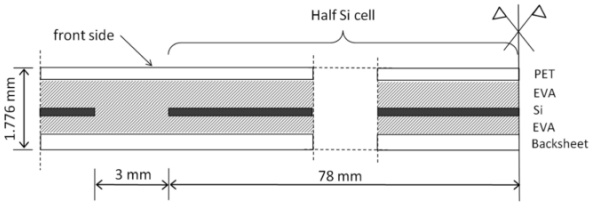

Figure 4.6: Sketch of the cross-section of the PV module near the symmetry line.

This type of module, which has a certain degree of flexibility, can be used in many applications where the substrate to be bonded is curved. To create pre-existing cracks and evaluate the crack opening depending on the imposed bending, Polymethylmethacrylate (PMMA) balls of 4 cm of diameter has been used. These balls were used to realize impacts at a velocity of 6 m/s and simulate the action of hail impacts [126].

Location of impacts can be clearly distinguished (see Fig.4.7) by the circular dark spots from where diagonal cracks, influenced by the crystallographic planes of cubic face centered monocrystalline Silicon, depart. These patterns are completely invisible with the naked eye and can only be detected by the EL technique.

Bending test on the resulting pre-cracked flexible modules has been performed using the test setup showed in Fig.4.9. In order to induce a tensile stress state inside solar cells, the curvature imposed to the module was such that the convex side after bending corresponds to the PET side (front side, see Fig.4.8).

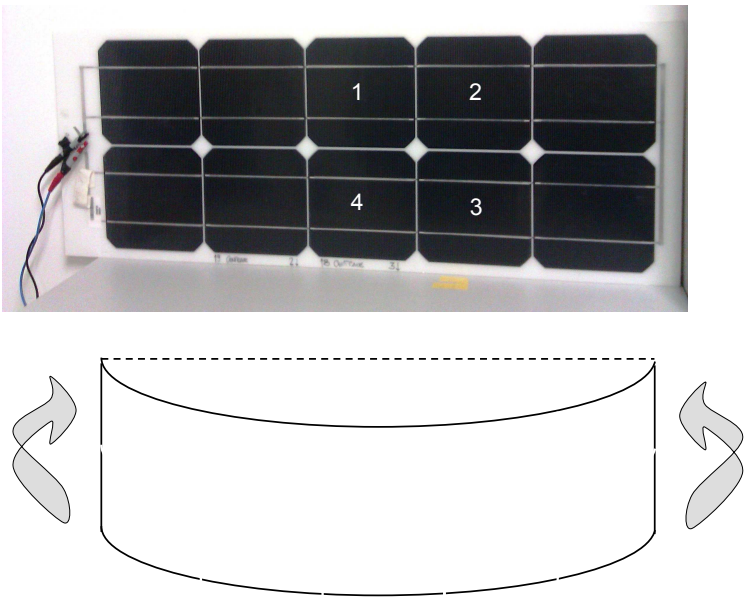

Figure 4.8: Sketch of the mechanical test. The cells 1-4 are monitored by EL and their images are shown in Fig.4.7.

Although a large displacements has been imposed to the thin plate, the tensile stresses inside Silicon were comparable with those found in classical PV modules under conventional bending tests. Indeed in those composites, having a thick glass cover (4 mm) and an unsymmetric structure, Si cells were much more distant from the neutral axis and therefore they were subjected to a tensile stress state comparable with that simulated in the present test, in spite of the much lower deflections induced by environmental loads [143, 11].

In the present tests, a voltage of 0.7 V was applied to the PV panels by the Genesys GENH60-12.5 power supplier. EL emission was detected by the pco.1300 solar camera and equipped by the Schneider Kreuznach XNP F1.4 lens with SWIR coating $800-1800$ nm. This measurement was performed inside a darkroom, shading all the possible sources of light to avoid reflection effects. By using nearly the maximum aperture of the camera (F1.8), its focus was adjusted during the bending test to obtain a perfect focus for all the various deflections of the module. An exposure time of 5 s for was used each photo. A post-processing of the acquired EL images was made by using the facilities of the software CamWare. In particular, cut-off filters of 600 and 8200 nm were used for all the images to make them comparable and remove very high and very low emission in the spectrum of the signal.

The EL images of the four solar cells in the middle of the panel, displaced in Fig.4.8, from the initial flat reference configuration to the maximum deflection configuration are shown in Fig.4.10. From the EL image are visible large electrically insulated cell portions

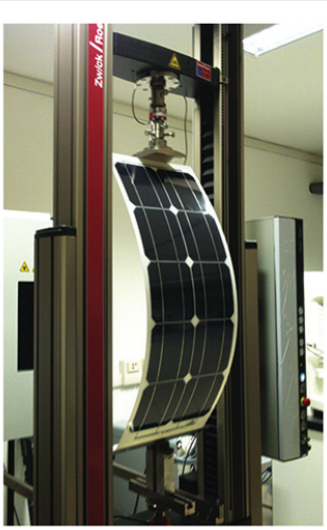

Figure 4.9: Test setup for cyclic bending tests.

(dark areas) and regions isolated by cracks but still partially conducting from the electrical point of view (circled with dashed lines in Fig.4.10). The difference between these two types of region can be explained by the fact that they have a different crack opening, but in both cases smaller than a critical value for complete electric insulation. In the unloaded condition a compressive stress is present in the cell, because of the thermoelastic mismatch between Silicon and the thermo-plastic materials encapsulating the module. This mismacth is the result of the cooling down of the module from the stress-free condition, corresponding to the lamination temperature of 150 °C, to the ambient temperature [146].

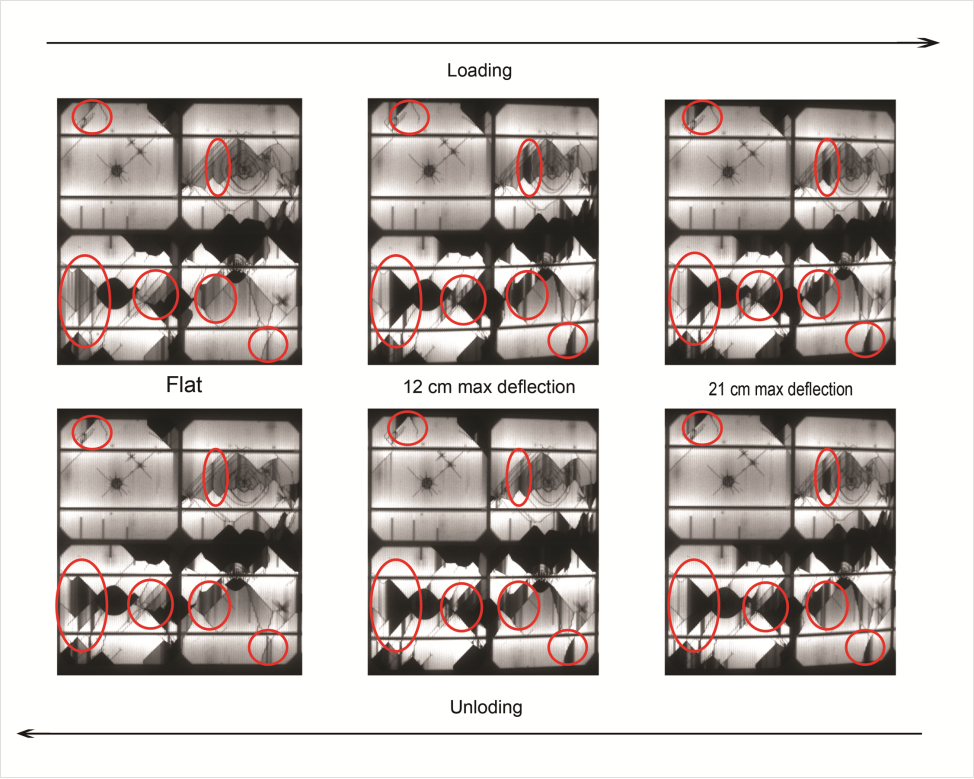

Figure 4.10: Evolution of EL signal during bending loading and unloading for different deflections.

The second type of test, the Vicker's indentation tests on monocrystalline Silicon solar cell were performed directly on Silicon solar cell in the Laboratory of Applied Materials Italia Srl (Olmi di S. Biagio di Callalta, Italy). Such tests are described in details Section 3.2.1. In Fig.4.11 is presented a scheme of the Vicker's test. The solar cell is placed on a rigid specimen table and the indentation is performed pressing the typical squared-based pyramid indenter into the surface of the solar cell, see Fig.4.11.

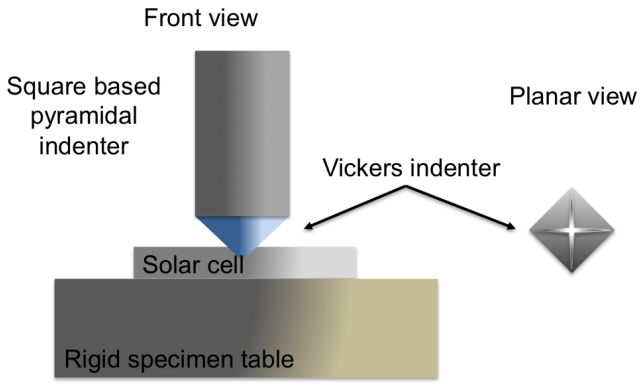

Figure 4.11: Sketch of the Vickers indentation test realized on mono-crystalline solar cells.

Finally mechanical line bending tests, performed at the Institute for Solar Energy Research Hamelin (Germany), were applied to mini-modules made of 3x3 polycristalline Silicon solar cells to induce cracks. The maximum applied load was selected to be equivalent to a uniform snow pressure of 5400 MPa, in terms of maximum tensile stress induced in the Silicon solar cells. The resulting 3-line-bending setup is shown in Fig.4.12.

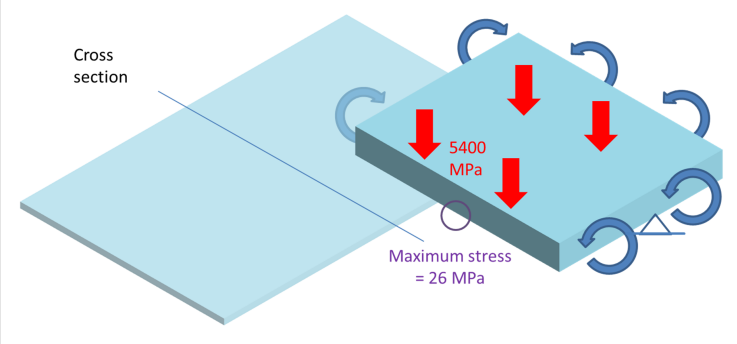

Figure 4.12: Sketch of the 3-line-bending setup corresponding to the equivalent snow load.

The maximum stress achieved, in the middle of the module was 26 MPa with a maximum deflection of 3.5 mm. The researchers at ISFH applied the load by placing a metal cylinder with a length of 80 cm and a weight of 29.8 kg in the center of the module, see Fig.4.13. The resulting deflection of the module was between 4 and 5 mm.

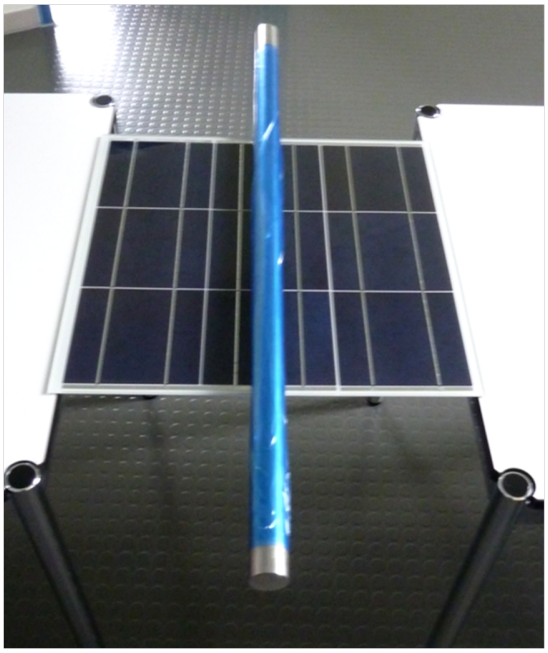

Figure 4.13: Mechanical line bending load applied on a mini-module.

4.3 Validation of the electric model

The focus of this Section is the validation of the electric model for a solar cell crossed by cracks. The localized resistance model (LR) model proposed in of Section 3.2 has been applied on a cell with a crack caused by impact tests. The results achieved have been compared the ones produced with by distribute resistance model (DR) described in Section 3.2.1, which takes into account the damages of the material due to the presence of the cracks. The comparison between the two models applied to the mono-crystalline Si confirms that the distribute resistance model (DR) of Section 3.2.1 is more accurate.

4.3.1 Electric response of solar cell with one crack

The model with a localized resistance (LR) for a finger crossed by a crack, described in Section 3.2, has been applied to the crack located at the top edge (see Fig.4.7) of the cell No.1 of Fig.4.8. Loaded and unloaded conditions have been considered in order to change the stress field in the cells. Indeed, the application of a bending stress to the panel determines an increase of the crack opening displacement of the pre-existing cracks. The parameters assumed for all the simulations are: I_{SC}=0 (solar cell not illuminated), R_{ohm}=0.1 Ωcm^2, V_T=25 mV, ρ_s=0.138Ω, I_{01}=1.48x10^{-12} A/cm^2. The values of the other parameters, specific for each simulation, are reported in the the corresponding tables, in this case the Tab. 4.3. The current density across the thickness (blue line in Fig.4.14) is compared to the distribution of the EL along the same grid line (black dots in Fig.4.14), suitably rescaled by a scale factor. The numerically simulated I_{tt} fits satisfactorily the experimental current determined from the EL data. The localized resistance R_{cr} due to the crack is just considered here as a free parameter, as V_0.

Table 4.3: Simulation data for a finger of the cell No.1 crossed by a crack with the model of Section 3.2.

	x_{min}	x_{cr1}	V_0	R_{cr1}	R_{ohm}
	cm	cm	V	Ω cm^2	Ωcm
Undeformed	3.47	1.65	0.579	0.02	0.1
Deformed	3.47	1.7	0.581	0.22	0.1

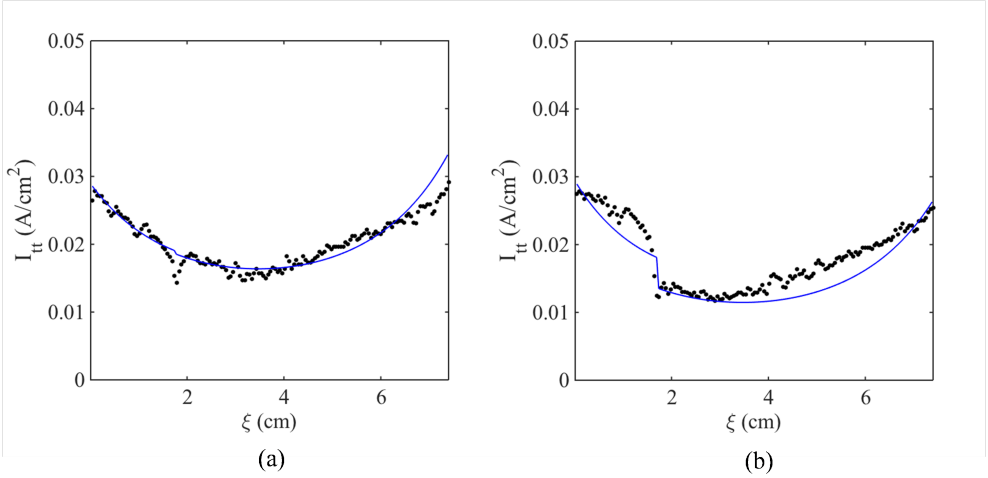

Figure 4.14: Current through the thickness of the solar cell vs. position along the finger for the (a) undeformed case and (b) the deformed configuration using the electric model described in Section 3.2.

However, as discussed in Section 3.2.1, the existence of a crack, for mono-crystalline Silicon, causes damage also in the material surrounding it, resulting in a decrease of the hardness in the damaged area. For this reason the cell No.1 in Fig.4.8 have been analyzed by using the Algorithm described in Section 3.2.1, which introduces a distributed damage in the form of a distributed series resistance dependent on the distance from the channel crack. In the Algorithm of Section 3.2.1, R_{ohm} is replaced by $R(x)$ as per Eq.(3.14). The current density through the thickness (solid line) and the experimental values along the same grid line (black dots), are shown in Fig.4.15, whereas the parameters for the simulations are collected in Tab. 4.4.

Table 4.4: Simulation parameter for a finger of the cell No.1 crossed by a crack with the electric model with distributed damage of Section. 3.2.1.

	x_{min}	x_{cr1}	V_0	R_{cr1}	R_{d1}	R_{ohm},	k
	cm	cm	V	Ωcm	Ω cm^2	Ω cm^2	-
Undeformed	3.47	1.65	0.581	0.02	0.65	0.1	40
Deformed	3.47	1.7	0.597	0.35	0.65	0.1	40

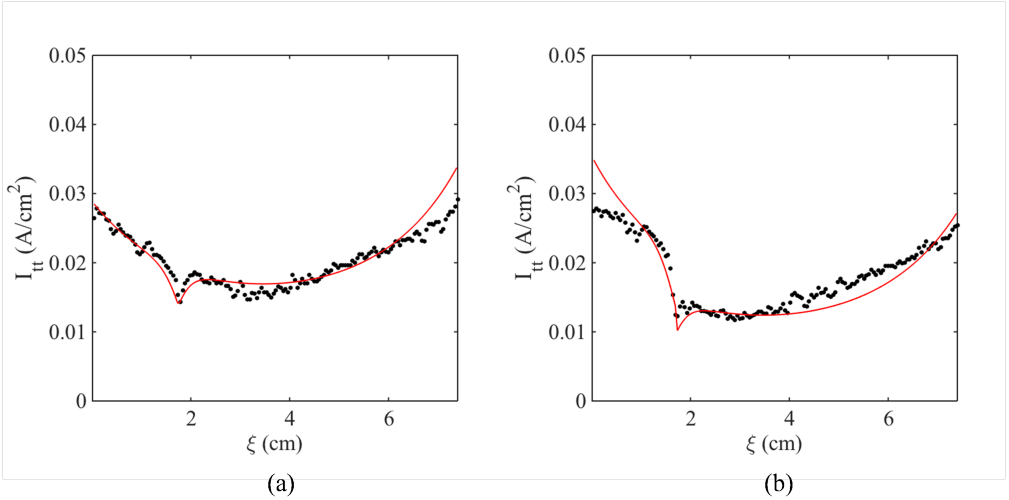

Figure 4.15: Current through the thickness of the solar cell vs. position along the finger for (a) the undeformed and (b) the deformed configuration using the electric model described in Section 3.2.1.

The two proposed electric models presented above, one with localized resistance only (LR model) and the other with distributed resistance (DR model) are compared in Fig.4.16 for the undeformed (case a) and the mechanical deformed in bending (case b) solar cell, using the same identified values $R_{cr,1}$ for both models. The solid line is the current through the thickness obtained with the Algorithm 1 of the model LR described in the Section 3.2, instead the dashed line shows the same current predicted by the model DR in Section 3.2.1. The parameters are collected in Tab. 4.5. The results show that the DR model is the most accurate to reproduce the experimental trend.

Table 4.5: Simulation parameter for a finger of the cell No.1 crossed by a crack.

	Model	x_{min}	x_{cr1}	V_0	R_{cr1}	R_{d1}	$R_{ohm,}$	k
		cm	cm	V	Ω cm	Ω cm^2	Ωcm^2	-
Undeformed	DR	3.47	1.65	0.581	0.02	0.65	0.1	40
Deformed	DR	3.47	1.7	0.597	0.35	0.65	0.1	40
Undeformed	LR	3.47	1.65	0.581	0.02	-	0.1	-
Deformed	LR	3.47	1.7	0.597	0.35	-	0.1	-

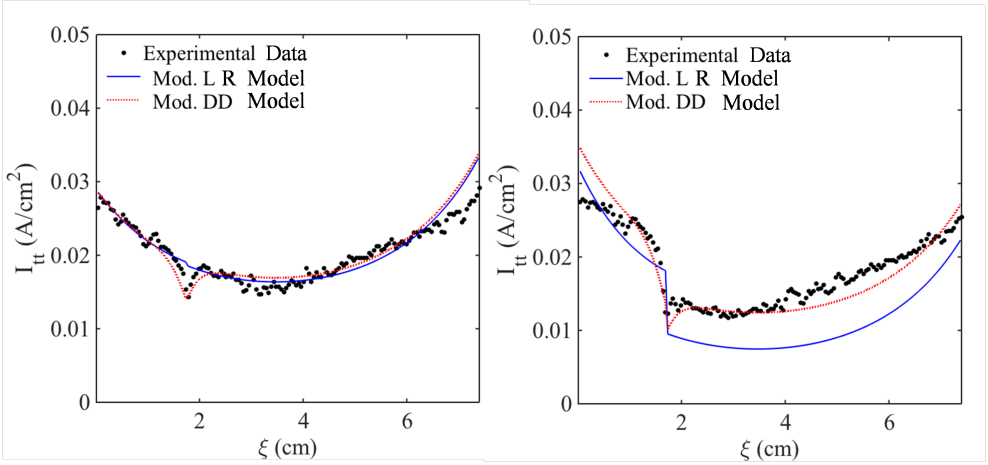

Figure 4.16: Comparison of the current through the thickness of the solar cell obtained with the model vs. position along the finger for (a) the undeformed and (b) the deformed configuration.

4.3.2 Simulation of the electric response of a cracked cell after indentation

Simulation of the electric response of cracked monocrystalline solar cells due to Vickers indentation is the focus of this Section, using the generalized electric crack model with localized resistance and distributed series resistance proposed in Section 3.2.1. The EL images of the solar cell, before and after the indentation test, are shown in Fig.4.17(a) and 4.17(b), respectively. From the EL image in Fig.4.17(b) it is possible to recognize the typical 45° cracks originated from the indentation point.

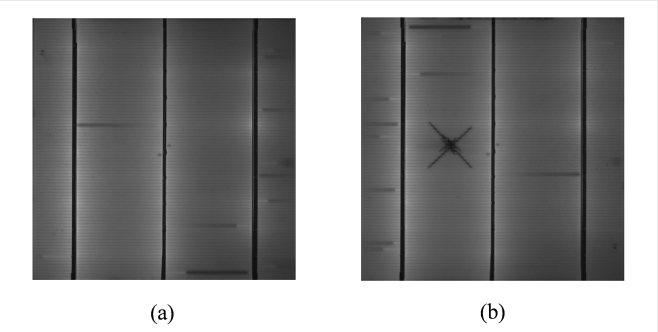

Figure 4.17: (a) Electroluminescence of monocrystalline solar cell before indention. (b) Electroluminescence of the same solar cell after Vickers' indentation.

The model DR in Section 3.2.1 is applied to four different fingers crossed by the cracks, at different distances from the point of Vickers indentation. The distribution of the current flowing through the thickness of the solar cell, I_{tt}, is shown in Fig.4.18 for the four selected fingers. For these simulations the following parameters were considered: R'_{hom}=0.1 Ωcm^2, V_T=25 mV, ρ_S=0.138 Ω, I_{01}=1.4810^{-12} A/cm^2, V_0=0.589 V. The values of the resistances related to the two cracks are identified by matching the spikes in the current. Fig.4.19, shows the dependency between crack resistances (R_{cr} and R_d) for both cracks vs. the distance d between the same cracks.

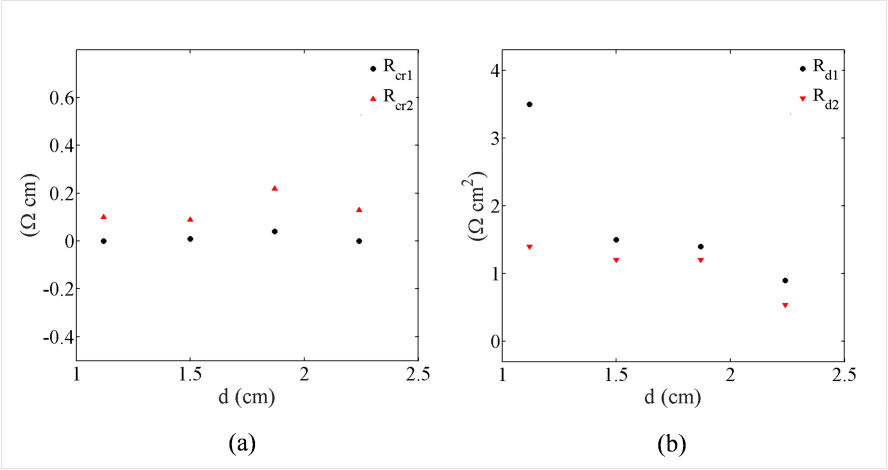

Figure 4.19: Model resistances described in Eq. (3.14) vs. distance d between cracks along the fingers.

Results show that the localized crack resistances R_{cr1} and R_{cr2} are almost independent

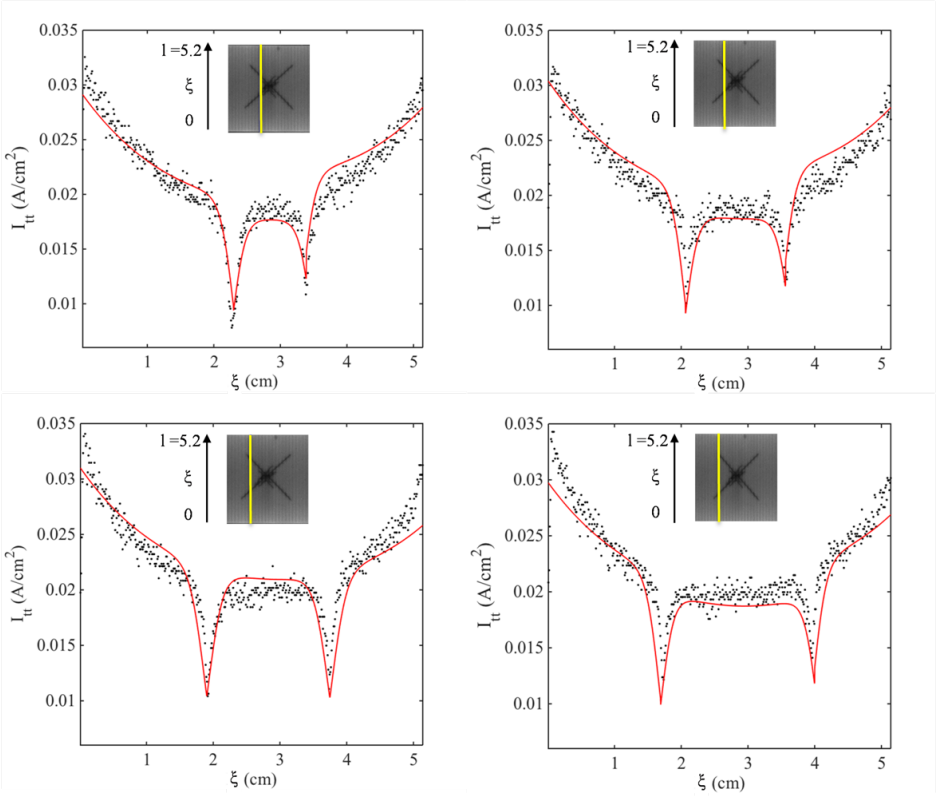

Figure 4.18: Current through the thickness of the solar cell, I_{tt}, vs. the coordinate ξ along the finger, for four different fingers.

of d (see Fig.4.19(a), in agreement with the expectation that they should depend on crack opening only. On the other hand, the resistances R_{d1} and R_{d2} are decreasing functions of the distance between cracks (see Fig.4.19(b), which implies a higher degradation of the Silicon properties near cracks due to the effect of crack interaction enhancing dislocations pile up.

4.3.3 Simulation of the electric response of a complete cell

Finally, to complete the validation of the electric model described in Chapter 3, the results of the simulation of a whole solar cell cracked by Vickers indentation is here proposed. The Algorithm used for this aim is detailed in Section 3.2.3. The results for the application of the electric model to the cell without cracks, see Fig.4.20, is preliminary performed to identify the model parameters. The current reaches the maximum at the busbar position, where it is collected. Nevertheless, in the EL image this is not possible to notice, because the metallic busbar covers the EL emission. The parameters used in this simulation are: ρ_S=0.138Ω, R_{ohm}=0.1Ωcm , I_{01}=1.48 $\times 10^{-12}$ A/cm^2, V_0=0.589 V.

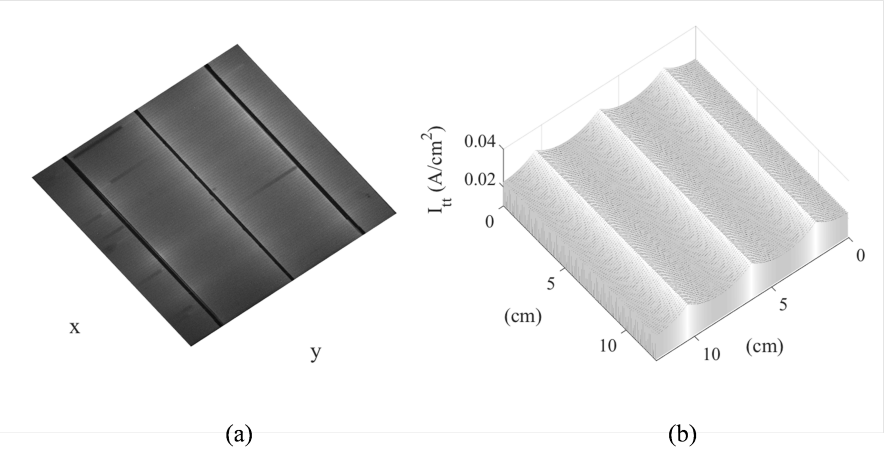

Figure 4.20: Comparison between EL image (a) and I_{tt} (b) obtained by the application of the electric model for the uncracked solar cell.

For the cracked solar cell, the coordinates of the cracks were inserted or, for easy configurations, they were automatically identified using image filters. The analysis of the EL image of the cell is made scanning finger lines, searching the presence of cracks. Applying the electric model to the EL image in Fig.4.21(a) the resulting current, I_{tt}, for the whole cell is shown in Fig.4.21(b). In this case the resistance R_{cr} was considered depending linearly on the distance from the center of the indentation, for simplification purpose. The relation between the resistance R_{cr} and the distance from the center is given by $R_{cr}=k_r d$, with $k_r=0.01$ Ωcm. The other parameters used in simulations are: ρ =0.138 Ω, $I_{01}=1.48\times10^{-12}$A/cm^2, V_0=0.589 V and the R_{ohm} is computed using the Algorithm of Section 3.2.1.

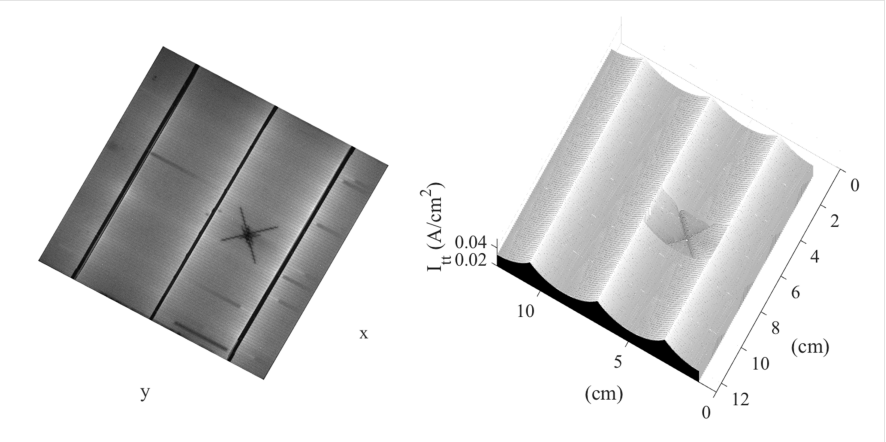

(a) (b)

Figure 4.21: Comparison between EL image (a) and I_{tt} (b) obtained by the application of the electric model in presence of a R_d(x) depending only from the distance from the center of the indentation.

4.4 Electric response to mechanic bending load of semi-flexible PV modules

In the sequel bending tests on pre-cracked semi-flexible PV modules, as described in Section 4.2, are considered to monitor the effect of cracking at different deformation levels by using EL imaging. The cracking evolution of the cell No.1 of Fig.4.8 has been analyzed into details. This cell has a crack between two busbars near the left edge of the cell far from the other cracks and the localized dimmer EL signal around the crack proves that the local electric resistance increases with deflection [140].

The geometry of the test and the application of a mono-axial bending allowed the use of the coarse-scale analysis for a single cross-section of the module, parallel to the bending plane. Therefore, a 2D plane strain model has been considered, in which the layers of the module are explicitly represented, with their specific mechanical and geometrical parameters. Furthermore, the symmetry of the problem can be exploited in order to analyze only half the module, as shown in Fig.4.23(a). The mesh adopted, constituted by 4-node isoparametric finite elements, is shown in Fig.4.23(c). At this scale, a linear elastic behavior has been assumed for all the materials composing the layers. The visco-elastic behavior typical of EVA is not taken into account, since only short term loading at a constant ambient temperature is imposed during this test. The mechanical properties used are reported in Tab. 4.6. As regards the boundary conditions, the vertical displacement is restrained at the free edge, whereas symmetry boundary constraints were applied along the symmetry cross-section. Then, a transversal displacement, which corresponds to the mid-span deflection of the experimental

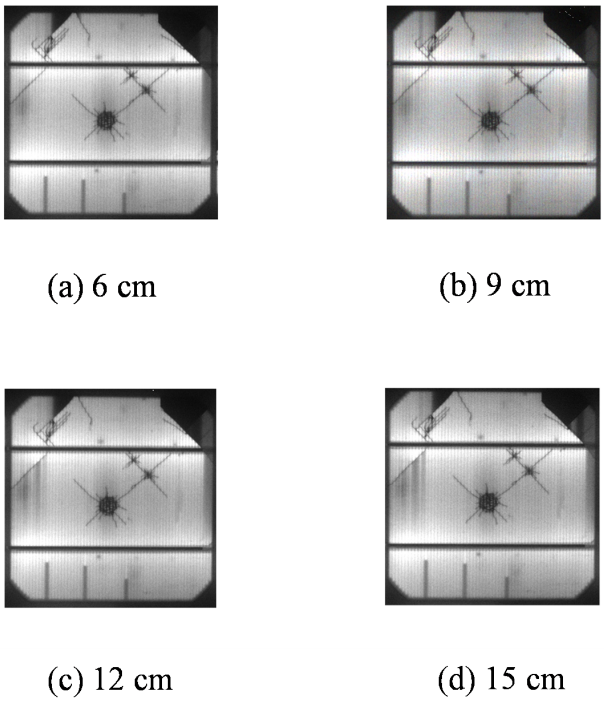

Figure 4.22: Electroluminescence images of cell No.1 of Fig.4.8, for different deflections of the PV module.

tests, was applied in the same cross-section (see Fig.4.23). Then, a transversal displacement, which corresponds to the mid-span deflection of the experimental tests, is applied in the same cross-section (see Fig.4.22), namely 6, 9, 12 and 15 cm. Whereupon for each of the considered values of deflection, the displacements along the boundaries of the solar cells are extracted, and used as input for the local-scale analysis Section 3.3.1. Following the finite element results for the solar cell No.1 in Fig.4.8, whose EL images are shown in Fig.4.22, are presented. With reference to the coarse-scale FE model represented in Fig.4.23(a), the region A-B consists of the location of the half cell investigated in the local model. A scheme of the displacements obtained along the boundaries of the cell for a given value of mid-span deflection is shown in Fig.4.23(b): the left side of the cell is subjected to a linear variation of the displacement in the x-direction, whereas the top and bottom surfaces are subjected to a non-linear displacement distribution in the z-direction, according to the deformation of the whole module. The cross section B-B is undeformed, for symmetry reasons.

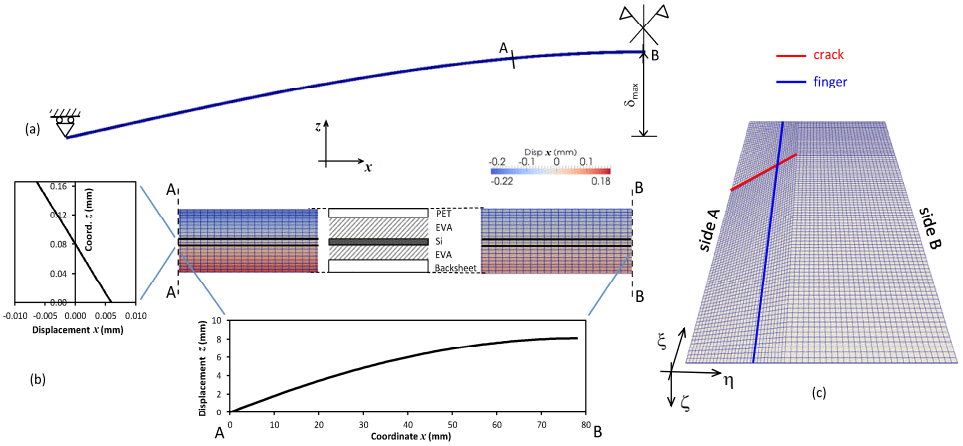

Figure 4.23: (a) The coarse-scale 2D finite element model of the PV module subjected to bending; (b) displacements passed to the local model of the solar cell located between points A and B (cell number 1 in Figs.4.8 and 4.22; (c) mesh of the local 3D finite element model of the solar cell.

Table 4.6: Material properties for the coarse-scale FE model

	E (GPa)	ν
PET	2.5	0.30
EVA	0.001	0.30
Si	160	0.22
Backsheet	2.8	0.30

According to the procedure described in Section 3.3.1, the displacements along the boundaries were passed to the local fine-scale model as boundary conditions imposed to the nodes belonging to the various facets of the cell. At this level, a 3D finite element model with 8-node isoparametric brick elements was adopted as shown in Fig.4.23(c). The crack observed near the left edge of the solar cell No.1 between the busbars in the EL test in Fig.4.22 is inserted in the model, before the generation of the 3D mesh. It discretization was done by interface elements described in Section 3.3.3. Other cracks are not modelled, because they are far apart from the considered one and their interaction is expected to be negligible. The behavior for the Silicon was assumed linear elastic and the mechanical properties are reported in Tab.4.6. The cohesive zone model outlined in Section 3.3.3 was used for modeling the non-linear response of cracks, with parameters typical of Silicon. In particular, we selected σ_{max}=τ_{max}=175 MPa, g_{nc}=g_{tc}=0.1 μm, r=0.035 μm, l_0=0.02 μm.

The analysis at the fine-scale model has been therefore performed for the four different imposed displacement distributions derived from the coarse-scale model in correspondence of the four mid-span deflections imposed. The contour plot of the in plane displacement in the ξ direction is shown in Fig.4.24 for the four considered cases. The contour plots show as the normal gap between the crack faces changes. Indeed the normal gap has the major role in determining the resistance of the crack to the electric current flux. Such a gap is an increasing function of the deflection applied to the PV module (to emphasize this correlation, the same range of colors has been selected for the four contour plots).

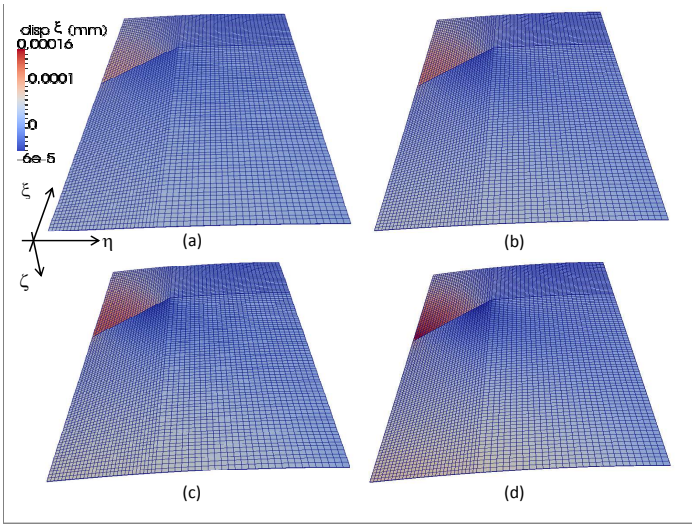

Figure 4.24: Deformed meshes and contour plots of the in plane displacement in direction ξ for the 3D local fine-scale model of the cracked cell for the following values of the mid-span deflection of the module: (a) 6 cm, (b) 9 cm, (c) 12 cm, and (d) 15 cm. Note the jump of displacements in correspondence of the discontinuity represented by the crack faces.

4.4.1 Identification of the relation between crack resistance and crack opening

The crack opening displacement along the crack was computed for each deformation level and as described in Section 3.2.3 the electric model can be extended to the whole cell. Herein we focused on a single finger crossed by the crack. The matching between the proposed model predictions and the experimental values of I_{tt}, for different deflections, allowed us to obtain the relation between crack resistance and crack opening displacement. This relationship has a general validity and is independent on boundary conditions, in analogy with the cohesive zone model relating the local tractions to crack opening and sliding. The predicted I_{tt} data with solid line in comparison with experimental data (in black dots) are shown in Fig.4.25. The $\xi-$coordinate ranges from 0 to $l = 7.4$ cm, i.e., from one busbar to another.

The finger under examination is highlighted in blue in Fig 4.25 and it corresponds to the finger in blue in Fig.4.23(c). The value of the crack opening in correspondence of the considered finger are: 0.13, 0.18, 0.22 and 0.27 μm, for the mid-span deflections of 6, 9, 12 and 15 cm, respectively.

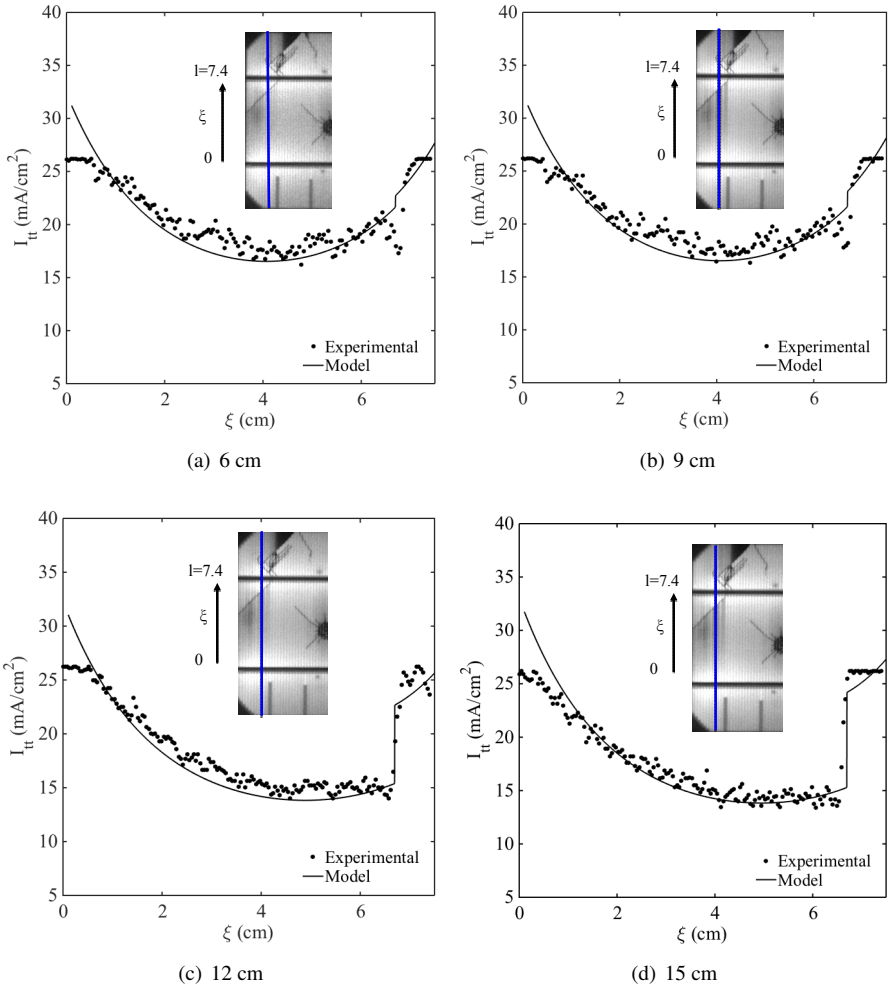

(a) 6 cm (b) 9 cm

(c) 12 cm (d) 15 cm

Figure 4.25: Current through the cell thickness in a monocrystalline-Si cell along a finger crossed by a crack for various mid-span deflections.

The following parameters of the electric model are identified by matching the experimental values of I_{tt} for a finger not crossed by cracks: $R_{\text{hom}} = 0.2\ \Omega\ \text{cm}^2$, V_{T} =25mV, ρ_{S} =0.13 Ω, $I_{01} = 1.48 \times 10^{-12}\text{A/cm}^2$. The point of the finger crossed by the crack is at the dis-

tance $\xi_{cr} = 6.6$ cm from the lower busbar and it is identified from the EL images. The value of ξ_0 where the voltage is minimum, and its value V_0, are identified by matching the value of 0.7 V of the voltage at the busbars imposed in the EL test. The localized resistance R_{cr} is identified by matching the jump in the current I_{tt} in correspondence of $\xi = \xi_{cr}$ and in general by minimizing the error between the numerically predicted and the experimental values of I_{tt} along the finger.
All the values of the identified parameters are collected in Tab.4.7. As a general trend, it has

Table 4.7: Values of the identified parameters of the electrical model.

Deflection (cm)	g_n (μm)	ξ_0 (cm)	V_0 (V)	R_{cr} (Ωcm)
6	0.13	3.97	0.582	0.03
9	0.17	3.97	0.582	0.04
12	0.22	4.79	0.577	0.43
15	0.27	4.85	0.577	0.53

been found that the coordinate ξ_0 of the minimum of the voltage progressively approaches the crack position ξ_{cr} as long as the deformation increases. The localized crack resistance is an increasing function of the crack opening, as shown in Fig.4.26. This trend is in agreement with recent experimental results reported in [124], where a glass-based mini-module with a solar cell notched by a laser was subjected to a Mode I three-point bending test. Kaesewieter et al. [124] measured the overall back and front size resistances of the solar cell, due to the combined effect of the localized crack and the distributed resistance, along crack opening measured via a microscope. Even if in the numerical model only a resistance instead of two has been used as in the experimental results presented in [124], the same significant increase in the resistance noticed in the experiments for crack openings larger than 6 μm has been found. The larger value of crack opening measured in experiments for the mini-module with glass superstrate instead of PET is reasonably due to the presence of residual thermoelastic compressive stresses that in PV modules with glass cover can reach up to 45 MPa [156] and are much higher than in the PET configuration.

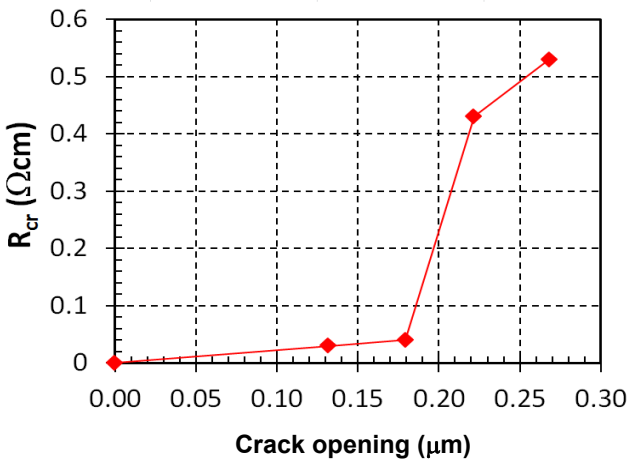

Figure 4.26: Correlation between localized crack resistance and crack opening.

4.5 Simulation of a polycrystalline solar cell

So far it has been focused on a particular solar cell material, i.e, the mono-crystalline Silicon. In this Section simulations obtained from the use of the electric model in Section. 3.2.2 are shown for polycrystalline Silicon, in comparison with experimental data. It describes the inhomogeneities due to the defect and grain boundaries as a random additional resistance dR. In the case of an intact solar cell the comparison between experimental data and the simulated results are shown in Fig.4.27. The parameters used in this simulation are: V_0=0.579 V, $x_{\min}$= 4.1 cm, R_{ave}=0.38 Ωcm^2 and dR=40% of the average value. In particular, in Fig.4.27 the black line corresponds to the distribution of the EL along the grid line (see the dotted line in the EL image on the top of the figure), the blue dashed line is the simulated current obtained by considering only R_{ave} and finally the red solid line corresponds to the simulated current by considering R_{ave} + dR.

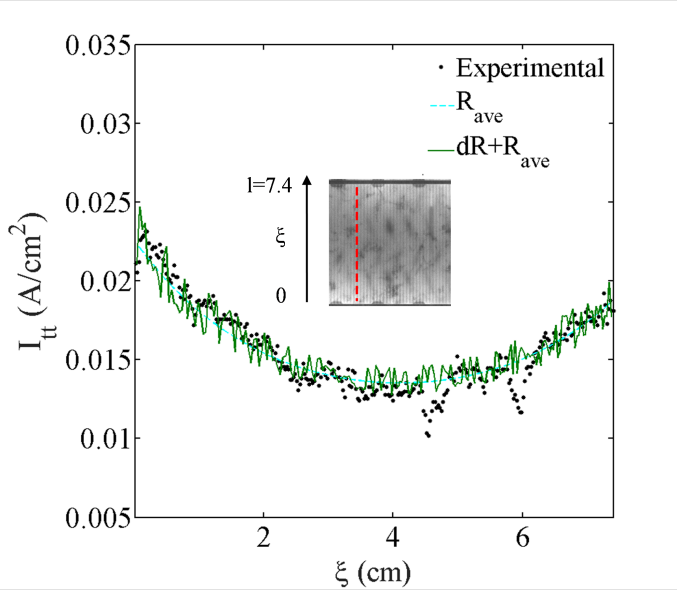

Figure 4.27: Current through the thickness for a intact polycrystalline solar cell.

The model of Section 3.2.2 was applied to a finger of a pre-cracked poly-crystalline cell too. The results are shown in Fig.4.28, following the same color notation of Fig.4.27. The parameters used are: V_0=0.575 V, x_{min}= 2.1 cm, R_{ave}=0.5 Ωcm^2, dR=40% of the average value, x_{cr}= 0.15 cm and R_{cr}=0.5Ωcm. In both cases a good matching of the experimental data is achieved by using an amplitude of the perturbative term, dR, of about 40% of the average value, R_{ave}.

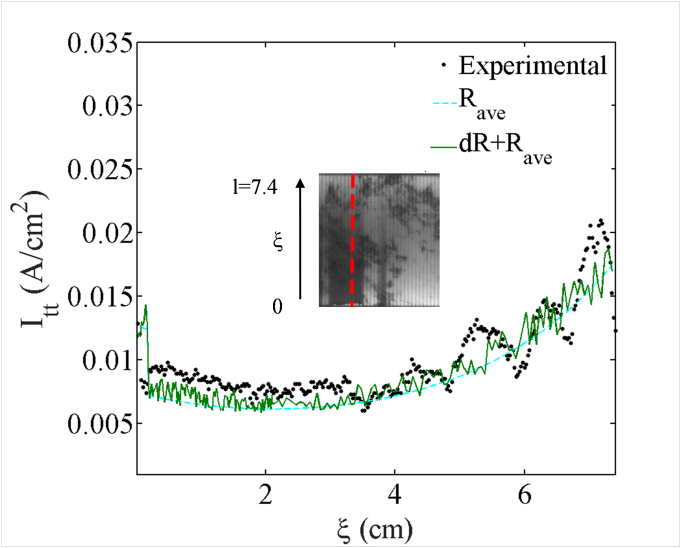

Figure 4.28: Current through the thickness for a pre-cracked polycrystalline solar cell.

Chapter 5

Accelerated aging of photovoltaic modules

As described in Chapter 1 significant degradation phenomena of photovoltaics (PV) modules are related to cracking [157,158] or humidity corrosion of the Silver front metallization [124]. While cracking degradation of solar cells and PV modules has been discussed in Chapter 4, in this Chapter the attention is on humidity corrosion effect and more in general on artificial weathering. Humidity corrosion is induced by chemical components resulting from the degradation of the lamination material ethylene venyl acetate (EVA) and the glass frit of the front side metallization of the cells [159,160]. Nowadays, corrosion is typically seen in damp heat tests at 85°C for 2000 hours to 3000 hours [161]. Thermo-cycling according to the IEC 61215 standard (Section 10.11) or humidity freeze tests cycle (Section 10.13) are used to consider temperature and humidity stresses. For this reason, in the present Chapter, to assess the role of these degradation phenomena, novel thermal and humidity cycles are proposed to simulate more realistic weather scenarios correlated to summer and winter periods typical of the Northern Italy and compare the induced degradation with that occurring in the case of standard IEC 61215 test.

5.1 Overview of standard qualification tests

The existing standards for the qualification of the PV modules consider a range of tests to be performed inside a climate chamber. Among them, the humidity freeze test (HF; IEC 61215, Section 10.12) and the temperature and humidity cyclic test (THC; IEC 60068-2-38 Section 6.3.1) are particularly severe.

The aim of the humidity freeze test is to determine the ability of the modules to withstand the effects of high temperature and humidity conditions due to temperatures below zero. It is based on 10 cycles where the temperature is fast raised from the room temperature up to +85°C in the presence of high relative humidity of 85%. These high temperature and humidity conditions are kept for at least 20 hours. Afterwards, the temperature is drastically reduced down to -40°C without relative humidity control. After 30 minutes, the temperature

is raised again up to the initial conditions to complete the cycle. The part of the cycle without humidity control must last up to 4 hours (see Fig.5.1(a)). The temperature and humidity cyclic tests, on the other hand, aims at assessing the damages in the case of use/storage in short time due to temperature change in a high relative humidity environment. In this cycle, the temperature is raised from the ambient temperature up to +85°C. A dwell time with 85% relative humidity and +85°C lasting at least 10 minutes follows. Afterwards, the temperature is slowly reduced down to -40°C with no humidity control and this temperature is kept for at least 1 hour before increasing it and complete the cycle, whose total time cannot exceed 6 hours (see Fig.5.1(b)). Again, 10 consecutive cycles are performed.

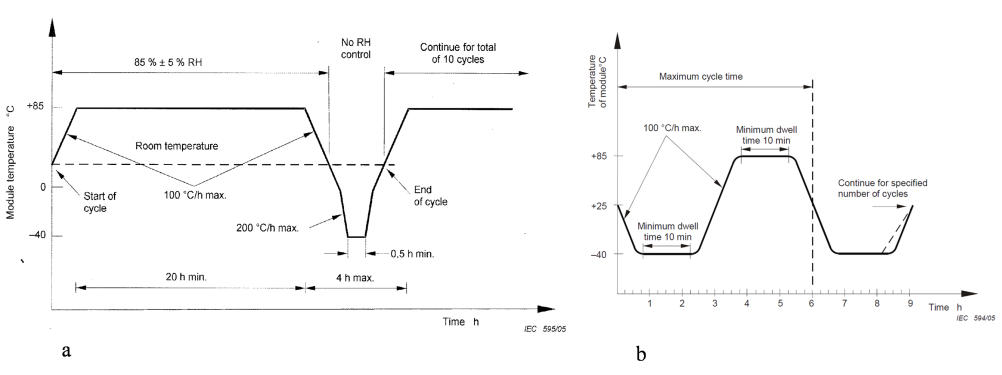

Figure 5.1: Module temperature and relative humidity profiles used in HF and THC standard qualification tests.

These two tests are very similar in terms of maximum and minimum temperatures. Also the humidity control, operated only during the dwell time at maximum temperature, is analogue for humidity freeze tests and temperature and humidity cyclic tests. Differences regard the velocities prescribes in the temperature ramps. In the humidity freeze tests, the maximum temperature gradients are 100°C/h for temperature above zero, and 200°C/h in the range below zero. In the temperature and humidity cyclic tests, the maximum gradient is 100°C/h regardless of the temperature level. The duration of the plateau at constant temperature is also different in the two tests. In the humidity freeze tests, +85°C must be kept for at least 20 hours, whereas in the temperature and humidity cyclic tests it can be very short (10 minutes). The temperature of -40°C must be kept at least for 30 minutes in the humidity freeze tests, whereas this time is twice for the temperature and humidity cyclic tests. The ratio between these durations is 20/0.5=40 and 1/6=0.17 in the humidity freeze tests and temperature and humidity cyclic tests, respectively.

5.2 Design of a realistic environmental test

To reproduce realistic conditions environmental climate data including ambient temperature (°C), solar irradiance I (W/m^2) and relative humidity RH (%)are considered. They are obtained from the ARPA public database for a location in the north of Italy The first two sets of data allow to to determine the module temperature, T_{mod} :

$$T_{\text{mod}} = T_{\text{amb}} + (NOCT - 20^{\circ}\text{C})S/80 \tag{5.1}$$

where T_{amb} is the ambient temperature, NOCT is the Nominal Operating Cell Temperature and S is the insolation in mW/cm^2 [162]. The NOCT temperature is defined by IEC standards as the cell temperature in a module exposed at 45° south to 800 W/m^2 irradiation at 20°C ambient temperature and with wind at a speed of about 1 m/s. The typical range for the NOTC is between 33°C and, in the worst case, 58°C. For this analysis the average value of NOCT=50°C is selected.

Climate data of the city of Piacenza in the north of Italy, representative of a humid subtropical climate (Cfa in the *Koeppen's classification* [163]) without any influence from the seaside are considered. The Climatic Classification is *zone E, 2259 GR/G*, similar to much of Northern Italy's inland plains, where sultry summers and very cold and wet winters prevail. Cities with a similar climate in Italy are, e.g. Parma, Brescia, Verona, Milano, Bologna, Forlí, Torino, Bolzano, Bergamo. A similar climate is also present in Tulcea, Kogalniceanu (Romania), Kozani (Greece), Easton (MD, USA), Hagerstown, Washington County (MD, USA). In order to identify critical situations, we analyze the field data provided by *Agenzia Regionale Prevenzione e Ambiente* (ARPA) Emilia Romagna. In the available period 2004-2011, the daily minimum air temperature is shown in Fig.5.2. The minimum was achieved in the winter of 2009 (13/01/2009), with a temperature of −10°C approximately. Therefore the severe year 2009 is considered for the subsequent statistical analysis.

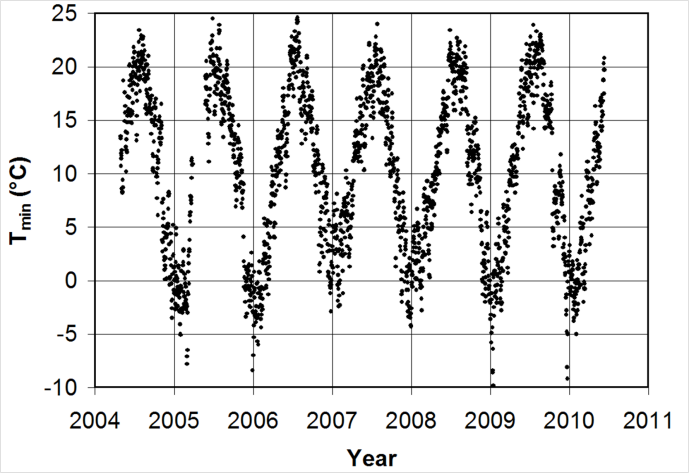

Figure 5.2: Minimum daily ambient temperature recorded in Piacenza in the period 2004-2011.

The data provided by ARPA are recorded every hour on the field (at 2 m of elevation from the soil) and constitute a significant data set; for this reason they require specific treatments to design a new cyclic tests. First, the hourly data are grouped in series of 24 values to obtain the variability of temperature within a single day. Afterwords, all the daily curves are plotted on a single graph to evaluate the statistical variability within a season and the module temperature is determined using Eq.(5.1). Fig.5.3 shows the resulting winter season temperature variation during the day.

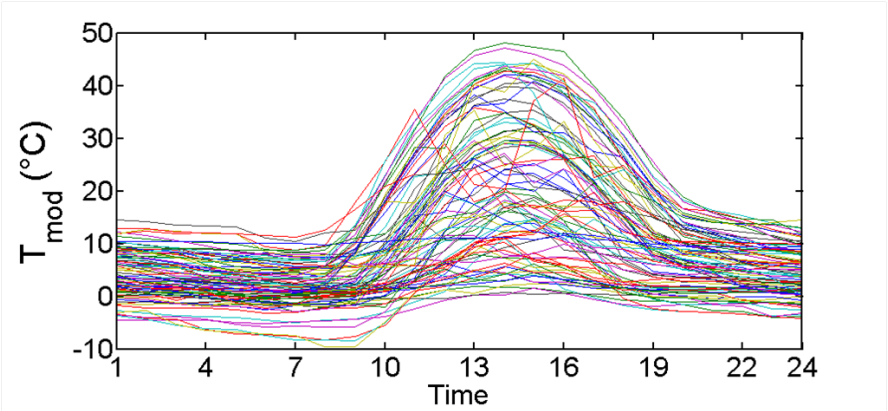

Figure 5.3: Module temperature variation during the day (the various curves correspond to different days in the winter season).

A significant statistical variability is noticed and, in general, the day with the minimum absolute temperature does not correspond to the day with the maximum one. Hence, in order to test the PV modules in a worst-case scenario, it is convenient to compute the envelope of the temperature diagrams for the winter and summer seasons, see Fig.5.4. As a result, the maximum temperature excursion within a day in winter is 60°C (−10°C/+50 °C) and it corresponds to the largest temperature applied to the modules during the year. Indeed, although the maximum module temperature can reach up to +70°C in summer, the minimum temperature is higher than 10°C and the humidity does not freeze. The ice formation takes place only in winter when temperatures lower than zero are reached. Finally, the maximum ambient humidity is close to 100% and it might occur at any hour, whereas the minimum humidity is about 10%.

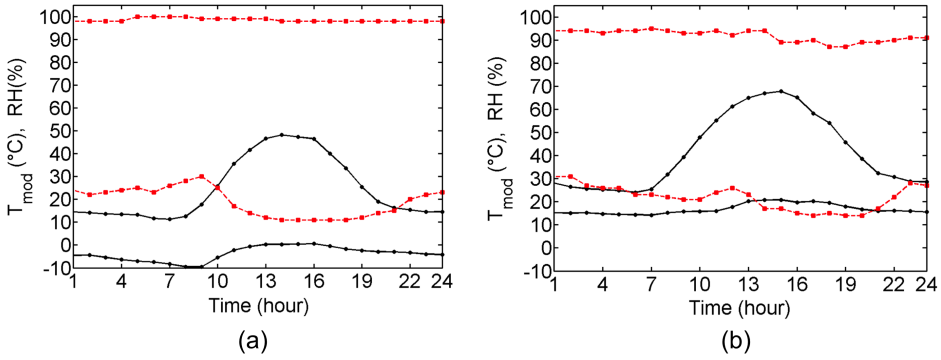

Figure 5.4: Envelopes of module temperatures (black, filled dots) and relative humidity (red, filled squares) during the day in the winter (a) and summer (b) seasons.

Using realistic data for a worst-case scenario, cyclic test have been designed, see its sketch in Fig.5.5. The parameters describing the cycle are: the maximum temperature, T_{max}, the minimum temperature, T_{min}, the duration of the plateau with constant T=T_{max}, Δt_1, the duration of the plateau with constant T=T_{min}, Δt_2, and the two velocities of the ascending and descending ramps, u and v. Considering the summer data in Fig.5.4(b), we set $\Delta t_1 = 4$h to simplify the real daily cycle. Instead, regarding the relative humidity values, we set a value of constant RH=85% during the plateau at maximum temperature, which corresponds to the maximum value usually achievable within a climate chamber. The comparison between the envelope of data and the proposed cycle is shown in Fig.5.6 for the summer season. In order to reduce the testing time, a speed-up of the idealized cycle in Fig.5.6, whose duration is 24 hours, has to be done. The acceleration ratios for the plateau regimes have been selected in order to allow the minimum time required for the relaxation of the EVA encapsulating material, as it happens in real conditions. Thus, we defined the acceleration ratios for the two

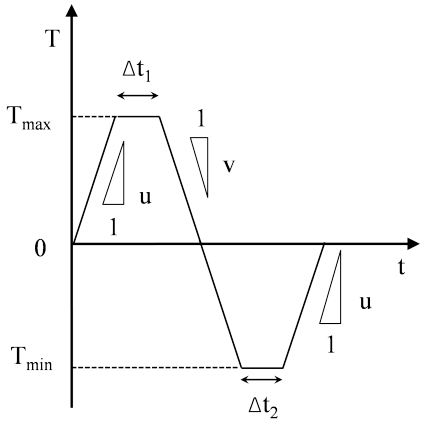

Figure 5.5: Sketch of the cycle and its control parameters.

plateau regimes as follows:

$$\begin{aligned} R_1 &= \Delta t_1 / \Delta_{\text{rel,Tmax}} \\ R_2 &= \Delta t_2 / \Delta_{\text{rel,Tmin}} \end{aligned} \tag{5.2}$$

where $\Delta_{\text{rel,Tmax}}$ and $\Delta_{\text{rel,Tmin}}$ are the times of relaxation of EVA at $T = T_{\max}$ and $T = T_{\min}$, respectively. These times are determined from the relaxation curves corresponding, for the summer cycle, to the temperatures +70°C and +20°C (which can be obtained by visual interpolation of module temperature variation during the day, when the tensile relaxation modulus becomes nearly constant. For both temperatures, a time of $1{\times}10^4$ s (approximately 2.5 hours) is required to achieve a tensile modulus slightly larger than the asymptotic one, corresponding to acceleration ratios of $R_1 = 4/2.5{=}1.6$ and $R_2 = 12/2.5{=}4.8$.

A single value for the acceleration ratio for the whole cycle is then chosen as the minimum between R_1 and R_2, thus allows to preserve the cycle shape. In this way the times is scaled down by a factor of 1.6 and the total cycle duration becomes 6 hours. Consequently, the velocities u and v of the accelerated test becomes $6 \times 1.6{=}9.6$ °C/h, which are feasible using a standard climate chamber.

The parameters adopted to describe the designed summer and winter cycles, are reported in Tab. 5.1.

Table 5.1: Parameters used in the proposed cycles.

Cycle	$T_{\max}$ °C	$T_{\min}$ °C	Δt_1 h	Δt_2 h	u °C/h
Summer	70	20	1	1	9.6
Winter	30	−20	1	1	9.6

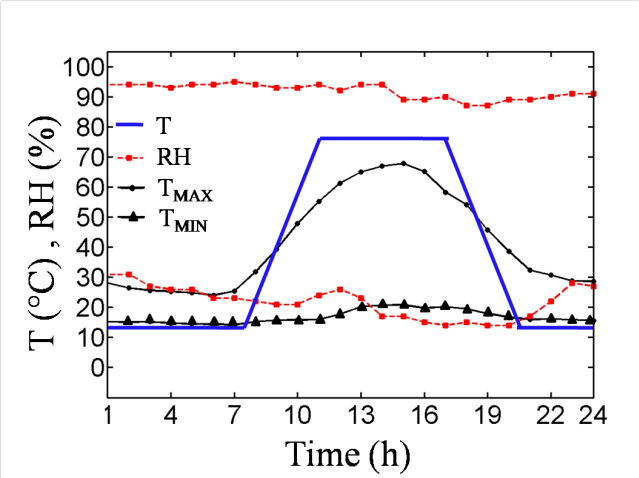

Figure 5.6: Comparison between the proposed idealized cycle (thick solid line) and the real temperature envelope (solid dotted line) for the summer cycle; relative humidity data are reported by a dashed dotted line.

5.3 Accelerated aging tests

In this Section, the specifics of the specimens (PV mini-modules) and the equipment used for the aging tests and the their monitoring have detailed. The tests have been carried out inside a climate chamber available at the Department of Structural, Geotechnical and Building Engineering of Politecnico di Torino (curtesy of Prof. R. Nelva) on mini-modules made by 3×3 polycrystalline Silicon solar cells, realized at the Institute for Solar Energy Research Hamelin.

5.3.1 Mini-modules specifics

The mini-modules, with an overall dimension of 50 × 50 cm^2, were laminated without junction box and without frame. Each mini-module consists of 3×3 multicrystalline 15.6 cm × 15.6 cm Silicon cells with two busbars protected by a 4 mm thick white glass bonded to the cells by an EVA-layer and separated from the backsheet by another EVA-layer . For the cell interconnection, 2 mm wide and 150 μm thick ribbons (busbar) were used. The ribbons were covered by 20 μm thick Sn62Pb36Ag2 on each side. The Sn62Pb36Ag2 is a low temperature solder wire with incorporated flux for soldering equipment in electronics and telecommunications. The backsheet used has a thickness of 0.17 mm and it is composed by three layer of tedlar-based foils. The solar cells were electrically connected in series. The modules were pre-cracked at the Institute for Solar Energy and the causes of the resulting failures are listed in Tab. 5.2. In particular, the mechanical load applied on the module No.2 is fully described in the experimental Section 4.2.

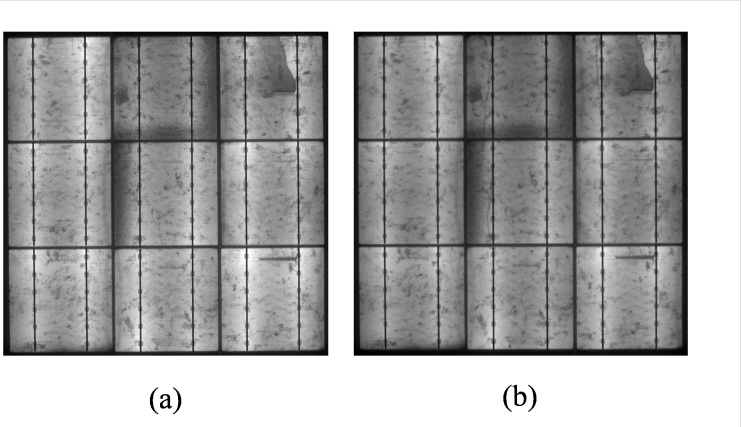

Figure 5.7: EL images of module No.2 before (a) and after (b) the mechanical load.

Table 5.2: Description of the mini-modules.

Module code	Crack cause
1	Lamination
2	Mechanical load
3	Lamination

The effect of the mechanical load on the module No.2 are shown by the EL image of Fig.5.7. The module before loading (Fig.5.7(a)) has a crack on the last cell of the first row. After the mechanical load a vertical crack, crossing all the three rows, appears in the central column of the module, in correspondence of the load. After the initial EL and electric measurements the modules disconnected from the electric supply have been inserted inside the climate chamber as shown in Fig.5.8.

Figure 5.8: PV module inside the climate chamber.

5.3.2 Climate chamber

A climate chamber is used to test the effects of particular environmental conditions on biological or industrial materials and on the electronic devices and components. Typical tests performed with a climate chamber are:

- Preparation of specimens for further physical tests or chemical tests;
- Environmental conditions for specimens;
- Stand-alone test for environmental effects on the specimens.

Thus, a climate chamber artificially reproduces both the exposure conditions of a material or device and the accelerated effects of exposure to the environment. Typical testing conditions are represented by:

- Weathering exposure to the sun (UV degradation) or to the rain;
- Moisture or relative humidity;
- Extreme temperatures;
- Cyclic corrosion;
- Salt spray;

- Vacuum;
- Thermal shock and abrupt changes;
- Electrodynamic vibrations;
- Electromagnetic radiation.

The samples or specimens are placed inside the climate chamber and subjected to these conditions to evaluate the reliability or measure typical parameters after the climatic cycle. For the present studies the Challenge 250 climate chamber by Angelantoni was used (see Fig.5.9). This model has the *climatic control*, which ensures to set up both humidity and temperature cycle condition. The measurable and controllable physical quantities of the Challenge 250, together with their ranges, are listed in Tab. 5.3.

Figure 5.9: Challenge 250 climate chamber by Angelantoni used to conditionate the PV modules.

The chamber interface consists of an LCD display, placed on the front panel, together with a PC with WinKratos Software installed.

5.3.3 WinKratos

We used the Angelantoni's software to set the cycles and monitor the climatic chamber, through a PC. This software, runs under Windows (XP/VISTA/7 Professional version or higher). Through WinKratos it is possible to create test profiles (programs), launch or interrupt the execution of a test in *manual* or *program* mode, display data in table or graphic form and generate a report showing test results. The software is designed to control not only single chamber but a whole test lab. It can then be *scaled* and updated, if new machines are added to existing ones, with minimal impact in terms of time and resources. In Fig.5.10 the two most important windows are reported: the editor (where is possible to design the cycle) and the channel control (where is possible to monitor the cycle). The designed cycle was

Table 5.3: Technical characteristic of the standard CH250 climate chamber.

Model	CH250	
Chamber volume	224	l
Temperature range	$-40 \div +180$	°C
Accuracy	$0.25 \div 0.3$	± °C
Humidity range (with $+5 \leq T \leq +95$ °C)	$10 \div 98$	%
RH accuracy (no less than ±0.25° C on psychometric difference)	$1 \div 3$	%
Dew point range for continuous tests	$+2 \div +94$	°C
Dew point range for discontinuous tests	$-20 \div +2$	°C
Cooling gas	R404 A	
Internal dimensions (LxDxH)	$600 \times 535 \times 700$	mm
Maximum temperature variation speed from $-40 \leq s \leq +180$°C	3.9	°C /min
Maximum temperature variation speed from $+180 \leq s \leq -40$°C	2.5	°C/min

adjusted and retrofitted thanks to the possibility of reading and modifying a *log* file generated by WinKratos. The subroutine for the post process of the file has been written in MATLAB language and its output is a *txt* file which includes all the actual temperature and the relative humidity measurements every 20 s inside the climate chamber.

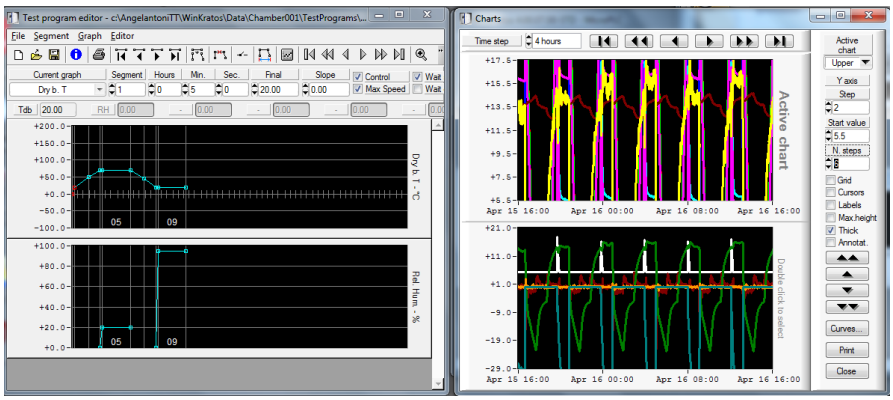

Figure 5.10: Winkratos windows to edit the cycle and monitor the cycle.

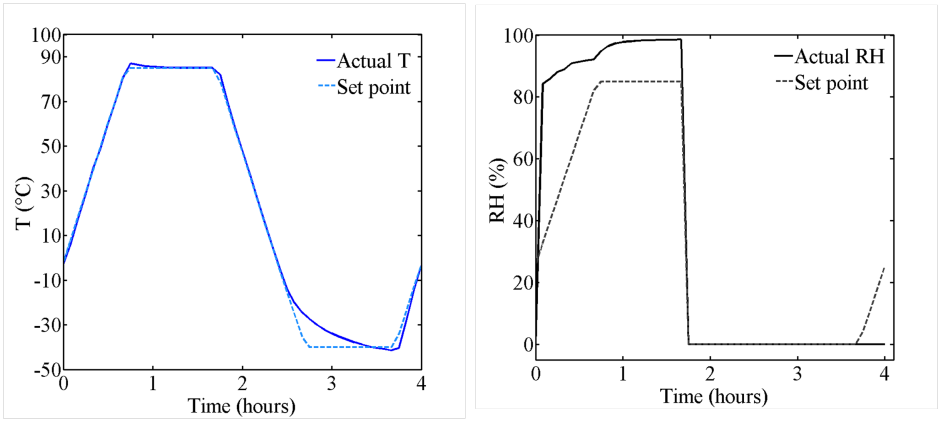

(a) (b)

Figure 5.11: Recorded temperature and humidity data inside the climate chamber and the corresponding set point values imposed in the cycles according to IEC 61215 standards.

5.4 Results of artificial aging tests

5.4.1 Cycles based on IEC 61215 standards

The results of the cyclic tests performed using extreme thermo-hygrometric cycles according to the IEC 61215 standards are herein summarized. The tests were performed on module No.1, whose cracking was induced during lamination (see Tab.5.2). The shape of the cycle is shown in Fig.5.1 and programmed by using the WinKratos facilities but with a different time scale which permits the relaxation of the EVA. The recorded temperature and humidity data with their imposed set point values are shown in Fig.5.11.

After the test, a detailed evaluation of cracking in Silicon cells was performed by using the EL technique.

Every 40 cycles, EL measurements were performed to monitor the evolution of the electrical damages and cracking. A series of EL images is shown in Fig.5.12. Using the same cut-off of 600 ÷ 2300 nm for the wavelength of all the EL images the module shows a strong darkening. Apart from a progressive evolution of the EL signal towards dimmer tones, due to the moisture diffusion which induces oxidation of the grid line, the solar cell in the middle of the PV module shows a significant degradation triggered by the presence of a crack. Examining the EL image of the module after 400 cycles in details, Fig.5.11(g), a wide area in the central solar cell becomes electrically isolated, presumably due to the crack crossing the grid line. After 500 cycles (Fig.5.12(h)) also the cell in the second row on the right one shows a problem in the fingers connection especially on the side adjacent to the cracked cell. In general, the appearance of dark spots is most likely related to diffusion of moisture inside the EVA and subsequent corrosion of the fingers. This phenomenon appears to be enhanced by the presence of cracks, due to the further moisture diffusion from the EVA layer through

the Silicon cell, in addition to diffusion from the solar cell edges. The results of the flash test measurement before testing and after accelerated aging are presented in Tab.5.4, where an overall reduction of 21% in the efficiency and of 20.9% in the maximum power, P_{MPP}, is reported.

Table 5.4: Flash test data of module No.1.

	I_{SC} A	V_{OC} V	I_{MPP} A	V_{MPP} V	P_{MPP} W	η %	FF %
Before aging	8.26	5.49	7.72	4.40	33.97	13.59	74.91
After 500 cycles	6.69	5.50	6.13	4.38	26.84	10.73	72.98

An overall electric resistance of the PV module due to the degradation effects, R_{D}, can be introduced and simply defined as following:

$$R_{\mathrm{D}} = \frac{V - V_{\mathrm{i}}}{I} \tag{5.3}$$

where V_{i} is the applied voltage to perform the EL test before the accelerated aging test, V is the actual applied voltage after 500 cycles, and I is the imposed current in both configurations. The evolution of of R_{D} for the module No.1 subjected to the IEC 61215 standards test is shown in Fig.5.13 and highlights a significant increase in the electric resistance due to aging degradation especially after 300 cycles.

5.4.2 Realistic thermo-hygrometric cycles

The environmental cycles designed based on summer and winter statistics are shown in Fig.5.14. The winter and summer cycles have been implemented in WinKratos, according to the climate chamber facilities and features, and the set point data together to the measured relative humidity and temperature during a cycle are shown in Figs.5.15 and 5.16, respectively for the winter and the summer seasons.

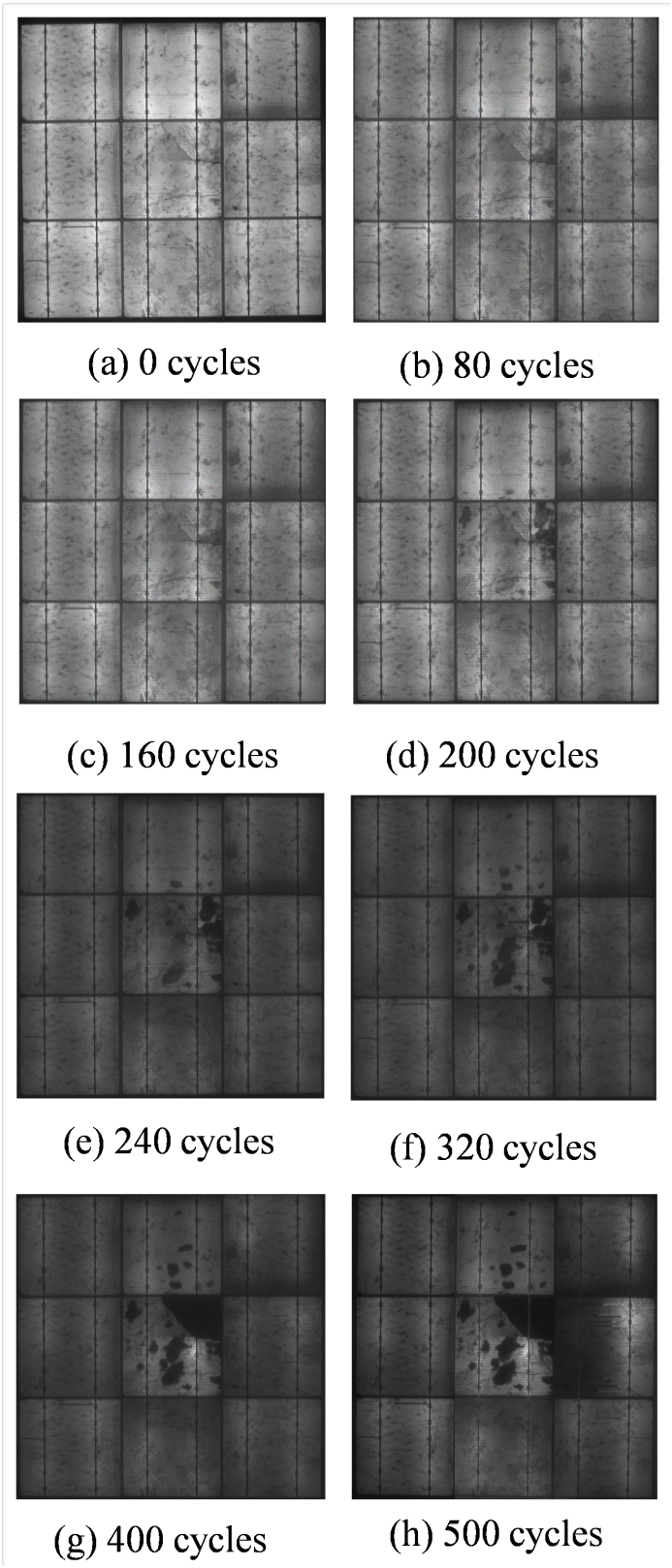

Figure 5.12: EL images of module No.1 showing the occurrence of electrical degradation phenomena.

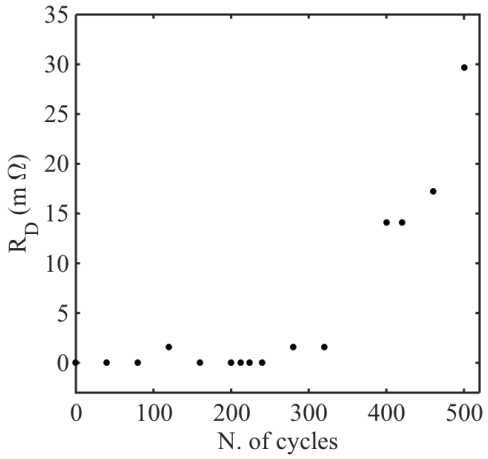

Figure 5.13: Degradation resistance vs. number of cycles for the module No.1.

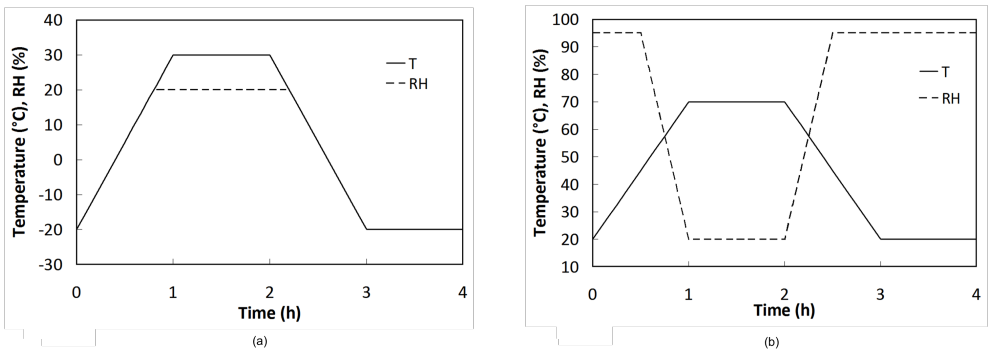

Figure 5.14: Designed realistic cycle for winter (a) and summer(b).

Aging tests are performed by considering a sequence of 200 winter cycles on the module No.2 (see Tab. 5.2), followed by 200 summer cycles, for a total of 800 hours of winter and 800 hours of summer testing.

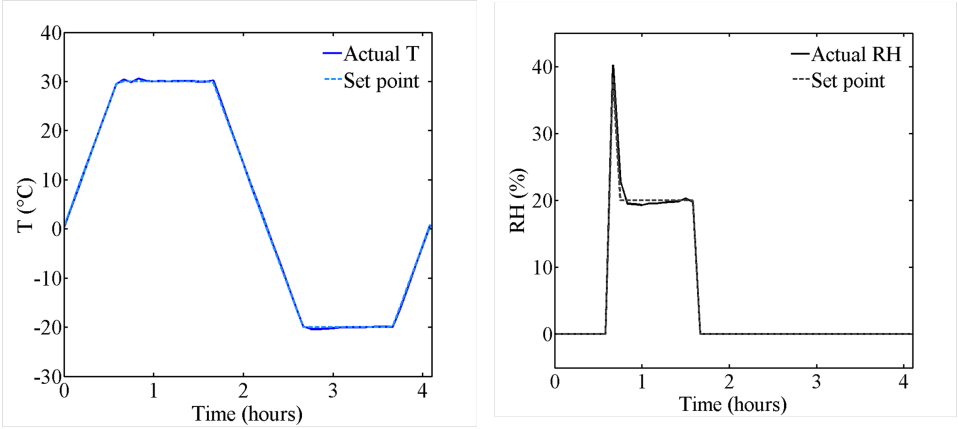

(a) (b)

Figure 5.15: Set point and measured data for temperature (a) and relative humidity (b) in the winter cycle.

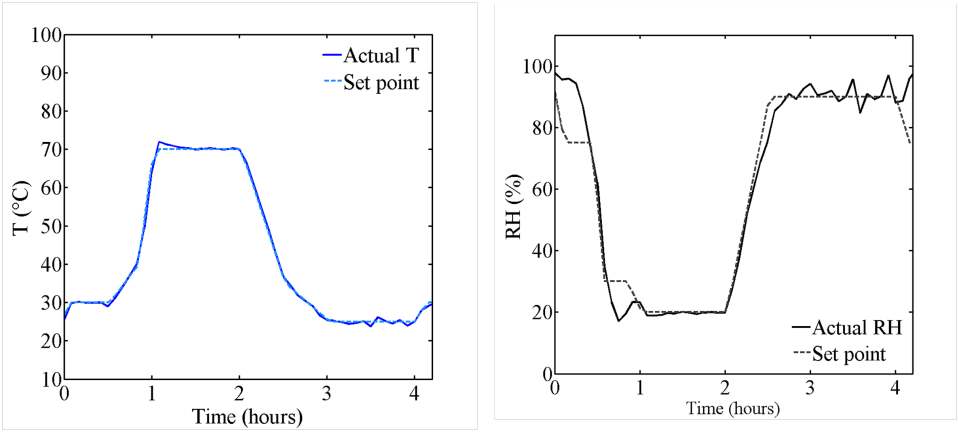

(a) (b)

Figure 5.16: Set point and measured data for temperature (a) and relative humidity (b) in the summer cycle.

The EL images of the PV module at the end of each set of cycles is shown in Fig.5.17. The EL images do not show a relevant impact of the designed cycles on crack evolution. Thus, the present cycles, which correspond extreme condition experienced in the field, do

not produce degradation phenomena as fast as the artificial cycle test based on IEC 61215 standards.

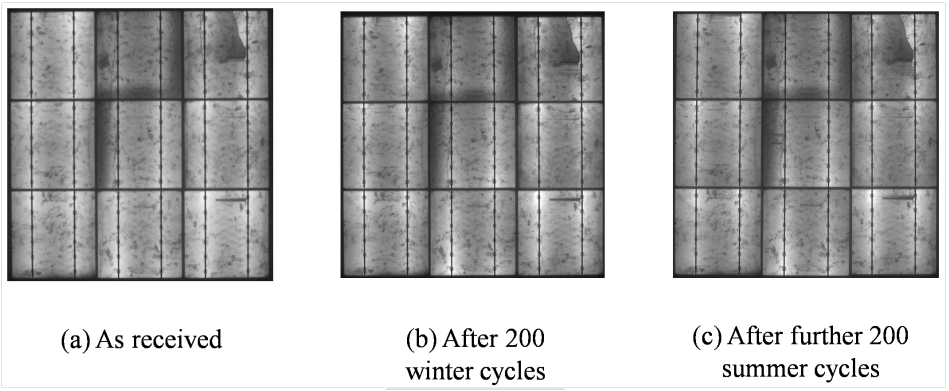

Figure 5.17: EL image of the PV module No.2: (a) as received; (b) after 200 winter cycles; (c) after further 200 summer cycles.

Table 5.5: Flash test data of No.2 as received, after bending and at the end of the environmental 400 cycles.

	I_{SC} A	V_{OC} V	I_{MPP} A	V_{MPP} V	P_{MPP} W	η %	FF %
Initial	7.97	5.49	7.48	4.40	32.89	13.16	75.14
After bending	7.89	5.50	7.39	4.40	32.47	12.99	74.82
After realistic cycles	7.92	5.50	7.38	4.36	32.18	12.87	73.96

From these cycles a reduction of 0.92% in the efficiency and of 0.89% in the P_{MPP} is found. The value of R_D for module No.2 subjected to the realistic test are shown in Figs. 5.18 and 5.19 for 200 winter cycles and further 200 summer cycles.

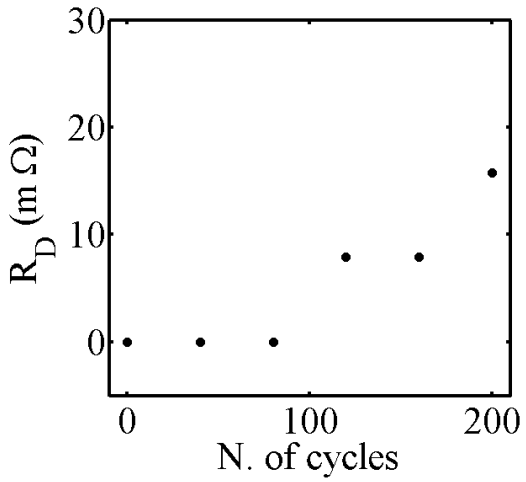

Figure 5.18: R_D in function of the number of cycles for module No.2 after 200 winter cycles.

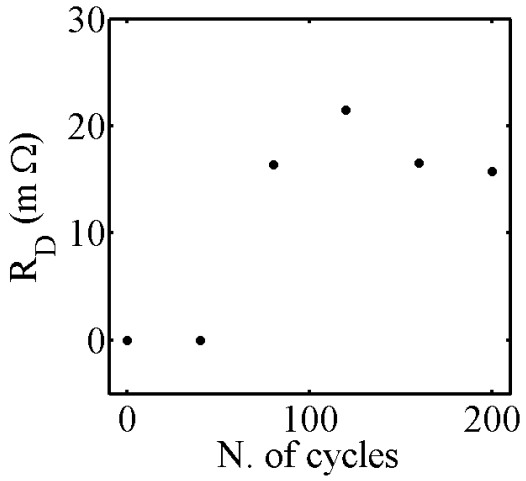

Figure 5.19: R_D in function of the number of cycles for module No.2 after 200 summer cycles.

5.4.3 Damp-heat test

The last test conducted and presented in this Chapter is the damp-heat test described in Section 5.1. This was performed on module No.3 of Tab.5.2 at the Institute for Solar Energy

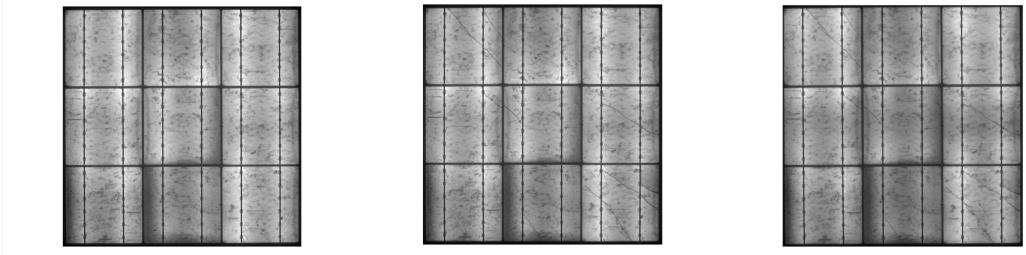

Figure 5.20: Module No.3: (a) initial state; (b) after transportation; (c) after the damp-heat test.

Hamelin. The EL images of the module are shown in Fig.5.20. Herein the initial condition after lamination is shown in Fig.5.20(a). The appearance of cracks after transport is evident from Fig.5.20(b). Finally, the EL image after 1000 hours of the Damp-Heat test according IEC 61215 standards is shown in Fig.5.20(c). This duration of the test was chosen to be similar and comparable to realistic hygrometric cycles. Also in this case, the degradation is modest as compared to that observed for HF cycle based on IEC 61215 standard test reported in Section 5.4.1. However we found a slightly darkening of the module in particular for the three cells in the central column of the module. The results of the flash measurement for the three situations are reported in Tab.5.6.

Table 5.6: Flash test data of No.3.

	I_{SC} A	V_{OC} V	I_{MPP} A	V_{MPP} V	P_{MPP} W	η %	FF %
Initial	7.87	5.49	7.47	4.40	32.85	13.14	76.01
After transportation	7.88	5.51	7.39	4.41	32.56	13.02	75.08
After DHT	7.86	5.50	7.38	4.37	32.26	12.91	74.68

It comes out an overall reduction of 0.84% in efficiency and of 0.92% in maximum power output P_{MPP}. The slightly reduction of the power output seen in the test is confirmed by results by Wohlgemuth [164, 165], Herrmann [166] and Saint-Lary [161]. Indeed, the high darkening reported in Saint-Lary [161] appears only after 2800 hours of DHT. In that case, moisture induced corrosion of the doped oxide that provides the electrical contact to the emitter of the Silicon cell.

Chapter 6

Thermo-mechanical spalling for the production of thin solar cells

The purpose of this Chapter is to study an innovative methodology to produce ultra thin solar cells made of thin layers of Silicon initially bonded to an Aluminum superstate, starting from a parental Silicon wafer. This bilayered system, which is the starting point to realized a solar cell, could be traditionally realized by wire sawing followed by Aluminum deposition. However for thin Silicon layers, the amount of Silicon losses due to the sawing can be too high for being cost competitive. Hence, an alternative to the wire sawing is required. The key idea is to exploit a process known as *kerf-less spalling* or *lift-off*, where an atomistically sharp crack propagation driven by thermal loading and induced by a suitable joining of dissimilar materials with a thermo-elastic mismatch in their material properties, leads to the separation of ultra-thin Silicon layers from the Silicon wafer. In this process the exfoliation of thin crystalline Silicon foils, starting from a Silicon substrate, is induced by the difference in thermal expansion coefficients and Young's moduli of the Silicon and a stressor layer, e.g. a metal. Usually an initial notch is introduced by laser cutting into the wafer only at the edges of the specimen.
This process briefly introduced in Chapter 1 answers to the requirement of the reduction of Silicon consumption in the production of thin film.
Via a controlled temperature variation it is demonstrated that it is possible to drive the initially sharp crack, introduced by laser, into the Silicon substrate and obtain the detachment of ultra-thin Silicon layers [41]. It has will also be shown that it is beneficial to use a directed cooling scheme for controlling the crack front propagation to achieve a crack path parallel to the Silicon surface [41, 167]. A numerical approach based on the finite element method (FEM) and Linear Elastic Fracture Mechanics (LEFM) is herein proposed to simulate, understand the mechanical process, compute the Stress Intensity Factors (SIFs) that characterize the stress field at the crack tip and predict crack propagation of an initial notch, depending on the geometry of the specimen and on the boundary conditions. A parametric study to evaluate the dependence of the crack path on the distance between the notch and the Aluminum-Silicon interface, the thickness of the stressor (Aluminum) layer and the applied load is also provided.

The feasibility to reuse the parental Silicon substrate in presence of a non-planar Si-Al interface after the first exfoliation is also investigated, in order to demonstrate the potential reduction of the sawing costs. The effect of the main process parameter, the velocity of immersion, on the resulting exfoliated layer is analyzed.
All the numerical results have been validated by experimental tests that have been performed by the writer at the Institute of Solar Energy of Hamelin with the support of the German Academic Exchange Service (DAAD) from August 2015 to January 2016 with an individual scholarship. Finally in the last Section, a topological characterization of the exfoliated surfaces is presented, based on confocal profilometer results obtained at the MUSAM-Lab of the School for Advanced Studies Lucca (IMT).

6.1 Analytical Model

Pioneering theoretical studies on the spalling phenomenon were carried out by Suo and Hutchinson [43]. They focused their attention on cracking process in brittle a substrate because of experimental evidence that cracks in thin films exposed to residual tension have a high tendency to extend parallel to the interface into the substrate [168, 169, 170, 171]. They analyzed various bi-layers composed by a brittle material as substrate and a thin film (see Fig.6.1).

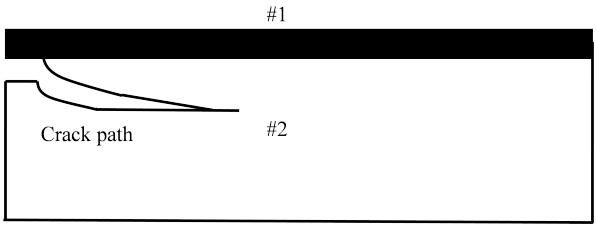

Figure 6.1: A crack in an infinitely wide bi-layer system composed by two materials: No.1 is the thin film and No.2 is the substrate. The wide plate is subjected to a remote tensile stress.

The residual stress in these structures is considered a particular combination of edge loads. In particular in [44] the two layers are assumed to be unstressed before bonding at a temperature equal to T_0 and subsequently cooled down to a temperature T. Residual stresses induced in these components by a uniform temperature variation from a stress-free reference condition are due to the thermo-elastic mismatch between the elastic properties and the thermal expansion coefficients (CTE) of the two joined materials. The theoretical analysis carried out by Suo and Hutchinson [43] was focused on finding the configurations preventing for a wide range of film/substrate under a generic type of edge load. The analytic model in [43] is based on the hypothesis of a two-dimensional semi-infinite plane made of a brittle material with a deposited thin film. Two load parameters controlling the crack tip singularity, P and M, were considered see Fig.6.2.

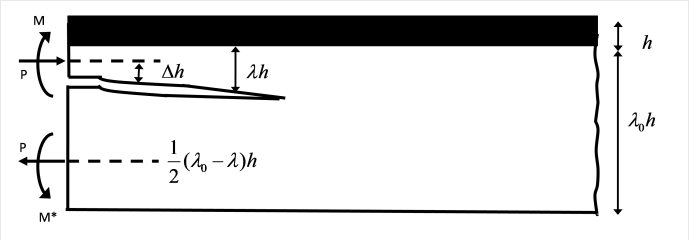

Figure 6.2: Geometry and conventions of the bilayer structure with a crack in the substrate (material 1). The dotted lines are the neutral axis.

The strain energy stored in the structure per unit width and per unit length far behind the crack tip is given by:

$$G = \frac{c_2}{16}\left[\frac{P^2}{Uh} + \frac{M^2}{Vh^3} + 2\frac{PM}{\sqrt{UV}h^2}\sin\gamma\right] \tag{6.1}$$

where $c_2 = (\kappa_2 + 1)/\mu_2$ (κ is Kolosoff's constant and μ is the shear modulus), the angle is restricted to $|\gamma| < \pi/2$, U and V are dimensionless positive numbers given by (6.2) and (6.3), respectively.

$$\frac{1}{U} = \frac{1}{A} + \frac{1}{\lambda_0 - \lambda} + \frac{12[\Delta + (\lambda_0 - \lambda)]^2}{(\lambda_0 - \lambda)^3} \tag{6.2}$$

$$\frac{1}{V} = \frac{1}{I} + \frac{12}{(\lambda_0 - \lambda)^3} \tag{6.3}$$

The quantities A and I are the dimensionless effective cross-section and the moment of inertia of the beam per unit width, respectively. The SIFs are depending linearly on P and M as follows:

$$\begin{aligned} K_{\mathrm{I}} &= \frac{P}{\sqrt{2Uh}}\cos\omega + \frac{M}{\sqrt{2Vh^3}}\sin(\omega + \gamma) \\ K_{\mathrm{II}} &= \frac{P}{\sqrt{2Uh}}\sin\omega - \frac{M}{\sqrt{2Vh^3}}\cos(\omega + \gamma) \end{aligned} \tag{6.4}$$

where the angle ω depends on λ, λ_0, α and β (the Dundurs' parameters which give a measure of stiffness ratio between the two materials).To achieve crack propagation, the stress intensity factor has to reach its critical value, the fracture toughness (K_{IC}). Satisfying the previous condition, two possibilities may occur during propagation: the crack may move out of the plane of the crack or may continue traveling parallel to the initial notch direction. In particular, to achieve a stable crack path and produce a planar thin layer, Mode II contributions should be avoided [172] which would result into a crack kinking. Thus, the condition to obtain a flat delamination is related to the steady-state crack-propagation condition, when $K_{\mathrm{II}} = 0$ and $K_{\mathrm{I}} = K_{\mathrm{IC}}$. Suo and Hutchinson [43] found that numerical solutions are very sensitive to the thickness ratio between the substrate and the stressor layer. Besides results are sensitive to

the Dundur's parameter. The steady-state condition is obtained by enforcing $K_{\mathrm{II}} = 0$ at the crack-tip in Eq. (6.4), leading to the following relation:

$$\frac{\cos(\omega + \gamma)}{\sin \omega} = \sqrt{\frac{V}{U}} \frac{Ph}{M} \tag{6.5}$$

The parameters α, β and λ_0 are given for a certain system with defined material and thickness. For a given dimensionless load Ph/M the unknown λ from Eq. (6.5) gives the steady-state cracking depth. The value of K_{I} is then computed by replacing λ in Eq. (6.4). In Suo and Hutchinson [44], thus, cooling down the metal to ambient temperature leads to a mismatch in the thermal expansion between the substrate and the stressor layer and it causes high stresses inside the substrate. To release this stress, the system bends. Assuming homogeneous, isotropic and linear elastic materials, the stress in the film, caused by the mismatch in the thermo-elastic properties and due to cooling from the bonding temperature (T_0) to the final temperature (T_1), is given by [44]:

$$\sigma = \frac{(\alpha_1 - \alpha_2)(T_0 - T_1)E_1}{1 - \nu_1} \tag{6.6}$$

Here, α_1 is the coefficient of thermal expansion of the film (material 1 in Fig.6.1), α_2 is the coefficient of thermal expansion of the substrate (material 2 in Fig.6.1), E_1 is the Young's modulus of the film and ν_1 is the Poisson's ratio of the film. If the substrate has a homogeneous defect density, the crack starts propagating from the first point where the stress intensity factor achieves the fracture toughness of the substrate. However, the exact path of the crack depends on the thermo-mechanical parameters of the system. To activate spalling, the upper layer needs a minimum thickness given by [173]:

$$h = \frac{\Gamma_2 E_1}{Z\sigma^2} \tag{6.7}$$

with Γ_2 is the fracture resistance of the substrate and Z [172] a dimensionless driving force that depends on the film-substrate elastic mismatch and on the crack pattern. Thus, from the model proposed in [43] it is possible to simulate the conditions leading to a flat crack propagation, parallel to the interface at a given depth, in the approximation of two-dimensional semi-infinite plane made of a brittle material with a deposited thin film. On the other and, the Finite Element Method (FEM) is required in case of a finite specimen, and a non uniform temperature distribution and it will be detailed in the next Section.

6.2 Finite element model

In order to achieve a flat crack path and produce a planar thin layer, essential for the production of solar cells, it is necessary to have a steady-state Mode I crack propagation, i.e., $K_{\mathrm{II}} = 0$ and $K_{\mathrm{I}} = K_{\mathrm{IC}}$ [45]. Under these conditions, the crack propagates in a collinear manner parallel to the bi-material interface. In this Section the numerical model of the spalling process is presented under the assumption of plane strain conditions by using the FE program FRactureANalysis Code (FRANC2D) [174]. The discretization of the continuum is performed by

using eight-node isoparametric finite elements. For a typical eight-node isoparametric finite element, the shape functions for the nodes along the edge 1-3 (see the sketch in Fig.6.3) are:

$$N_1 = -\frac{1}{2}\,\xi(1-\xi) \tag{6.8a}$$

$$N_2 = (1-\xi^2) \tag{6.8b}$$

$$N_3 = \frac{1}{2}\,\xi(1+\xi) \tag{6.8c}$$

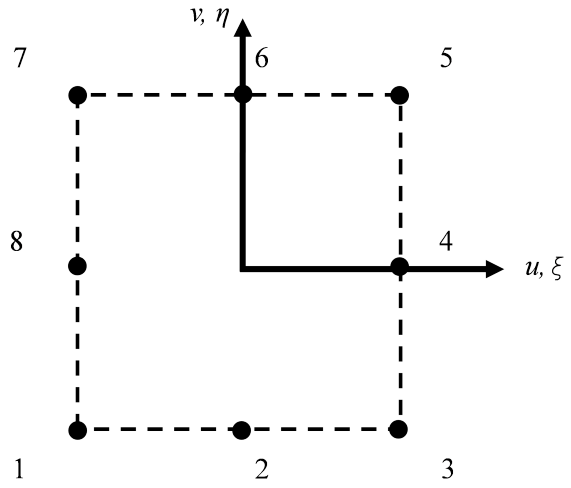

Figure 6.3: Q8 isoparametric finite element.

The x-coordinate and the displacements in the horizontal and vertical directions along this edge are obtained by interpolation:

$$x = \sum_{i=1}^{3} N_i\, x_i, \tag{6.9a}$$

$$u = \sum_{i=1}^{3} N_i\, u_i, \tag{6.9b}$$

$$v = \sum_{i=1}^{3} N_i\, v_i. \tag{6.9c}$$

In particular, placing the origin of the reference system at the node No.1 and denoting the length of the side 1-3 as l, then $x_1 = 0$, $x_2 = \omega\, l$ and $x_3 = l$, where $\omega\, l$ denotes the position of

the middle node, with $0 < \omega < 1$. From Eq. (6.9a) we obtain:

$$x/l = \omega + 0.5\,\xi + 0.5\,(1 - 2\omega)\,\xi^2. \tag{6.10}$$

In case of homogeneous materials, the choice of $\omega = 1/4$, leads to the typical *quarter point singular finite element* and the possibility to follow the singular trend typical of LEFM for a crack. In such a case, in fact, the x-coordinate is given by:

$$\frac{x}{l} = \left(\frac{1+\xi}{2}\right)^2. \tag{6.11}$$

The displacement along the side 1-3 is given by:

$$u = [1 - 3(x/l)^{\frac{1}{2}} + 2(x/l)]u_1 + [4(x/l)^{\frac{1}{2}} - 4(x/l)]u_2 + [-(x/l)^{\frac{1}{2}} + 2(x/l)]u_3 \tag{6.12}$$

and the strain in the x-direction is now:

$$\varepsilon_x = \frac{\partial u}{\partial x} \sim x^{-\frac{1}{2}}, \tag{6.13}$$

with a singularity of order 1/2. This element is the easiest and most powerful technique used in finite elements to model a stress singularity typical of crack propagating inside a homogeneous and isotropic medium. The quarter-point singular element has been generalized by Staab [175] in order to capture singularities of order different from $-1/2$. In fact, it is possible to capture a generic singularity by varying the placement of the mid-side node between the quarter-point and the mid-point position. The unknown singular coefficients, i.e. the order of the stress-singularity and the generalized stress-intensity factors, are computed by post-processing the finite element solution. Extension of the method to cracks impinging bi-material interfaces and re-entrant corners are discussed in [176].

6.2.1 MATLAB finite element pre-processors

Automatic mesh refinement at the crack tip is adopted during crack propagation in order to avoid the presence of geometrically distorted elements. The simulation of crack propagation, using the present model, requires a series of operations. To generate geometry and meshes, the pre-processor CASCA and a specific user-defined subroutine written in MATLAB are used. The first subroutine allows adding and modifying materials and their parameters of the finite elements based on their position starting from the input file generated by CASCA. The input files (in *.inp* format) include the following list of data:

- Information on the mesh (i.e. number of nodes, number of elements, number of materials);
- Material property definition (isotropic or orthotropic material, Young's modulus, Poisson's ratio, thickness, material density and K_{IC});
- Element connectivity data (element number, material and nodes numbers for each element);

- Nodal data (node number, $x-$coordinate and $y-$coordinate).

Starting from this initial input file, the MATLAB subroutine assigns to each element the proper material number, based on element nodal coordinates and the prescribed layered structure geometry, and it re-writes the modified file. In the case herein investigated, the material 1 is the thin film (Aluminum) and the material 2 is the substrate (Silicon) and the algorithm for the attribution of the material flag number is reported in Algorithm 4.

```
for i = 1 to N_ET total number of elements do
    Set material to 0;
    for j = 1 to N_NE number of nodes for each element do
        if y_node > y_intef then
            Set material flag to 1;
            else
                Set material flag to 2
            end
        end
    end
end
Write the modified input file
```

Algorithm 4: Numerical algorithm for the assignment of the material flag to each element of the mesh.

Afterwords the temperature excursion ΔT is specified node-wise by a second pre-processor developed in MATLAB. This pre-processor produces an ASCII input file, *.tdi*, which contains the list of nodes of the previously generated element model and the corresponding temperature excursion to be imposed.

From the temperature distribution imposed, using a triangular mesh, FRANC is computing the thermal strain to be imposed to the element. The algorithm is divided in four Sections (see Fig.6.4) to write the counter-clockwise thermal distribution with the coordinate and the corresponding temperature for each point.

It is summarized in Algorithm 5.

The software FRANC2D solves the linear system of equations resulting from the FE discretization. For each crack-tip position, the code computes the Mode I and the Mode II SIFs at the crack-tip. It allows to use the J-integral [72], the modified crack closure integral technique [68], or the displacement correlation technique [70] that, for the present study, provide the same numerical results. The computed SIFs are used to predict the crack growth propagation direction based on three possible fracture criteria: the maximum shear stress criterion [177], the maximum energy release rate criterion [80], and the minimum strain energy density criterion [178]. By comparing the equivalent stress-intensity factor, determined from the SIFs according to one of these criteria, and the material fracture toughness, K_{IC}, the crack propagates if and only if it achieves K_{IC}. Then, a new crack-tip location is determined by imposing a small user-defined crack increment in the suggested crack propagation direction. Subsequently the code deletes elements along the incremental crack path, updates crack geometry, and performs automatic local re-meshing. The details on procedures for crack

Import the specified thermal distribution obtained from a preliminary heat-transfer analysis;
Section 1: y=0 and $0 < x < L_x$
for $i = 1$ **to** N_x number of nodes along L_x , length of the specimen in the x − direction **do**
  Write in the *tdi* file the coordinate and the corresponding temperature;
  $(x_i, y), T$;
end
Section 2: $x = L_x$ and $0 < y < L_y$
for $i = 1$ **to** N_y number of nodes along L_y , length of the specimen in the y − direction **do**
  Write in the *tdi* file the current coordinate and the corresponding temperature;
  $(x, y_i), T$;
end
Section 3: $y = L_y$ and $L_x < x < 0$
for $i = N_x$ **to** 1 **do**
  Write in the *tdi* file the current coordinate and the corresponding temperature;
  $(x_i, y), T$;
end
Section 4: $x = 0$ and $L_y < y < 0$
for $i = N_y$ **to** 1 **do**
  Write in the *tdi* file the current coordinate and the corresponding temperature;
  $(x, y_i), T$;
end

Algorithm 5: Numerical algorithm for the generation of the thermal distribution.

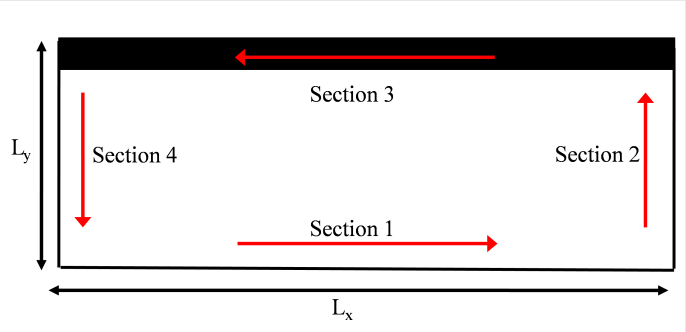

Figure 6.4: Sketch of the region and the writing order used in the Algorithm 5 to create the thermal distribution file.

propagation and re-meshing schemes have not been modified with respect to the original formulation and are described in [82].For the following analysis, the J-integral method is used for the computation of the stress-intensity factors and the minimum strain energy density (SED) is chosen [82] as the criterion to determine the crack growth direction.

6.3 Numerical simulations

6.3.1 Determination of the Mode I steady-state crack propagation

In this Section, the determination of the condition to achieve a Mode I crack propagation for the spalling experiment presented in [41] is investigated. The 2D geometry considered and the boundary conditions are schematically shown in Fig. 6.5(a). The geometrical parameters are selected to be in accordance with the experimental geometry tested in [41]: the thickness of the Silicon substrate is $\lambda_0 h = 675\ \mu$m, while the thickness of the Aluminum layer is $h = 120\ \mu$m. The initial notch depth is $a_0 = 190\ \mu$m, and the span of the specimen is 14 mm. The relevant material parameters are chosen from the literature and are collected in Tab.6.1.

Table 6.1: Material parameters used in the simulations.

Parameters		Silicon	Aluminum
E	(GPa)	139	68
K_{IC}	(MPa $m^{0.5}$)	0.75	24
ν		0.276	0.34
CTE	($^\circ C^{-1}$)	0.26×10^{-5}	2.3×10^{-5}

Analysis of the temperature range required to avoid crack arrest.

The influence of the crack depth, λh, and of the distribution of the imposed temperature variation are investigated. The thermal distribution is considered to be a key parameter to

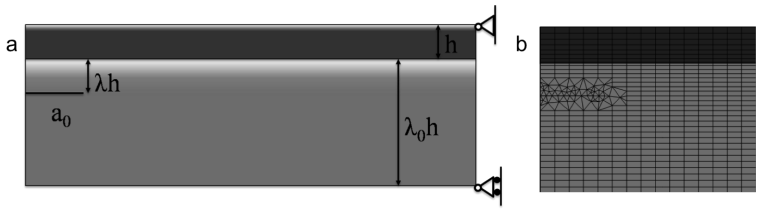

Figure 6.5: (a) Geometry of the Silicon substrate with an Aluminum layer evaporated on the top of it, in a 2D plane strain configuration and restrained at a x=14 mm; (b) zoom of the FE mesh near the crack tip.

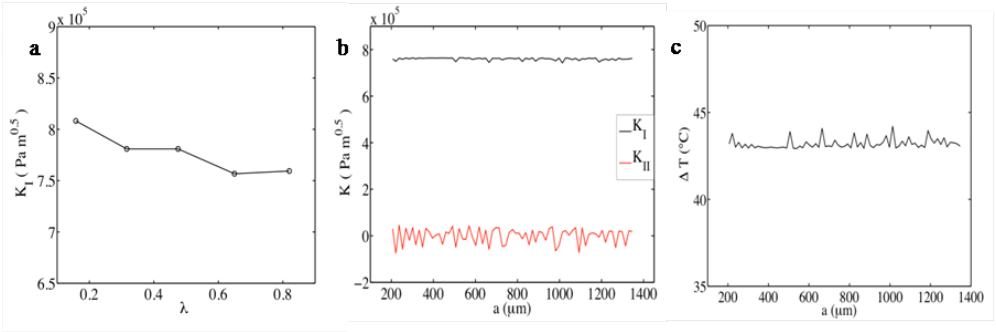

Figure 6.6: (a) Influence of the crack depth λ on K_{I} (λ = 0.158, 0.316, 0.475, 0.65 and 0.82); (b) SIFs in function of the crack length a for λ=0.65 and a uniform ΔT = 40°C; (c) ΔT_{C} necessary to achieve crack propagation ($K_{\mathrm{I}} = K_{\mathrm{IC}}$).

control crack propagation and avoid crack deflection and roughness. The FE mesh with a given notch position λh is shown in Fig.6.5(b). The value of the Mode I SIF, K_{I}, related to the crack opening mode, is depicted in Fig.6.6(a) vs. λh.

First, a ΔT = 40°C from the stress-free reference temperature over the whole specimen is considered. The smallest value of K_{I} is achieved for λ=0.65, see Fig. 6.6(a). These results are very close to the analytical predictions in [41], obtained for an infinite body. From the computed Mode I stress-intensity factors, $K_{\mathrm{I}}(a, \Delta T)$, corresponding to a crack length a and a given temperature range ΔT, the critical temperature range leading to crack propagation, $K_{\mathrm{I}} = K_{\mathrm{IC}}$, can be computed by a proportionality relation due to the linearity of the problem, i.e., $\Delta T_{\mathrm{C}} = \Delta T\ K_{\mathrm{IC}}/K_{\mathrm{I}}(a, \Delta T)$. An example of computation is shown in Fig.6.6(b) and Fig.6.6(c) for λ=0.65.

In practical applications, a convenient way to induce spalling can be to heat the sample from one side and then cooling it down by a progressive immersion of the sample in water from the opposite side, see [41]. In this case, the resulting ΔT is neither constant in time nor homogeneous over the whole body. Therefore, the steady-state crack growth cannot

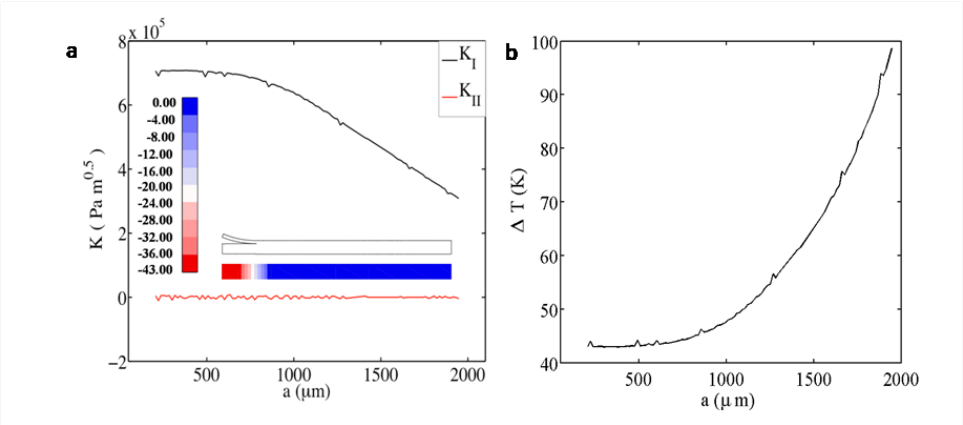

Figure 6.7: (a) SIFs, deformed mesh and the discrete thermal distribution, where $\Delta T_1 = 43°$C is applied for 1 mm and the other part of the sample has $\Delta T_2 = 0°$ C; (b) ΔT_C necessary to avoid crack arrest and propagate the crack till the end of the sample.

be analyzed with the semi-analytical model by Suo and Hutchinson [44] but needs to be numerically investigated. The effect of a nonuniform ΔT is investigated by considering $\Delta T_1 = 43°$C applied to the first 1 mm of the specimen and then $\Delta T_2 = 0°$ C to the rest of the specimen as shown in Fig.6.7(a). The plot of K_I vs. crack length a shows that in this case the Mode I stress-intensity factor is diminishing with increasing a. This is the result of a reduced fracture driving force due to a smaller ΔT at the crack tip as long as the crack moves towards the center of the sample. When $\Delta T < 41.7°$ C, then the crack arrests.

Therefore, to maintain $K_I(a) = K_{IC}$ at the crack tip during an exfoliation experiment, a possible way is to increase the temperature range ΔT during crack propagation. Fig.6.7(b) shows the temperature range from the stress-free condition that has to be applied to the first portion of the sample (geometry from Fig.6.7(a)) to propagate the crack for about 700 μm. A higher value of ΔT within the first portion of the sample is also beneficial since it leads to a larger crack opening, but the crack would eventually stop in any case in correspondence of a length a=a^* when $K_I(a^*) < K_{IC}$. This behavior was also observed in the experiments [41]. Therefore, these results pinpoint that by tuning the imposed temperature range, the crack propagation can be controlled or even stopped. By limiting and localizing the area in which the exfoliation conditions are met, the formation of multiple crack fronts can be avoided, and thus surface roughness can be minimized [41].

Parametric study

In this Section the steady-state position of the crack tip in the direction orthogonal to the Aluminum-Silicon interface is evaluated as a function of different thicknesses of the Aluminum stressor layer (h equal to 20, 50, 70, 100, 120, and 125 μm) and a comparison with novel experimental results is proposed. For the following simulations, the thermal load resulting from the simulated thermal distribution obtained by solving the problem of heat transfer

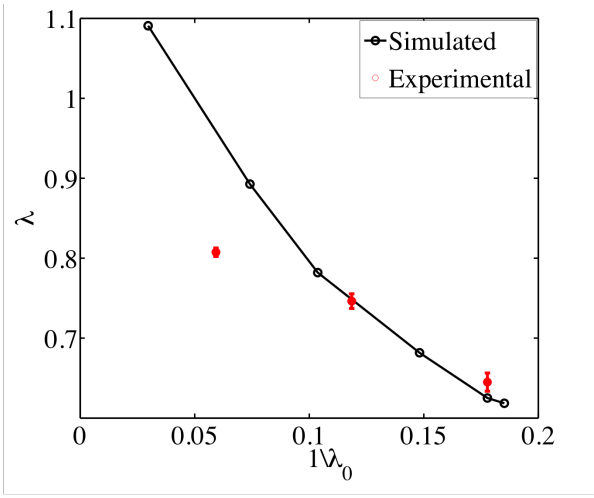

Figure 6.8: Comparison between the steady-state cracking depth as a function of film substrate thickness ratio and the experimental results (in red) for h=40, 80, 120 μm.

in Comsol Multiphysics [41] corresponding to a time of 2 s after the immersion of the sample in the water is adopted. The resulting steady-state cracking depth λ as a function of the film substrate thickness ratio λ_0 is compared with the experimental results for h=40, 80, and 120 μm. The corresponding values of the thickness of the exfoliated bi-layered thin films for the three different Aluminum thicknesses are 32.3 ± 3.6 μm, 59.7 ± 6.2 μm, and 77.4 ± 47.7 μm. The simulation results are in good agreement with the ones presented in [41] and in the case of 80 and 120 μm there is a pretty good matching between simulated results and measured ones, as shown in Fig.6.8. The achieved presented in this Section have been published in [167].

Influence of the Silicon anisotropy

Silicon is an anisotropic material whose different proprieties based on the direction are due to the crystal lattice. At ordinary, pressure it is crystallized in a diamond structure and has a density of 2.329 g/cm^3 [179]. The Hook's constitutive law :

$$\begin{aligned} \sigma_{ij} &= C_{ijkl}\epsilon_{ij} \\ \epsilon_{ij} &= S_{ijkl}\sigma_{kl} \end{aligned} \tag{6.14}$$

where the stiffness C and the compliance S are tensors of rank four and the stress and the strain tensors are of rank two. In particular, in Silicon the tensors C and S depend on three independent elastic constants, thanks to the combination of cubic symmetry and the equivalence of the shear condition. Thus, the tensors can be expressed with respect to a specific basis, usually the <100> direction for the cubic structures. In this way the stress tensor

component are:

$$\begin{aligned} \sigma_{ii} &= C_{11}\epsilon_{ii} + C_{12}(\epsilon_{jj} + \epsilon_{kk}) \\ \sigma_{ij} &= C_{44}\epsilon_{ij} \end{aligned} \tag{6.15}$$

Moreover, it is possible to obtain the stress components for each direction of interest with a proper rotation of the system. The material parameters are in this way given for each direction of interest. The thermo-elastic parameters of Silicon depending on the crystal orientation are listed in Tab. 6.2 [179].
In this Section the influence of the anisotropy of the Silicon crystal is investigated, using the same Aluminum thickness (120 μm) and the thermal distribution corresponding to t = 2s after the immersion of the sample in the water bath. Experiments and simulations were carried out with two different angles of immersion (and crack propagation) with respect to the <110> lattice plane of the Si-wafer: 45° (standard orientation, <100>-direction) and 90° (<110>-direction).

Table 6.2: Material parameters used in the simulations for two different crystal orientations.

Material Parameters		Silicon <100>	Silicon <110>
E	(GPa)	139	169
K_{IC}	(MPa m$^{0.5}$)	0.75	0.71
ν	–	0.276	0.34
CTE	(° C^{-1})	0.26×10^{-5}	2.6×10^{-5}

The computed values of K_I for the two different angles of immersion are shown in Fig.6.9. For the standard orientation (<100> direction), shown by the dotted blue lines, K_I outbalances K_{IC} but it is lower than for the other immersion angle corresponding to the <110> direction. The results of the final exfoliated layer thickness in stationary conditions are different for the two orientations. In the <110> direction, the exfoliated layer is 75.91 μm thick and for the <110> direction it is 63.64 μm thick. The experimentally measured exfoliated layer thicknesses in direction <100> is 77.0 ± 7.7 μm and in direction <110> is 65.1 ± 10.2 μm. Both values are very close to the numerical ones. Significant results of this research have been published in [167].

6.3.2 Re-use of the parental substrate for multiple exfoliation

In this Section the feasibility to reuse the parental Silicon substrate in presence of non-planar Si-Al interface after the first exfoliation is assessed. In general, multiple reuse of a substrate wafer in thermally induced spalling [41] has been shown to be feasible by Bellanger

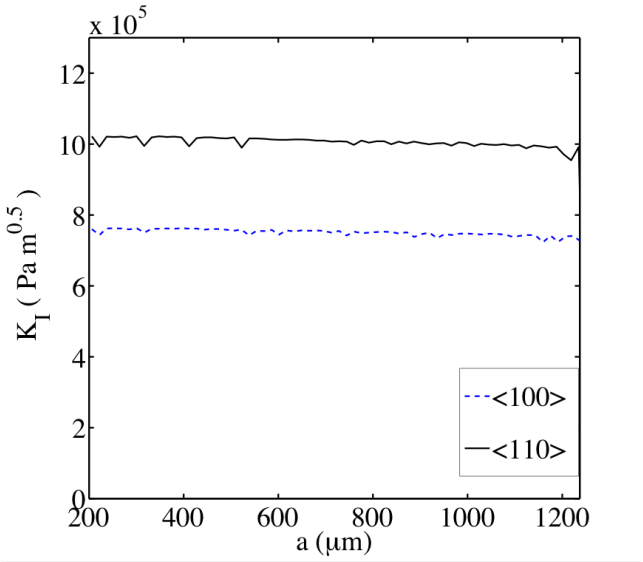

Figure 6.9: Comparison between simulated SIFs for two angles of immersion respect to the <110> lattice plane of the Si-wafer: 45° (standard orientation, <100> direction, blue dotted line) and 90° (<110> direction, black line).

et al. [47], using a bi-layer component with three notches realized by laser along its sides. Here, the crack propagation in the of thermally induced spalling process proposed in [41] is investigated with the numerical method based on the Finite Element Method (FEM) and Linear Elastic Fracture Mechanics (LEFM) previously presented. In particular, a non-planar Silicon-Aluminum (stressor layer) interface caused by previous exfoliations is investigated by inducing a groove into the free surface of the Silicon substrate to be re-used. In addition, experimental tests on substrates prepared with an initial groove having a high deviation from planarity have been performed by the author at Institute of Solar Energy Hamelin, with the founds of an individual scholarship provided by the German Academic Exchange Service (DAAD), to validate the numerical results. A partial reduction in the amplitude of the transferred groove on the Si-Al interface for low width of the groove is reported, which is a promising result for future applications.

Numerical model

The finite element analysis program FractureANalysis Code (FRANC2D) described in Section 6.2.1 is used to simulate the crack path and the required thermal load to be imposed to achieve a steady-state crack propagation [167] in the case of a non-planar Si-Al interface, shown in Fig.6.10(a). The amplitude of the groove in the $y-$direction is set equal to b=20 μm, which is an extreme value used as benchmark test in the following experiments, to evaluate a worst case scenario after the first exfoliation. Different lengths of the groove, L, in the $x-$direction are exterminated, i.e., L=125, 250, 500, 800 and 1000 μm. A thermal load of ΔT=−43 °C is applied, which is the temperature difference with respect to the stress-free temperature measured in the experiments. From the semi-analytic model in [43], a Mode I steady crack growth at a crack depth λh=77.50 μm is expected far from the groove, and λh=96.25 μm below the groove. Numerical results, shown in Fig.6.10(b), are in satisfactory agreement with the analytically expected ones.

The crack path during crack propagation is shown in Fig.6.11(a) for the various considered values of L. The sketch of the non-planar interface is also reported in the same figure. Figure 6.11(b) shows that the amplitude of the discontinuity transferred to the Silicon substrate after the exfoliation in the $y-$direction (b') remains of the same order of magnitude as compared to the groove depth of the sample prior to its first exfoliation. However, for L<250 μm, a reduction of b' is noticed, see Fig.6.11(b). Thus, numerical results suggest the feasibility of reusing Silicon substrates provided that the non-planarity of their surface after the first exfoliation has proper geometrical features, i.e., the extension of the groove is less than 250 μm. The resulting width of the transferred groove (L') after spalling is also evaluated. To overcome the fluctuations due to the numerical oscillation of the crack path in the $y-$direction, a threshold value in the $y-$direction defined as a percentage (99.2%) of the minimum value achieved is used to evaluate the extension of L'. Fig.6.12 shows in black the transferred width of the groove (L'), after spalling, as a function of the original one (L).
The error is defined as the sum of the numerical uncertainly in the $x-$direction and the threshold error. Considering the threshold and y_m the average value in the region L', the latter contribution to the error is defined as x_t -x_m, where x_t is the region where $y < y_t$ and x_m is the region where $y < y_m$. The red dotted line represents the condition in which the transferred groove has the same dimension of the original one (L'=L). Thus, the dimension of the base

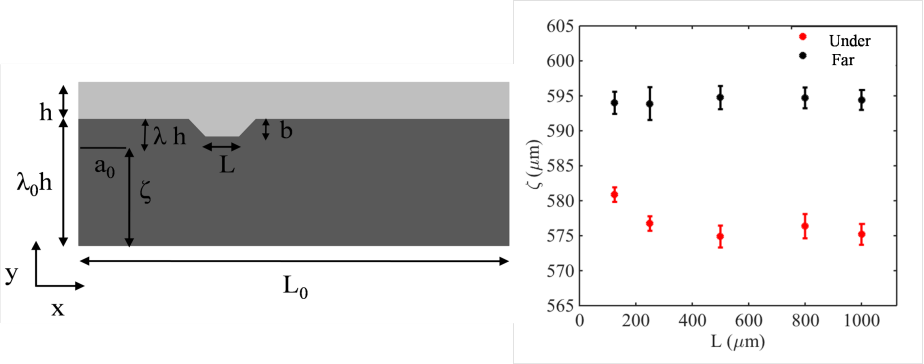

(a) (b)

Figure 6.10: (a) Geometry of the sample with the initial groove. The span of the specimen is 14 cm, the thickness of the Silicon substrate is $\lambda_0 h$=675 μm, the thickness of the aluminium is h=125 μm, the initial crack depth is λh=83 μm, the initial notch size is a_0=190 μm, the height of the groove is b=20 μm, the width of the groove is L. (b) Mean value of simulated crack path $\zeta = h(\lambda_0 - \lambda)$ far from the groove at the equilibrium (black dot) and in the region under the groove (red dot), where the error bars are given by the relative errors respect to the initial crack position.

of the groove is generally reduced.
Moreover, the cross-section area (see the sketch in Fig.6.13(a)) of the groove transferred on the parental substrate after the exfoliation with the initial one is compared in Fig.6.13(b). The black dots are the cross-section areas obtained from numerical simulation and the red dashed line is the linear fit. Thus, the results demonstrate that cross-section the area of the groove after exfoliation increases linearly with the dimension of the initial width of a groove.

Experimental validation

The samples used in the experimental tests have been realized in the Laboratory at the Institute for Solar Energy Hamelin. The shape of the groove is created in Silicon with a dicing saw and etching in Potassium Hydroxide (KOH) to remove defects from the surface, whose etch rate is strongly affected by the crystallographic orientation of the Silicon (anisotropic). The etching parameters used are: 50% of KOH concentration, temperature of 90°C and 2 min as the duration process. Afterwards, Aluminum is evaporated on top of the Silicon wafer as to see in Fig.6.14(a). The cross-section of the parental Silicon substrate after exfoliation is shown in Fig.6.14(b), where the black arrow indicates the center of the initial groove. The amplitude of the groove transferred on the substrate is reduced to about 76% after reuse, as it can be seen from Fig.6.14(b). The particular shape of the rough region can be the result of dynamic effects occurring during crack propagation that were not considered in the numerical simulations.

The the surface of the samples near the edge are examined in details since it is the part

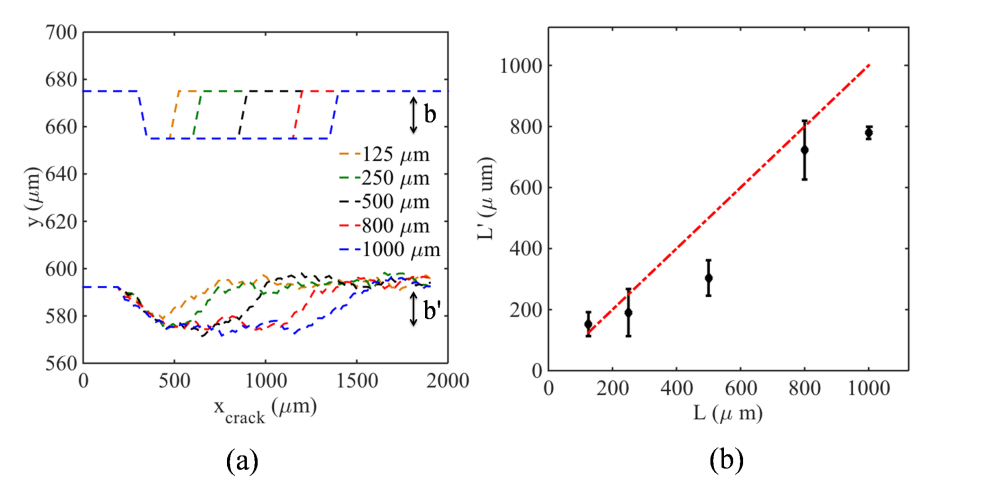

Figure 6.11: (a) On the top: sketch of the geometry of the initial groove along the Silicon-Aluminium interface. On the bottom: simulated crack path showing the effect of the initial groove after reuse.(b) Amplitude of the groove transferred on the substrate after crack propagation.

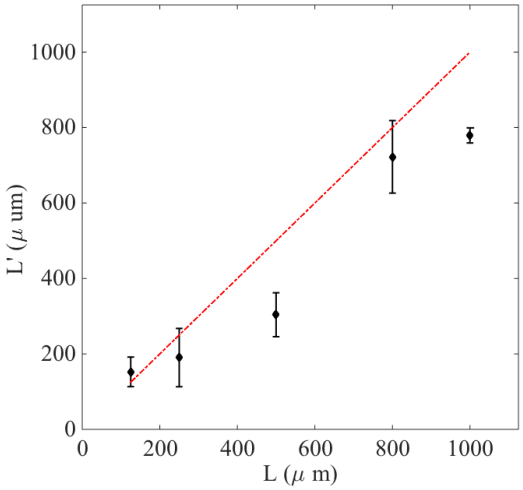

Figure 6.12: Width of the groove after the exfoliation *L*' vs. original width *L*.

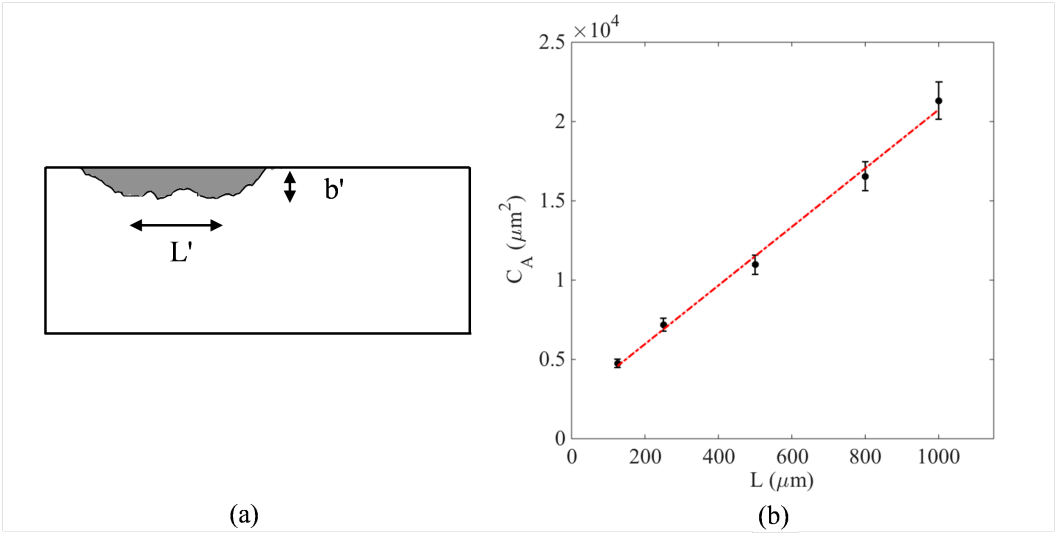

Figure 6.13: (a) Sketch of the removed cross-section area C_A (grey region) inside the parental substrate after the exfoliation with respect to the flat surface due to the presence of the groove, with hight b' and width L' transferred to the substrate. (b) Resulting cross-section area C_A (black dots) vs. width L of the groove. The red dashed line is the linear fit of the resulting data.

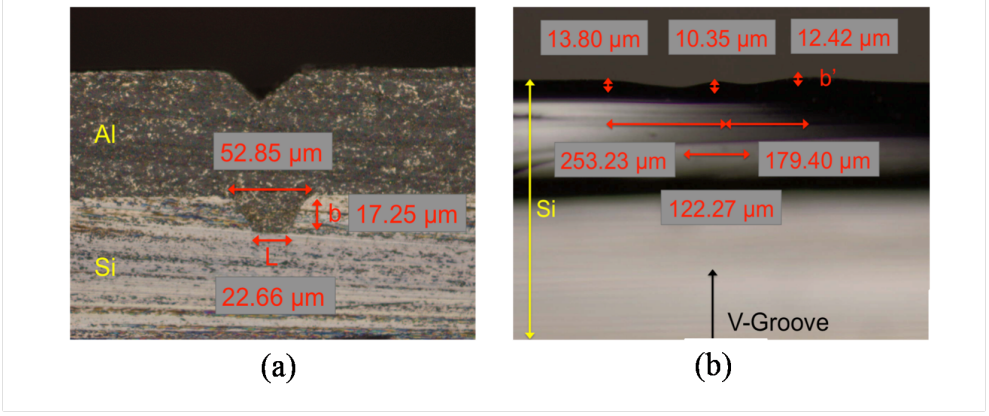

Figure 6.14: (a) Silicon and Aluminium bilayer with initial groove. (b) Cross-section of the Silicon parental substrate after exfoliation.

where the new process has to start. This region is also interesting because it has the largest differences in the heights, for two reasons. The former is the non ideal alignment of the laser cut, and the latter is due to the transient regime before the achievement of the steady state conditions for crack propagation for propagating crack from the initial notch. The surface measurements were carried out with the Leica DCM-3D, a contactless confocal profilometer available in the laboratory of the Research Unit MUSAM-Multi-scale Analysis of Materials at the IMT School for Advanced Studies Lucca. Fig.6.15(a) shows the surface of the initial region (5×1.5 mm) of a sample, with a whole dimension of 5×50 mm, where 5 important lines are identified. Lines from 1 to 3 are parallel to the $y-$direction, in particular the first is near the edge (x=500 μm), the second is in the first half of the sample (x=1500 μm), and the third one is in the middle of the sample (x=2500 μm). The line No.4 crosses the entire sample along the $x-$direction starting from y=750 μm. The last line, No.5, is oblique and it meets the edge of the samples. On the bottom of Fig.6.15, three additional graphs are shown with the profilometric section corresponding to the lines described above. The first of these three graphs (Fig.6.15(b)) shows the profile of the lines parallel to the $x-$direction. In particular, the dotted line No.1, is the nearest to the edge, has oscillation around its average value of 65.94 μm with a variance of 51.13 μm. In this region the crack has not reached the quasi-steady condition and the fluctuations are due to that reason. The dashed line corresponds to the profile No.2 and it shows a transient regime with very small fluctuations. Finally the solid line corresponds to the profile No.3 shows a smooth profile until the steady state conditions are met far from the edge. Herein the average is 62.03 μm and the variance 71.32 μm. The second diagram (Fig.6.15(c)) shows the heights along the profile line No.4. Herein is visible as the central part of the sample is very flat and the oscillations are localized only at the edges, with a global average elevation of 59.66 μm. The variation at the center is probably caused by a mismatch of the laser cut position at the two sides of the sample. The third graph (Fig.6.15(d)) shows the profile No. 5, where the oblique line has a mean value of 67.20 μm and a variance of 89.92 μm. Thanks to this measurement we can assume that also the resulting surface is mostly affected by a border roughness and the highest effect is taking place near the laser crack, probably due to local thermal heating.

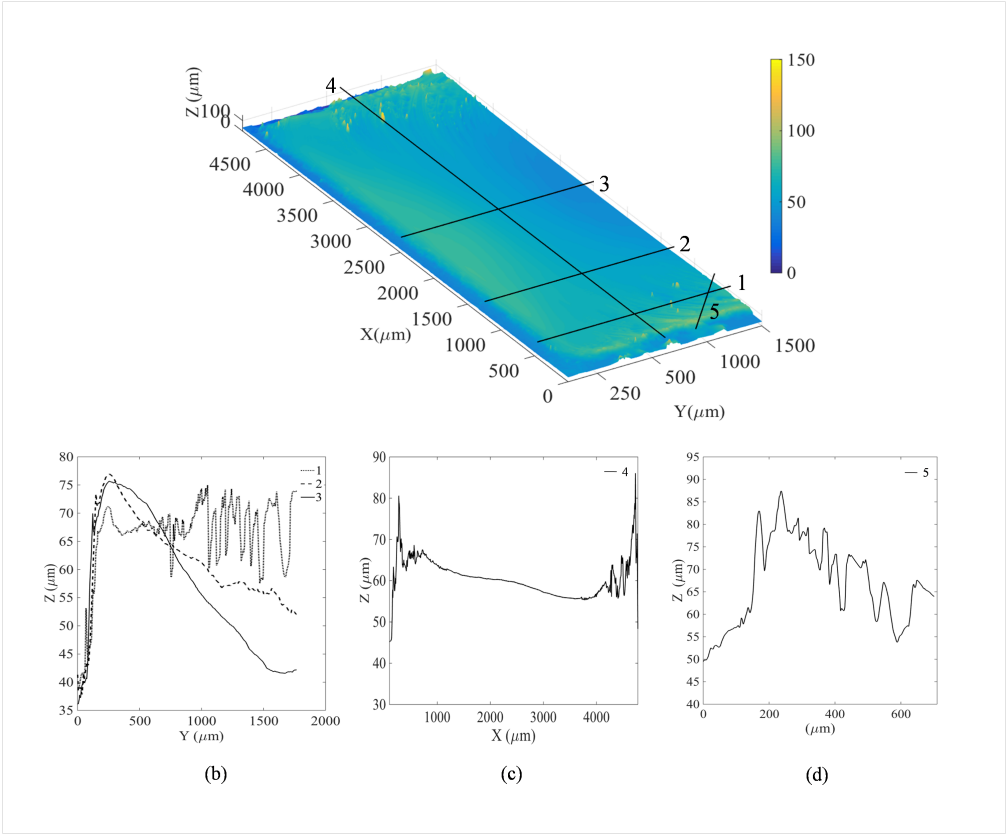

Figure 6.15: Top part: (a) the surface the initial region (5×1.5 mm) of a sample, with a whole dimension of 5x50 mm, where 5 significant lines are identified. Bottom part: (b) Lines 1-3 are parallel to the $y-$direction. (c) The line crosses the entire sample along the $x-$direction. (d) The last line is oblique and it matches the border of the sample.

Remarkable achievements proposed in this Section have been presented at the SiliconPV 2016 conference and submitted to Energy Procedia.

6.3.3 Experimental assessment of the Silicon fracture toughness

The Critical Stress Intensity Factor K_{IC}, used in Chapter 2, is considered as a material parameter. In the simulation presented in this Chapter, a value of $K_{IC} = 0.75$ MPa m$^{0.5}$ was deduced from literature for the Silicon in the <100> direction [179]. However, toughness of Silicon depends on its size as notice in [180], and it is for instance much higher at the microscale, see [181, 182, 183] for fracture in MEMS. Hence, the estimation of the proper value of K_{IC}

to be used is a challenging task. In this Section the results of an experimental campaign together with a numerical study to identify the value of K_{IC} of the monocrystalline Silicon used in wafer substrates are reported. For this particular case, the geometry of the specimens is rectangular as shown in Fig.6.16.

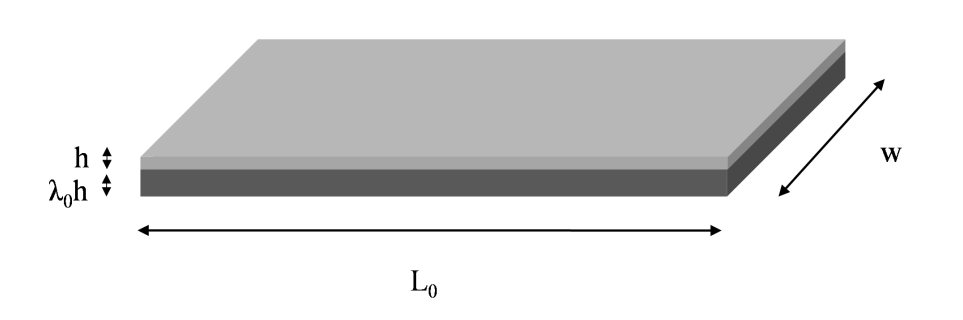

Figure 6.16: Tridimensional sketch of the rectangular sampled tested, where w is the width, L_0 is the length, $\lambda_0 h$ is the thickness of the Si substrate and h is the thickness of the Aluminum.

Different widths of the rectangular samples, w, are considered. The produced samples are immersed all together in the cooling bath up to 15 mm, with a velocity of 5 mm/s. The goal in this case is to identify the K_{IC} value by matching the experimentally exfoliation length measured for the different values of w.

Experimental campaign

The experimental test described in this Section have been carried out, during the period spent at the Institute for Solar Energy Research Hamelin, from August 2015 to January 2016. Thus, after the Aluminum deposition on Silicon achieved thanks to a thermal evaporation technique, wafers were cut with a dicing-saw. In every test run, three samples for each width were realized: 5 mm, 10 mm, 20 mm. The length of the samples was equal to L_0 = 50 mm. A series of laser cuts at a distance λh from the bi-material interface were made to the samples, see Fig.6.5. For each run, 9 samples were processed and, to ensure a simultaneous immersion of the samples in the cooling bath, a special clamping system was realized to fix them. The experimental setup is shown in Fig.6.17. In the figure the clamping with the sample, the lamp used to warm up the sample and the cooling bath are displayed.

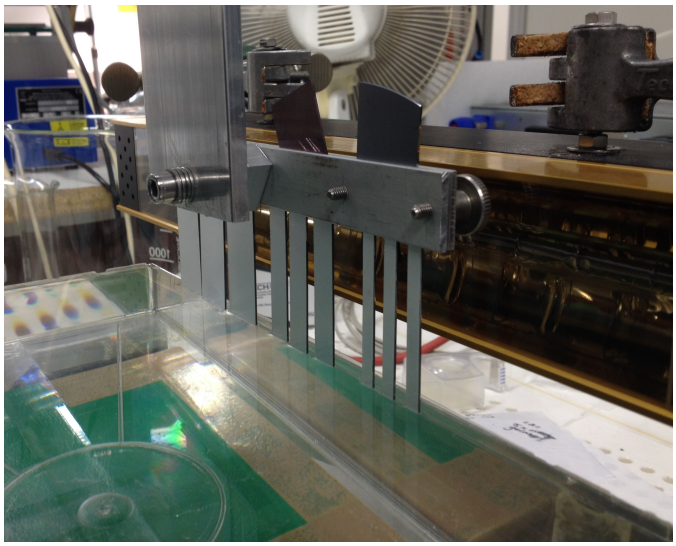

Figure 6.17: Experimental setup, where 9 samples are fixed to the clamping system and immersed simultaneously in the cooling bath.

The samples at the end of an exfoliation run are shown in Fig.6.18.
Tabs.6.3 and 6.4 summarize the significative results of this campaign. In particular, due to the final crack front, not always completely parallel, the exfoliation length on the right, l_{right}, and on the left side, l_{left} are reported respectively in Tabs.6.3 and 6.4.

Table 6.3: Exfoliation length for the first run.

w mm	Name	l_{right} mm	l_{left} mm
5	1	28.2	28.6
5	2	27.5	27.8
5	3	28.9	29.1
10	1	32.1	32.5
10	2	28.6	28.8
20	1	7.0	7.3
20	2	10.1	11.0
20	3	10.4	11.3

The exfoliation length as function of the width of the samples is shown in Fig.6.19 and Fig.6.20, where is possible to notice a decrease of the delamination length d, computed as the average between l_{right} and l_{left} by increasing the width of the sample.

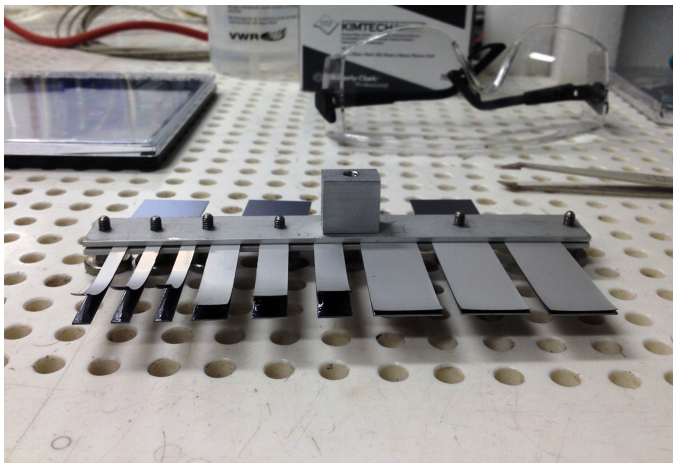

Figure 6.18: Exfoliated samples fixed to the clamping system after the immersion in the cooling bath.

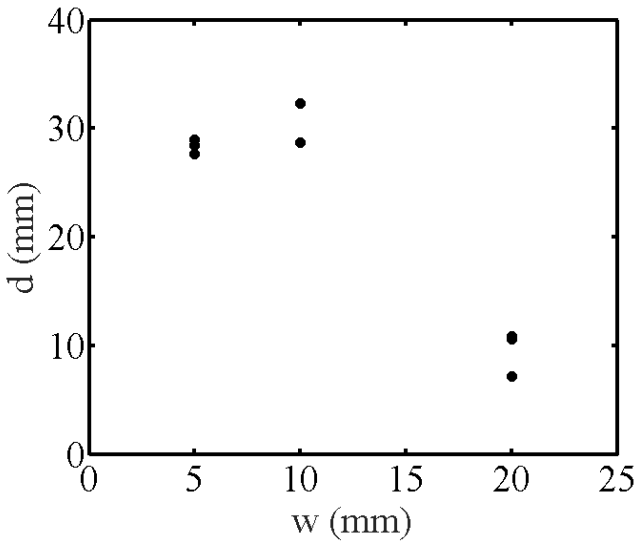

Figure 6.19: Delamination length for the first run.

Table 6.4: Exfoliation length for the second run.

w mm	Name	l_{right} mm	l_{left} mm
5	1	34.8	35.4
5	2	35.3	35.3
5	3	33.0	33.2
10	1	34.7	34.0
10	2	34.0	33.0
10	3	26.8	27.9
20	1	11.2	11.7
20	2	13.6	1.7
20	3	12.0	10.6

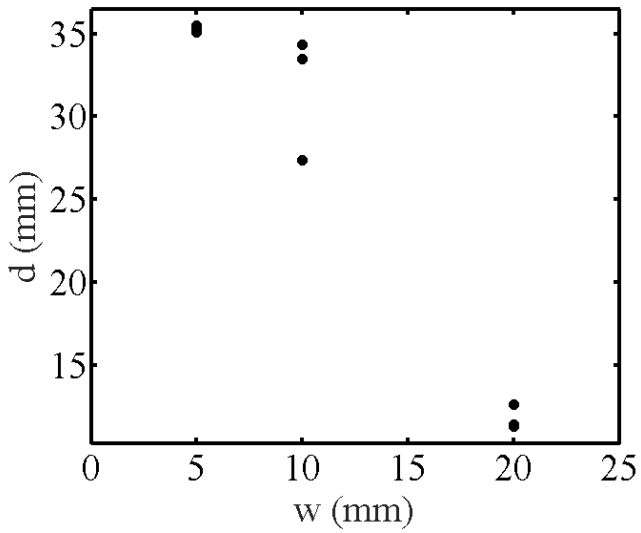

Figure 6.20: Delamination length for the second run.

The results obtained shown that the variance of the surface is not relevantly influenced from the width of the samples.

Numerical simulation

The Stress Intensity Factor for Mode I, in case of steady state condition, is a function of:

$$K_I = \frac{\Delta T}{w} f\left(\frac{a}{L_0}, \frac{l}{L_0}, \frac{h}{t}, \frac{\lambda h}{\lambda_0 h}\right) \tag{6.16}$$

where a is the crack length, $t = h(1 + \lambda_0)$ the thickness of the bilayer, L_0 is the length of the stripes equal to 50 mm, l is the part of the sample that is not immersed in the cooling bath. For the simulations, the geometry used is shown in Fig.6.21 and the parameters are the same as those reported in Tab. 6.1.

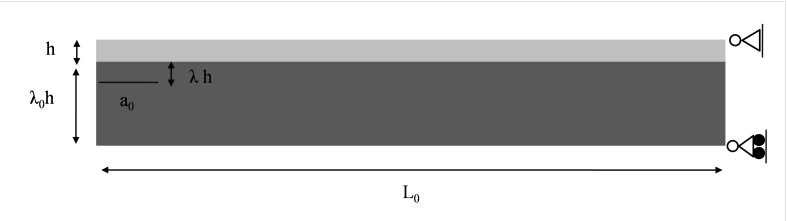

Figure 6.21: Geometry of the Si substrate with the evaporated layer of Al on the top of it, in a 2D configuration and clamped in x=50 mm. The parameter are the thickness of the Si layer $\lambda_0 h$ =675 μm, the thickness of the Aluminum layer h=120 μm, the initial notch length is a_0=190 μm and the span of the specimen is 50 mm.

The simulation results for K_I of run No.2 are shown together with the experimental ones for each series of samples shown in Figs.6.22, 6.23 and 6.24. In particular, the dotted line corresponds to the simulated Mode I stress intensity factor for a width w= 5 mm, the dashed line for w= 10 mm and the solid line for w=20 mm. The K_IC value of 0.75 MPa m$^{0.5}$ is reported in the graphs with a dashed-dotted horizontal line. Finally, $a_i = l_{i_{\mathrm{left,right}}}/L_0$ is the vertical lines corresponding to the normalized experimental exfoliation length (on the left and right side respectively) where i is the index for the width of the samples. Two lines for each a_i are reported because, especially in the wider samples, the crack arrested not with a front parallel to the section, see Figs.6.19 and 6.20. The intersection between the vertical line obtained from the experiment the corresponding simulation curve provides the identified value of K_IC. While the results for w=5 mm and w=20 mm show a good agreement with K_IC=0.75 MPa m$^{0.5}$, the case of w=10 mm has a higher variability. Hence, from this results, the actual K_IC value for the tested material is comprised in the range from 0.397 MPa m$^{0.5}$ to 0.980 MPa m$^{0.5}$.

6.3.4 Influence of the immersion velocity

The aim of this Section and of the experimental campaign, whose results are herein summarized, is the study of the influence of the immersion velocity during the spalling process on the sample roughness and on the exfoliation length. We started from the results presented in [41] where the optimal immersion velocity was found to be equal to 5 mm/s by a trial and error procedure. Indeed, they noticed more than a crack front with low velocity (1 mm/s), because the condition for crack propagation are met at the same time in different positions in the sample. With this purpose we carried out a wider campaign to evaluated if it is possible to achieve the same results on samples with a rectangular shape. For this aim, we realized rectangular bilayer with a dimension of 5 mm $\times$ 50 mm. The velocities tested were 3 mm/s,

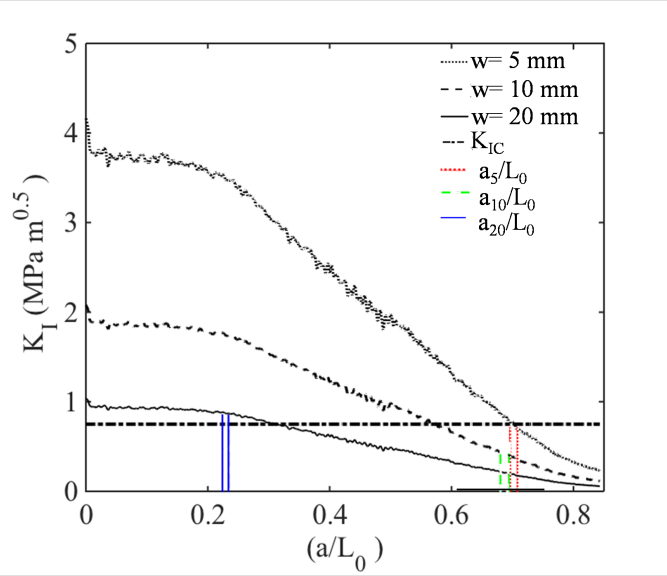

Figure 6.22: Simulation of the propagation process combined with the experimental results of the first set of samples of run No.2.

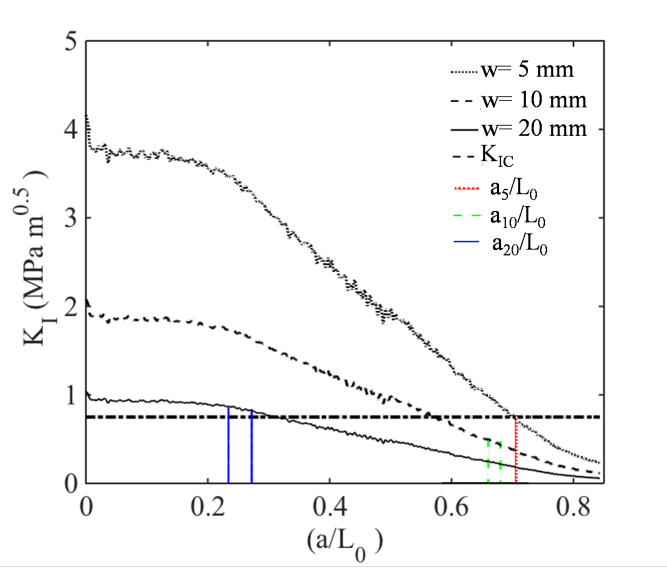

Figure 6.23: Simulation of the propagation process combined with the experimental results of the second set of samples of run No.2.

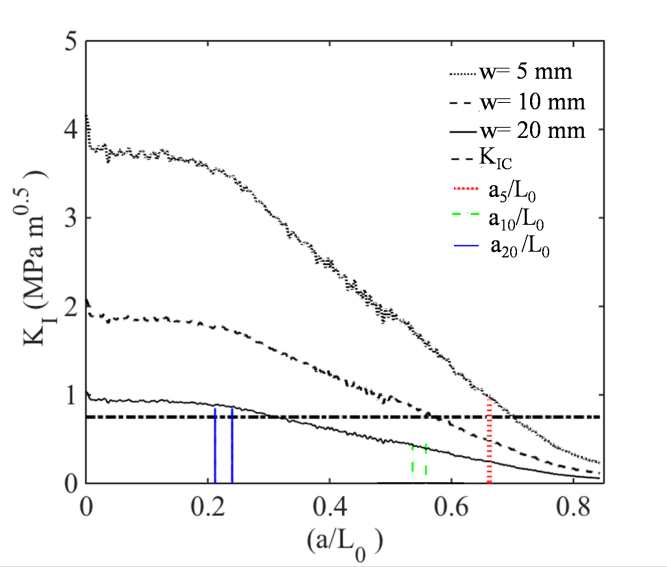

Figure 6.24: Simulation of the propagation process combined with the experimental results of the third set of samples of run No.2.

5 mm/s and 10 mm/s. The delamination length achieved, d, is shown in Fig.6.25 as a function of the tested velocities where for each sample two values corresponding to l_{left} and l_{right} are reported. It comes out that, except for the case of 3 mm/s, the sample are not significantly influenced by the velocity of immersion. The velocity of 5 mm/s shows the maximum delamination length, with low variability, for the some imposed temperature excursion.

The confocal profilometer described in Section 6.3.2 is also used to have a closer look at topography of the surface of the exfoliated layer. Two interesting regions are examined: the center and the right side, see the sketch in Fig.6.26.

In the following figures (Figs.6.27, 6.28, 6.29) the surface topographies of the center and right side regions of the samples, for corresponding velocities are displayed. The surface topographies show a small variation of the heights in the center of the sample, with Δz of about 4 μm.

From the measurements the variance of the surface heights is also computed and correlated to the to velocity of immersion, for the central portion (Fig.6.30) and lateral portion of the samples (6.31).

The variance σ^2 in the central region is almost the same in the two test (high reproducibility of the phenomenon) and it is almost independent of v. The variability of the variance is less than 0.25 μm^2. A different trend is noticed for the right side, with a high variability of σ^2 from sample to sample and a general increase of σ^2 by increasing the velocity of immersion.

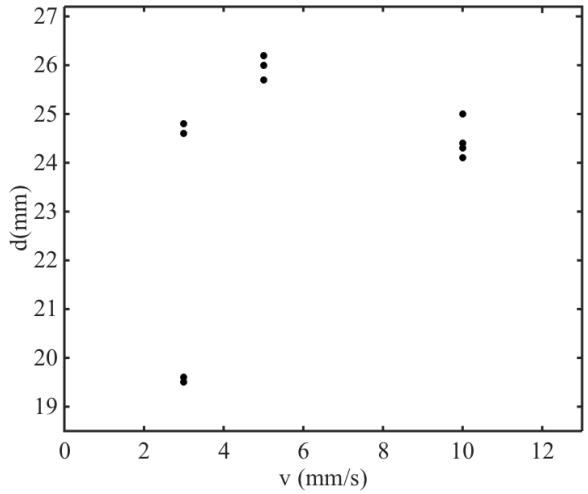

Figure 6.25: Delamination length for three different velocities.

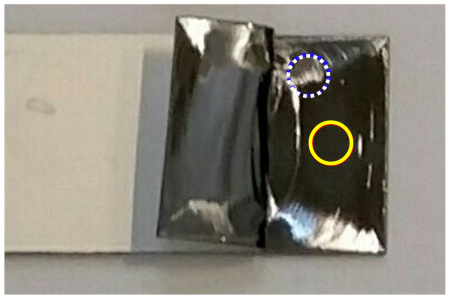

Figure 6.26: Photo of the measurement positions on a sample with dimension 5×50 mm. The yellow circle with solid line corresponds to the center and the white circle with dashed line is the right side of the sample.

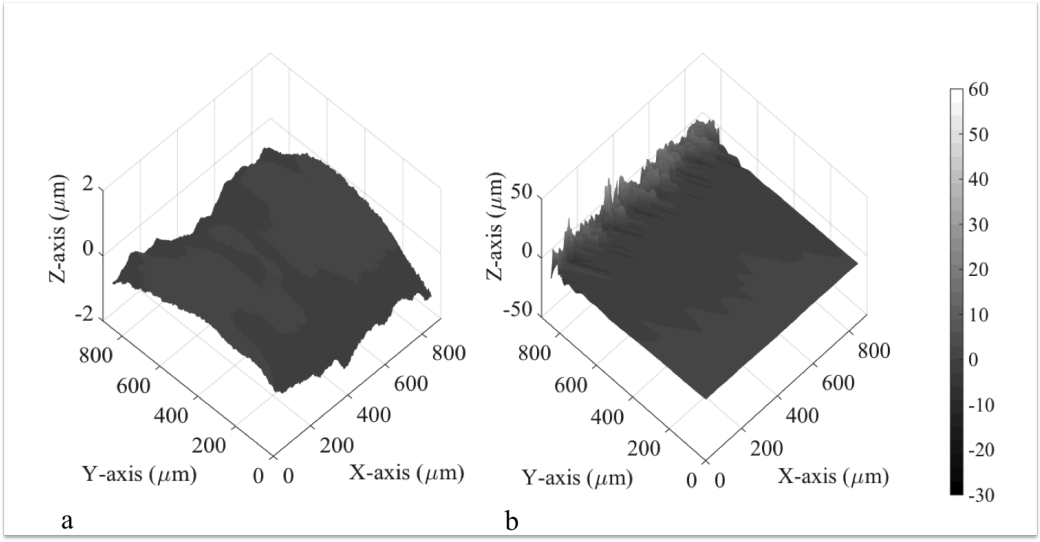

Figure 6.27: Surface topography of a sample with width of 5 mm in the center (a) and right side (b). This sample was exfoliated with a velocity of immersion of 3 mm/s.

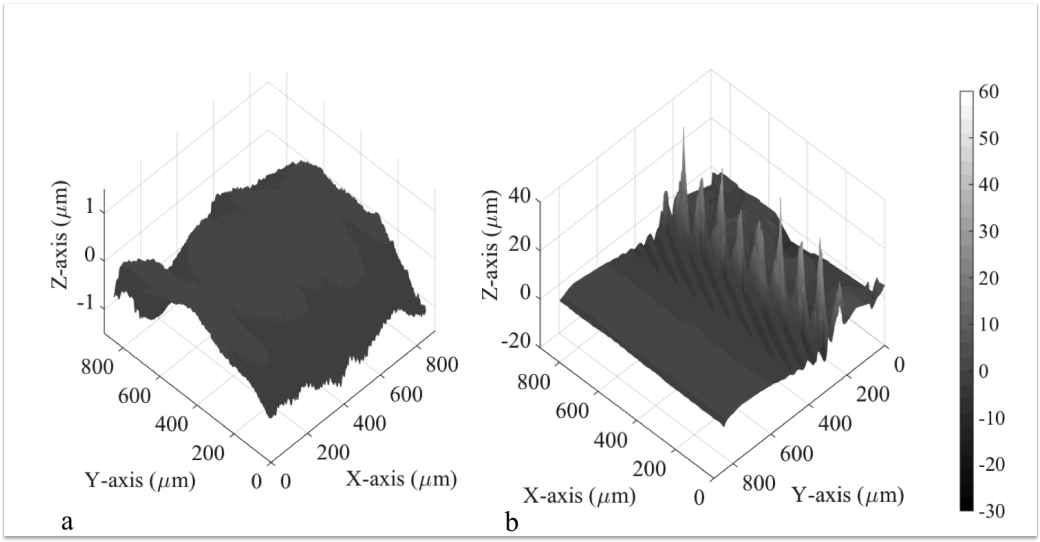

Figure 6.28: Surface topography of a sample with width of 5 mm in the center (a) and right side (b). This sample was exfoliated with a velocity of immersion of 5 mm/s.

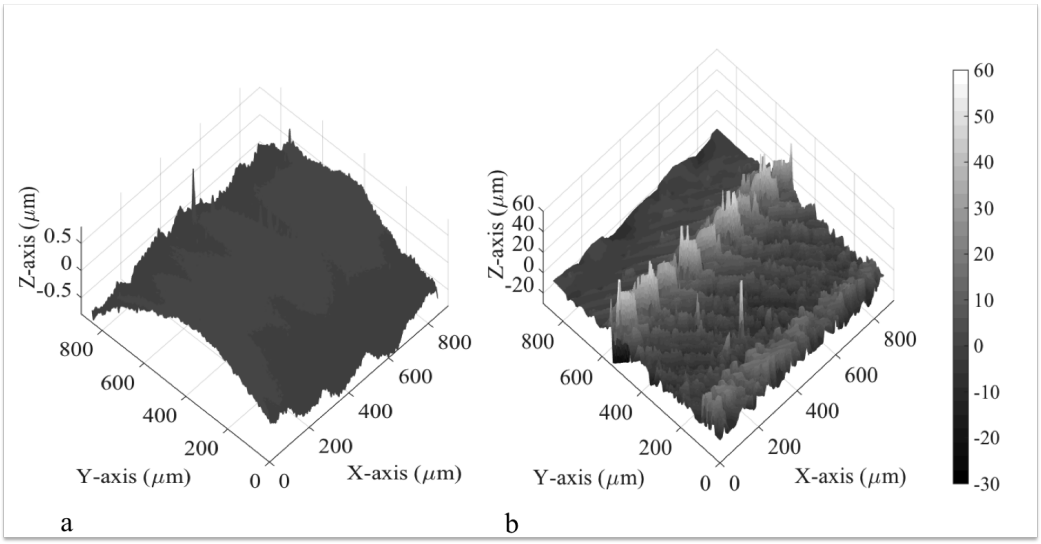

Figure 6.29: Surface topography of a sample with width of 5 mm in the center (a) and right side (b). This sample was exfoliated with a velocity of immersion of 10 mm/s.

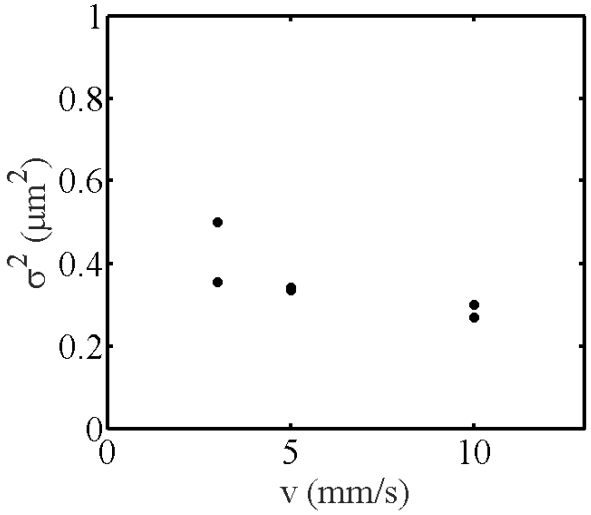

Figure 6.30: Variances of the heights for the central part of the exfoliated layer.

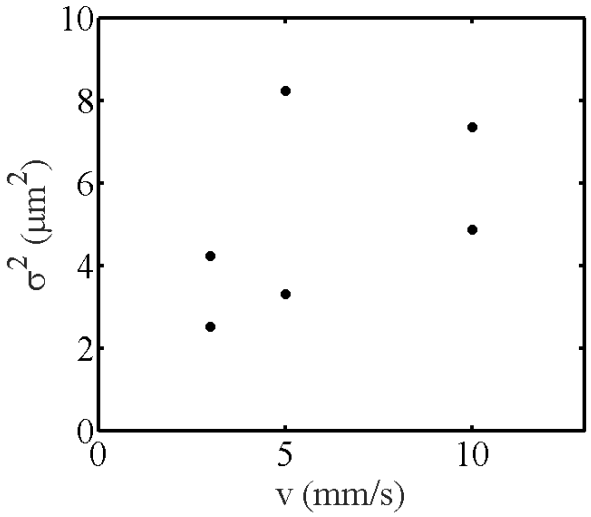

Figure 6.31: Variances of the heights for the right side of the exfoliated layer.

6.4 More advanced morphological characterization

This Section summarizes the most relevant results of the topography analysis of the delaminated Silicon layers. Studies on the roughness of surfaces are of interest for engineers and physicists due to the relevance of this topic in tribology. Indeed rough surfaces have property of randomness, i.e. they appear disordered and irregular [184, 185, 186, 187, 188]. Surface textures were typically measured by contact profilometers, where a stylus moves over the surface. In this way, the continuous function of heights, $z(x)$, was sampled at discrete intervals of length, δ, obtaining a discrete curve $z(x_i)$, where i = 1,..., N =L/δ, and N is the total number of sampled heights.
The statistical analysis of the delaminated surfaces is herein performed with the code proposed in [189]. This code is able to perform 2D and 3D statistical characterizations of the height field. Starting from the histogram data, it is possible to compute the statistical distribution of the profile heights and all the statistical parameters (mean value, root mean square value, skewness and kurtosis). In addition, it identifies the peaks as the local maxima of the profile. The profile slopes and the peak curvatures are computed via standard finite difference schemes from the elevations and the corresponding statistical distributions and their parameters are evaluated. In the 3D analysis, asperities, whose shape is assumed to be elliptical, are identified according to the method proposed by Greenwood [190]. It is based on the computation of the principal curvatures κ_1 and κ_2 at any surface height:

$$\kappa_1 = \begin{cases} -2\dfrac{-z_{i-1,j} + 2z_{\mathrm{i,j}} - z_{\mathrm{i+1,j}}}{-x^2_{\mathrm{i\text{-}1,j}} + 2x^2_{\mathrm{i,j}} - x^2_{\mathrm{i+1,j}}} & \text{if} \quad z_{\mathrm{i,j}} > z_{\mathrm{i\text{-}1,j}}, z_{\mathrm{i,j}} > z_{\mathrm{i+1,j}} \\ 0 & \text{otherwise} \end{cases} \tag{6.17}$$

$$\kappa_2 = \begin{cases} -2\dfrac{-z_{\text{i-1,j}} + 2z_{\text{i,j}} - z_{\text{i+1,j}}}{-y^2_{\text{i-1,j}} + 2y^2_{\text{i,j}} - y^2_{\text{i+1,j}}} & \text{if} \quad z_{\text{i,j}} > z_{\text{i-1,j}}, z_{\text{i,j}} > z_{\text{i+1,j}} \\ 0, & \text{otherwise} \end{cases} \tag{6.18}$$

The geometric mean curvature is the computed as: $\kappa = \kappa_1\kappa_1$. This definition is useful for distinguishing between maxima and saddle points of the surface. Indeed using Eqs.(6.17) and (6.18), all the cases where κ is different from zero identify asperities. The code proposed in [189] provides the first three moments of the spectral density function, i.e. the variance of the asperity heights, m_0, the variance of the profile slopes, m_2, the variance of the asperity curvatures, m_4 , and the bandwidth parameter α defined as $m_0 m_4/m_2^2$. The three moments concern the statistical properties determined from the empirical distribution functions computed for a given finite sampling interval δ different from zero.

Starting from these parameters, it is possible to compute the dimensionless asperity heights $s = \frac{z}{\sqrt{m_0}}$ and the dimensionless asperity geometric mean curvatures $g = \frac{\kappa}{\sqrt{m_4}}$. The analysis code presented in [189] allows the computation of the joint probability distribution functions (PDFs) of asperity heights and curvatures of rough surfaces. In addition to the statistical characterization, the code is also able to characterize the spectrum of the surface and therefore possible *fractality*. This phenomenon manifests itself in the following features [191]:

- The statistical self-similarity of crack configurations, whose metric dimension does not correspond to D the topological one. Usually it has the fractional value which is given by the Hausdorff-Besicovitch metric dimension [192];
- The multifractality of the spatial distribution of defects, pores, and cracks in a deformed medium [192, 193, 194, 195] and the power laws of their size distributions [196, 197];
- The scaling invariance of pore dimension and cracked surfaces in solids [192, 193, 194, 196, 197] .

The methods for determining the fractal dimension of the crack surface reviewed in [132] are three:

- Slit Island Analysis (SIA)
- Methods of Vertical Sections (MVS),
- Fourier Analysis of the Distribution Profiles (FAP).

The results presented in this paragraph are obtained via Fourier Analysis of the Distribution Profiles. The determination of the fractal dimension of statistically surfaces by the FAP method is based on the spectrum of the profile power (the sum of the amplitudes squared). The power spectral density functions (PSD) of the surface profiles is evaluated according to a fast Fourier transform of the related height fields [198].
The PSD is computed here in two orthogonal directions, averaging over all the surface profiles. The orientation adopted is either generic in case of isotropic surface or *ad hoc* along specific directions of anisotropy identified by optical or scanning electron microscopy. In

case of a fractal surface, the profile PSDs are expected to have a power-law dependency on the frequency ω [199] as follows:

$$\Phi = G^{2D_p-2}\omega^{-(5-2D_p)} \tag{6.19}$$

where $1 < D_p < 2$. From the linear fit of the PSD function in a bi-logarithmic plane, the code proposed in [189] evaluates the parameters D_p and G. For isotropic surfaces, the fractal dimension is computed as $D = D_p + 1$. The statistical parameters described above are plotted vs. the velocity of immersion of the tested specimen for the central and right side of the sample in Fig.6.32 and Fig.6.33, respectively. In the center, m_0 and α show a slight decrease by increasing v, while m_2 and m_4 increase with the velocity of immersion. The statistical parameters related to the right side of the sample instead show an increase of all the moments (m_0, m_2 and m_4) with the velocity, whereas the bandwidth parameter α decreases by increasing the immersion velocity.

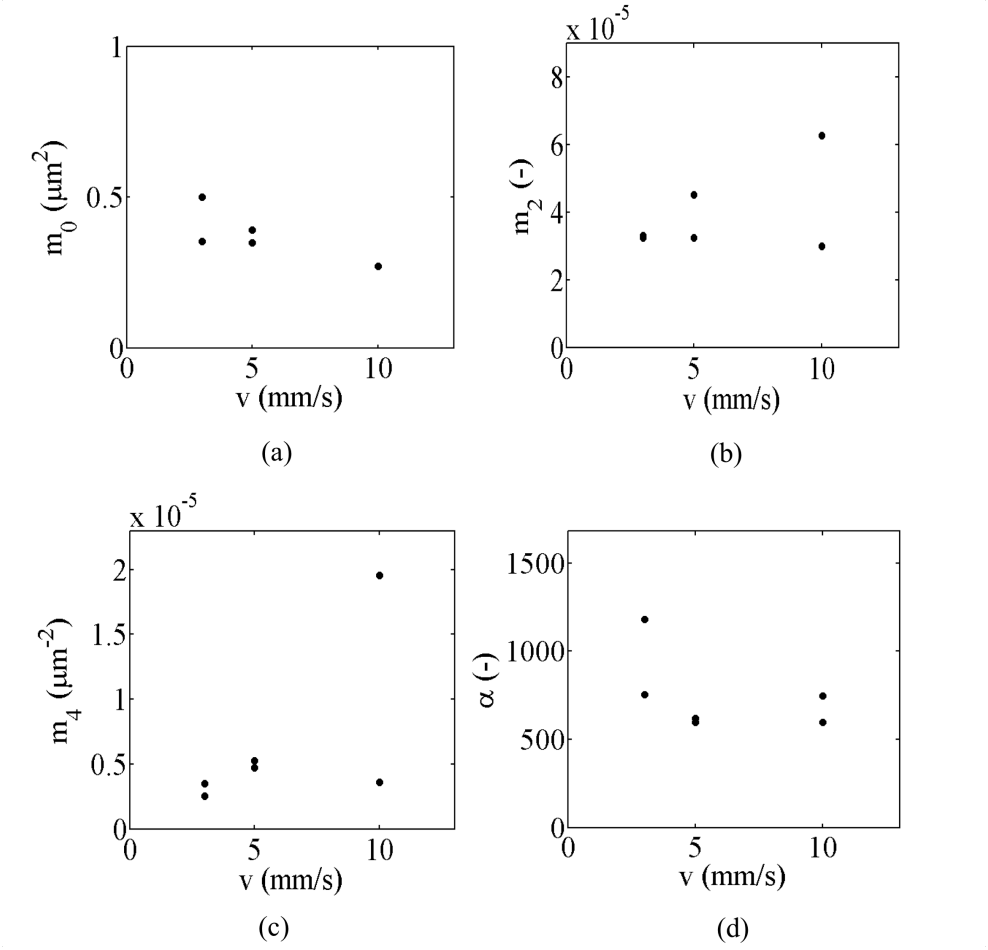

Figure 6.32: (a) Variance of the asperity heights m_0, (b) variance of the profile slopes m_2, (c) variance of the summit curvatures m_4 and (d) bandwidth parameter α in function of the velocity of exfoliation in the center of the sample.

A similar analysis is performed in relation to the different width w of the samples see the test obtained Section6.3.3. Figs. 6.34 and 6.35 show the statistical parameters above as functions of the width for the central and the right parts of the sample, respectively. For the central part, m_0, m_4 and α have a slight decrease by increasing w, while m_0 is almost constant . In the right side of the samples, m_0, m_2 and m_4 are increasing functions of the width, whereas the bandwidth parameter shows a decreasing trend, see Fig.6.35.

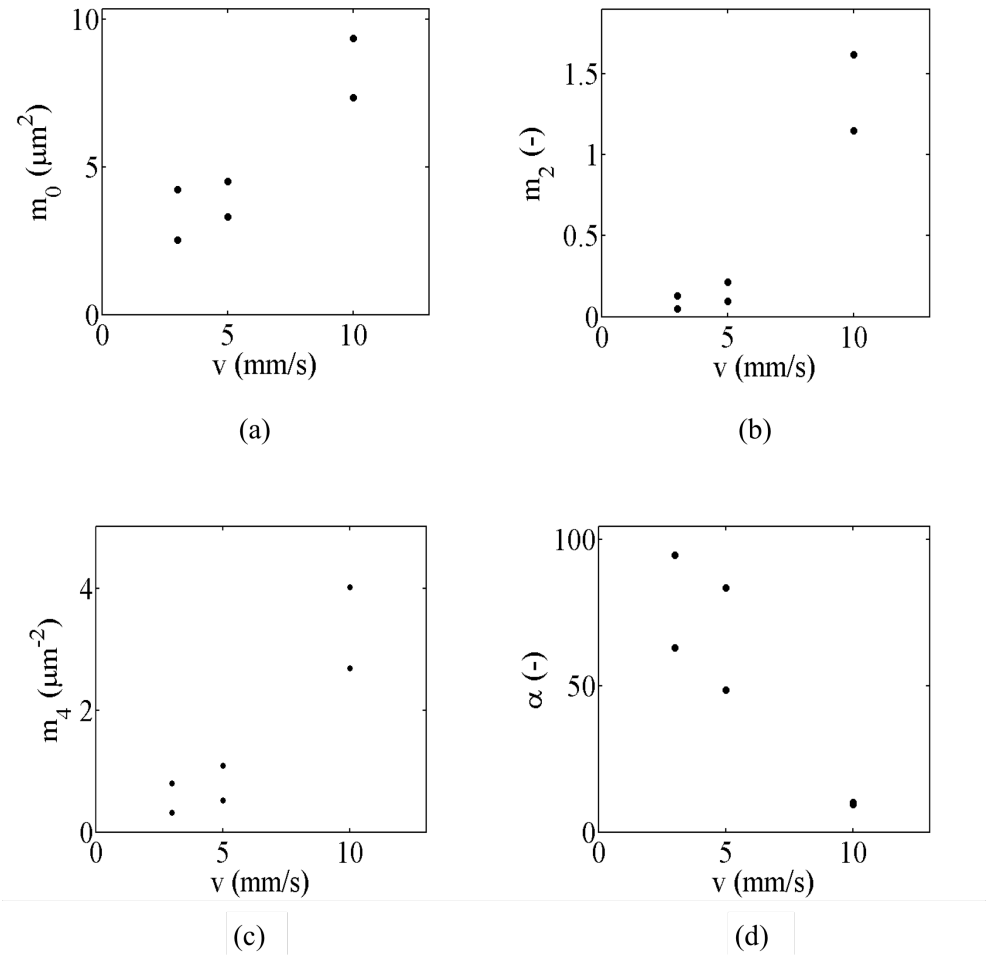

Figure 6.33: (a) Variance of the asperity heights m_0, (b) variance of the profile slopes m_2, (c) variance of the summit curvatures m_4 and (d) bandwidth parameter α in function of the velocity of exfoliation for the right side of the sample.

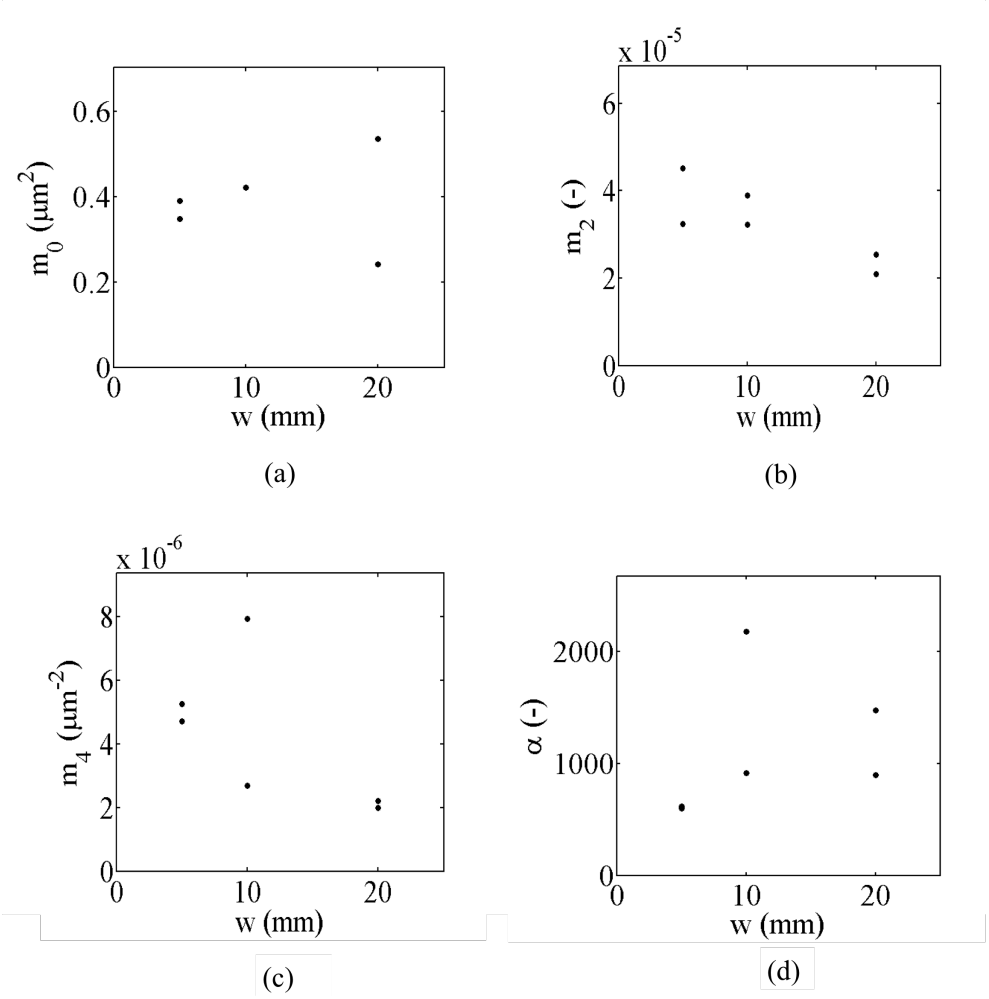

Figure 6.34: (a) Variance of the asperity heights m_0, (b) variance of the profile slopes m_2, (c) variance of the summit curvatures m_4 and (d) bandwidth parameter α in function of the width of exfoliation in the center of the sample.

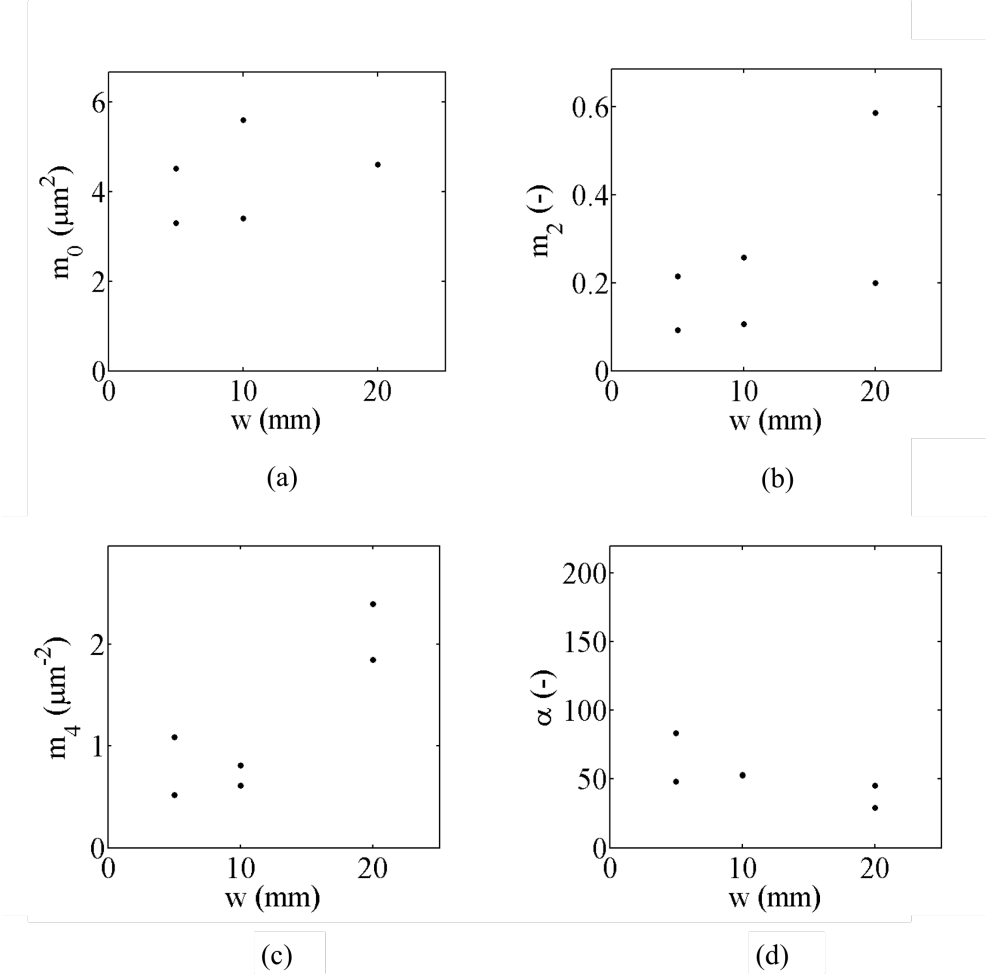

Figure 6.35: (a) Variance of the asperity heights m_0, (b) variance of the profile slopes m_2, (c) variance of the summit curvatures m_4 and (d) bandwidth parameter α in function of the width of exfoliation for the right side of the sample.

Finally, the PSD curves for the central and the right side region of the sample 5 mm wide exfoliated with a velocity of immersion of 5 mm/s are shown in Figs.6.36 and 6.37, respectively. From the PSD it is evident the presence of spikes at specific frequencies. They correspond in the spatial space, with a periodic nature. These waves in the spatial space are also visible by optical measurements performed with the confocal profilometer, see Fig.6.38.

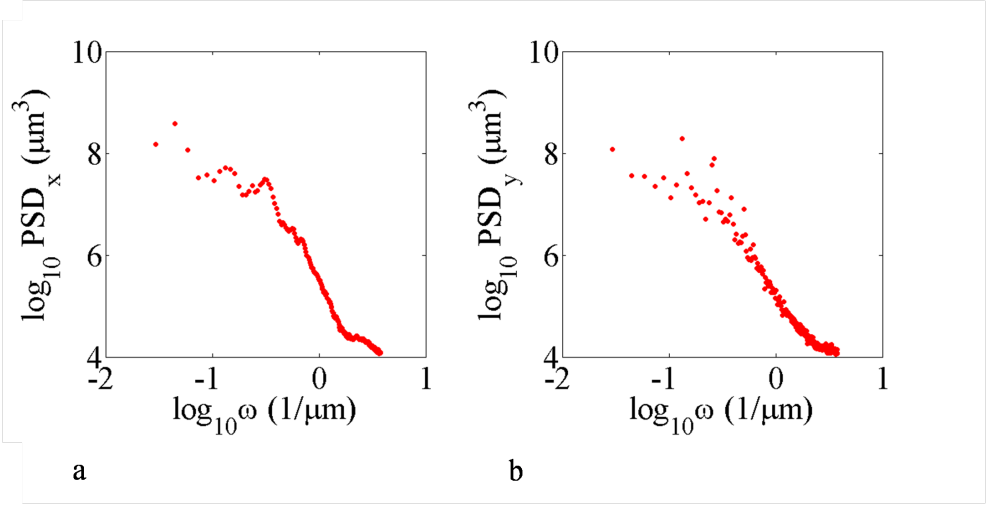

Figure 6.37: PSD curves for the right side of a sample with w= 5 mm and v=5 mm/s in the $x-$direction (a) and in the $y-$direction (b).

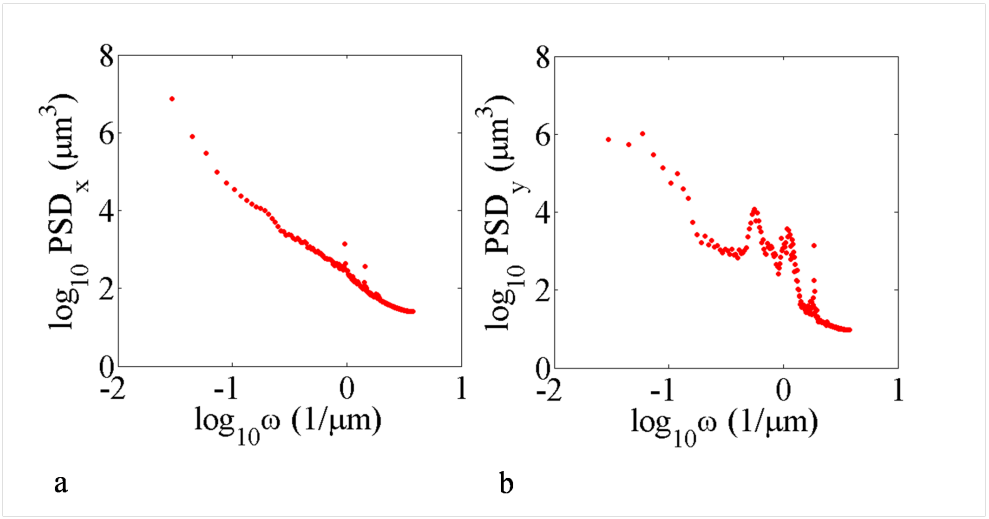

Figure 6.36: PSD curves for the central part of a sample with w= 5 mm and v=5 mm/s in the $x-$direction (a) and in the $y-$direction (b).

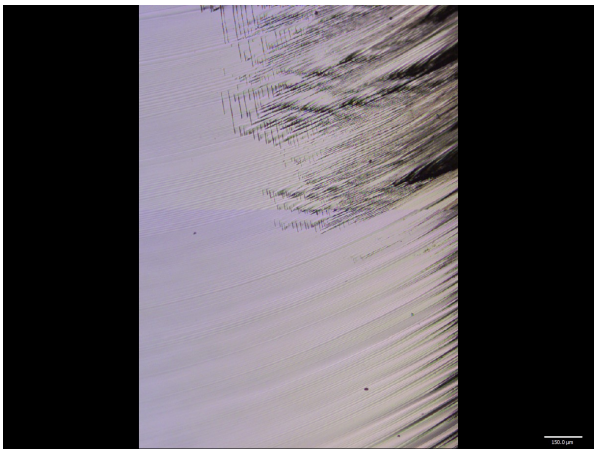

Figure 6.38: Optical measurement on a sample 5 mm wide and exfoliated using a velocity of immersion of 5 mm/s.

By fitting the PSD curves in the linear part, the fractal dimension for each surface is obtained. The Fractal dimension is function of the velocity and of the width, as shown in Figs.6.39 and 6.40, respectively, with two opposite trends: D decreases with the velocity and increases with the width.

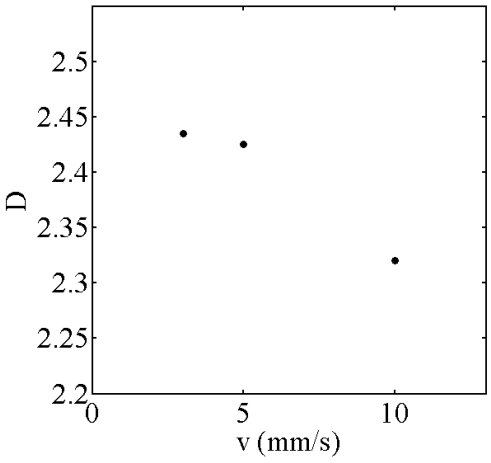

Figure 6.39: Fractal dimension in function of the immersion velocity for samples with width w= 5 mm.

It is possible to conclude, from the experimental results, that the analyzed velocities have

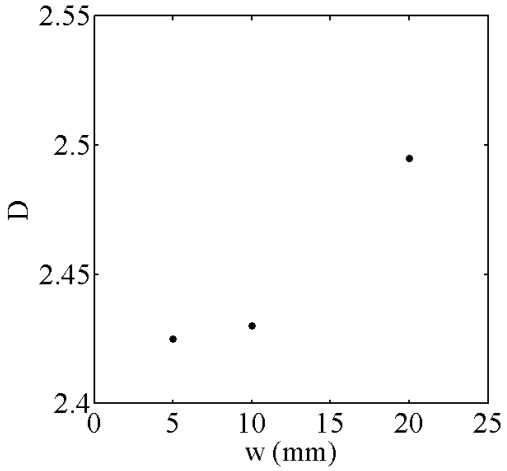

Figure 6.40: Fractal dimension in function of the width for the immersion velocity v= 5 mm/s.

a slight impact on the surface of the exfoliated layer and in addition that the variability of the statistical parameters in the central part of the sample is not particularly relevant, also in the case of the rectangular shape. Thus, together with the results of Section 6.3.2, the computed variance gives good prospective for the re-use of the thicker Silicon substrates.

Chapter 7

Conclusions

In this dissertation two important fields of photovoltaics have been investigated. The former has been the durability of PV modules and the latter the reduction of production costs of thin film Silicon for the production of solar cells. The main focus has regarded the proposal of experimental diagnostic techniques and interpretative models based on linear and nonlinear fracture mechanics for studying the phenomena of fracture in Silicon photovoltaics.
In Chapter 2 the formulations concerning the Linear Elastic and Nonlinear theories for fracture mechanics of quasi-brittle materials as Silicon have been summarized.
In Chapter 3 the mathematical formulation for a mono-dimensional electric model, applied to cracked solar cells, has been proposed. It has also been extended to the case of localized and distributed resistances in mono-Si solar cells, in case of poly-Si and finally to simulate a complete EL image of a solar cell. The aim of the originally proposed electric models concerned with the development and the use of techniques for a quantitative analysis of the electroluminescence signal to detect and quantify the effect of cracks in Silicon caused by mechanical loads on the electric power output.
The experimental results regarding the proposed electric models have been presented in Chapter 4. These experimental data have been acquired during an extensive experimental campaign conducted in the Laboratory of the Department of Structural, Geotechnical and Building Engineering of Politecnico di Torino and also in collaboration with the Laboratories of the Applied Materials Italia s.r.l. of Treviso.
Thanks to that, the validation of the electrical model presented in Chapter 3 has been achieved together with the assessment of the coupling between the electric field and the mechanical one. One of the main results achieved in Chapter 4 regards the identification of the relation between the crack resistance and the crack opening, see Fig.7.1. This is expected to be extremely important for future application of the relation as a constitutive law for the crack coupling the electric field with the mechanically induced deformation.

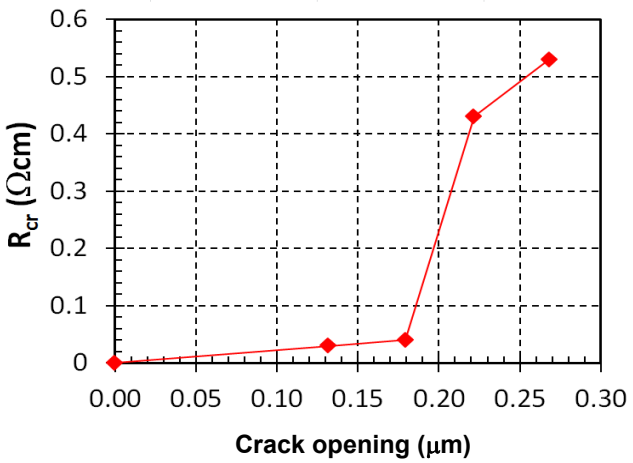

Figure 7.1: Correlation between localized crack resistance and crack opening.

Moreover, two electric models, one with local resistance (LR) and the other with discrete resistance (DR) have been compared. Results have shown that the model RD is the most accurate to reproduce the experimental trend in cracked monocrystalline Si solar cell, see Fig.7.2. Finally, the electric model in case of polycrystalline Silicon has been validated by describing the inhomogeneities due to defects and grain boundaries as an additional random resistance contribution. Different results have been reached in case of the realistic thermo-hygrometric tests, see Fig.7.5.

Concerning environmentally-induced degradation phenomena, the humidity corrosion and the artificial weathering effects have been investigated through an extensive experimental campaign in the Laboratory of the Department of Structural, Geotechnical and Building Engineering of Politecnico di Torino, considering different types of defects detected by EL measurements. The key results have been presented in Chapter 5. The degree of degradation in case of tests based on IEC 612115 standards was much higher than in case of realistic thermo-hygrometric cycles.

The evolution of the EL signal, in case of tests based on IEC 612115 standards, has shown dimmer tones due to moisture diffusion and a significant degradation of the central cell triggered by the presence of a crack, see Fig.7.3. The EL images shown in Fig.7.3 are related to a mini-module as received (a); after 200 cycles (b); after 400(c) cycles and finally after 500 cycles (d).

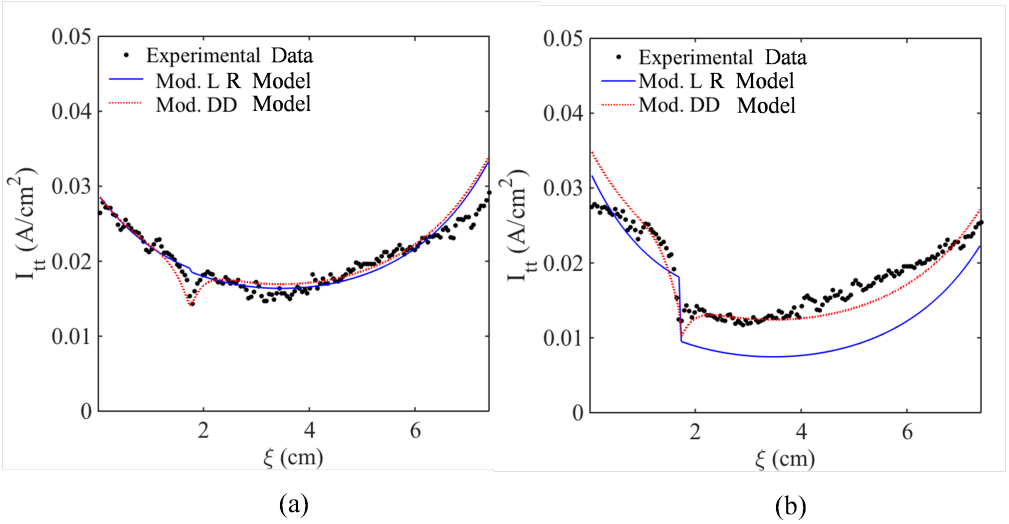

Figure 7.2: Comparison of the current through the thickness of the solar cell obtained with the two electric models vs. position along the finger for (a) the undeformed and (b) the deformed configuration.

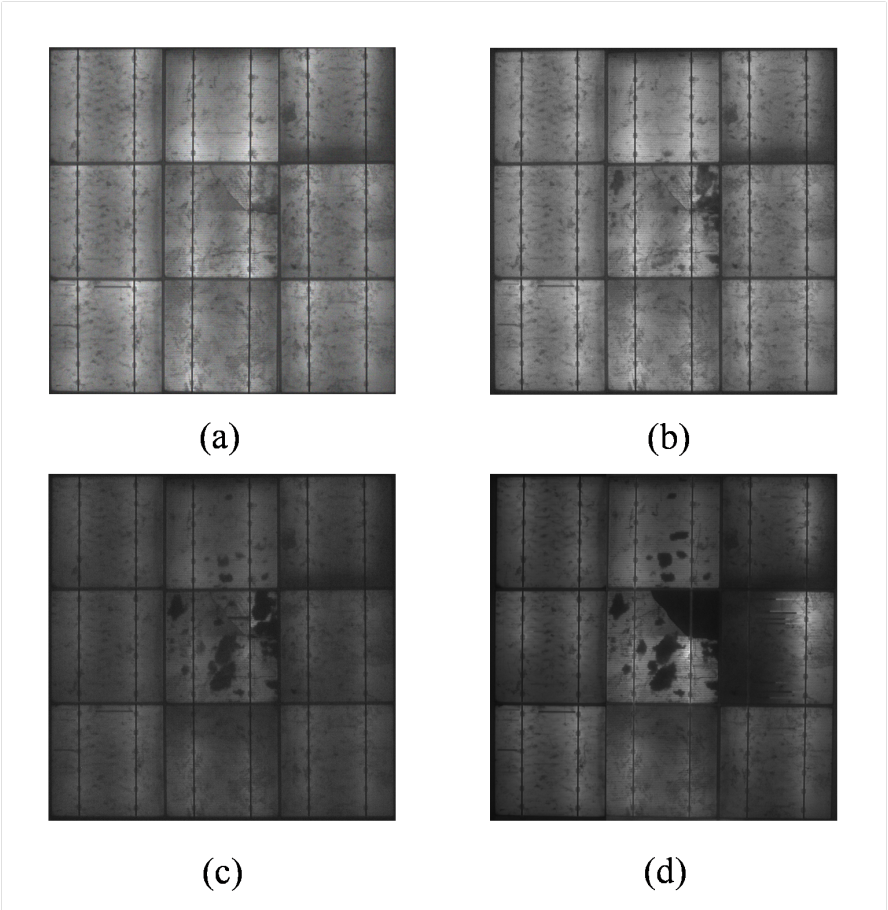

Figure 7.3: Evolution of the electroluminescence signal for a PV module as received (a); after 200 cycles (b); after 400 (c) cycles and finally after 500 cycles (d) according to the IEC 612115 specifics.

The resistance due to the degradation effects had a significant increase especially after the cycle 300, as Fig.7.4 shows.

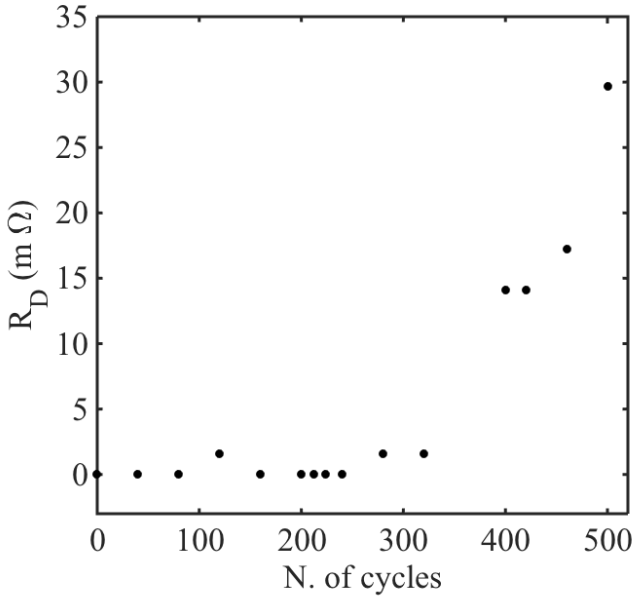

Figure 7.4: Resistance due to the degradation vs. number of cycles for module No.1.

Different results have been reached in case of the realistic thermo-hygrometric tests, see Fig.7.5.

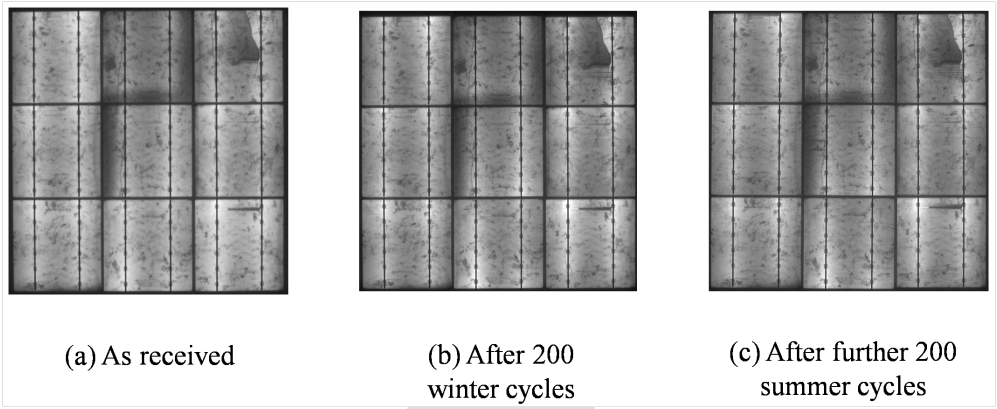

Figure 7.5: Evolution of the electroluminescence signal for a PV module in case of realistic thermo-hygrometric tests.

Thus, tests based on IEC standards appear to provide results quite far form those obtained under realistic ambient conditions. Nevertheless, in recent years thanks to the damp heat test cycle the improving of the PV module has been possible.
In Chapter 6 the study of an innovative methodology to produce thin layers of Silicon, starting from a parental substrate that is split into many thinner wafers, has been presented [165, 166, 161]. Remarkable results have demonstrated the importance of the thermal control on the spalling process to achieve a smoother surface. The additional studies on the re-use issue, linked to the roughness of the surface, have exhibited the feasibility of a multiple-reuse of the parental substrate thanks to the reduction of the resulting transferred roughness. Indeed, the amplitude of the discontinuity transferred to the Si substrate after the exfoliation in the y-direction (b') remains in the same order of magnitude as the depth of the groove at 20 μm before the first exfoliation, see Fig.7.6.

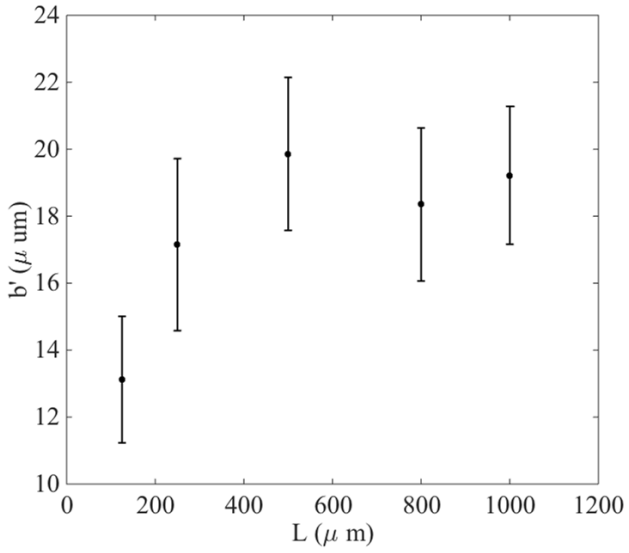

Figure 7.6: Amplitude of the discontinuity transferred to the Si substrate after the exfoliation in the $y-$direction (b') vs. original width L.

The same behavior has been shown for the dimension of the transferred base of the groove, which is generally reduced compared to the original one (see Fig.7.7).

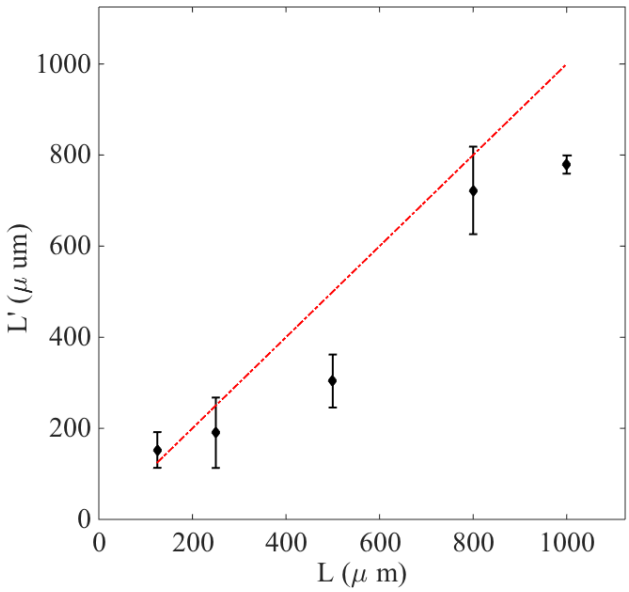

Figure 7.7: Width of the groove after the exfoliation *L*' vs. original width *L*.

A cost estimation of solar cell production based on the analyzed kerf-less technology developed at the Institute for Solar Energy Research Hamelin was presented in [200]. The cost of the solar cell produced with this particular kerf-less technology, called which stands for MEtal supported MOnocrystalline Silicon (MEMO), has been compared to the costs of production of a standard Si cell and three advanced cell concepts: Passivated Emitter Rear Cell (PERC-like), Hetero-junction with Intrinsic Thin layer (HIT) and Interdigitated back contact solar cell (ICB). The cost estimation model included detailed price tags for every step in the module supply chain including costs of capital [200]. An additional adjustment function took into account the different efficiency potentials of the investigated cell technologies and allowed the comparison on system level.
The actual technically feasible limits for standard Silicon cells process are reported in [27] have been compared with the other cell concepts in [200]. The limit values adopted in [200] for the standard Silicon cells process are: poly Si feedstock price of 20 $/kg, diamond wire wafering, Si consumption of 290 μm per solar cell and a kerf loss of 130 μm.
For the MEMO process, wire and slurry were not needed for exfoliation and therefore they are omitted in the cost analysis. The remaining wafer production costs (such as utility, building and maintenance) have been adapted in [200] from the standard process, because a cost analysis for kerf-less wafering at industrial scale was not available. In this case the Si thickness considered for the cost analysis was 50 μm. The major cost in the MEMO process remains the evaporation of Aluminum. For this reason the costs for the deposition of the Al stressor layer should be reduced to make the MEMO process price-competitive.

Another possibility presented in [200] is the choice of an appropriate alternative metal, as for instance Nickel [38, 201, 202], which leads to a reduction of the production costs but not of the material price. Thus, this option is less competitive compared to a different Al deposition technique. Afterwards the costs of the cell and module production including the cell-to-module losses for each solar cell type have been considered in [200]. The resulting prices, finally, have been normalized to the standard Si cell price to access the relative price advantages of the different cell and module concepts [200]. The final module prices for the different solar cells concept are shown in Fig.7.8.

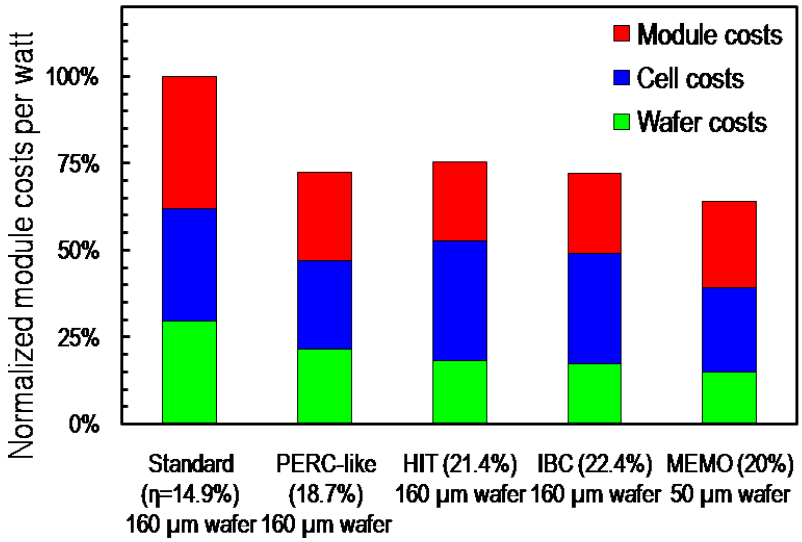

Figure 7.8: Efficiency-adjusted module prices normalized to standard p-type solar cells for MEMO and three other advanced cell concepts, adapted from [200].

It comes out that a MEMO device has an expected module conversion efficiency of 20%, with 11 to 36% lower costs on module level compared to other cell concepts. These savings are payed off if the cell process can be kept simple and competitive conversion efficiencies can be reached, just as for the MEMO device. Passivated emitter and rear cells (PERC) seem to be most competitive among the other cell technologies. MEMO has a relative price advantage of 11 % compared to PERC. These cost savings are due to due to the reduced Si consumption. Further price reductions in the standard wafer production would lead to a lower cost advantage for the kerfless process. However the module and cell cost portions of the MEMO process are not higher than for the other future technologies. Thus, spalling approach can be competitive if the efficiency of a MEMO devices is improved. In addition the

kerf-less process and the numerical method developed may be applied also to the exfoliation of other bilayer for different application and device, whose initial cost is higher than Si, i.e. GaAs or Ge [203, 204]. In this way the cost reduction and the material saving have a higher impact on the final products.
Future prospects of the present work may regard the simulation and investigation of the moisture diffusion from the EVA layer through the channel crack in Silicon cell, which induces oxidation of the grid line.

Bibliography

[1] B. P. Jelle and C. Breivik. State-of-the-art building integrated photovoltaics. *Energy Procedia*, 20:68–77, 2012.

[2] A.E. Becquerel. Recherches sur les effets de la radiation chimique de la lumiére solaire au moyen des courants électriques, 1839.

[3] A.E. Becquerel. Mémoire sur les effets électriques produits sous l'influence des rayons solaires, 1839.

[4] D. Chapin, C. Fuller, and G. Pearson. A new silicon p-n junction photocell for converting solar radiation into electrical power, 1954.

[5] D.C. Reynolds, G. Leies, L.L. Antes, and R.E. Marburger. Photovoltaic effect in cadmium sulfide. *Physical Review*, 96(2):533, 1954.

[6] D.A. Cusano. CdTe solar cells and photovoltaic heterojunctions in II VI compounds, 1963.

[7] M.B. Prince. Silicon solar energy converters. *Journal of Applied Physics*, 26:534–540, 1955.

[8] J.J Loferski and J. Joseph. Theoretical considerations governing the choice of the optimum semiconductor for photovoltaic solar energy conversion. *Journal of Applied Physics*, 27(7):777–784, 1956.

[9] J.J. Wysocki and P. Rappaport. Effect of temperature on photovoltaic solar energy conversion. *Journal of Applied Physics*, 31(3):571–578, 1960.

[10] W. Shockley and J.H. Queisser. Detailed balance limit of efficiency of p-n junction solar cells. *Journal of applied physics*, 32(3):510–519, 1961.

[11] M. Paggi, M. Corrado, and M.A. Rodriguez. A multi-physics and multi-scale numerical approach to microcracking and power-loss in photovoltaic modules. *Composite Structure*, 95:630–638, 2013.

[12] S. Rein, , K. Bothe, and B. Sattler. Qualitätssicherung und-kontrolle in der photovoltaikproduktion. *FVS, BSW-Solar*, pages 120–127, 2007.

[13] *IEC 61215 - Crystalline silicon terrestrial photovoltaic (PV) modules*.

[14] M. Koentges, C. Packard S. Kurtz, U. Jahn, K.A. Berger, K. Kato, T.Friesen, H. Liu, and M. Van Iseghem. IEA PVPS task 13, performance and reliability of photovoltaic systems. subtask 3.2: review of failures of photovoltaic modules. Technical Report ISBN 978-3-906042-16-9, Institute for Solar Energy Research Hamelin and National Renewable Energy Laboratory and TUEV and Austrian Institute of Technology and National Institute of Advanced Industrial Science and Technology and Institute of Electrical Engineering-Chinese Academy of Sciences and Electricitéde France, 2014.

[15] *Degradation mechanisms in Si module technologies observed in the field; their analysis and statistics*, 2011.

[16] *IEC 61646 - Thin-film terrestrial photovoltaic (PV) modules*.

[17] *IEC 60904-3 - Photovoltaic devices*.

[18] C.A. Gueymard, D. Myers, and K. Emery. Proposed reference irradiance spectra for solar energy systems testing. *Solar energy*, 73(6):443–467, 2002.

[19] R. Tscharner, K.H.S. Rao, R. Schwarz, and A.V. Shah. Evaluation of photovoltaic panels with ir thermography, 1985.

[20] *Analysis of PV Modules by Electroluminescence and IR Thermography*, Hamburg, Germany, 2009. Proceedings of 24th European Photovoltaic Solar Energy Conference.

[21] S. Zamini, R. Ebner, G.Újvári, and B. Kubicek. Non-destructive techniques for quality control of photovoltaic modules: Electroluminescence imaging and infrared thermography. *Photovoltaics International*, 15:126–135, 2012.

[22] K. Kato. Taiyoko hatsuden sisutem no fuguai jirei fairu. Technical report, 2010.

[23] F.J. Pern. Ethylene-vinyl acetate (eva) encapsulants for photovoltaic modules: degradation and discoloration mechanisms and formulation modification for improved photostability. *Angew. Makromol. Chem.*, 252:195–216, 1997.

[24] J. Schlothauer, S. Jungwirth, B. Roeder, and M. Koehl. Flourescence imaging - a powerful tool for the investigation of polymer degradation in pv modules. *Photovoltaics International*, 10:149–154, 2010.

[25] F.J. Pern. Factors that affect the eva encapsulant discoloration rate upon accelerated exposure. *Solar Energy Materials and Solar Cells*, pages 587–615, 1996.

[26] *Cell cracks measured by UV fluorescence in the field*, Frankfurth, Germany, 2012. Proceedings of 27th European Photovoltaic Solar Energy Conference.

[27] S. Raithel, Liu T, P. Lee, and B. Weiss. International technology roadmap for photovoltaic results 2013. Technical report, March 2014.

[28] S. Nagatsuka, S. Shibaoka, and J. Tsuchishima. Wire saw and slicing method thereof. Technical report, 1999. US Patent 5,904,136.

[29] Applied Materials. Advanced wire sawing technology for solar photovoltaic cells. Technical report, Applied Materials, 2012.

[30] *Investigations on the wire wear due to material removal mechanisms in the wire sawing process*, 2011. 5th International Workshop on Science and Technology of Crystalline Silicon Solar Cells.

[31] F. Henley, S. Kang, Z. Liu, L. Tian, J. Wang, and Y.L. Chow. Beam-induced wafering technology for kerf-free thin pv manufacturing. In *Photovoltaic Specialists Conference (PVSC), 2009 34th IEEE*, pages 001718–001723. IEEE, 2009.

[32] L. Lichtensteiger and C. Pfeffer. Production of free-standing solid state layers by thermal processing of substrates with a polymer. Technical report, November 18 2010. US Patent App. 12/740,373.

[33] F. Henley, A. Lamm, S. Kang, Z. Liu, and L.Tian. Direct film transfer (dft) technology for kerf-free silicon wafering. In *Proceedings of the 23rd European Photovoltaic Solar Energy Conference*, pages 1090–1093, 2008.

[34] Rolf Brendel. A novel process for ultrathin monocrystalline silicon solar cells on glass. In *14th European Photovolaic Solar Energy Conference, Jun*, 1997.

[35] H. Tayanaka, K. Yamauchi, and T. Matsushita. Thin-film crystalline silicon solar cells obtained by separation of a porous silicon sacrificial layer. In *Proceedings of 2nd World Conference Photovoltaic Solar Energy Conversion*, pages 1272–1275, 1998.

[36] J. H. Petermann, D. Zielke, J. Schmidt, F. Haase, E.G. Rojas, and R. Brendel. 19% - efficient and 43 μ m-thick crystalline si solar cell from layer transfer using porous silicon. *Prog. Photovolt: Res. Appl.*, 20:1–5, 2012.

[37] S. Schaefer, M. Ernst, S. Kajari-Schroeder, and R. Brendel. Multilayer etching for kerf-free solar cells from macroporous silicon. *Energy Procedia*, 38:933–941, 2013.

[38] R.A. Rao, L. Mathew, S. Saha, S. Smith, D. Sarkar, R. Garcia, R. Stout, A. Gurmu, E. Onyegam, and D. Ahn. A novel low cost 25μm thin exfoliated monocrystalline si solar cell technology. In *Photovoltaic Specialists Conference (PVSC), 2011 37th IEEE*, pages 001504–001507. IEEE, 2011.

[39] F. Dross, J. Robbelein, B. Vandevelde, E. Van Kerschaver, I. I. Gordon, G. Beaucarne, and J. Poortmans. Stress-induced large-area lift-off of crystalline si films. *Appl Phys A-Mater.*, 89:149–152, 2007.

[40] R. Martini, M. Gonzalez, F. Dross, A. Masolin, J. Vaes, D. Frederickx, and J. Poortmans. Epoxy-induced spalling of silicon. *Energy Procedia*, 27:567–572, 2012.

[41] J. Hensen, R. Niepelt, S. Kajari-Schroeder, and R. Brendel. Directional heating and cooling for controlled spalling. *IEEE Journal of Photovoltaic*, 1:195–201, 2015.

[42] M. Tanielian, S. Blackstone, and R. Lajos. A new technique of forming thin free standing single-crystal films. *J. Electrochem. Soc.*, 132:507–509, 1985.

[43] Z. Suo and J. W. Hutchinson. Steady-state cracking in brittle substrates beneath adherent films. *International Journal of Solids and Structures*, 25:1337–1353, 1989.

[44] Z. Suo and J.W. Hutchinson. Interface crack between two elastic layers. *International Journal of Solids and Structures*, 43:1–18, 1990.

[45] A. G. Evans, B. J. Dalgleish, M. He, and J. W. Hutchinson. On crack path selection and the interfacial fracture energy in biomaterial systems. *Acta Metallurgica et Materialia*, 34:3249–3254, 1989.

[46] S.W. Bedell, D. Shahrjerdi, B. Hekmatshoar, K. Fogel, P.A. Lauro, J. A. Ott, N. Sosa, and D. Sadana. Kerf-less removal of si, ge, and iii-v layer by controlled spalling to enable low-cost pv technologies. *IEEE J. Photovolt.*, 2:141–147, 2012.

[47] P. Bellanger, M.C. Brito, M.D. Pera, I. Costa, G. Gaspar, R. Martini, M. Debucquoy, and J.M. Serra. New stress activation method for kerfless silicon wafering using ag/al and epoxy stress-inducing layers. *IEEE Journal of Photovoltaic*, 5:1228–1234, 2014.

[48] T. L. Anderson. *Fracture Mechanics. Fundamentals and applications (3_{rd} Editon)*. Taylor & Francis, New York, 2005.

[49] A. A. Griffith. The phenomena of rupture and flow in solids. *Philosophical Transactions, Series A*, 221:163–198, 1920.

[50] C.E. Inglis. Stress in a plate due to the presence of cracks and sharp corners. *Transactions of the Institute of Naval Architect*, 55:219–241, 1913.

[51] G.R. Irwin. Fracture dynamics. *Fracturing of Metals, American Society for Metals*, 152:147–166, 1948.

[52] E. Orowan. Fracture and strength of solids. *Reports on progress in physics*, 12(1):185, 1949.

[53] G.R. Irwin. Onset of fast crack propagation in high strength steel and aluminum. In *Proc. Sec. Sagamore Conf*, volume 2, page 289.

[54] H.M. Westergaard. Bearing pressures and cracks, 1939.

[55] G.R. Irwin. Analysis of stresses and strains near the end of a crack traversing a plate. *Journal of Applied Mechanics*, 24:361–364, 1957.

[56] M. L. Williams. On the stress distribution at the base of a stationary crack. *Journal of Applied Mechanics*, 24:109–114, 1957.

[57] Royal Society, editor. *The Distribution of Stress in the Neighbourhood of a Crack in an Elastic Solid*. Royal Society, October 1946. Proceedings of the Royal Society of London. Series A.

[58] L. Lapidus and G. F. Pinder. *Numerical Solution of Partial Differential Equations in Science and Engineering*. John Wiley & Sons, New York, 1982.

[59] O. C. Zienkiewicz and R. L. Taylor. *The Finite Element Method. (4th edition)*. McGraw-Hill, New York, 1989.

[60] F.J. Rizzo. An integral equation approach to boundary value problems of classical elastostatics. *Quarterly of Applied Mathematics*, 25:83–95, 1967.

[61] Peter Wriggers. *Nonlinear finite element methods*. Springer Science & Business Media, 2008.

[62] O.C. Zienkiewicz and R.L. Taylor. *The finite element method: solid mechanics*, volume 2. Butterworth-heinemann, 2000.

[63] S.K. Chan, I.S. Tuba, and W.K. Wilson. On the finite element method in linear fracture mechanics. *Engineering Fracture Mechanics*, 2:1–17, 1970.

[64] C.F. Shih, H.G. Delorenzi, and M.D. German. Crack extension modeling with singular quadratic isoparametric elements. *International Journal of Fracture*, 1:647–3651, 1976.

[65] D.M. Tracey. On the use of isoparametric finite elements in linear fracture mechanics. *International Journal for Numerical Methods in Engineering*, 11:487–502, 1977.

[66] D.M. Parks. Stiffness derivative finite element technique for determination of crack-tip stress intensity factors. *International Journal of Fracture*, 10:487–502, 1974.

[67] T.K. Hellen. On the method of virtual crack extension. *International Journal for Numerical Methods in Engineering*, 9:187–207, 1975.

[68] E. R. Rybicki and M. F. Kanninen. A finite element calculation of stress intensity factors by a modified crack closure integral. *Engineering Fracture Mechanics*, 9:931–938, 1977.

[69] S. Ramamurthy, T. Krishnamurthy, K. Badari Narayana, K. Vijayakumar, and B. Dattaguru. Modified crack closure integral method with quarter point elements. *Mechanics Research Communications*, 13:179–186, 1986.

[70] I.S. Raju. Calculation of strain-energy release rates with higher order and singular finite elements. *Engineering Fracture Mechanics*, 28:251–274, 1987.

[71] R. Singh, B. Carter, P. Wawrzynek, and A. Ingraffea. Universal crack closure integral for sif estimation. *Engineering Fracture Mechanics*, 60:133–146, 1998.

[72] J.R. Rice. A path independent integral and the approximate analysis of strain concentration by notches and cracks. *Journal of Applied Mechanics*, 35:379–386, 1968.

[73] G. P. Cherepanov. Calculation of fracture parameters for a general corner. *Journal of Applied Mathematics and Mechanics*, 31:504, 1967.

[74] B. Budiansky and J. Rice. Conservation laws and energy release rates. *Journal of Applied Mechanics*, 40:201–203, 1973.

[75] F.Z. Li, C.F. Shih, and A. Needleman. A comparison of methods for calculating energy release rates. *Engineering Fracture Mechanics*, 21:405–421, 1985.

[76] K. J. Miller and R. F. Smith, editors. *J-integral of a mixed mode crack and its application*, London, 1979. Pergamon. Proceedings of the 3rd International Conference on Mechanical Behavior of Materials.

[77] H.D. Bui. Associated path independent j-integral for separating mixed modes. *Journal of the Mechanics and Physics of Solids*, 31:439–448, 1983.

[78] J. Č,ervenka and V. E. Saouma. Numerical evaluation of 3d sif for arbitrary finite element meshes. *Engineering Fracture Mechanics*, 57:541–563, 1997.

[79] J. F. Yau, S. S. Wang, and H. T. Corten. Multifractal scaling laws in the breaking behaviour of disordered materials. *Journal of Applied Mechanics*, 47:335–341, 1980.

[80] F. Erdogan and G.C. Sih. On the crack extension in plates under plane loading and transverse shear. *Journal of Basic Engineering*, 85:519–525, 1963.

[81] T.K. Hellen and W.S. Blackburn. The calculation of stress intensity factors for combined tensile and shear loading. *International Journal of Fracture*, 11:605–617, 1975.

[82] C.G. Sih. Strain-energy-density factor applied to mixed mode crack problems. *International Journal of Fracture*, 10:305–321, 1974.

[83] Z.P. Bazant. Size effect in blunt fracture: Concrete, rock, metal. *Journal of Engineering Mechanics*, 110:518–535, 1984.

[84] D.S. Dugdale. Yielding in steel sheets containing slits. *Journal of the Mechanics and Physics of Solids*, 8:100–104, 1960.

[85] G. I. Barenblatt. *The mathematical theory of equilibrium cracks in brittle fracture, Advances in Applied Mechanics*, volume VII. Academic Press, New York, 1962.

[86] A. Hillerborg, M. Modeer, and P. E. Petersson. Analysis of crack formation and crack growth in concrete by means of fracture mechanics and finite elements. *Cement and Concrete Research*, 6:773–782, 1976.

[87] F.H. Wittmann, editor. *Influence of material parameters and geometry on cohesive crack propagation*, Amsterdam, 1986. Elsevier. Proceedings of an International Conference on in Fracture Mechanics of Concrete, Lausanne, Switzerland, 1985.

[88] A. Carpinteri. Softening and snap-back instability in cohesive solids. *International Journal for Numerical Methods in Engineering*, 28:1521–1537, 1989.

[89] Z.P. Bazant, J. Ozbolt, and R. Eligehausen. Fracture size effect: review of evidence for concrete structures. *ASCE Journal of Structural Engineering*, 120:2377–2398, 1994.

[90] Z. Bazant, editor. *Mixed mode fracture of rock-concrete interfaces*, Prague, Czech Republic, 1994. US-Europe Workshop on Fracture and Damage of Quasi-Brittle Materials: Experiment, Modeling and Computer Analysis.

[91] A. Carpinteri. *Non linear crack models for nonmetallic materials*. Kluwer Academic Publisher, Dordrecht, 1999.

[92] A. Signorini. Sopra alcune questioni di elastostatica. *Atti della Societa Italiana per il Progresso delle Scienze*, 1933.

[93] Gaetano Fichera. *Problemi elastostatici con vincoli unilaterali: il problema di Signorini con ambigue condizioni al contorno*. Accademia Nazionale dei Lincei, 1964.

[94] A. Hillerborg. Application of the fictitious crack model to different materials. *International Journal of Fracture*, 51:95–102, 1991.

[95] Z.P. Bazant and M.T. Kazemi. Determination of fracture energy, process zone length and brittleness number from size effect, with application to rock and concrete. *International Journal of Fracture*, 44:111–131, 1990.

[96] Z. P. Bazant and M.T. Kazemi. Size dependence of concrete fracture energy determined by rilem work-of-fracture method. *International Journal of Fracture*, 51:121–138, 1991.

[97] J. Planas and M. Elices. Nonlinear fracture of cohesive materials. *International Journal of Fracture*, 51:139–157, 1991.

[98] J. Mazars, G. Pijaudier-Cabot, and C. Saourdis. Size effect and continuous damage in cementitious materials. *International Journal of Fracture*, 51:159–173, 1991.

[99] M. Corrado, M. Paggi, and A. Carpinteri. A multi-scale numerical method for the study of size-scale effects in ductile fracture. *Metals*, 4:428–444, 2014.

[100] A. Carpinteri. Post-peak and post-bifurcation analysis on cohesive crack propagation. *Engineering Fracture Mechanics*, 32:265–278, 1989.

[101] M. Paggi and P. Wriggers. A nonlocal cohesive zone model for finite thickness interfaces - part i: mathematical formulation and validation with molecular dynamics. *Computational Materials Science*, 50:1625–1633, 2011.

[102] A. Sapora and M. Paggi. A coupled cohesive zone model for transient analysis of thermoelastic interface debonding. *Computational Mechanics*, 53:845–857, 2013.

[103] G. Bfer. An isoparametric joint/interface element for finite element analysis. *International journal for numerical methods in engineering*, 21:585–600, 1985.

[104] V. Tvergaard. Effect of fiber debonding in a whisker-reinforced metal. *Materials Science and Engineering A*, 2, 1990.

[105] N. Point and E. Sacco. Delamination of beams: an application to the dcb specimen. *International Journal of Fracture*, 79:225–247, 1996.

[106] M. Ortiz and A. Pandolfi. Caltech asci technical report 090. *International Journal for Numerical Methods in Engineering*, 44:1267–1282, 1999.

[107] J. Segurado and J. LLorca. A new three-dimensional interface finite element to simulate fracture in composites. *International Journal of Solids and Structures*, 44:2977–2993, 2004.

[108] P.D. Zavattieri, P.V. Raghuram, and H.D. Espinosa. A computational model of ceramic microstructures subjected to multi-axial dynamic loading. *Journal of the Mechanics and Physics of Solids*, 49:27–68, 2001.

[109] S. Li, M.D. Thouless, A.M. Waas, J.A. Schroeder, and P.D. Zavattieri. Use of mode-i cohesive-zone models to describe the fracture of an adhesively-bonded polymer-matrix composite. *Composites Science and Technology*, 65:281–293, 2005.

[110] C. Leppin and P. Wriggers. Numerical simulation of rapid crack propagation in viscoplastic materials. *Computers and Structures*, 61:1169–1175, 1996.

[111] J.C.J. Schellekens and R. de Borst. A non-linear finite element approach for the analysis of mode-i free delamination in composites. *International Journal of Solid and Stuctures*, 30:1239–1253, 1993.

[112] M. Paggi and P. Wriggers. A nonlocal cohesive zone model for finite thickness interfaces - part II: FE implementation and application to polycrystalline materials. *Computational Materials Science*, 50:1634–1643, 2011.

[113] G. Beer. An isoparametric joint/interface element for the analysis of fractured rock. *Int J Numer Meth Eng*, 21:585–600, 1985.

[114] V. Tvergaard. Effect of fibre debonding in a whisker-reinforced metal. *Materials Science and Engineering: A*, 125(2):203–213, 1990.

[115] N. Point and E. Sacco. Delamination of beams: an application to the dcb specimen. *International Journal of Fracture*, 79(3):225–247, 1996.

[116] J. Segurado and J. LLorca. A new three-dimensional interface finite element to simulate fracture in composites. *International Journal of Solids and Structures*, 41(11):2977–2993, 2004.

[117] S. Li, M.D. Thouless andA.M. Waas, J.A. Schroeder, and P.D. Zavattieri. Use of mode-i cohesive-zone models to describe the fracture of an adhesively-bonded polymer-matrix composite. *Composites Science and Technology*, 65(2):281–293, 2005.

[118] C. Leppin and P. Wriggers. Numerical simulation of rapid crack propagation in viscoplastic materials. *Computers & structures*, 61(6):1169–1175, 1996.

[119] J.C.J. Schellekens and R. De Borst. On the numerical integration of interface elements. *International Journal for Numerical Methods in Engineering*, 36(1):43–66, 1993.

[120] M. Ortiz and A. Pandolfi. A class of cohesive elements for the simulation of three-dimensional crack propagation. *International Journal for Numerical Methods in Engineering*, 44(9):1267–1282, 1999.

[121] M.Ortiz and A. Pandolfi. Finite-deformation irreversible cohesive elements for three-dimensional crack-propagation analysis. *International Journal for Numerical Methods in Engineering*, 44(9):1267–1282, 1999.

[122] L. Fraas and L. Partain. *Solar Cells and their Applications, Second Edition*. John Wiley & Sons, Singapore, 2010.

[123] O. Breitenstein and S. Rißland. A two-diode model regarding the distributed series resistance. *Solar Energy Materials and Solar Cells*, 110:77–86, 2013.

[124] J. Kaesewieter, F. Haase, M.H. Larrodé, and M. Koentges. Cracks in solar cell metallization leading to module power loss under mechanical loads. *Energy Procedia*, 55:469–477, 2014.

[125] T. Fuyuki, H. Kondo, Y. Kaji, A. Ogane, and Y. Takahashi. Analytic findings in the electroluminescence characterization of crystalline silicon solar cells. *Journal of Applied Physics*, 101:0237111–0237115, 2007.

[126] M. Paggi, I. Berardone, A. Infuso, and M. Corrado. Fatigue degradation and electric recovery in silicon solar cells embedded in photovoltaic modules. *Scientific Reports*, 4:1–7, 2014.

[127] P.K. Kulshreshtha, K.M. Youssef, and G. Rozgonyi. Nano-indentation: A tool to investigate crack propagation related phase transitions in pv silicon. *Solar Energy Materials & Solar Cells*, 96:166–172, 2012.

[128] G. E. Dieter. *Mechanical metallurgy*. Mc Graw-Hill Book Co., New York, 1988.

[129] I. Yonenaga. Hardness, yield strength, and dislocation velocity, in elemental and compound semiconductors. *Materials Transactions*, 46:1979–1985, 2005.

[130] B. Ya. Farber, S. Y. Yoon, K. P. D. Lagerlof, and A. H. Heuer. Microplasticity during high temperature indentation and the peierls potential in sapphire (α-al2o3) single crystals. *Physica Status Solidi A*, 137:485–498, 1993.

[131] Yu V. Milman I. V. Gridneva and V. I. Trefilov. Phase transition in diamond-structure crystals. *Physica Status Solidi*, 14:177–182, 1972.

[132] V. S. Ivanova and G. V. Vstovskii. Mechanical properties of metals and alloys from synergetical viewpoint. *ltogi Nauki i Techniki. Metallovedenie i Termicheskaya Obrabotka*, 24:43–83, 1990.

[133] G. Coletti, C.J.J. Tool, and L.J. Geerligs. Quantifying surface damage by measuring mechanical strength of silicon wafers. In *Presented at the 20th European Photovoltaic Solar Energy Conference and Exhibition*, volume 6, page 10, 2005.

[134] B.R. Lawn, D.B. Marshall, and P. Chantikul. Mechanics of strength-degrading contact flaws in silicon. *Journal of Materials Science*, 16(7):1769–1775, 1981.

[135] D.B. Marshall, B.R. Lawn, and A.G. Evans. Elastic/plastic indentation damage in ceramics: The lateral crack system. *Journal of the American Ceramic Society*, 65:561–566, 1982.

[136] M.J. Buehler and H. Gao. Dynamical fracture instabilities due to local hyperelas- ticity at crack tips. *Nature*, 439:307–310, 2006.

[137] P. Puech, S. Pinel, R. Jasinevicius, and P. Pizani. Mapping the three-dimensional strain field around a microindentation on silicon using polishing and raman spectroscopy. *Journal of Applied Physics*, 88:4582–4585, 2000.

[138] F. Demangeot, P. Puech, V. Domnich, Y.G. Gogotsi, S. Pinel, P.S. Pizani, and R.G. Jasinevicius. Raman mapping devoted to the phase transformation and strain analysis in si micro-indentation. *Advanced Engineering Materials*, 4:543–546, 2002.

[139] I. Berardone, M. Corrado, and M. Paggi. A generalized electric model for mono and polycrystalline silicon in the presence of cracks and random defects. *Energy Procedia*, 55:22–29, 2014.

[140] M Paggi, M Corrado, and I Berardone. A global/local approach for the prediction of the electric response of cracked solar cells in photovoltaic modules under the action of mechanical loads. *Engineering Fracture Mechanics*, 2016.

[141] E. Pietropaoli and A. Riccio. A global/local finite element approach for predicting interlaminar and intralaminar damage evolution in composite stiffened panels under compressive load. *Applied Composite Mateerials*, 2011.

[142] J. Reinoso, A. Blàzquez, A. Estefani, F. París, J. Ca nas, E. Arévalo, and F. Cruz. Experimental and three-dimensional global local finite element analysis of a composite component including degradation process at the interfaces. *Composites B*, 43:1929–1942, 2012.

[143] M. Sander, S. Dietrich, M. Pander, M. Ebert, and J. Bagdahn. Systematic investigation of cracks in encapsulated solar cells after mechanical loading. *Solar Energy Materials and Solar Cells*, 2013.

[144] J. Reinoso, M. Paggi, and R. Rolfes. A computational framework for the interplay between delamination and wrinkling in functionally graded thermal barrier coatings. *Computational Materials Science*, 2015.

[145] U. Eitner. *Thermomechanics of Photovoltaic Modules*. PhD thesis, Zentrum fuer Ingenieurwissenschaften der Martin-Luther-Universität Halle-Wittenberg, Germany, 2011.

[146] M. Paggi, S. Kajari-Schroeder, and U. Eitner. Thermomechanical deformations in photovoltaic laminates. *Journal of Strain Analysis for Engineering Design*, 2011.

[147] M. Paggi and A. Sapora. An accurate thermoviscoelastic rheological model for ethylene vinyl acetate based on fractional calculus. *International Journal of Photoenergy*, 2015.

[148] M. Paggi and J. Reinoso. An anisotropic large displacement cohesive zone model for fibrillar and crazing interfaces. *International Journal of Solids and Structures*, 2015.

[149] Y. Takahashi, Y. Kaji, A. Ogane, Y. Uraoka, and T. Fuyuki. Luminoscopy-novel tool for the diagnosis of crystalline silicon solar cells and modules utilizing electroluminescence. In *Photovoltaic Energy Conversion, Conference Record of the 2006 IEEE 4th World Conference on*, volume 1, pages 924–927. IEEE, 2006.

[150] A.M. Gabor, M. Ralli, S. Montminy, L. Alegria, C. Bordonaro, J. Woods, L. Felton, M. Davis, B. Atchley, and T. Williams. Soldering induced damage to thin si solar cells and detection of cracked cells in modules. In *21st European Photovoltaic Solar Energy Conference, Dresden, Germany, September*, pages 4–8, 2006.

[151] P. Wuerfel, T. Trupke, T. Puzzer, E. Schaffer, W. Warta, and S. Glunz. Diffusion length of silicon solar cells from luminescence images. *Journal of Applied Physics*, 101:123110, 2007.

[152] *Combined quantitative analysis of electroluminescence images and LBIC mappings*, Milan, Italy, 2007. Proceedings of 22nd European Photovoltaic Solar Energy Conference.

[153] K. Bothe, P. Pohl, J. Schmidt, T. Weber, P. Altermatt, B. Fischer, and R. Brendel. Electroluminescence imaging as an in-line characterisation tool for solar cell production. In *21st European Photovoltaik Solae Energy Conference, Dresden*, 2006.

[154] D. Hinken, K. Ramspeck, K. Bothe, B. Fischer, and R. Brendel. Series resistance imaging of solar cells by voltage dependent electroluminescence. *Applied Physics Letters*, 91:182104, 2007.

[155] J. Haunschild, M. Glatthaar, M. Kasemann, S. Rein, and E.R. Weber. Fast series resistance imaging for silicon solar cells using electroluminescence. *Physica Status Solidi*, 3:227–229, 2009.

[156] S.O. Ojo and M. Paggi. A thermo-visco-elastic shear-lag model for the prediction of residual stresses in photovoltaic modules after lamination. *Composite Structures*, 136, 2015.

[157] S. Kajari-Schroeder, I. Kunze I, and M. Koentges. Criticality of cracks in pv modules. *Energy Procedia*, 27:658–663, 2012.

[158] S. Kajari-Schroeder, I. Kunze, U. Eitner, and M. Koentges. Spatial and orientational distribution of cracks in crystalline photovoltaic modules generated by mechanical load tests. *Solar Energy Materials and Solar Cells*, 2011.

[159] R. Khatri, S. Agarwal, I. Saha, S. K. Singh, and B. Kumar. Study on long term reliability of photo-voltaic modules and analysis of power degradation using accelerated aging tests and electroluminescence technique. *Energy Procedia*, 8:396–401, 2011.

[160] *The effect of accelerated aging tests on the optical proprities of silicone and EVA encapsulants*, 2009. Proceedings of 24th European Photovoltaic Solar Energy Conference.

[161] *Photovoltaic Modules Reliability on Accelerated and Natural Test - The ELVIRE Project*. IEEE, 2012. Proceedings of 27th European Photovoltaic Solar Energy Conference and Exhibition.

[162] J.R. Ross. Flat-plate photovoltaic array design optimization. In *14th Photovoltaic Specialists Conference*, volume 1, pages 1126–1132, 1980.

[163] A. N. Strahler. *Geografia fisica*. Piccin-Nuova Libraria, Padova, 1993.

[164] J.H. Wohlgemuth, D.W. Cunningham, A.M. Nguyen, and J. Miller. Long term reliability of pv modules. In *Proceedings of the 20th European Photovoltaic Solar Energy Conference*. Citeseer, 2005.

[165] *Equating damp heat testing with field failures of PV modules*. IEEE, 2013. Proceedings of 39th Photovoltaic Specialists Conference (PVSC).

[166] *Outdoor Weathering of PV Modules - Effects of Various Climates and Comparison with Accelerated Laboratory Testing*. IEEE, 2011. Proceedings of 37th IEEE Photovoltaic Specialists Conference (PVSC).

[167] I. Berardone, S. Kajari-Schroeder, R. Niepelt, J. Hensen, V. Steckenreiter, and M. Paggi. Numerical modelling and validation of thermally-induced spalling. *Energy Procedia*, 77:855–862, 2015.

[168] R.M. Cannon, R.M. Fisher, and A.G. Evans. Decohesion of thin films from ceramic substrates. In *MRS Proceedings*, volume 54, page 799. Cambridge Univ Press, 1985.

[169] M.S. Hu, M.D. Thouless, and A.G. Evans. The decohesion of thin films from brittle substrates. *Acta Metallurgica*, 36:1301–1307, 1988.

[170] M.D. Thouless, A.G. Evans, M.F. Ashby, and J.W. Hutchinson. The edge cracking and spalling of brittle plates. *Acta Metallurgica*, 35:1333–1341, 1987.

[171] M.D. Drory, M.D. Thouless, and A.G. Evans. On the decohesion of residually stressed thin film. *Acta Metallurgica*, 36:2019–2028, 1988.

[172] A. G. Evans, M. D. Drory, and M.S. Hu. The cracking and decohesion of films. *Journal of Materials Research*, 3:1034–1049, 1988.

[173] J. W. Hutchinson and Z. Suo. Mixed-mode cracking in layered materials. *Advances in Applied Mechanics*, 29:63–191, 1992.

[174] T. N. Bittencourt and P.A. Wawrzynek. Quasi-automatic simulation of crack propagation for 2d LEFM problems. *Engineering Fracture Mechanics*, 55:321–334, 1996.

[175] G.H. Staab. A variable power singular element for analysis of fracture mechanics problems. *Computers & Structures*, 9:449–457, 1983.

[176] A. Carpinteri, M. Paggi, and N. Pugno. Numerical evaluation of generalized stress-intensity factors in multi-layered composites. *International journal of solids and structures*, 43(3):627–641, 2006.

[177] M.D. Tracey. Finite elements for determination of crack tip elastic stress intensity factors. *Engineering Fracture Mechanics*, 3:255–265, 1971.

[178] M.A. Hussain, S.L. Pu, and J. Underwood. Strain energy release rate for a crack under combined mode i and mode ii. *Fracture Analysis, ASTM STP*, 2:2–28, 1993.

[179] A. Masolin, P. O. Bouchard, R. Martini, and M. Bernacki. Thermo-mechanical and fracture properties in single-crystal silicon. *Journal of Materials Science*, 48:979–988, 2013.

[180] R.O. Ritchie, J.F. Knott, and J.R. Rice. On the relationship between critical tensile stress and fracture toughness in mild steel. *Journal of the Mechanics and Physics of Solids*, 21(6):395–410, 1973.

[181] S. Mariani, A. Ghisi, A. Corigliano, and S. Zerbini. Modeling impact-induced failure of polysilicon mems: a multi-scale approach. *Sensors*, 9(1):556–567, 2009.

[182] Aldo Ghisi, Stanislaw Kalicinski, Stefano Mariani, Ingrid De Wolf, and Alberto Corigliano. Polysilicon mems accelerometers exposed to shocks: numerical–experimental investigation. *Journal of Micromechanics and Microengineering*, 19(3):035023, 2009.

[183] A. Corigliano, R. Ardito, C. Comi, A. Frangi, A. Ghisi, and S. Mariani. Microsystems and mechanics. *Procedia IUTAM*, 10:138–160, 2014.

[184] M. Paggi and M. Ciavarella. The coefficient of proportionality κ between real contact area and load, with new asperity models. *Wear*, 268(7):1020–1029, 2010.

[185] G. Zavarise, M. Borri Brunetto, and M. Paggi. On the resolution dependence of micromechanical contact models. *Wear*, 262(1):42–54, 2007.

[186] M. Ciavarella, J.A. Greenwood, and M. Paggi. Inclusion of interaction in the greenwood and williamson contact theory. *Wear*, 265(5):729–734, 2008.

[187] G. Zavarise, M. Borri-Brunetto, and M. Paggi. On the reliability of microscopical contact models. *Wear*, 257(3):229–245, 2004.

[188] M.Paggi and Q.C. He. Evolution of the free volume between rough surfaces in contact. *Wear*, 336:86–95, 2015.

[189] C. Borri and M. Paggi. Topological characterization of antireflective and hydrophobic rough surfaces: are random process theory and fractal modeling applicable? *Journal of Physics D: Applied Physics*, 48(4):045301, 2015.

[190] J.A. Greenwood. A simplified elliptic model of rough surface contact. *Wear*, 261(2):191–200, 2006.

[191] G.P. Cherepanov, A. S. Balankin, and V. S. Ivanova. Fractal fracture mechanics a review. *Engineering Fracture Mechanics*, 51(6):997–1033, 1995.

[192] B. Mandelbrot. *The Fractal Geometry of Nature*. W. H. Freeman and Company, 1^{st} ed. edition, 1977.

[193] A.S. Balankin. Fractal mechanics of deformable media and fracture topology of solids. *Doklady Akad Nauk Minerologia USSR*, 322:869–874, 1992.

[194] Z.Q. Mu and C. W.Lung. Studies on the fractal dimension and fracture toughness of steel. *Journal of Physics D: Applied Physics*, 21(5):848, 1988.

[195] J.J. Mecholsky, D.E. Passoja, and K.S. Feinberg-Rigel. Quantitative analysis of brittle fracture surfaces using fractal geometry. *Journal of the American Ceramic Society*, 72:60–65, 1989.

[196] B. M. Smirnov. *Physics of Fractal Clusters*. Nauka, Moscow, 1991.

[197] J. Feder. *Fractals*. Plenum Press, New York, 1991.

[198] H.O. Peitgen and D. Saupe. *The Science of Fractal Images*. Springer-Verlag, New York, 1988.

[199] J.J. Wu. Characterization of fractal surfaces. *Wear*, 239(1):36–47, 2000.

[200] R. Niepelt, J. Hensen, V. Steckenreiter, R. Brendel, and S. Kajari-Schöder. Kerfless exfoliated thin crystalline si wafers with al metallization layers for solar cells. *Journal of Materials Research*, 30(21):3227–3240, 2015.

[201] Y. Kwon, C. Yang, S.H. Yoon, H.D. Um, J.H Lee, and B. Yoo. Spalling of a thin si layer by electrodeposit-assisted stripping. *Applied Physics Express*, 6(11):116502, 2013.

[202] S.W. Bedell, K. Fogel, P. Lauro, D. Shahrjerdi, J.A. Ott, and D. Sadana. Layer transfer by controlled spalling. *Journal of Physics D: Applied Physics*, 46(15):152002, 2013.

[203] A.C. Sweet, K.L. Schulte, J.D. Simon, M.A. Steiner, N. Jain, D.L. Young, A.J. Ptak, and C.E. Packard. Controlled exfoliation of (100) gaas-based devices by spalling fracture. *Applied Physics Letters*, 108(1):011906, 2016.

[204] A.C. Sweet, J.D. Simon, D.L. Young, A.J. Ptak, and C.E. Packard. Effect of material choice on spalling fracture parameters to exfoliate thin pv devices. In *Photovoltaic Specialist Conference (PVSC), 2014 IEEE 40th*, pages 1189–1192. IEEE, 2014.